

Synthesis and Structural Characterization of Coordination Frameworks and Their Potential Applications

**THESIS SUBMITTED FOR THE
DEGREE OF DOCTOR OF PHILOSOPHY (SCIENCE)
JADAVPUR UNIVERSITY**



By

GURUPADA BAIRY, M.Sc.

Registration No: SCHEM1106723

Index No.: 67/23/Chem./28

**DEPARTMENT OF CHEMISTRY
JADAVPUR UNIVERSITY
KOLKATA-700032
WEST BENGAL, INDIA**

2025

Prof. (Dr.) C. Sinha
PhD, FAScT, FESS, FRSC,
Professor & Former Head,
Department of Chemistry



JADAVPUR UNIVERSITY
KOLKATA - 700 032, I N D I A
Mobile: +91-7044231277
e-mail: crsjuchem@gmail.com

CERTIFICATE FROM THE SUPERVISOR

This is to certify that the thesis entitled “*Synthesis and Structural Characterization of Coordination Frameworks and Their Potential Applications*” submitted by **Mr. Gurupada Bairy**, who got his name registered on **02.05.2023** (**Registration No: SCHEM1106723 and Index No.: 67/23/Chem./28**) for the award of Ph.D. (Science) degree of Jadavpur University, is absolutely based upon his own work under the supervision of Prof. Chittaranjan Sinha and that neither this thesis nor any part of it has been submitted for either any degree/diploma or any other academic award anywhere before.

Date: 03/07/2025


(Prof. Chittaranjan Sinha)

Signature of the Supervisor & date with seal


Department of Chemistry
Jadavpur University
Kolkata -700032

Professor of Chemistry
Department of Chemistry
Jadavpur University
Kolkata-700 032

Declaration of the Scholar

I hereby affirm that this written submission genuinely reflects my creative methodologies in my own verbiage, and where others' ideas have been integrated, I have diligently provided appropriate citations from verified sources. I also assert that I have consistently upheld all fundamental principles of academic integrity and honesty, ensuring that no aspect of my submission is misleading, fabricated, or falsified. I acknowledge that any violation of these standards may lead to disciplinary actions from the university and may also entail legal repercussions related to improperly cited sources or for which necessary permissions have not been obtained.

Date: 03.07.2025


Gurupada Bairy



*DEDICATED TO MY
BELOVED PARENTS*

*AND
GRANDPARENTS*

*who made all of this possible, with
endless love, support, and
prayer.*

Acknowledgements

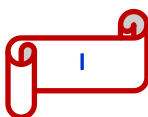
"Analytical Chemistry Building

Ground floor, Chittaranjan Sinha Research Lab"

The past five years were an arduous and protracted trial that compelled me to re-evaluate my scientific aptitude. At times, I grappled with the urge to abandon this endeavour altogether. However, the successful completion of this dissertation would not have been possible without the invaluable assistance of numerous individuals throughout my research career. Now, I wish to express my heartfelt gratitude to those who played a direct or indirect role in the successful culmination of my thesis.

I am deeply grateful to my supervisor, Professor Chittaranjan Sinha, for welcoming me into his lab and entrusting me with such a challenging project. His unwavering support, encouragement, and guidance have been instrumental in bolstering my confidence and progress throughout my research and Ph.D. studies. I am immensely appreciative of the invaluable advice and training he has provided to prepare me for the road ahead. It is an honour to be a member of his esteemed research group, as I could not have asked for a better advisor and mentor for my doctoral journey.

I extend my profound gratitude to the distinguished members of my Research Advisory Committee-Professor Nikhil Guchhait (Subject Expert, Department of Chemistry, UCSTA, Kolkata), Professor Kajal Krishna Rajak (Head, Dept. of Chemistry, JU), and Professor Chittaranjan Sinha (Supervisor, Dept. of Chemistry, JU, Kolkata)-for their invaluable guidance and unwavering support during the semi-annual RAC meetings. Moreover, I express my sincere appreciation to Professor Swapan Kumar Bhattacharya, the former Head of the



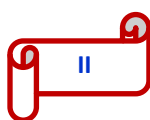
Department of Chemistry, along with all other faculty members, for fostering an environment conducive to research and for their approachability in offering assistance whenever required.

I would like to express my deep appreciation to all collaborators, particularly Prof. Partha Pratim Ray from the Department of Physics at Jadavpur University, Kolkata and Dr. Subrata Kundu from CSIR-CECRI in Karaikudi, Tamil Nadu, for their unwavering support.

I express my heartfelt gratitude to all the faculty and non-teaching staff, notably Mr. Baidyanath Paul and Mr. Atikur Rahaman, for their consistently supportive demeanour. I am equally grateful to the authorities at Jadavpur University for granting me access to the essential infrastructure, underscoring the importance of their assistance in facilitating my endeavours.

Reflecting on this journey, I am deeply aware that its success was anchored in the unwavering support of my esteemed seniors and friends: Dr. Basudeb Dutta (KIIT, Bhubaneswar), Dr. Arka Dey (NIT, Durgapur), Dr. Saumitra Bhowmik (UIIC, USA), Dr. Pubali Das (JU, Kolkata), Dr. Arnab Samanta (Brainware University, Barasat), Dr. Milan Maji (Univ. of California Riverside, USA), Dr. Mihir Sasmal (JU, Kolkata), Dr. Suman Mandal (IACS, Kolkata), Dr. Kartic Manna (IIT Bombay), and Mr. Sunny Goon (IICB, Kolkata). Their relentless assistance has ranged from scientific guidance to personal advice, illuminating every moment-even during meals and casual outings. Their genuine friendship has been a cornerstone of this journey, deserving heartfelt recognition and profound gratitude.

The progression of this journey was profoundly shaped by the invaluable contributions of my dedicated labmates, whose steadfast support enabled its success: Dr. Arup Kumar Adak, Dr. Suvendu Maity, Dr. Kaushik Naskar, Dr. Sunanda Dey, Dr. Angeera Chandra, Dr. Srikanta Jana, Dr. Sukanya Paul, Dr.



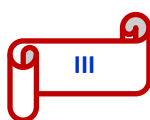
Suprava Bhunia, Dr. Mukul Bikash Maity, Dr. Manik Shit, Dr. Sambhunath Bera, Mrs. Sangita Ghosh, Mr. Himadri Shekar Chatterjee, Mr. Kumarjit Chowdhury, Mr. Soumya Jyoti Ghosh, Mr. Sabir Ahamed, Mr. Arka Patra, Mr. Koushik Saha, and Mr. Sudip Ranjan Jana. The challenges we faced together, and the cherished memories we created along the way, underpin the unyielding commitment and profound connections that have fundamentally enriched this transformative experience.

I would like to express my deep gratitude to my close friends for their untiring support and encouragement during my research period. I owe a significant debt to Animesh, Prasanta, Manotosh, Sandipan, Krishnendu, Toushique, Dolon, Farhin, and Tuhin, whose assistance with data analysis and provision of essential chemicals was invaluable to the completion of my research work.

I wish to convey my deep gratitude to my friend Soumya Dutta for his unwavering support, continual encouragement, motivational presence, and assistance throughout the entirety of my work.

Last but not the least, I wish to convey my deepest gratitude to my dear friends Alamgir, Sarthak, Amit, Abhijit, Manoj, Sukanta, Narugopal, Santu, Jeet and Sourav, whose unwavering companionship and support were invaluable throughout the entirety of this journey. Their steadfast presence during both joyful and challenging times provided the encouragement and motivation I needed. Without their backing, this journey would have been far less manageable and fulfilling.

In contemplating the profound impact of those who hold significance in my life, particularly my parents, Dida (Late Sarathi Sawh), Baba (Late Dilip Bairy), and Ma (Laksmi Bairy) no measure of gratitude seems sufficient to truly acknowledge their unwavering faith in me and the freedom they afforded me to pursue my own path. Indeed, their selfless love, care, and countless sacrifices



have been instrumental in shaping my journey, and I hold deep admiration for their resolve. Their consistent moral and emotional support, along with their heartfelt prayers, have been pillars upon which I stand, and I realize that I can never fully repay the immense love and affection they have bestowed upon me.

I just can't express enough how grateful I am to my wife (Mrs. Nandita Maity) for all her amazing support during my research journey. Right from the beginning, she's been my steadfast companion, and honestly, I wouldn't have managed without her being there at every turn. Her encouragement, patience, and wise insights have truly been the backbone of this project's success.

I wish to convey my profound gratitude to my brothers, sisters, and other family members for their unwavering love, care, and invaluable support and prayers, which played a crucial role in the successful completion of my thesis.

I extend my deepest gratitude to all those who contributed significantly to the success of my thesis, and I sincerely regret not being able to acknowledge each person individually.

Ultimately, I invoke the blessings of the Almighty upon the path of my research, as I embark on a profound quest for understanding.

Gurupada Bairy

Gurupada Bairy
Department of Chemistry
Jadavpur University
Kolkata- 700 032, India.



JADAVPUR UNIVERSITY

KOLKATA-700 032

MARK SHEET

NO.: CW/19052/ 1597

(For Ph.D/M. Phil. Course Work)

Results of the	PH.D. COURSE WORK EXAMINATION, 2024		
In	SCIENCE		
Name	GURUPADA BAIRY	Class Roll No.	002320104008
Examination Roll No.	PHDCHEM24108		
held in	DECEMBER, 2023		

Subject Code / Name	Credit Hr.(c)	Marks
COMPULSORY UNITS:: CHEM/PHD/CPE-RPE/A/B RESEARCH & PUBLICATION ETHICS, RESEARCH METHODOLOGY & REVIEW WORK	8	82
ELECTIVE UNITS :: CHEM/PHD/I-1 :: APPLICATION OF SPECTROSCOPIC STUDIES IN CHEMICAL RESEARCH CHEM/PHD/I-2 :: MATERIALS, CATALYSES & ELECTROCHEMICAL STUDIES CHEM/PHD/I-3 :: METALS IN LIFE & REACTION DYNAMICS CHEM/PHD/I-4 :: SINGLE CRYSTAL X-RAY STR. SUPRAMOLECULAR CHEM. & DFT COMPUTN.	8	74

Total Marks :156 (out of 200)

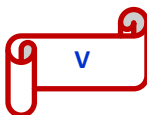
Remarks: P

Prepared by :

Checked by :

Date of issue : 23 / 04 / 2024

Controller of Examinations



Preface

[Index No.: 67/23/Chem./28]

The research detailed in this thesis, titled “**Synthesis and Structural Characterization of Coordination Frameworks and Their Potential Applications**” commenced in august, 2019 and have been carried out in the Department of Chemistry, Jadavpur University.

The thesis is divided into six chapters, and each is comprehensively summarized below, reflecting the thoughtful consideration given to the subject matter.

Chapter 1 summarises about the Coordination Polymers (CPs) or Metal-Organic Frameworks (MOFs) and their integrated applications. CPs represent a fascinating class of materials that have consolidated significant attention due to their tuneable structural motifs and diverse properties. Strategically incorporating π -electron rich organic ligands and inorganic secondary building units (SBUs) like metal ions/clusters, different functional groups, researchers have successfully engineered CPs/MOFs with enhanced structural robustness and chemical stability. This approach not only facilitates the formation of intricate higher-dimensional networks but also allows for the fine-tuning of electronic and optical properties. The synergistic interactions between the organic and inorganic components play a crucial role in determining the overall performance of these materials, making them suitable for a wide range of applications, including gas storage, ion exchange, drug delivery, electrical conductivity, molecular magnetism, catalysis, and sensing. Various synthetic methods including slow diffusion and hydrothermal techniques have been exploited in producing high-quality CPs with desirable structural properties. The synthesized CPs were characterized using a range of spectroscopic methods, such as single-crystal X-ray diffraction (SCXRD), thermogravimetric analysis (TGA), powder X-ray diffraction (PXRD), and infrared spectroscopy (IR). Each characterization technique provided unique insights into the structural, thermal, and vibrational properties of the CPs, confirming the successful synthesis and purity of the materials. These polymers are primarily assembled through a variety of non-covalent interactions, including $\pi \cdots \pi$ stacking, C-H $\cdots\pi$ interactions, and hydrogen bonding. The $\pi \cdots \pi$ stacking contributes to the electronic properties and conductivity of the materials, making them suitable for applications in electronics and photonics. C-H $\cdots\pi$ interactions play a crucial role in the structural integrity and dimensionality of the polymers, while hydrogen bonding provides additional stability and can influence the thermal and mechanical properties. The combination of metal ion coordination, structural tunability, and high porosity

not only improves the performance of CPs in detecting target molecules or ions but also opens new avenues for the development of advanced sensing technologies. Additionally, the incorporation of redox-active ligands and suitable choice of metal centres can enhance the electrochemical performance by providing additional pathways for charge transport, making them suitable for applications in energy storage and conversion devices. **Chapter 1** presents a concise overview of the research conducted by MOF, highlighting its significance and contributions to the field. The chapter outlines the primary objectives of the study, emphasizing the innovative methodologies employed and the key findings that emerged. MOF's research addresses critical gaps in existing literature, providing new insights that enhance our understanding of the subject matter. The motivation behind this research is rooted in the desire to advance knowledge and foster further exploration in the area, making it a valuable resource for scholars and practitioners alike.

Chapter 2 delves into the synthesis and structural characterization of a cadmium (II)-based 1D coordination polymer, precisely identified as $[\text{Cd}(\text{glu})_2(\text{pbiq})_2(\text{H}_2\text{O})]_n$ (**1**), derived from glutaric acid (**H₂glu**) and 4-(6-(pyridin-4-yl)benzo[4,5]imidazo[1,2-*c*]quinazoline) (**pbiq**). The H-bonding and $\pi \cdots \pi$ interactions have constructed a three-dimensional supramolecular architecture that exhibits a strong emission at 416 nm in acetonitrile, illustrating the critical importance of molecular interactions in shaping photophysical attributes. Nitroaromatics (NAs) and trinitrophenol (TNP) present a significant concern due to their ability to selectively suppress the intense emission of **1**, with TNP demonstrating the highest degree of quenching with a detection limit of 1.51×10^{-7} M. The semiconducting behavior of the material (band gap: 3.31 eV) enabled the fabrication of an electronic device. Its current-voltage (*I-V*) characteristics show significant non-ohmic conductivity (Λ : 1.10×10^{-3} S m⁻¹) and a low energy barrier (Φ_B : 0.69 eV).

The **Chapter 3** reports a novel pyridylimidazoquinazoline-coordinated two-dimensional (2D) cadmium(II) metal-organic framework, designated as $\{[\text{Cd}_2(5\text{-nip})_2(\text{pdiq})_2(\text{H}_2\text{O})_2(\text{CH}_3\text{OH})] \cdot \text{H}_2\text{O}\}_n$ (CP **1**) [**H₂nip** = 5-nitroisophthalic acid and **pdiq** = 6-(pyridin-4-yl)-5,6-dihydrobenzo[4,5]imidazo[1,2-*c*]quinazoline]. The combination of C-H $\cdots\pi$ and $\pi \cdots \pi$ interactions within CP **1** results in its formation as a three-dimensional (3D) supramolecular architecture. Notably, the remarkable luminescent properties of CP **1** are precisely suppressed by trinitrophenol (TNP), even amidst the presence of potentially disruptive nitroaromatic explosives (NAEs), with a limit of detection of 2.75×10^{-7} M. The

CP **1** displays enhanced electrical conductivity on an electronic device with a metal-semiconductor (MS) junction. The current-voltage (I - V) plot reveals a substantial increase in electrical conductivity under illumination (from $1.12 \times 10^{-3} \text{ S m}^{-1}$ in the dark to $6.33 \times 10^{-3} \text{ S m}^{-1}$ under light), accompanied by a decrease in the energy barrier (from 0.53 eV in the dark to 0.42 eV under light).

In **Chapter 4**, a robust 3D luminescent coordination polymer, $[\text{Zn}_2(\text{tdc})_4(\text{pdiq})_3]$ (**1**), featuring pyridyl-imidazoquinazoline (**pdiq**) and 2,5-thiophenedicarboxylic acid (H_2tdc), has been synthesized successfully. The stability of the compound's architecture is significantly reinforced by the $\pi \cdots \pi$ interactions occurring between the imidazolium and phenyl groups. The significant dispersibility of Zn-MOF in acetonitrile potentially boosts fluorescence intensity, playing a crucial role in the precise and selective turn-off ratiometric detection of Al^{3+} ions, with a detection limit as low as $1.39 \times 10^{-7} \text{ M}$. Moreover, trinitrophenol instantly quenches the fluorescence emission of Zn-MOF, demonstrating a detection limit of $1.54 \times 10^{-7} \text{ M}$, underscoring the importance of this method in sensitive chemical sensing applications. The Tauc plot is applied to assess the semiconducting band gap of 3.33 eV, and there is a notable enhancement in electrical conductivity when exposed to light, shifting from $1.14 \times 10^{-3} \text{ S m}^{-1}$ in darkness to $5.35 \times 10^{-3} \text{ S m}^{-1}$ under illumination, reflecting its promising attributes in advanced semiconductor technology.

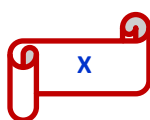
In **Chapter 5**, a cobalt-based redox-active coordination polymer (Co-CP), is synthesized through the deliberate use of (*E*)-*N*-(pyridin-4-ylmethylene)-4*H*-1,2,4-triazol-4-amine, serving as an unsymmetric bridging agent, and is meticulously end-capped with carboxylate-O coordination via 2,5-thiophenedicarboxylate. The Co-CP is instrumental in advancing the electrocatalytic process for the Oxygen Evolution Reaction (OER) in alkaline environments, highlighting its importance in the field of catalysis. The integration of Ni^{2+} at different concentrations into the Co-CP matrix has led to the formation of Ni@Co-CP composites, which have shown a significant improvement in electrocatalytic performances. The optimized catalyst, Ni-2@Co-CP, featuring an amorphous structure, demonstrates exceptional electrocatalytic efficiency for the OER, with a reduced over potential of 290 mV, current density of 10 mA/cm^2 , and Tafel slope of 35 mV/dec and a charge transfer resistance of 6.97 Ω , as determined by electrochemical impedance spectroscopy (EIS).

Chapter 6 provides a comprehensive summary of the research findings, reflecting the depth and significance of the work undertaken in this study.

List of Abbreviations

CP	Coordination Polymer
MOF	Metal-Organic Framework
PCP	Porous Coordination Polymer
ICP	Intercatenated Coordination Polymer
NIPA	5-Nitroisophthalic acid
TDC	2,5-Thiophene dicarboxylic acid
GA	Glutaric acid
NAEs	Nitroaromatic Explosives
NAs	Nitroaromatics
DMF	N,N'-dimethylformamide
MeOH	Methanol
EtOH	Ethanol
CH ₃ CN	Acetonitrile
Et ₃ N	Triethylamine
IPA	Isopropyl alcohol
H ₂ O	Water
DMSO/dmsO	Dimethyl Sulfoxide
H ₂ SO ₄	Sulfuric acid
PXRD	Powder X-Ray Diffraction
AIE	Aggregation Induced Emission
PET	Photo-Induced Electron Transfer
ICT	Intramolecular Charge Transfer
FRET	Fluorescence Resonance Energy Transfer
ESIPT	Excited-State Intramolecular Proton Transfer
SCXRD	Single Crystal X-Ray Diffraction
pdiq	6-(pyridin-4-yl)-5,6-dihydrobenzo[4,5]imidazo [1,2-c]quinazoline
pbiq	4-(6-(pyridin-4-yl)benzo[4,5]imidazo[1,2- c]quinazoline)
UV-Vis	Ultraviolet-Visible
FT-IR	Fourier transform infrared spectroscopy
TGA	Thermogravimetric Analysis
NMR	Nuclear Magnetic Resonance
TNP	2,4,6-Trinitrophenol/Picric acid
TNT	2,4,6-Trinitrotoluene
TMS	Tetramethylsilane
TLC	Thin-layer chromatography
mL	Millilitre
μM	Micromolar

μL	Microlitre
L	Litre
nM	Nanomolar
mM	Millimolar
LOD	Limit of detection
HOMO	Higher Occupied Molecular Orbitals
LUMO	Lower Unoccupied Molecular Orbitals
K_a	Association Constant
K_d	Dissociation Constant
K_{SV}	Stern-Volmer Constant
K_q	Bimolecular Quenching Rate Constant
η	Refractive Index
λ	Wavelength
τ	Fluorescence Lifetime
Φ	Quantum Yield
T	Temperature
%T	Percentage of Transmittance
K	Kelvin
H	Hours
Min.	Minute
S	Second
F	Oscillator Strength
$^\circ$	Degree
\AA	Angstrom
g	Gram
mg	Milligram
SDB	Schottky diode barrier
MS	Metal-semiconductor
ESI	Electrospray ionization
DFT	Density functional theory
CCDC	Cambridge Crystallographic Data Centre
TDDFT	Time-dependent density functional theory
MS	Mass Spectroscopy
CHISQ	Chi-squared (χ^2)
NIH	National Institutes of Health
IOM	Institute of Medicine
ATSDR	Agency for Toxic Substances and Disease Registry (ATSDR)
CDC	Centers for Disease Control and Prevention
eV	Electron Volt
SCLC	Space charge limited current



L _D	Diffusion length
SBU	Secondary building units
WHO	World Health Organization
MSDS	Material Safety Data Sheet
TFD	Thin Film Diode
SDGs	Sustainable development goals
1D	One-dimensional
VOC	Volatile organic compounds
SBH	Schottky barrier height
USEPA	United States Environmental Protection Agency
OER	Oxygen evolution reaction
HER	Hydrogen evolution reaction
pmta	(<i>E</i>)- <i>N</i> -(pyridin-4-ylmethylene)-4 <i>H</i> -1,2,4-triazol-4-amine
EIS	Electrochemical impedance spectroscopy
XPS	X-ray photoelectron spectroscopy
FESEM	Field Emission Scanning Electron Microscopy
HRTEM	High Resolution Transmission Electron Microscopy
EDX	Energy Dispersive X-Ray Analysis
LSV	Linear sweep voltammetry
RHE	Reversible Hydrogen Electrode
CA	Chronoamperometry
TOF	Turnover frequency
CV	Cyclic voltammetry
ECSA	Electrochemically active surface area
C _{dl}	Double-layer capacitance
HAADF-TEM	High-angle annular dark-field scanning transmission electron microscopy
Nafion	Perfluorosulfonic acid
NF	Nickel Foam

Contents

Acknowledgements	I-IV
Preface	VI-VIII
List of Abbreviations	IX-XI

Chapter 1	Page
Introduction: Coordination Polymers and Their Importance	
1.1 Coordination Polymers	2
1.2 Linkers and Connectors	8
1.3 Preparation of coordination polymers (CPs)	12
1.4 Applications of CPs/MOFs	14
1.4.1 Sensor Application	16
1.4.1.1 Advantages of Fluorescence Technique in Quantitative Analysis	17
1.4.1.2 Fluorescence Sensing Mechanism	18
1.4.1.2.1 Photoinduced Electron Transfer (PET)	18
1.4.1.2.2 Intra and Intermolecular Charge Transfer (ICT)	19
1.4.1.2.3 Chelation Enhanced Fluorescence (CHEF) and Chelation Enhanced Quenching (CHEQ)	20
1.4.1.2.4 Förster Resonance Energy Transfer (FRET)	22
1.4.1.2.5 Excited-State Intramolecular Proton Transfer (ESIPT)	22
1.4.1.2.6 Excimer / Exciplex Formation	23
1.4.1.3 Metal ion sensor	24
1.4.1.3.1 Aluminium (Al^{3+}) Sensing	26
1.4.1.4 Molecular Sensor	26
1.4.1.4.1 Trinitrophenol (TNP) Sensing	27
1.4.2 Electrical Conductivity	28
1.4.2.1 Diode and Schottky Barrier	28
1.4.2.2 Advantages of Schottky Diode	29
1.4.2.3 Applications of Schottky Diode	30
1.4.2.4 Diode Parameters	31
1.4.2.5 Charge transport parameter	31
1.4.3 Electrocatalytic Water Splitting Application	32
1.4.3.1 Mechanistic aspects of Electrocatalytic Water Splitting	33
1.4.3.2 Parameters involved for Electrocatalytic Water splitting	33
1.4.3.2.1 Overpotential	34
1.4.3.2.2 Tafel Slope	34
1.4.3.2.3 Electrochemical Impedance Spectroscopy	35
1.4.3.2.4 Stability	35
1.4.3.2.5 Electrochemical Active Surface area and Turn Over Frequency	35
1.5 Aim and Scope of the Dissertation	36
1.6 Physical Measurements	37
1.7 References	39

Chapter 2		Page
In Situ Oxidation of Pyridyl-Dihydrobenzoimidazoquinazoline and the Synthesis of a Highly Luminescent Cd(II) Coordination Polymer: A Promising Candidate for Mutagenic Nitroaromatic Detection and Device Fabrication		
Abstract		53
2.1 Introduction		54
2.2 Experimental Section		56
2.2.1 Materials and General Methods		56
2.2.2 Synthesis of Ligand (H ₂ pbiq)		57
2.2.3 Synthesis of [Cd(glu) ₂ (pbiq) ₂ (H ₂ O)]		60
2.2.4 Synthesis of pbiq		60
2.2.5 Single-Crystal X-ray Diffraction (SC-XRD)		63
2.2.6 Theoretical Calculations		65
2.2.7 Device Fabrication		65
2.3 Results and Discussion		66
2.3.1 Crystal Structure of [Cd(glu) ₂ (pbiq) ₂ (H ₂ O)] _n		66
2.3.2 Powder X-ray Diffraction (PXRD) and Thermogravimetric Analysis (TGA) Experiment		68
2.3.3 Sensing Property toward NAEs		69
2.2.4 Electrical Characterization		76
2.5 Conclusions		79
2.6 References		79
Chapter 3		Page
2D Cd(II)-MOF of Pyridyl-Imidazoquinazoline: Structure, Luminescence, and Selective Detection of TNP and Fabrication of Semiconducting Devices		
Abstract		89
3.1 Introduction		90
3.2 Experimental Section		92
3.2.1 Materials and General Methods		92
3.2.2 Synthesis of the Ligand (pdiq)		93
3.2.3 Synthesis of {[Cd ₂ (5-nip) ₂ (pdiq) ₂ (H ₂ O) ₂ (CH ₃ OH)]·H ₂ O} _n		95
3.2.4 General X-ray Crystallography		96
3.2.5 Theoretical Calculations		98
3.2.6 Device Fabrication		98
3.3 Results and Discussion		99
3.3.1 Structure of {[Cd ₂ (5-nip) ₂ (pdiq) ₂ (H ₂ O) ₂ (CH ₃ OH)]·H ₂ O} _n		99
3.3.2 PXRD and TGA Analysis		100
3.3.3 Sensing Property towards NAEs		101
3.3.4 Optical Characterization		106
3.3.5 Electrical Properties of a Schottky Device		107
3.4 Conclusions		112
3.5 References		112
Chapter 4		Page
Rational synthesis of a pyridyl-imidazoquinazoline based multifunctional 3D Zn(II)-MOF: structure, luminescence, selective and sensitive detection of Al³⁺ and TNP, and its semiconducting device application		

Abstract	121
4.1 Introduction	122
4.2 Experimental Section	124
4.2.1 Materials and General Methods	124
4.2.2 Synthesis of ligand (pdiq)	125
4.2.3 Synthesis of $[\text{Zn}_2(\text{tdc})_4(\text{pdiq})_3]$	127
4.2.4 General X-ray Crystallography	128
4.2.5 Theoretical calculations	130
4.2.6 Device Fabrication	130
4.3 Results and Discussion	131
4.3.1 Structural description of $[\text{Zn}_2(\text{tdc})_4(\text{pdiq})_3]$	131
4.3.2 PXRD and TGA analysis	133
4.3.3 Photoluminescence Properties	134
4.3.4 Ratiometric Fluorescence Sensing of Al^{3+}	135
4.3.5 Sensing of Nitroaromatics (NAs)	140
4.3.6 Optical Characterization	144
4.3.7 Electrical Characterization	145
4.4 Conclusions	150
4.5 References	150

Chapter 5

Page

Triazolyl-pyridylimine bridging 1D Co(II) redox coordination polymer and its Ni-composite: Structure, surface characterisation and application in the water splitting reaction

Abstract	161
5.1 Introduction	162
5.2 Experimental Section	164
5.2.1 Materials and General Methods	164
5.2.2 Preparation of pmta	165
5.2.3 Synthesis of $[\text{Co}_3(\text{pmta})_2(2,5\text{-tda})_2(\text{H}_2\text{O})_8(\text{OH})_2] \cdot x\text{H}_2\text{O}$	167
5.2.4 Preparation of Ni@Co-CP composites	168
5.2.5 X-ray crystallography analysis	168
5.2.6 Electrochemical Measurements	170
5.3 Results and Discussion	171
5.3.1 General Characteristics of Co-CP/Ni@Co-CP Composites	171
5.3.2 Crystal Structure Assay of Co-CP	173
5.3.3 Electron Microscopic Studies	174
5.3.4 X-ray photoelectron spectroscopy (XPS) measurements	177
5.3.5 Electrocatalytic OER study	179
5.3.6 Post OER characterization of Ni@Co-CP Composites	185
5.4 Conclusions	187
5.5 References	187

Chapter 6

Page

6.1 Summary of the research work	195
----------------------------------	-----

Appendix

Page

List of Publications	198
Right and Permission	200

Chapter 1

Introduction: A Literature Survey

When our dreams are fresh, we are excited about them. Even just thinking about it can feel you with passion. At that time, we build many plans in our mind. As time go by, motivation factor gets diminishing. Why? Because, we keep think a lot and do not go beyond thinking.

In the beginning, many fear factors stop us to make early decisions. Sometimes our doubt and sometimes there is fear of failure prevent us to begin.

Remember:

*"Faith is taking the first step even when you don't see the whole staircase."
~Martin Luther King, Jr.*



The Beginning.....

1.1 Coordination Polymers

The history of the evolution of coordination compounds spans nearly two centuries, with significant discoveries and breakthrough being made at the end of 19th Century. In the early 19th century, chemists started to identify that certain compounds possessed distinct characteristics and bonding structures, setting them apart from the straightforward ionic and covalent compounds that were well comprehended during that period. A coordination complex is a compound that is characterized by a central atom or ion, typically metallic, referred to as the coordination center, bonded by a specific set of surrounding molecules or ions, commonly referred to as ligands or complexing agents. Jöns Jacob Berzelius, a Swedish chemist, laid the groundwork for the investigation of these compounds by demonstrating the critical function of metal ions in forming complex structures in accordance with organic molecules. This seminal work set the stage for subsequent advancements in this field.

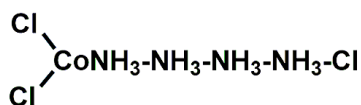
The origins of coordination chemistry may be sketched from 1597, when German alchemist Andreas Libavius reported the formation of the deep blue $[\text{Cu}(\text{NH}_3)_4]^{2+}$ complex, regarded as the first well-defined inorganic coordination compound.¹ Moving into the early 18th century, the synthesis of Prussian blue ($\text{KFe}[\text{Fe}(\text{CN})_6]$), marked another significant milestone in the history of coordination chemistry.² Further advancements came in 1760 with the preparation of potassium hexachloroplatinate(IV) dianion.³

During this time, chemists identified certain compounds known as “double salts,” such as Mohr’s Salt $(\text{NH}_4)_2\text{SO}_4 \cdot \text{FeSO}_4 \cdot 6\text{H}_2\text{O}$ and $\text{AlF}_3 \cdot 3\text{KF}$, which were combinations of simple salts in specific but seemingly arbitrary ratios. These compounds raised several questions regarding their conductivity and distinct colors. Alongside these, adducts formed by metal salts and neutral molecules like ammonia also drew attention. A notable example is $\text{CoCl}_3 \cdot 6\text{NH}_3$, originally synthesized before 1798 by French chemist B. M. Tassaert.¹ Similar to double salts, these ammonia-metal complexes showed consistent but curious stoichiometries-compounds such as $\text{CoCl}_3 \cdot 6\text{NH}_3$, $\text{CoCl}_3 \cdot 5\text{NH}_3$, $\text{CoCl}_3 \cdot 4\text{NH}_3$, and $\text{CoCl}_3 \cdot 3\text{NH}_3$ were well-known, each displaying unique characteristics. However, attempts to isolate compounds like $\text{CoCl}_3 \cdot 2\text{NH}_3$ or $\text{CoCl}_3 \cdot \text{NH}_3$ were unsuccessful, leaving chemists puzzled by the pattern.

Although a few analytical techniques helped determine the composition of these compounds, their chemical structure remained highly controversial. Sophus Mads Jørgensen, a Danish chemist and founder of coordination compounds, prepared large number of compounds and measured their conductances and proposed the structure of these compounds based on structure of C-chain compounds (C-catenation) as proposed by Van’t

Chapter 1: Introduction

Hoff in organic chemistry. The major problem was the valence and coordination number. As a result, highly improbable structures were proposed by Jørgensen as shown below for $\text{CoCl}_3 \cdot 4\text{NH}_3$.



The foundation of modern coordination chemistry largely stems from the research conducted by Alfred Werner during the 1880s and 1890s. He studied the behavior of several metal halide complexes with ammonia, including various ammonia “adducts” of PtCl_4 , represented as $\text{PtCl}_4 \cdot n\text{NH}_3$ (where $n = 2\text{--}6$). He observed that the electrical conductivity of their aqueous solutions correlated with the number of ions produced per mole. Moreover, the concentration of non-coordinated (‘free’) chloride ions was precisely determined via quantitative precipitation as silver chloride (AgCl) upon the addition of aqueous silver ions (Ag^+). He proposed the seminal Coordination Theory of complex compounds. Because of break through contribution Alfred Werner awarded the Nobel Prize in 1893 “*in recognition of his work on the linkage of atoms in molecules by which he has thrown new light on earlier investigations and opened up new fields of research especially in inorganic chemistry*”.⁴

Molecular chemistry focuses on the chemical interactions that occur between atoms, forming compounds through covalent and other types of bonding.⁵ Conversely, supramolecular chemistry focuses on the interactions among discrete molecules, governed primarily by non-covalent forces such as hydrogen bonding, electrostatic attractions, π - π stacking, van der Waals interactions, and other intermolecular forces.⁵ In 1987, the field of supramolecular chemistry reached a new level of sophistication with the groundbreaking work of researchers Donald J. Cram, Jean-Marie Lehn, and Charles J. Pedersen, who were honored with the Nobel Prize “*for their development and use of molecules with structure-specific interactions of high selectivity*”.⁶

Supramolecular coordination chemistry (SCC) stands as a swiftly advancing field within coordination chemistry, encompassing discrete systems where carefully chosen metal centers engage in self-assembly via linkers that possess multiple binding sites arranged with precise angularity, thereby forming a distinct supramolecular complex.⁷

An emerging area within coordination chemistry is the study of coordination polymers, a term first introduced by Professor J.C. Bailar in 1967. A coordination polymer represents a significant category of materials that encompass inorganic or organometallic polymers characterized by metal cation centres or clusters, which serve as nodes, and ligands acting as bridges to link adjacent metal ions.

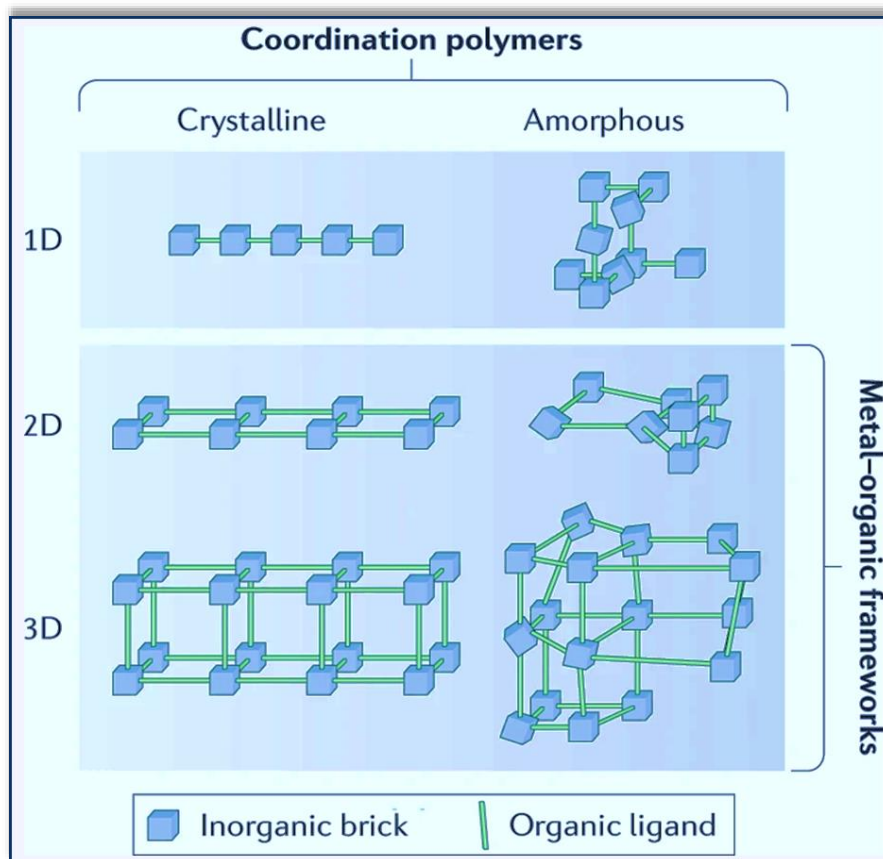


Figure 1.1 Design of 1, 2 and 3 dimensionally CPs. Adapted with permission from ref. [8](#) and modified. Copyright 2018 Nature Portfolio.

These polymers manifest as coordination compounds constructed from metal-ligand units that repetitively assemble into extended networks, propagating in one, two, or three dimensions to form architecturally ordered structures. As outlined by IUPAC, coordination polymers are uniquely defined as compounds that persistently extend in a linear (1D), planar (2D), or volumetric (3D) manner through coordination bonds ([Figure 1.1](#)). The presence of permanent cavities within these coordination polymers identifies them as Porous Coordination Polymers (PCPs), or alternatively classified as Metal-Organic Frameworks (MOFs) or Metal-Organic Coordination Networks (MOCNs).^{[9,10](#)}

Beginning in the early 1990s, research into porous coordination polymers has expanded significantly, leading to the widespread publication of numerous well-engineered microporous structures in scientific literature. The drive to investigate coordination polymers has gained momentum due to their adaptable frameworks, which hinge on diverse multifunctional organic bridging groups and metal centres, as detailed by Huang et al. in 2012.^{[11](#)} Essential components for constructing diverse geometries of coordination polymers include the strategic combination of metal ions with organic linkers, the ligand's size, and the

Chapter 1: Introduction

interactive capabilities between metal ions and ligands, as emphasized by Valente et al. (2010)¹² and Yaghi et al. (1997, 2000, 2003).¹³⁻¹⁵

The study of coordination polymers is of considerable significance, evidenced by the plethora of research reports that emphasize their crucial attributes. The spatial arrangement of metal ions within a supramolecular network profoundly influences both the unique properties of the materials formed and their binding ligands. To construct a stable and adaptable coordination polymer, it requires thoughtful selection of metal centers and precise control over their spatial separation between them.

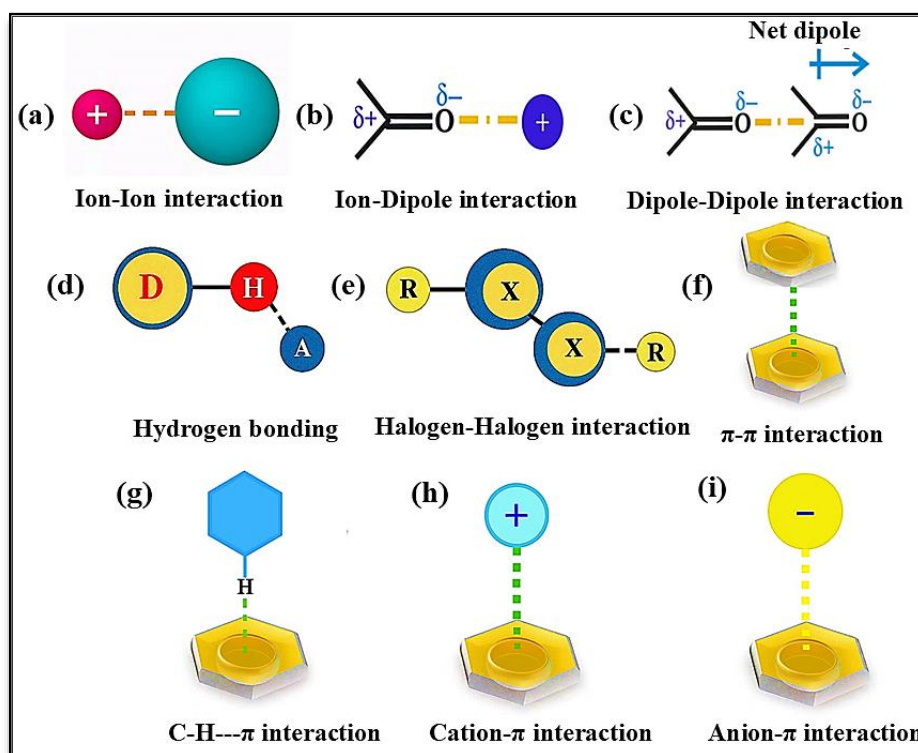


Figure 1.2 Illustration of the various types of supramolecular interactions.

The choice of linkers and metal nodes offers vast potential for researchers to design new compounds featuring diverse and fascinating structural motifs and topologies. Additionally, advancements in computational resolution methods and technological progress in X-ray measurement techniques have significantly facilitated the study of crystals (Robin & Fromm, 2006).¹⁶ Coordination polymers (CPs) are primarily found in the solid state, where atoms or molecules occupy fixed positions, restricting their movement relative to one another (Janiak, 2003).¹⁷ In such architectures, the building units are linked via coordination bonds, supported by secondary interactions like hydrogen bonding, π - π stacking, and van der Waals forces (**Figure 1.2**). These interactions facilitate the formation of small molecular units in solution, which then self-assemble into extended coordination polymer frameworks (**Figure 1.3**) (Kitagawa & Noro, 2004).¹⁸ Within these polymers, metal ions/metal clusters typically

act as nodal points, while ligands serve as linkers. X-ray crystallography remains the most reliable method for elucidating coordination polymer structures, whereas solution-based techniques typically detect only oligomeric fragments.

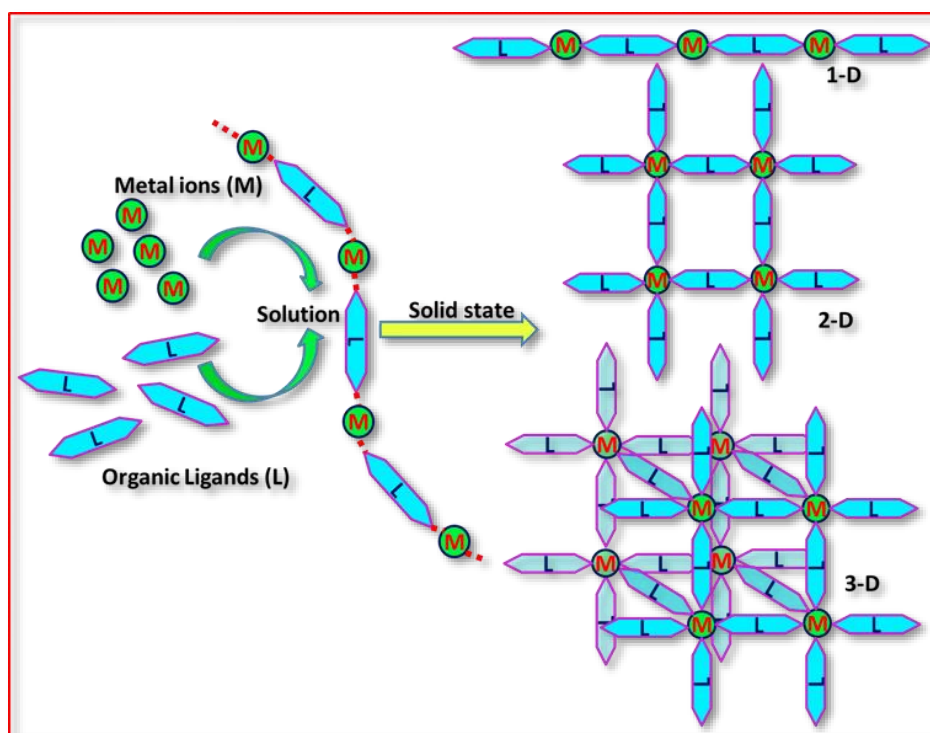


Figure 1.3 Diagram illustrating coordination polymer formation.

Coordination polymers represent particular chemical entities, and the initial phase in designing a structure with specific functions and characteristics involves comprehending the fundamental geometric principles. O'Keeffe and Yaghi introduced a foundational strategy by translating the crystal structures of coordination polymers into fundamental topological nets, which has greatly aided in the systematic design and characterization of new framework (Rosi et al., 2002).¹⁹ Several synthetic methods have been developed to construct specific structures from molecular building blocks. The CPs have emerged as a significant addition to the traditional classification (**Figure 1.4**), holding an important place in the field of materials science.¹⁸ Despite their prominence, the formulation of specific complexes with anticipated structures and properties remains a formidable challenge. This complexity stems from various factors such as the properties of ligands and metal centers, fluctuations in pH and temperature, the nature of counter ions, the metal-to-ligand stoichiometry, and the choice of solvents used during synthesis (Ma et al., 2014; Cui et al., 2012; Hao et al., 2012; Effendy et al., 2004).²⁰⁻²³

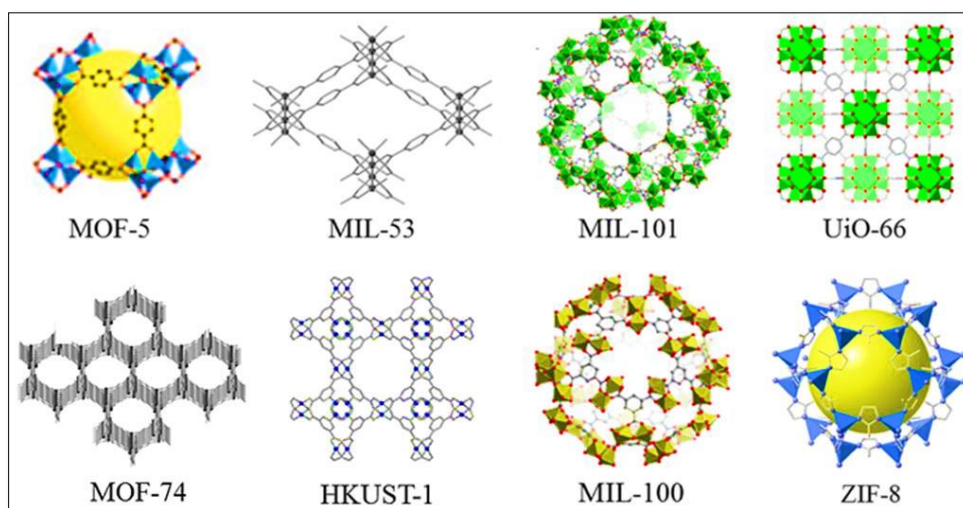


Figure 1.4 Various Categories of Porous Coordination Polymers (Lee et al., 2013).²⁴ Adapted with permission from ref. 24. Copyright 2013 Springer.

In 1998, Kitagawa et al. introduced a classification system for porous coordination polymers (PCPs) (Figure 1.5), delineating three distinct generations based on their structural characteristics and stability.²⁵ First-generation materials are characterized by an irreversible collapse of their framework upon the exclusion of guest molecules/ions in the pores of the PCPs, leading to a loss of structural integrity. In contrast, second-generation materials exhibit a stable and robust framework with rigid pores that retains its structure after the removal of guest molecules, making them suitable for selective and specific applications in adsorbent materials such as zeolites. The third generation of materials is distinguished by their inherent flexibility, featuring dynamic pores that respond reversibly to external stimuli. This unique property enhances their deliverable characteristics, positioning them as promising candidates for advanced applications in various fields.

Third generation porous coordination polymers (PCPs) exhibit a unique flexible structure that endows them with exclusive properties. These materials can be broadly categorized into two principal types, determined by their structural transformation abilities: (i) rigid or robust PCPs, and (ii) flexible PCPs. Unlike their robust counterparts, which remain stable and do not undergo structural transformation when exposed to strainuous external factors like temperature changes, guest molecules, magnetic fields, electric fields, or light irradiation, flexible PCPs demonstrate significant structural adjustment when exposed to these stimuli. The development of such flexible materials opens new avenues for research and application across various fields.

Fourth-generation coordination polymers (Multifunctional CPs) are engineered to exhibit integrated functionalities-such as magnetic, luminescent, catalytic, and electronic

properties-within a single framework. Through strategic incorporation of functional moieties or co-ligands, these materials enable synergistic behavior, advancing applications in molecular electronics, catalysis, energy conversion, and multifunctional sensing.

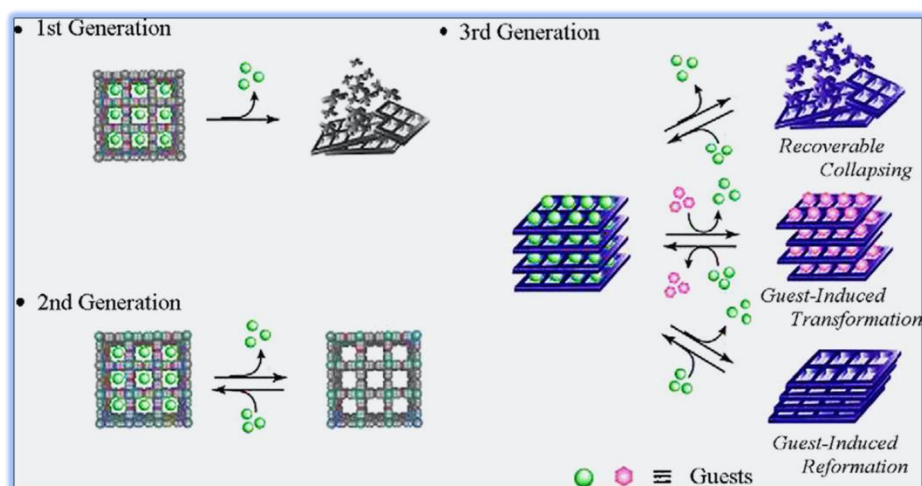


Figure 1.5 Classifications of PCPs by Kitagawa et al.²⁵ Adapted with permission from ref. 25 and modified. Copyright 2013 Elsevier.

Fifth-generation coordination polymers and MOFs focus on sustainability, biocompatibility, and intelligent design. Key features include green synthesis using eco-friendly methods, frameworks suitable for biomedical use, and AI-driven approaches for predictive design and optimization. This generation marks a convergence of materials chemistry with data science and sustainability, aiming to develop advanced, responsible, and application-ready materials.

1.2 Linkers and Connectors

Linkers and connecting moieties serve as essential components in the architecture of coordination polymers, forming the foundational framework upon which their structure is built. They significantly affect the configuration and number of coordination centers in the structure.¹⁷ Auxiliary components like counter ions, template agents, non-coordinating guests, and ligands play a substantial role in shaping the overall process and merit careful consideration for their impact. Transition metal-based coordination polymers exhibit coordination numbers ranging from 2 to 7, resulting in a diverse array of geometric configurations that are critically determined by the central metal ion and its valence state. The possible coordination geometries include linear, trigonal, tetrahedral, and a variety of polyhedral structures such as square planar, square pyramidal, trigonal bipyramidal, octahedral, pentagonal bipyramidal, and trigonal prismatic, among other potentially distorted structures. Metal ions possessing a d^{10} configuration, such as Cu^{I} and Ag^{I} ions, contribute to a

Chapter 1: Introduction

variety of geometric structures, as detailed by Schröder and Munakata groups.^{26,27} Lanthanide ions typically exhibit intrinsic polyhedral coordination geometries, commonly associated with coordination numbers ranging from 7 to 10, plays a pivotal role in crafting intricate and uncommon topology.

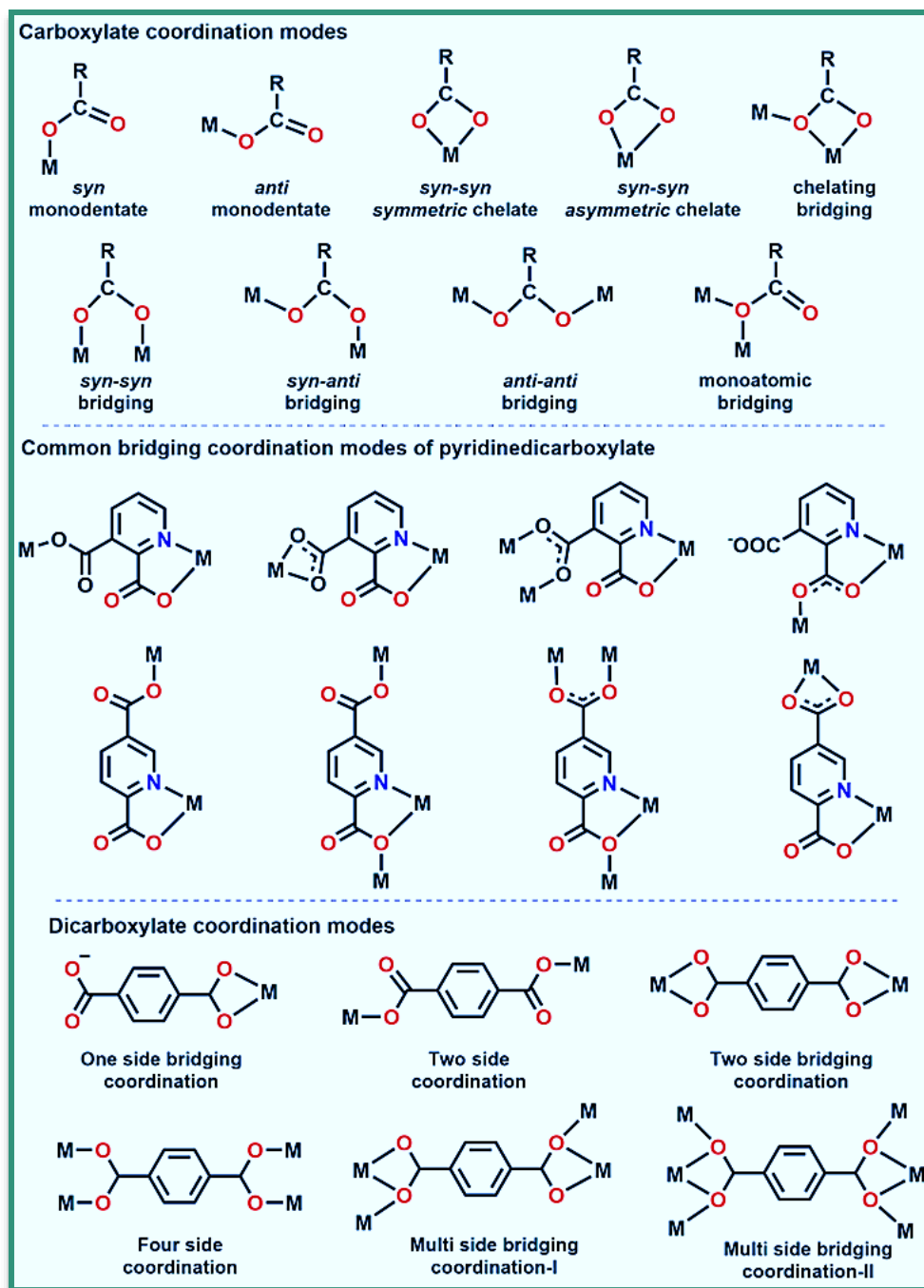


Figure 1.6 Various coordination modes of carboxylates/dicarboxylates.

The linkers, encompassing vital organic functional groups such as $-\text{COOH}$, $-\text{NH}_2$, $-\text{OH}$, $-\text{SH}$, $-\text{SO}_3\text{H}$, and $-\text{PO}_3\text{H}$, play a crucial role in binding with metal ions to construct diverse geometric structures, as described by Sel et al.²⁸ Professor Kitagawa has conducted

Commonly used carboxylic acid linkers include adipic acid, 1,4-benzenedicarboxylic acid (terephthalic acid), 1,3,5-benzenetricarboxylic acid (trimesic acid), 1,2,4,5-benzenetetracarboxylic acid, and 2,6-naphthalenedicarboxylic acid. Geometrically fixed organic linkers are crucial components in the construction of highly topological frameworks with thermal and mechanical stability while maintaining their porosity even after the desorption of solvent species present in the cavities (Lin et al., 2014).³¹ Aliphatic dicarboxylates such as malonate, succinate, glutarate, and adipate exhibit significant conformational adaptability, which contributes to the formation of diverse structural frameworks and topologies.^{32,33} The research efforts of Prof. Yaghi, O’Keeffe, and their team have extensively explored coordination polymer synthesis, particularly focusing on the assembly of continuous rod-shaped motifs facilitated by the incorporation of structurally rigid dicarboxylates. Among various linkers, carboxylate-based ligands are widely used due to their versatile binding modes.

N-donor ligands play a key role in assembling large-scale metal ion networks that display significant structural variety and multifunctional behavior. A wide array of nitrogen-containing donor ligands is utilized in coordination chemistry, including but not limited to pyridine, imidazole, pyrazole, triazole, pyrimidine, pyrazine, tetrazole, amino groups, Schiff bases, pyrrole, terpyridine, phenanthroline, dipyrin, and azide. Flexible nitrogen-donor ligands possess conformational freedom and considerable structural diversity, making them particularly valuable in synthetic strategies. Early studies employed simple pyridine-based ligands due to their capacity to bind metal centers, resulting in the construction of fundamental coordination complexes. The introduction of bipyridine expanded the structural diversity, allowing for the creation of more complex frameworks due to its bidentate nature. Terpyridine further advanced this progression by introducing a tridentate coordination mode, which facilitated the development of intricate three-dimensional structures. The development of tetrapyridine ligands marked a pivotal point, enabling the formation of highly interconnected networks with enhanced stability and functionality. Benzimidazole ligands demonstrate rotational and bending flexibility during coordination with metal centres, due to the presence of $-(CH_2)_n-$ spacers ($n = 1$ to 6). This inherent flexibility is a driving force behind the construction of highly stable and architecturally complex network structures. The successful construction of targeted coordination polymers is strongly influenced by the conformational flexibility and steric effects of nitrogen-donor organic ligands (Wang et al., 2013; Kan et al., 2012).^{34,35} The presence of an imidazole ring and a conjugated π -system enables this N-donor ligand to function as a hydrogen bond donor and participate in π - π

stacking, which in turn supports the development of complex supramolecular structures.³⁶⁻³⁸ In 2017, Zhou group introduced a novel coordination polymer, NJU-Bai, which leverages the incorporation of piperazine to improve methane storage capabilities.³⁹ This study highlights the significant benefits of utilizing piperazine groups within coordination polymers. Furthermore, aromatic dicarboxylates have emerged as excellent co-ligands due to their strong coordination ability and versatile binding modes.³⁸ The use of nitrogen-based donor ligands in combination with dicarboxylate linkers has significantly advanced the synthesis of porous coordination frameworks (**Figure 1.7**). The versatility of the mixed-ligand strategy in producing structurally novel and functionally diverse materials is well exemplified in the research of Krishnamurthy and Agarwal (2014).⁴⁰

1.3 Preparation of coordination polymers (CPs)

Various synthetic methods have been developed to create these polymers, each offering distinct advantages and challenges.

The slow evaporation, or room temperature technique, represents a significant synthesis approach, eliminating the need for external energy inputs. This method leverages the natural process of evaporation to concentrate mixtures, whereby the rate of evaporation is determined by the boiling point of the solvent employed. Solvents with lower boiling points evaporate swiftly, while those with higher boiling points necessitate a prolonged period for full evaporation.⁴¹ In 2008, Tranchemontagne group made a significant advancement in the arena of coordination polymers by introducing a number of frameworks (MOF-74, MOF-5, MOF-177, MOF-199, and IRMOF-0).⁴² Coordination polymers, especially metal-organic frameworks, are frequently synthesized using solvothermal/hydrothermal techniques. Gándara et al. demonstrated the solvothermal synthesis of highly crystalline MOF-519 and MOF-520 at 150 °C for 96 hours.⁴³ The solvothermal method is widely utilized for material synthesis, but it presents significant challenges, particularly with thermally sensitive precursors and sophisticated reaction equipments. Leading researchers, including M. Wiebcke and S. Agarwal, have highlighted this limitation, noting that the high temperatures and pressures of solvothermal processes can result in the degradation of these fragile compounds.^{40,44} Additionally, this method often requires lengthy reaction times, which can negatively impact efficiency and scalability, posing considerable barriers to its broader application.

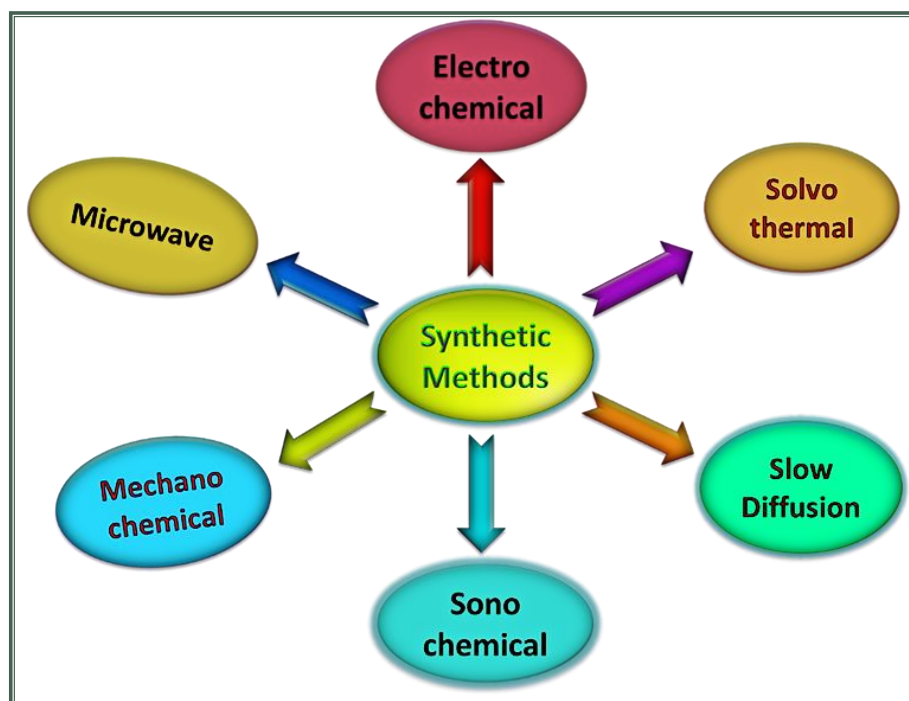


Figure 1.8 Types of synthetic methods.

Thus, to ensure the production of high-quality crystals at shorter time, alternative methods have been utilized, including microwave-assisted, sonochemical, electrochemical, and mechanochemical methods (**Figure 1.8**). Cr-MIL-100 was the first coordination polymer to be synthesized in just 4 hours at 22 °C using a microwave-assisted method.⁴⁵ As reported by Jhung et al., this method successfully preserves the textural characteristics achieved by the conventional process (4 days at 220°C).⁴⁴ Another example (MOFs-5) of a microwave irradiation method with a shorter reaction time was reported by Choi et al.⁴⁶ Their approach, however, is severely limited by differences in instrumentation and reaction conditions. Sonochemical method is recognized for its efficiency and speed, resulting in the formation of crystals with significantly smaller particle sizes compared to traditional solvothermal techniques. In the sonochemical process, the solution mixture is placed in a Pyrex vessel that is coupled with a sonicator probe, which emits ultrasonic waves to induce sonication.^{47,48} The application of ultrasound facilitates enhanced mass transfer and reaction rates, leading to the rapid formation of high-quality crystalline materials. Recently, the sonochemical method has been utilized for the synthesis of MOF-5, Mg-MOF-74, ZIF-8 and HKUST-1.⁴⁹⁻⁵² Lee and his team reported that sonochemical methods are more effective in producing high-quality IRMOF-3 membranes over microwave-assisted method, thereby contributing to improved CO₂ capture capabilities.⁵³ In 2005, a novel electrochemical method; harnesses electric energy to drive chemical reactions, was introduced for synthesizing CPs. The pioneering coordination polymer synthesized using this technique was HKUST-1.⁵⁴ The electrochemical

process presents notable benefits, including a swift method for synthesis, complete utilization of organic linkers with remarkable Faraday efficiency, and the use of metal electrodes in lieu of metal salts. Additionally, the synthesis occurs under more controlled and gentle conditions when compared to microwave or solvothermal methods.⁵⁵ In 2008, Pichon et al. introduced the mechanochemical approach, a process that operates without the need for solvents; making it an environment friendly alternative.⁵⁶ The reaction completes rapidly, producing an ample yield.

This study discusses various synthesis methods, highlighting their respective drawbacks such as including stringent operational conditions, reliance on specialized equipment, low product yields, and high costs, which limit their suitability for industrial applications. In contrast, the room temperature synthesis method emerges as a more favorable alternative due to its ease of synthesis, cost-effectiveness, and environmental friendliness, making it well-suited for industrial applications. It is worth highlighting, however, that this technique is time-consuming, which poses a challenge in terms of efficiency. Overall, while the room temperature method presents significant advantages, its time requirements must be addressed to enhance its practicality in industrial settings.

1.4 Applications of CPs/MOFs

Environmental degradation, pollution, and climate change have become critical global challenges, prompting increasing involvement from environmentalists and analytical chemists in devising effective remediation strategies. especially those focused on water quality as per Sustainability Development Goals. These initiatives support the objectives of the United Nations Sustainable Development Goals (SDGs), especially those focused on water quality (SDG 6), climate response (SDG 13), and ocean conservation (SDG 14). These pollutants include inorganic contaminants such as heavy metal ions, radioactive species, oxyanions, and oils, as well as organic pollutants including dyes, pesticides, pharmaceutical residues, and oils.⁵⁷ Additionally, biomedical waste and emerging contaminants further complicate remediation efforts.⁵⁸ The development and implementation of advanced analytical techniques and environmentally friendly materials are crucial for the effective monitoring and removal of these pollutants, contributing to sustainable environmental management and public health protection.

In the last twenty years, the CPs and MOFs have attracted significant attention in the field of porous materials due to their exceptionally high surface areas, crystalline nature, and highly tunable pore structures.⁵⁹ These organic-inorganic hybrid materials offer a level of

Chapter 1: Introduction

design versatility and functionality that far surpasses traditional porous solids such as zeolites, activated carbons, mesoporous silica, and clays.⁶⁰ The precise control over their structural and chemical characteristics at the molecular scale has propelled CPs and MOFs into a diverse array of advanced application like gas storage and separation (H_2 , CH_4 , and CO_2).⁶¹ In the field of sensing, the frameworks' responsive nature to guest molecules, coupled with their luminescent or conductive properties, allows for highly sensitive and selective detection of various analytes.⁶² Moreover, CPs/MOFs exhibit unique photo- and electroactive behaviors, enabling their use in light-responsive materials, electronic devices, and as platforms for photochromism and charge transport.⁶³

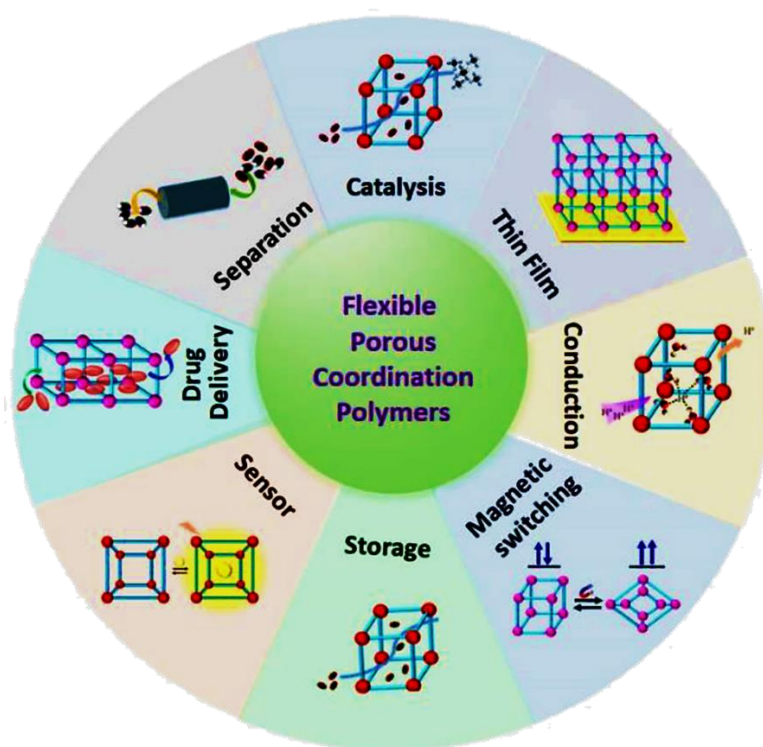


Figure 1.9 Schematic representation of the applications of flexible PCPs. Adapted with permission from ref. ⁶⁷. Copyright 2021 Elsevier.

Heterogeneous catalysis represents another critical area where CPs and MOFs have made significant strides. Their well-defined pore environments, combined with the ability to incorporate catalytic sites within the framework (either as part of the metal cluster or the organic linker), make them ideal candidates for size-selective and recyclable catalysts.⁶⁴ In electrochemical applications, MOFs have emerged as promising materials for supercapacitors, batteries, and electrocatalysis, benefiting from their structural tunability, high conductivity (in selected frameworks), and redox-active components.⁶⁵ Furthermore, recent advancements have explored the integration of MOFs with other functional materials—such as nanoparticles, polymers, and biomolecules—resulting in composite systems with

synergistic properties.⁶⁶ These developments are pushing the boundaries of CP/MOF applications into areas like drug delivery, environmental remediation, and even quantum materials (Figure 1.9).⁶⁷

Despite their extensive application in various scientific and industrial domains, the CPs/MOFs still possess vast untapped potential in key frontier areas such as sensing, electrical conductivity, and electrochemical performance.⁶⁸ While notable progress has been made, these fields remain underexplored compared to more mature applications like gas storage or catalysis.⁶⁹ Challenges such as framework stability under operational conditions, low intrinsic conductivity of many MOFs, and limited understanding of charge transport mechanisms continue to hinder broader implementation.⁷⁰ By strategically modifying the metal centers and organic linkers, introducing redox-active or conductive components, and optimizing framework architecture, this work seeks to advance the fundamental understanding and practical applicability of these materials.⁷¹ Ultimately, the goal is to bridge the gap between structural design and real-world device integration, paving the way for next-generation multifunctional materials suitable for sensing technologies, energy storage, and electronic applications.⁷²

1.4.1 Sensor Application

The CPs, particularly MOFs are increasingly vital in modern sensor applications. Their modular chemistry enables the design of selective, responsive systems suitable for detecting gases, heavy metals, organic pollutants, biomolecules, and more. The growing need for precise and responsive sensors spans multiple fields-including environmental monitoring, industrial automation, healthcare diagnostics, agriculture, robotics, food safety, and security-where real-time detection and analysis are essential (Figure 1.10). In biosensing, CPs are employed for the fluorescent or electrochemical detection of glucose, pathogens, and DNA sequences due to their specific binding sites and signal transduction capabilities.⁷³ Gas sensors based on CPs are utilized for detecting toxic gases like NO₂ or NH₃ at low concentrations via adsorption-induced fluorescence quenching or conductivity change.⁷⁴ Colorimetric and electrochemical CP sensors aid in heavy metal ion detection, crucial in both water purification and food safety.⁷⁵ Their use in agricultural monitoring includes sensing soil nutrients or pesticides, while in automation and robotics, CPs can act as intelligent sensing layers in wearable or embedded devices.⁷⁶ Furthermore, in security and defense, CPs have shown promise for detecting explosives and chemical warfare agents, due to their high specificity and luminescent behavior upon interaction with nitro compounds.⁷⁷ This wide scope is visually represented in the accompanying schematic, showing central CP structures

linked to icons representing diverse domains such as biosensing, gas sensing, environmental safety, wearable tech, industrial monitoring, agriculture, food spoilage, health, security, and robotics, emphasizing the transformative potential of CPs in next-generation smart sensing platforms.

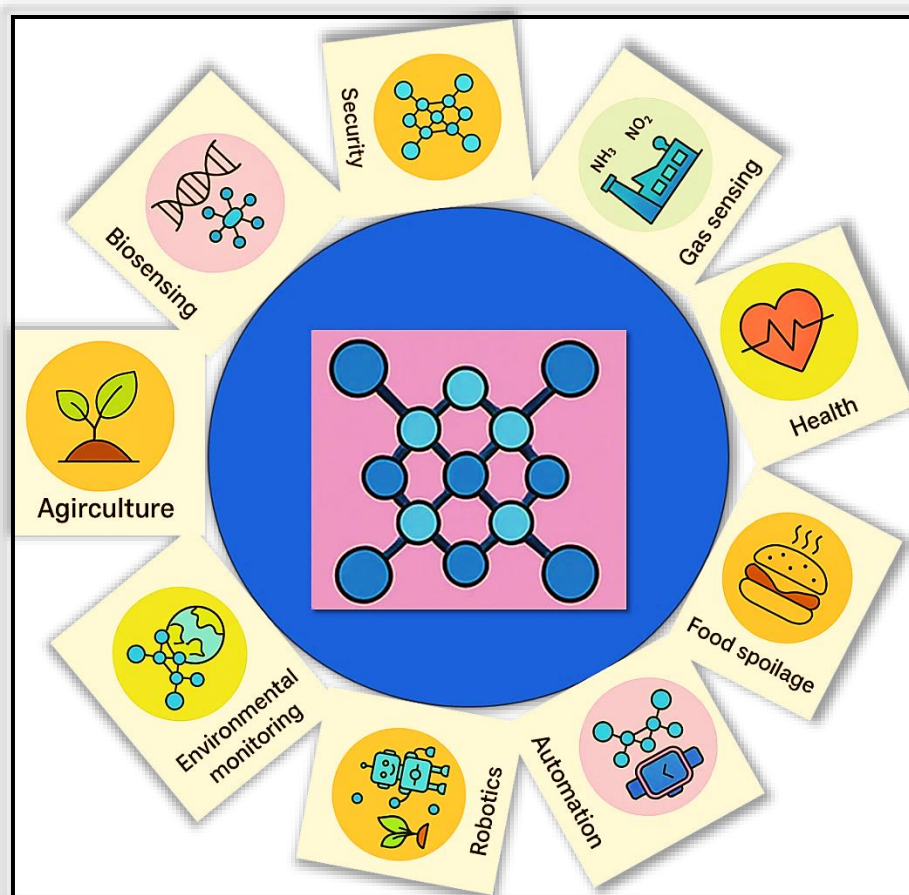


Figure 1.10 Various sensor applications of coordination polymers.

1.4.1.1 Advantages of Fluorescence Technique in Quantitative Analysis

In the analytical field, the precise quantification of ions and elements is achieved through various sophisticated techniques such as volumetric, spectrophotometric, gravimetric, and electrochemical methods. Significant attention is given to the utilization of advanced instruments, including voltammetry,⁷⁸ inductively coupled plasma mass spectrometry (ICP-MS),⁷⁹ and inductively coupled plasma atomic emission spectrometry (ICP-AES).⁸⁰ The methods also incorporate atomic absorption spectroscopy (AAS)⁸¹, alongside the use of advanced thin chitosan films⁸², and flame atomic absorption spectroscopy (FAAS).⁸³ Each technique plays a decisive role in the meticulous detection of ions and molecules.

Fluorescence and UV-Visible spectroscopy hold significant importance in the identification of analytes and facilitating cellular imaging within biological systems. The key

advantage of these techniques lies in their remarkably low detection limits, which allows them to discern even minute quantities of substances. In the realms of biochemical and chemical sciences, the fluorescence technique is indispensable due to its exceptional sensitivity and ability to selectively detect targets rapidly, making it a cost-effective approach characterized by operational simplicity, high temporal resolution, and ease of signal detection.

1.4.1.2 Fluorescence Sensing Mechanism

The fluorescence sensing mechanism involves a wide range of photophysical and photochemical processes. Among the major photophysical processes are photoinduced electron transfer (PET), intramolecular charge transfer (ICT), chelation-enhanced fluorescence (CHEF), chelation-enhanced quenching (CHEQ), Förster resonance energy transfer (FRET), excited-state intramolecular proton transfer (ESIPT), and the generation of excimers and exciplexes.

1.4.1.2.1 Photoinduced Electron Transfer (PET)

Photoinduced Electron Transfer (PET) is a key mechanism in the design of sensors. The mechanism operates through electron transfer from an excited donor species to an adjacent acceptor, which often suppresses the fluorescence signal. Upon binding with a target analyte, such as a metal ion or biomolecule, the PET process is disrupted or enhanced, causing a measurable change in fluorescence intensity. This modulation forms the basis of "turn-on" or "turn-off" sensing systems.

In a typical PET sensor, the fluorophore is linked to a receptor unit through a spacer. In the absence of an analyte, the receptor functions as an electron donor, transferring electrons to the excited fluorophore and thereby quenching its emission (**Figure 1.11**).⁸⁴ Upon analyte binding, such as Zn^{2+} or H^+ , the redox properties or spatial alignment of the donor are altered, inhibiting PET and restoring fluorescence. This switch-like response allows for selective and sensitive detection.

Recent advances include the integration of PET mechanisms into supramolecular architectures, nanoparticles, and coordination polymers, enabling applications for use in environmental analysis, medical imaging, and chemical sensing making it a foundational principle in modern sensor design.

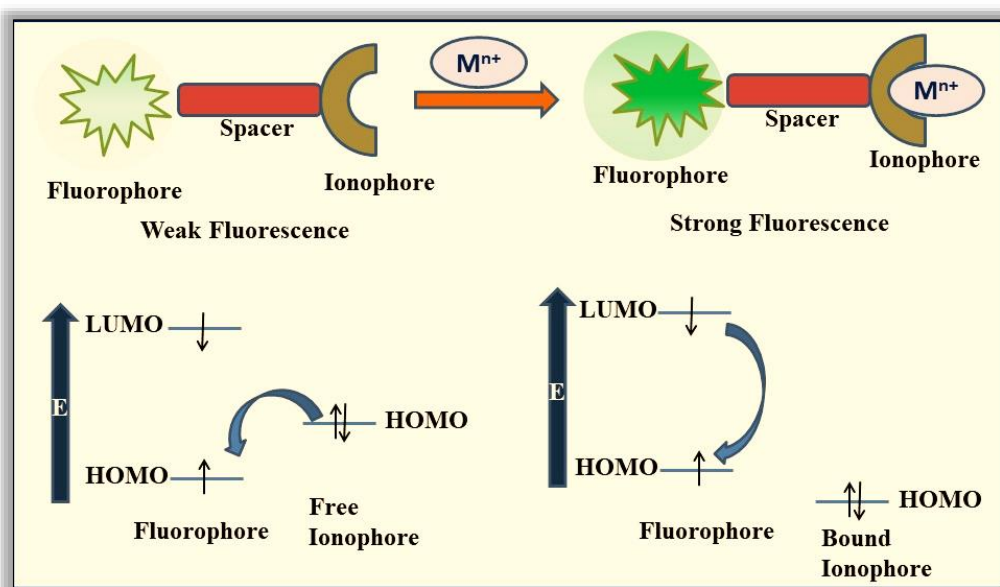


Figure 1.11 Schematic diagram for PET mechanisms.

1.4.1.2.2 Intra and Intermolecular Charge Transfer (ICT)

Charge transfer processes play a pivotal role to the development of photoluminescent materials and molecular sensing systems. Intramolecular charge transfer (ICT) occurs within a single molecule possessing distinct donor (D) and acceptor (A) units, linked through a π -conjugated bridge. Upon photoexcitation, an electron is transferred from D to A, generating a polarized excited state, often leading to large Stokes shifts and environment-sensitive emission—a key feature in fluorescence sensing and bioimaging applications.^{85,86} Conversely, intermolecular charge transfer involves electron transfer between two separate molecular entities, forming charge-transfer complexes in the excited state. These complexes may show altered emission properties or fluorescence quenching, depending on the medium and interaction strength, and are widely applied in supramolecular sensing and organic photovoltaics.^{87,88} Both ICT modes are central to the development of high-performance optical probes, contributing to selectivity and sensitivity enhancements in analyte detection (Figure 1.12).

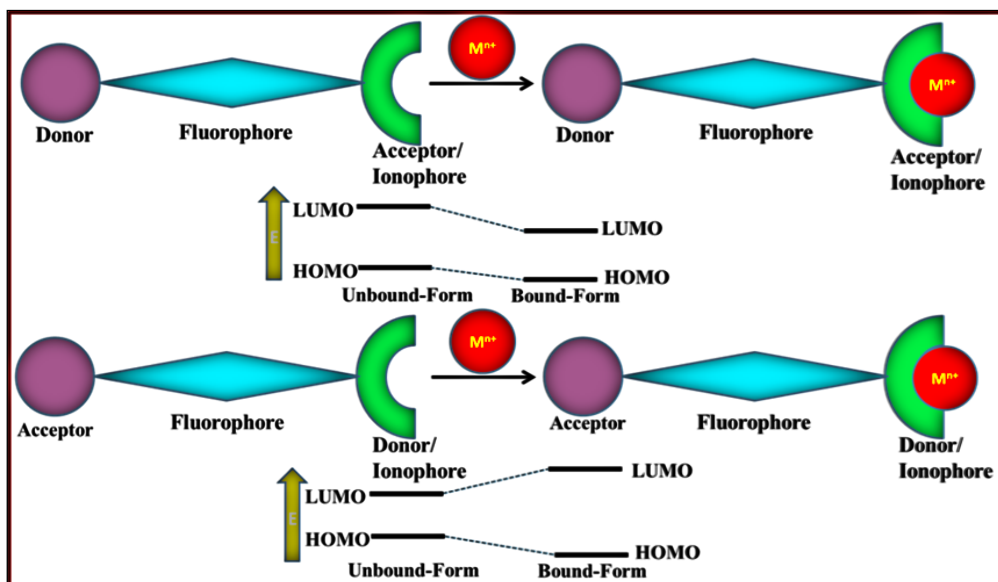


Figure 1.12 Illustration of the intramolecular charge transfer (ICT) mechanism.

1.4.1.2.3 Chelation Enhanced Fluorescence (CHEF) and Chelation Enhanced Quenching (CHEQ)

The fluorescence behavior of metal-responsive probes can be profoundly altered by chelation, leading to either signal amplification or suppression depending on the system's design. Chelation-Enhanced Fluorescence (CHEF) refers to the phenomenon where coordination of a metal ion to a fluorophore results in a substantial increase in fluorescence emission. This enhancement is typically attributed to the restriction of internal rotations and suppression of non-radiative decay processes such as photoinduced electron transfer (PET), owing to the conformational rigidity imposed by chelation.^{89,90} This mechanism has been widely exploited in the development of probes for biologically relevant metal ions like Zn^{2+} , Al^{3+} , and Cd^{2+} . Conversely, Chelation-Enhanced Quenching (CHEQ) involves fluorescence suppression upon metal coordination, commonly observed with paramagnetic metal ions (e.g., Cu^{2+} , Fe^{3+}) that facilitate non-radiative energy dissipation via electron or energy transfer pathways.^{91,92} The contrasting outcomes of CHEF and CHEQ enable dual-modality probe design, offering turn-on and turn-off signaling platforms (Figure 1.13).

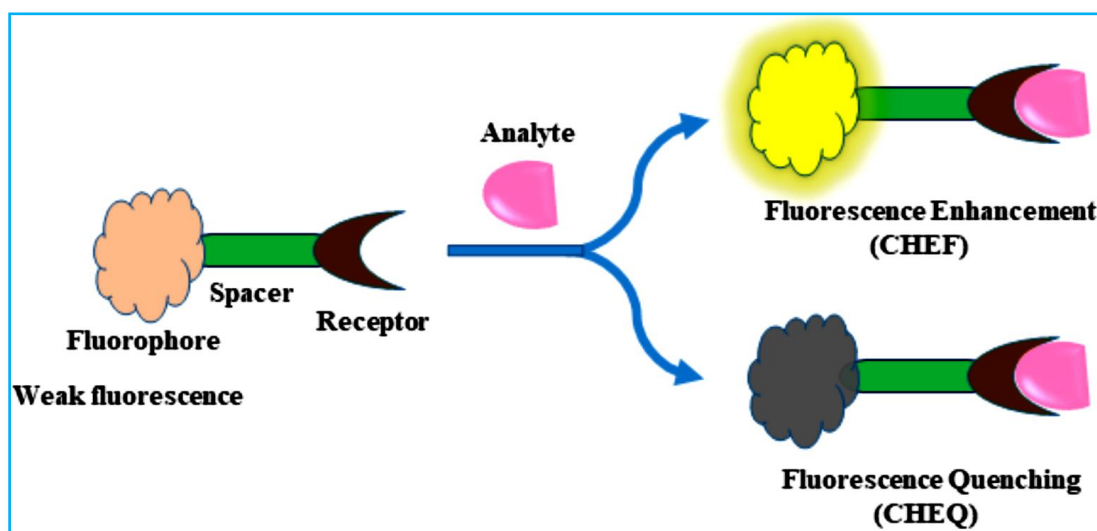


Figure 1.13 Schematic diagram of CHEF processes.

Fluorescence quenching alters both the emission intensity and photoluminescence lifetime of fluorophores. As depicted in **Figure 1.14**, quenching is typically classified into dynamic (collisional) and static mechanisms.

(i) Dynamic Quenching

Dynamic quenching occurs through collisional interactions between the excited fluorophore (A^*) and quencher molecules (Q), forming a transient encounter complex $[A^*Q]$. This non-radiative process shortens the fluorescence lifetime and is often enabled by spin-orbit coupling. This effect is especially pronounced in the presence of heavy atoms, as they facilitate intersystem crossing to the energetically favorable triplet state.

(ii) Static Quenching

Static quenching arises when the fluorophore (A) forms a stable, non-emissive ground-state complex (AQ) with an excess of quencher (Q) prior to excitation. While the fluorescence intensity decreases due to a reduced population of free fluorophores, the excited-state lifetime of the remaining emissive species remains unchanged.

Understanding the distinction between dynamic and static quenching is critical for accurate interpretation of sensor responses and for the design of lifetime-based fluorescent probes.

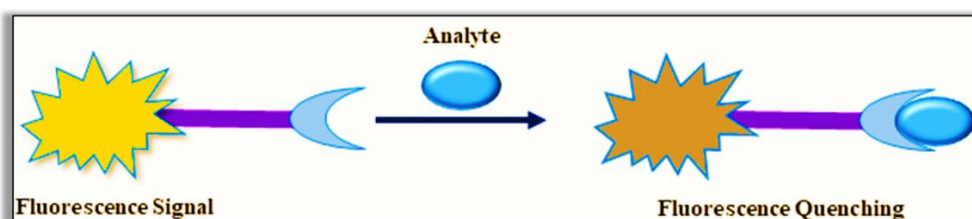


Figure 1.14 Schematic Diagram of Quenching Response.

1.4.1.2.4 Förster Resonance Energy Transfer (FRET)

Förster Resonance Energy Transfer (FRET) is a photophysical mechanism where an excited donor fluorophore transfers its energy to a nearby acceptor chromophore through non-radiative dipole-dipole coupling, without photon emission.⁹³ The efficiency of FRET is highly sensitive to the donor-acceptor separation (Figure 1.15), typically effective within 1-10 nm, and is governed by the Förster distance (R_0), which relies heavily on the degree of spectral overlap, donor quantum yield, and dipole orientation.⁹⁴ A strong spectral overlap between the emission spectrum of donor and absorption spectrum of acceptor is essential, along with proper alignment of dipoles and high donor quantum efficiency.⁹⁵ The result of FRET includes reduced donor fluorescence intensity and lifetime, and increased acceptor emission if it is fluorescent, which forms the basis for ratiometric sensing.^{93,95} Detection of FRET is commonly achieved using techniques such as steady-state fluorescence spectroscopy, time-resolved fluorescence analysis, or fluorescence lifetime imaging microscopy (FLIM).^{94,96} This mechanism has been widely applied in biological research for real-time tracking of interactions between proteins, enzymatic processes, and nucleic acid hybridization. In recent years, FRET has been integrated into nanoscale sensors using quantum dots, carbon dots, and coordination polymers, significantly enhancing detection sensitivity and selectivity for metal ions and small molecules.⁹⁷

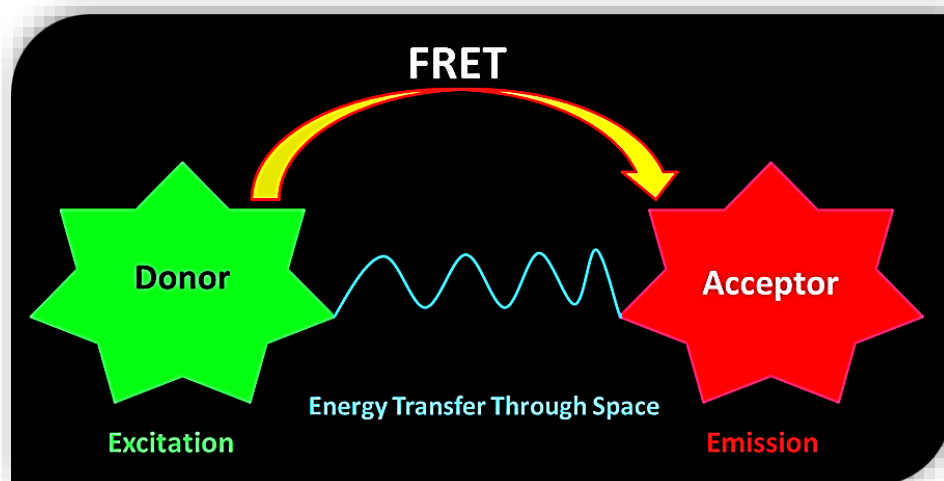


Figure 1.15 A schematic overview of the through-space energy transfer process.

1.4.1.2.5 Excited-State Intramolecular Proton Transfer (ESIPT)

Excited-State Intramolecular Proton Transfer (ESIPT) is a rapid photophysical phenomenon in which a proton is transferred internally within a molecule from a hydrogen-bond donor site to an acceptor site following photoexcitation.⁹⁸ This intramolecular proton

Chapter 1: Introduction

transfer is driven by changes in electron distribution upon excitation, which enhance the donor's acidity and the acceptor's basicity in the excited state, facilitating the proton migration.⁹⁹ ESIPT typically proceeds within femtoseconds to picoseconds and results in a tautomeric excited state with distinct photophysical properties.¹⁰⁰ Mechanistically, the process initiates when the molecule absorbs a photon, leading to its transition from the enol ground state (E) to an electronically excited enol state (E^*), which rapidly undergoes proton transfer to yield the excited keto form (K^*); this species can emit fluorescence, returning to the ground keto state (K), which then quickly relaxes back to the enol ground state (E).^{98,101} This sequence of photophysical events is commonly depicted using a Jablonski diagram, which illustrates the transitions between electronic states (Figure 1.16). A hallmark of ESIPT systems is their large Stokes shift and dual emission, enabling reduced self-quenching and high signal-to-noise ratios in fluorescence sensing.¹⁰² Moreover, the efficiency of ESIPT is highly sensitive to environmental variables such as solvent polarity, viscosity, and pH, making ESIPT-active fluorophores valuable tools in molecular sensing, bioimaging, and optoelectronic applications.

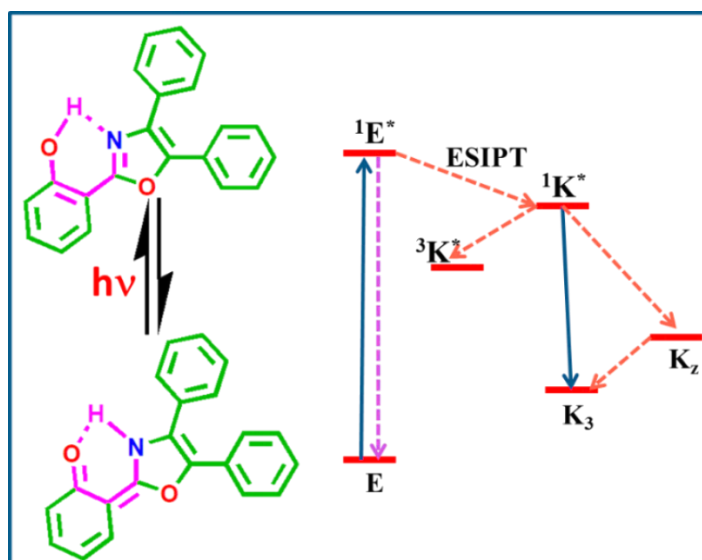


Figure 1.16 Schematic diagrams shows ESIP processes.

1.4.1.2.6 Excimer / Exciplex Formation

Excimers (excited-state dimers) and exciplexes (excited-state complexes) are transient, non-covalent species formed when an excited-state fluorophore interacts with a ground-state molecule-identical in the case of excimers and structurally distinct in the case of exciplexes.¹⁰³ These complexes do not exist in the ground state and form upon photoexcitation due to transient electronic interactions such as π - π stacking or charge transfer.¹⁰⁴ The formation is favored in fluidic or flexible media, at higher fluorophore

concentrations, and under conditions allowing close molecular proximity.¹⁰⁵ Mechanistically, an excited monomer (M^*) interacts with a ground-state molecule (M or A) forming $(MM)^*$ or $(D\cdots A)^*$, which emits red-shifted fluorescence upon relaxation (Figure 1.17).¹⁰⁶ Their broad emission, large Stokes shift, and environmental sensitivity make them valuable in sensing, supramolecular chemistry, and organic electronics.

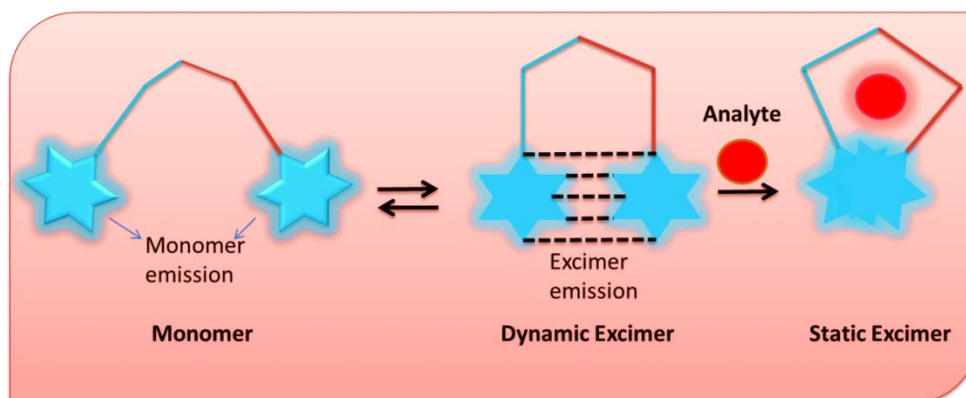


Figure 1.17 Excimer formation-based fluorescent sensing mechanism.

1.4.1.3 Metal Ion Sensor

Metal ion sensors are essential tools for detecting and quantifying metal ions in environmental, industrial, and biological systems, helping monitor toxic contaminants, ensure industrial process quality, and diagnose health issues related to metal imbalances.¹⁰⁷ Coordination Polymers (CPs), particularly luminescent CPs (LCPs), offer highly sensitive and selective detection through changes in fluorescence or luminescence upon interaction with target metal ions. CPs can detect a broad spectrum of metal ions, including toxic heavy metals (e.g., Pb^{2+} , Hg^{2+} , Cd^{2+}) and essential metals (e.g., Zn^{2+} , Fe^{2+}/Fe^{3+} , Cu^{2+}), as well as trace elements (e.g., Cr, Mn, Co, Mo, Al, Si, Se, Sn). Their structural tunability allows the design of highly selective sensors that operate via fluorescence quenching/enhancement or electrochemical responses, ensuring accurate and real-time detection even at trace levels.¹⁰⁸ Their structural flexibility and porous nature enhance sensitivity and real-time detection, while their luminescent properties provide an easy-to-read signal in diverse environments.¹⁰⁹ CP-based sensors offer high selectivity, versatility, and non-invasive monitoring, with key applications in environmental safety and healthcare diagnostics. As research advances, these sensors promise to play a pivotal role in addressing global challenges in both public health and sustainability.

Chapter 1: Introduction

Table 1.1 Threshold limits of biologically important and toxic metals in the human body. ¹¹⁰⁻¹¹²

Metal	Biological Role	Threshold Limit / Reference Dose	Excess/Toxic Effects	Source /Agency
Iron (Fe)	Essential (hemoglobin, enzymes)	10-30 $\mu\text{mol/L}$ serum (normal); $>60 \mu\text{mol/L}$ = overload	Liver damage, diabetes, heart issues	WHO, NIH
Zinc (Zn)	Essential (enzymes, immunity)	70-120 $\mu\text{g/dL}$ plasma; UL: 40 mg/day (adults)	Nausea, immune suppression, copper deficiency	WHO, IOM
Copper (Cu)	Essential (enzymes, antioxidant)	70-140 $\mu\text{g/dL}$ serum; UL: 10 mg/day	Liver and kidney damage, neurological effects	WHO, IOM
Magnesium (Mg)	Essential (ATP, muscle, nerves)	1.7-2.3 mg/dL serum; UL: 350 mg/day (supplements)	Diarrhea, cardiac issues	NIH, WHO
Calcium (Ca)	Essential (bones, signaling)	8.6-10.2 mg/dL serum; UL: 2500 mg/day	Kidney stones, calcification of soft tissues	NIH, WHO
Selenium (Se)	Essential (antioxidant enzymes)	60-120 $\mu\text{g/L}$ plasma; UL: 400 $\mu\text{g/day}$	Hair/nail loss, selenosis, nerve damage	WHO, IOM
Chromium (Cr^{3+})	Essential (insulin metabolism)	0.1-0.5 $\mu\text{g/L}$ plasma; UL not defined	DNA damage, cancer (Cr^{6+})	ATSDR, EPA
Lead (Pb)	Toxic (no safe level)	$<5 \mu\text{g/dL}$ blood (CDC reference); No safe limit in children	Neurotoxicity, developmental delay	CDC, WHO
Mercury (Hg)	Toxic (no biological role)	$<5 \mu\text{g/L}$ blood (inorganic); $<1 \mu\text{g/g}$ hair (methylmercury)	Kidney, CNS damage, developmental toxicity	WHO, EPA
Cadmium (Cd)	Toxic (no biological function)	$<5 \mu\text{g/L}$ blood; $<1 \mu\text{g/g}$ creatinine (urine)	Kidney damage, bone demineralization, cancer	ATSDR, WHO
Arsenic (As)	Toxic (possible trace role)	$<10 \mu\text{g/L}$ blood (total); $<35 \mu\text{g/L}$ urine (inorganic)	Skin lesions, cancer, cardiovascular disease	WHO, EPA
Aluminum (Al)	Toxic (no biological role)	$<10 \mu\text{g/L}$ blood (normal); $<60 \mu\text{g/L}$ in dialysis patients	Neurotoxicity, possible Alzheimer's link	ATSDR, WHO
Nickel (Ni)	Possibly essential	$<0.2 \mu\text{g/L}$ serum; UL: 1 mg/day	Allergies, lung fibrosis, cancer risk	WHO, EPA
Manganese (Mn)	Essential (enzyme cofactor)	4-15 $\mu\text{g/L}$ blood; UL: 11 mg/day	Neurological symptoms, parkinsonism	WHO, IOM

1.4.1.3.1 Aluminium (Al^{3+}) Sensing

Aluminum (Al^{3+}) ions are widely prevalent in the environment and biological systems, where their abnormal accumulation is linked to neurotoxicity and various diseases, necessitating sensitive and selective detection methods. This dissertation presents the strategic synthesis of new fluorescent coordination polymers (CPs) engineered for highly selective sensing of Al^{3+} ions in aqueous media. The CPs, constructed from rationally chosen luminescent organic ligands coordinated with metal nodes, exhibit strong fluorescence emission centered around 450 nm, which undergoes significant quenching (>85%) upon interaction with Al^{3+} ions. The sensing system achieves a detection limit as low as 0.5 μM , outperforming numerous conventional fluorescent sensors^{107,113} and exhibits remarkable selectivity against competing metal ions such as Fe^{3+} , Cu^{2+} , Zn^{2+} , and Mg^{2+} , confirmed through comparative fluorescence titration studies.¹¹⁴ Powder X-ray diffraction (PXRD) and scanning electron microscopy (SEM) analyses verify the well-defined crystalline structure and morphology of the CPs. Complementary spectroscopic studies reveal that the fluorescence quenching arises from coordination interactions between Al^{3+} ions and electron-rich ligand sites, which facilitate non-radiative decay processes.¹¹⁵ Importantly, the CP sensors maintain fluorescence responsiveness in biologically relevant media, with successful detection of Al^{3+} in simulated serum samples, highlighting their potential utility in biomedical diagnostics.¹¹⁶ This dissertation advances the understanding of CP-based fluorescent sensors and provides a promising approach for real-time, cost-effective, and portable monitoring of biologically relevant aluminum ions.

1.4.1.4 Molecular Sensor

Molecular sensing involves detecting specific molecules or analytes by monitoring measurable changes in a sensor material. Owing to their large surface area, structural flexibility, and selective interaction with specific analytes, coordination polymers (CPs) have established themselves as highly effective materials for precise and reliable molecular sensing. Among these, luminescent coordination polymers (LCPs), incorporating luminescent metal ions or organic linkers, are particularly effective. They undergo noticeable changes in fluorescence or luminescence upon interaction with specific analytes, providing a straightforward and non-invasive detection method.⁶² The synthesis of LCPs focuses on selecting appropriate metal centers and organic ligands to optimize luminescent response and stability. These materials are used to detect a broad spectrum of contaminants, such as heavy metal ions and volatile organic substances, and have shown potential in real-time environmental monitoring.¹¹⁷ In healthcare, LCPs are being developed for detecting disease

biomarkers and harmful substances such as trinitrophenol (TNP), enhancing early diagnosis and safety.¹¹⁸ Despite challenges in selectivity and stability, LCP-based sensors offer great promise for diverse applications spanning environmental surveillance and healthcare diagnostics.

1.4.1.4.1 Trinitrophenol (TNP) Sensing

Trinitrophenol (TNP), a highly toxic nitroaromatic compound widely used in explosives and industrial applications, poses significant environmental and health risks due to its persistence and bioaccumulative nature (Agency for Toxic Substances and Disease Registry).^{119,120} Sensitive and selective detection of TNP is essential for environmental monitoring and public safety. Coordination polymers (CPs), known for their crystalline porous structures and adjustable luminescent behavior, have gained prominence as efficient systems for the molecular detection of TNP. The quenching mechanism is attributed to efficient electron or energy transfer between the electron-rich CP frameworks and electron-deficient TNP molecules, resulting in significant fluorescence intensity reduction.^{121,122} Successive fluorescence titration experiments demonstrated high sensitivity with detection limits reaching nanomolar levels and strong selectivity toward TNP over other nitroaromatics.^{123,124} The reversible quenching behavior indicates potential for sensor reusability. Given TNP's acute toxicity (oral LD₅₀ ~100 mg/kg) and environmental hazards, including aquatic toxicity and human health effects such as skin irritation and hematologic damage, the development of CP-based sensors provides a promising approach for rapid, on-site detection to mitigate exposure risks.^{125,126} Various CPs based on metal centers such as copper, zinc, and iron, coordinated with organic ligands like 1,4-benzenedicarboxylate (BDC) or imidazole derivatives, have demonstrated significant selectivity toward TNP, primarily due to the strong affinity between the nitro functional groups of TNP and the coordinated metal sites in the polymer matrix.^{127,128} Moreover, the structural flexibility of these CPs allows them to adapt upon TNP binding, enhancing the signal response and improving detection reliability. This dissertation also discusses the challenges in sensor performance, including issues of stability, selectivity in complex environments, and potential interference from other nitroaromatic compounds. Future directions for the development of more robust and selective CP-based sensors for TNP detection, including the incorporation of advanced materials like metal-organic frameworks (MOFs) and functionalized ligands, are also explored.¹²⁹

1.4.2 Electrical Conductivity

A diode is a fundamental electrical component characterized by two terminals, strategically designed to permit the flow of current in a singular direction. One terminal exhibits low resistance while the opposite terminal presents higher resistance, effectively blocking reverse current flow. Of special note is the "hot carrier semiconducting diode," more commonly known as a Schottky diode, which arises from the interface between metal and semiconductor materials, forming a critical barrier. In particular, the n-type diode utilizes metal as the cathode and a p-type semiconductor as the anode, highlighting the sophisticated engineering involved in its construction.

1.4.2.1 Diode and Schottky Barrier

A comprehensive examination of diodes, particularly focusing on Schottky barrier diodes, highlighting their fundamental principles and diverse applications. Diodes, as semiconductor devices, play a critical role in electronics by permitting current flow in one direction while obstructing it in the reverse, thereby serving as indispensable components in electronic circuits.¹³⁰ The Schottky barrier diode, noted for its metal-semiconductor junction, offers distinct advantages, including a reduced forward voltage drop and rapid switching speeds. The discussion encompasses the operational mechanisms, construction details, and the significant influence of these diodes' unique properties on performance across various electronic applications. In a Schottky diode, the cathode functions as the n-type semiconductor, while the metallic portion serves as the anode material of the diode, establishing a significant interaction between the two components (**Figure 1.18**).¹³¹⁻¹³³ An intrinsic electrostatic barrier arises due to the differing work functions of the metal and semiconductor. This effect becomes especially significant when the metal's work function (ϕ_m) exceeds that of the semiconductor (ϕ_s), promoting the flow of electrons from the semiconductor into the metal.^{134,135} As equilibrium is attained between their Fermi levels, a depletion region is formed, marking a critical aspect of the diode's operation.

The diffusion potential V_{do} is represented as

$$V_{do} = \phi_m - \phi_s \dots \dots \dots (1)$$

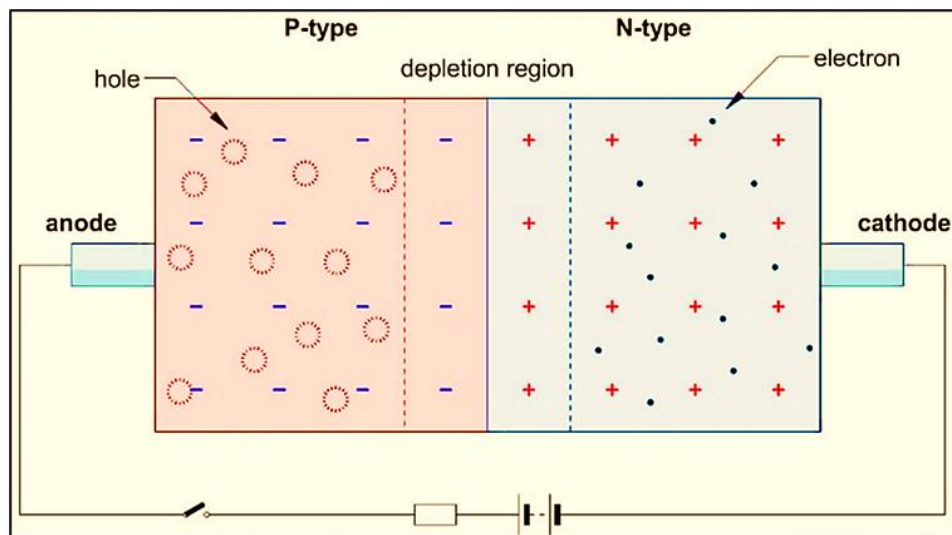


Figure 1.18 Schottky barriers and work function for semiconductors.¹³⁶

For an n-type semiconductor, when the work function (ϕ_m) of metal is greater than that of the work function of semiconductor (ϕ_s), the energy bands bend upward near the interface, creating a potential barrier that electrons must overcome to move into the metal. In contrast, for a p-type semiconductor under similar conditions, band bending does not hinder hole transport, often resulting in an ohmic contact. Conversely, when ϕ_m is less than ϕ_s , the energy bands bend downward, enabling easy electron flow and forming an ohmic contact in n-type semiconductors, while for p-type semiconductors, this leads to a rectifying behavior due to restricted hole injection.¹³⁷

1.4.2.2 Advantages of Schottky Diode

Low turn on voltage: For optimal performance of a Schottky diode, it is crucial to ensure the voltage is precisely regulated within the range of 0.2 to 0.45 volts.

Fast recovery time: High-speed switching applications are optimized by a swift recovery period that uses only a minimal amount of stored electrical charge, ensuring efficient performance.

Low junction capacitance: Capacitance level is very low if the contact area is very small.

High Switching Speed

Schottky diodes exhibit extremely fast switching characteristics because their operation is based on majority carrier conduction, meaning there is no charge storage or recombination delay as seen in PN junction diodes. This allows them to switch on and off within nanoseconds.

Compact and Thermally Stable

Schottky diodes have a simple metal-semiconductor junction structure that requires fewer layers and fabrication steps than PN junction diodes, making them compact and easy to integrate into miniaturized circuits. Their low power loss and reduced heat generation enhance thermal stability, allowing reliable operation even under high current conditions.

1.4.2.3 Applications of Schottky Diode

Schottky diodes are fundamental components in radio frequency applications and radio detection systems, primarily due to their low capacitance, high switching speed, and exceptional frequency capabilities. Their most significant application lies in rectifiers, where they outperform traditional p-n junction diodes by exhibiting a lower forward voltage drop and higher current density. This efficiency allows Schottky diodes to operate with reduced power consumption compared to standard diodes. Furthermore, the Schottky barrier functions effectively as a circuit element in dual power supply systems, enhancing overall performance and reliability.

Solar cell applications: Schottky diodes are commonly used in solar cells to address the challenge of low voltage drop, as significant voltage reductions are typically unexpected in these systems. These diodes are preferred because they help minimize energy loss, ensuring that the cell operates at its optimal capacity.

Clamp diode: A clamp diode, specifically a Schottky diode, plays an essential role in transistor circuits by managing the speed during the switching process. Its function is crucial to ensuring efficient and smooth operation within the circuit.

High-speed digital systems

Schottky diodes are ideal for high-speed digital applications such as clock generation, logic level shifting, and signal protection in high-frequency data lines, where they enhance performance by preventing transistor saturation in Schottky TTL logic circuits. Additionally, their low junction capacitance ensures clean signal transitions in timing circuits, FPGAs, and microprocessor interfaces, preserving signal integrity in high-speed systems.

Signal Demodulation

Schottky diodes are widely used in signal demodulation, making them ideal for detecting low-level signals in AM/FM receivers, envelope detectors, and RF circuits with high sensitivity and minimal distortion.

Power Rectification

Schottky diodes are ideal for power rectification in switch-mode power supplies and DC-DC converters due to their low forward voltage drop and fast switching speed, which reduce power loss and improve overall efficiency.

Reverse Battery Protection

Schottky diodes are commonly used for reverse battery protection, as their low forward voltage drop minimizes power loss while effectively blocking reverse current to prevent damage to sensitive electronic components.

1.4.2.4 Diode Parameters

Ideality Factor (η): The ideal performance of a Schottky diode is characterized by its ideality factor. This factor gauges the current in the low voltage region, revealing a direct proportionality to the rate of change in voltage with respect to the natural logarithm of current, expressed as $dV/d\ln I$.

Series Resistance (R_s): In a series of Schottky diodes, the total resistance encountered is referred to as series resistance, and it is here that the current navigates through all the resistors.

Barrier Height (ϕ): The Schottky barrier height (SBH) is a critical parameter characterizing the interface between a metal and a semiconductor, as it governs the rectifying behavior and charge transport across the junction. In the case of an n-type semiconductor, the SBH corresponds to the energy difference between the metal's Fermi level and the conduction band minimum of the semiconductor. For a p-type semiconductor, it is defined by the energy separation between the metal's Fermi level and the valence band maximum of the semiconductor. This barrier plays a key role in determining the electronic properties and efficiency of metal-semiconductor devices.

1.4.2.5 Charge Transport Parameter

Mobility (μ): Carrier mobility denotes the speed at which electrons or holes move through a material under an electric field. In semiconductors, it is influenced by carrier concentration, impurity levels (such as donors and acceptors), electric field strength, and temperature—all of which affect scattering and transport efficiency.

Transit time (τ): The duration it takes for a carrier to journey from the cathode to the anode—or the other way around—is known as the transit time. This interval encompasses both the time associated with freely moving carriers and the duration needed for carriers that are temporarily trapped in the traps.

Diffusion Length (L_D): The current flow across a metal-semiconductor junction is primarily governed by the transport of majority charge carriers. One of the key mechanisms facilitating this transport is the diffusion of carriers from the semiconductor into the metal. According to diffusion theory, the diffusion length defines the characteristic distance over which carriers migrate before recombination, typically corresponding to the width of the depletion region where the concentration gradient is counterbalanced by the built-in electric field.

1.4.3 Electrocatalytic Water Splitting Application

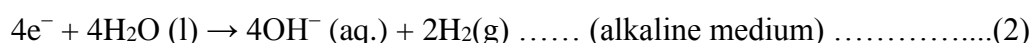
Electrolysis of water stands out as a significant method for producing high-purity hydrogen, especially when weighed against conventional approaches, which inevitably lead to greenhouse gas emissions. Photocatalytic water splitting, although promising, is contingent upon direct sunlight exposure, raising concerns about the uninterrupted energy supply. In contrast, electrocatalytic techniques have the potential to mitigate the limitations seen in other approaches. Nevertheless, the oxygen evolution reaction (OER) and hydrogen evolution reaction (HER) entail intricate mechanistic steps, resulting in increased overpotentials. This substantial overvoltage requirement poses a significant challenge to achieving high current densities, thereby complicating large-scale hydrogen production.¹³⁸ The pH of the electrolyte significantly influences catalyst stability, particularly as ion diffusion toward the electrode surface is markedly impacted in extreme acidic (pH = 0) and alkaline (pH = 14) conditions. In acidic electrolytes, abundant H^+ ions facilitate their approach to the electrode surface, promoting efficient hydrogen adsorption during HER.¹³⁹⁻¹⁴¹ Conversely, the OER poses a challenge because OH^- ions must be generated from water molecules, a process that demands additional energy. This involves complex mechanistic steps including OH^- ion adsorption, oxide formation, and O_2 molecule cleavage, requiring the transfer of four protons and electrons, and thereby necessitating elevated anodic overpotentials, particularly in acidic environments.¹⁴²⁻¹⁴⁴ The corrosive dissolution of active catalysts within an acidic medium presents significant challenges, making the supply of stable and constant current difficult. This complication is further exacerbated by issues related to OER overpotential and stability, posing formidable obstacles to achieving optimal cell voltage in water electrolyzers. The development of bi-functional catalysts suitable for acidic conditions remains a demanding endeavor. Similarly, in alkaline environments, the rapid diffusion of OH^- ions is compromised, making OER kinetically favorable while reintroducing problems for HER due to the dependency on water as a source of H^+ ions. In neutral environments, the poor ionic conductivity curtails the efficiency of electroactive species, demanding even higher

overvoltage compared to acidic and alkaline mediums.^{145,146} Consequently, there is an urgent need to furnish alternative catalysts with rapid surface modifications.

1.4.3.1 Mechanistic Aspects of Electrocatalytic Water Splitting

Water splitting reaction is a non-spontaneous process, with positive free energy change of +237 kJ/mol. Additionally, the octet configuration of the water molecule presents challenges in breaking it down into its oxygen and hydrogen components. The equilibrium potential necessary for electrochemical water splitting is 1.23 V. The increased potential required for this process is referred to as overpotential. The sequence of reactions varies according to the pH conditions, as detailed below:

Cathodic HER reaction:



Anodic OER reaction:

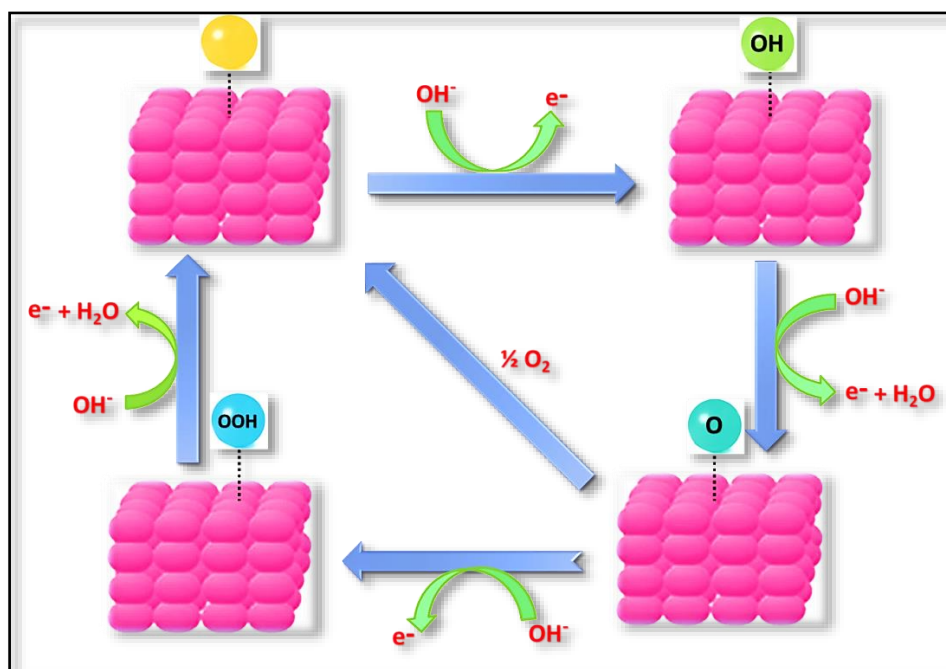


Figure 1.19 Mechanistic pathways for OER in alkaline condition.

1.4.3.2 Parameters Involved for Electrocatalytic Water splitting

The evaluation and comparison of the activity of catalytic materials in the electrocatalytic water splitting process necessitate the consideration of certain vital parameters, which are widely acknowledged in the scientific community.

1.4.3.2.1. Overpotential

In the examination of HER and OER processes, it was determined that the standard reduction potential for HER is 0 V vs RHE, while for OER it is 1.23 V. This reveals that the minimum thermodynamic potential necessary for water-splitting is 1.23 V. Despite this theoretical requirement, the reaction is not initiated due to various kinetic barriers associated with the electrodes and electrolyte. These barriers necessitate additional potential beyond the theoretical value, known as overpotential. Overpotential is typically divided into three primary categories: (i) activation overpotential, (ii) concentration overpotential, and (iii) overpotential resulting from uncompensated resistance (R_u). The activation overpotential depends on the intrinsic activity of the catalytic material on the electrode surface. So, it can be neglected by the suitable efficient catalyst. The concentration overpotential is defined as when the electrode reaction was started, the sudden drop observed on the interface. This can be eliminated by, stirring of the electrolyte solution. The overpotential observed from the R_u will be eliminated by ohmic drop compensation via the electrochemical work station itself. Otherwise, it can also be done manually by multiplying the current density with the observed R_u .

1.4.3.2.2. Tafel Slope

The intrinsic kinetics at the electrode-electrolyte interface were examined through the analysis of the Tafel slope, a key parameter derived from the Butler-Volmer equation under strongly anodic or cathodic conditions. The significance of the Tafel slope lies in its ability to provide insight into electrochemical mechanisms, as the Tafel equation indicates that the current density (j) is directly proportional to the exchange current density (i_0) and inversely proportional to the Tafel slope (b). The relationship is mathematically expressed as follows:

$$i = i_0 \log (\eta/b)$$

Here, i represents the current density, i_0 denotes the exchange current density, η is the overpotential, and b refers to the Tafel constant. The Tafel slope, typically reported in mV per decade, is a critical kinetic parameter obtained from polarization curves by plotting the logarithm of the current density against the corresponding overpotential. This measurement is instrumental in assessing the kinetics of electrode reactions and is influenced by different overpotential regions. It is essential to carefully extract Tafel slope values to gain a reliable understanding of charge transfer kinetics. To ensure precision, potentiostatic measurements are commonly employed to record log current densities, facilitating the extraction of meaningful Tafel slope values in the context of oxygen evolution reaction or hydrogen evolution reaction studies.

1.4.3.2.3. Electrochemical Impedance Spectroscopy

Electrochemical Impedance Spectroscopy (EIS) offers valuable insight into reaction kinetics and is typically performed using an AC technique in either potentiostatic or galvanostatic mode. This technique facilitates the measurement of electrochemical responses at interfaces or surfaces, determined by the applied frequency of AC perturbation potential, typically ranging from 5 to 10 mV, though extending up to 500 mV in certain scenarios. In processes like, OER and HER under extreme pH conditions such as 0.5 M H₂SO₄ and 1M KOH, the reaction pathway is entirely governed by kinetic processes, with no significant contribution from Warburg impedance. On the contrary, in situations marked by reduced kinetics, the process is dominated by Warburg impedance rather than charge transfer mechanisms.

1.4.3.2.4. Stability

A crucial parameter for any electrocatalyst is its stability, ensuring the robustness of the materials, especially for prolonged electrocatalytic water splitting processes. To ascertain the stability of the catalyst, both potentiostatic and potentiodynamic analyses were conducted. The potentiostatic method encompassed chronoamperometry, where the potential remains constant while monitoring the current over time, and chronopotentiometry, where the current remains constant while observing changes in potential over time. These analyses were performed under static conditions to elucidate the differences in catalytic activities before and after the stability study. Additionally, as part of the potentiodynamic strategy, cyclic voltammetry was performed at high scan rates for 1000 to 5000 repeated cycles.

1.4.3.2.5. Electrochemical Active Surface area and Turn Over Frequency

The intrinsic activities, such as electrochemical active surface area (ECSA), turnover frequency (TOF), and mass activity, play crucial roles in assessing the effectiveness of an electrocatalyst. To determine ECSA, which indicates the surface area availability, two predominant methods are adopted: (i) measuring double layer capacitance (C_{dl}) across multiple scan rates within the non-faradaic potential range; and (ii) focusing on the redox features, where the area of oxidation or reduction peaks highlights the substances that have undergone specific reactions. Turnover Frequency (TOF) offers crucial insight into a catalyst's capacity to promote the generation of hydrogen or oxygen at the active surface within a specified overpotential range. TOF is determined using the formula

$$TOF = jM/4mF,$$

where j represents the current density, M denotes the molar concentration of metals, m refers to the mass loading, and F is the Faraday constant. Understanding catalytic loading is vital for

assessing a catalyst's performance, as materials deposited on conductive substrates can exhibit substantial loading. In such situations, evaluating mass activity is significant, as it provides a more reliable measure of performance under the necessary overpotential conditions. In such circumstances, it is essential to employ ECSA normalized current instead of area normalized current, as it offers a substantive comprehension of the observed overpotentials at the targeted current densities. From the perspective of activity and stability, it is crucial to examine these intrinsic parameters in order to identify alternative catalysts for effective electrocatalytic water splitting, ensuring minimal energy input.

1.5 Aim and Scope of the Dissertation

Above short discussions on CPs/MOFs illuminates the profound impact and robust scientific basis towards the design of materials for newer applications on SDGs, urging us to explore the intricate world of chemical innovation. Through groundbreaking design and synthesis, these materials emerge as key players in solving pressing challenges on the energy and environment. Let's embrace the opportunity to harness their transformative potential and strive for a sustainable future.

Research in this dissertation will focus on the synthesis of bridging heterocyclic ligands and the coordination polymers/MOFs. These CPs/MOFs will be used for detecting the explosives and heavy metal ions in the environment, emphasizing their importance in safety and pollution monitoring. By combining the development of energy-efficient materials with cutting-edge sensor technology, this research aims to provide a comprehensive solution to pressing environmental challenges, paving the way for future advancements in both fields.

This study focuses on the synthesis, structural and spectroscopic analysis, and potential applications of CPs/MOFs using common 3d metals (Zn, Co) and a 4d metal (Cd). It employs various carboxylic acids (e.g., glutaric acid, 5-nitroisophthalic acid, 2,5-thiophene dicarboxylic acid) as bridging linkers, along with complex nitrogen-donor ligands such as 6-(Pyridin-4-yl)-5,6-dihydrobenzo[4,5]imidazo[1,2-c]quinazoline and (*E*)-1-(Pyridin-4-yl)-*N*-(4*H*-1,2,4-triazol-4-yl)methanimine (**Figure 1.20**). The materials are synthesized using a solution phase slow diffusion technique at room temperature. They have undergone comprehensive characterization through various spectroscopic methods, with an in-depth analysis presented in the following chapters (**Chapters 2-5**).

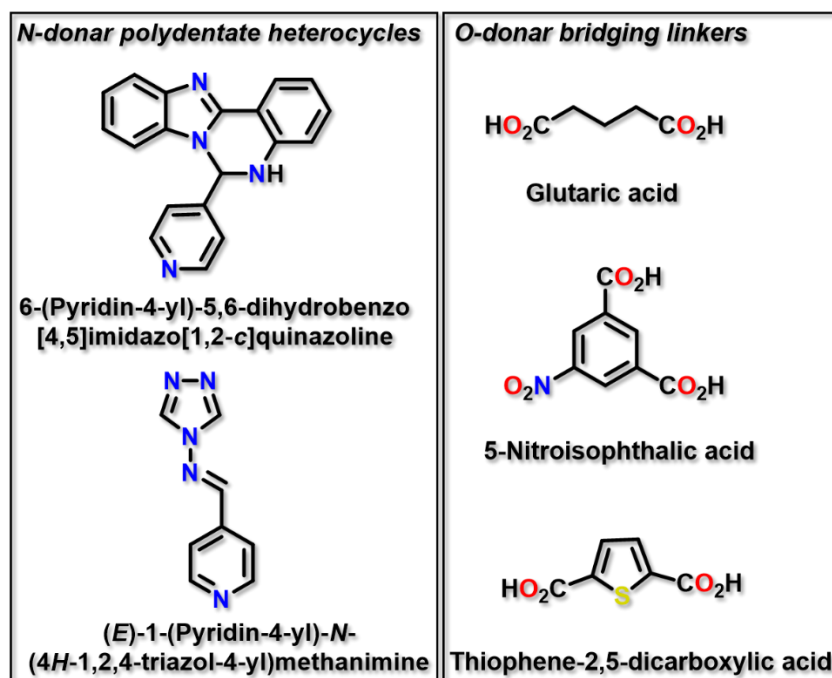


Figure 1.20 Representative examples of N- and O-donor organic linkers used in the synthesis of CPs/MOFs for this dissertation.

1.6 Physical Measurements

- (i) **FT-IR spectra:** Collected Infrared (IR) spectral range was 400-4000 cm^{-1} using a PerkinElmer SPECTRUM II LITA FT-IR spectrometer.
- (ii) **UV-vis spectra:** The UV-Vis absorbance spectral analysis was conducted with a PerkinElmer Lambda 25 spectrophotometer, using a 1 cm path length quartz cuvette within the 190-900 nm wavelength.
- (iii) **Single crystal X-ray diffractometer (SC-XRD):** Single-crystal X-ray diffraction data were collected using a Bruker SMART APEX III diffractometer equipped with graphite-monochromated $\text{MoK}\alpha$ radiation ($\lambda = 0.71073 \text{ \AA}$), as well as an APEX II CCD system utilizing $\text{CuK}\alpha$ radiation ($\lambda = 1.54178 \text{ \AA}$). Data acquisition was performed at a controlled temperature of 273 K using a suitable single crystal of the compound.
- (iv) **Powder X-Ray Diffraction (PXRD):** Powder X-ray diffraction (PXRD) patterns were recorded at ambient temperature over a 2θ range of 5° to 55° , using a Bruker diffractometer equipped with $\text{Cu K}\alpha$ radiation ($\lambda = 1.54178 \text{ \AA}$), operated at 40 kV and 40 mA.
- (v) **Thermogravimetric analysis (TGA):** Thermogram was collected from a PerkinElmer Pyris Diamond TG/DTA thermal analyzer. The measurements were conducted under inert environment at a constant flow rate of $50 \text{ cm}^3/\text{min}$. The

temperature was gradually increased from 30 to 800 °C at a uniform heating rate of 10 °C/min.

- (vi) **Fluorescence spectra:** Fluorescence measurements were conducted using a PerkinElmer LS55 spectrofluorimeter, with a high-purity quartz cuvette of 1 cm path length to eliminate any background fluorescence interference. This setup ensured precise and reliable emission data acquisition.
- (vii) **Lifetimes measurements:** Luminescence lifetime studies were conducted using an advanced time-correlated single photon counting (TCSPC) setup from Horiba Jobin-Yvon. The emission decay signals were recorded with a Hamamatsu microchannel plate photomultiplier (model R3809), and the resulting data were processed and analyzed using the IBH DAS6 software package.
- (viii) **Field Emission Scanning Electron Microscopy (FESEM) Analysis:** Field emission scanning electron microscopy (FE-SEM) coupled with Energy Dispersive X-ray Spectroscopy (EDS) was carried out using the Carl Zeiss SUPRA 55VP system, which is integrated with a dedicated EDS detector for elemental analysis.
- (ix) **High Resolution Transmission Electron Microscope (HRTEM) Analysis:** High-resolution transmission electron microscopy (HR-TEM) analysis was performed using a Thermo Scientific Tecnai G2 F20 instrument operating at an accelerating voltage of 200 kV, equipped with an EDAX system for elemental identification. Additionally, a Talos F-200S microscope was employed for high-angle annular dark-field (HAADF) imaging and elemental mapping to gain further insight into the material's structural and compositional details.
- (x) **X-Ray Photoelectron Spectroscopy (XPS) Analysis:** X-ray photoelectron spectroscopy (XPS) measurements were conducted utilizing two advanced systems: the Theta Probe AR-XPS from Thermo Fisher Scientific (UK) and the ESCALAB 250Xi model by Thermo Scientific. These instruments enabled precise surface chemical analysis of the samples.
- (xi) **pH study:** The pH measurements of the solutions, ranging from 2 to 12, were conducted using a Systronics digital pH meter (Model 335, India). Calibration of the pH meter was performed using standard buffer solutions from Acros Organics with pH values of 4.0, 7.0, and 10.0.
- (xii) **DFT Computational Study:** The molecular geometry of the compound in the gas phase was optimized through Density Functional Theory (DFT) calculations

performed using the *Gaussian 09* software suite. The analysis and visualization of the computational results were carried out with the help of the GaussSum graphical interface.

(xiii) **Electrical Study:** To construct metal-semiconductor junction devices configured in a layered ITO/Material/Al setup, we applied thin films of the synthesized compound to a cleaned ITO-coated glass substrates using the doctor blade technique. The aluminum, serving as the top metal contact, was deposited onto plain glass slides via thermal evaporation in a high-vacuum coating system sustained at a pressure of 10^{-6} Torr. The devices underwent electrical characterization through current-voltage measurements using a Keithley 2635B Sourcemeter, utilizing a standard two-probe setup.

(xiv) **Electrochemical Study:** The electrochemical performance was investigated using a Metrohm AUTOLAB-M240 system through various techniques, including cyclic voltammetry (CV), linear sweep voltammetry (LSV), and chronoamperometry (CA). A conventional three-electrode setup was employed, comprising a Hg/HgO reference electrode, a graphite rod as the counter electrode, and nickel foam (NF) as the working electrode. To fabricate the working electrode, a slurry was prepared by mixing the active material with polyvinylidene fluoride (PVDF) as the binder and N-Methyl-2-pyrrolidone (NMP) as the solvent.

1.7 References

- (1) Constable, E. C. *Chemistry*, **2019**, *1*, 126-163.
- (2) Grandjean, F.; Samain, L.; Long, G. J. Characterization and utilization of Prussian blue and its pigments. *Dalton Trans.*, **2016**, *45*, 18018-18044.
- (3) Graddon, D. P. An introduction to co-ordination chemistry : International series of monographs in inorganic chemistry, Pergamon Press Ltd., London, **1961**.
- (4) Bowman-James, K.; Alfred Werner Revisited: The Coordination Chemistry of Anions. *Acc. Chem. Res.*, **2005**, *38*, 671-678.
- (5) Dinolfo, P. H.; Hupp, J. T. Supramolecular Coordination Chemistry and Functional Microporous Molecular Materials. *Chem. Mater.*, **2001**, *13*, 3113-3125.
- (6) Huang, F.; Anslyn, E. V. Introduction: Supramolecular Chemistry, *Chem. Rev.*, **2015**, *115*, 6999-7000.
- (7) Winpenny, P.; Doménech-Carbó, A.; Leyva-Pérez, A.; Armentano, D.; Pardo, E.; Ferrando-Soria, J. Self-Assembly of Catalytically Active Supramolecular

- Coordination Compounds within Metal-Organic Frameworks. *J. Am. Chem. Soc.*, **2019**, *141*, 10350-10360.
- (8) Bennett, T. D.; Horike, S. Liquid, glass and amorphous solid states of coordination polymers and metal-organic frameworks. *Nat. Rev. Mater.* **2018**, *3*, 431-440.
 - (9) Eddaoudi, M.; Moler, D. B.; Li, H. L.; Chen, B. L.; Reineke, T. M.; O'Keeffe, M.; Yaghi, O. M. Modular Chemistry: Secondary Building Units as a Basis for the Design of Highly Porous and Robust Metal-Organic Carboxylate Frameworks. *Acc. Chem. Res.*, **2001**, *34*, 319-330.
 - (10) Biradha, K.; Ramanan, A.; Vittal, J. J. Coordination polymers versus metal-organic frameworks. *Cryst. Growth Des.*, **2009**, *9*, 2969-2970.
 - (11) Huang, Y.; Liu, S.; Lin, Z.; Li, W.; Li, X.; Cao, R. Facile synthesis of palladium nanoparticles encapsulated in amine-functionalized mesoporous metal-organic frameworks and catalytic for dehalogenation of aryl chlorides. *J. Catal.*, **2012**, *292*, 111-117.
 - (12) Valente, C.; Choi, E.; Belowich, M. E.; Doonan, C. J.; Li, Q.; Gasa, T. B.; Stoddart, J. F. Metal-organic frameworks with designed chiral recognition sites. *Chem. Commun.*, **2010**, *46*, 4911-4913.
 - (13) Yaghi, O.; Davis, C. E.; Li, G.; Li, H. Selective guest binding by tailored channels in a 3-D porous zinc (II)-benzenetricarboxylate network. *J. Am. Chem. Soc.*, **1997**, *119*, 2861-2868.
 - (14) Yaghi, O. M. Departments-leading the Way-A molecular world full of holes. *Chem. Innov.*, **2000**, *30*, 3-4.
 - (15) Yaghi, O. M.; O'Keeffe, M.; Ockwig, N. W.; Chae, H. K.; Eddaoudi, M.; Kim, J. Reticular synthesis and the design of new materials. *Nature*, **2003**, *423*, 705-714.
 - (16) Robin, A. Y.; Fromm, K. M. Coordination polymer networks with O- and N-donors: what they are, why and how they are made. *Coord. Chem. Rev.*, **2006**, *250*, 2127-2157.
 - (17) Janiak, C. Engineering coordination polymers towards applications. *Dalton Trans.*, **2003**, *14*, 2781-2804.
 - (18) Kitagawa, S.; Kitaura, R.; Noro, S. I. Functional porous coordination polymers. *Angew. Chem., Int. Ed.*, **2004**, *43*, 2334-2375.
 - (19) Rosi, N. L.; Eddaoudi, M.; Kim, J.; O'Keeffe, M.; Yaghi, O. M. Advances in the chemistry of metal-organic frameworks. *CrystEngComm.*, **2002**, *4*, 401-404.

- (20) Ma, D. Y.; Guo, H. F.; Qin, L.; Li, Y.; Ruan, Q. T.; Huang, Y. W.; Xu, J. Construction of a new 2D cadmium (II) coordination polymer based on N-and O-donor ligands: synthesis, luminescence and biological activities. *J. Chem. Crystallogr.*, **2014**, *44*, 63-69.
- (21) Cui, G. H.; He, C. H.; Jiao, C. H.; Geng, J. C.; Blatov, V. A. Two metal-organic frameworks with unique high-connected binodal network topologies: synthesis, structures, and catalytic properties. *CrystEngComm.*, **2012**, *14*, 4210-4216.
- (22) Hao, H. J.; Liu, F. J.; Su, H. F.; Wang, Z. H.; Wang, D. F.; Huang, R. B.; Zheng, L. S. Syntheses, structures and fluorescence of two coordination complexes of Zn (II) and 1,3-bis (2-methylimidazolyl) propane: solvent effect. *CrystEngComm.*, **2012**, *14*, 6726-6731.
- (23) Effendy; Marchetti, F.; Pettinari, C.; Pettinari, R.; Rcciutelli, M.; Skelton, B. W.; White, A. H. (Bis (1, 2, 4-triazol-1-yl) methane) silver (I) phosphino complexes: Structures and spectroscopic properties of mixed-ligand coordination polymers. *Inorg. Chem.*, **2004**, *43*, 2157-2165.
- (24) Lee, Y. R.; Kim, J.; Ahn, W. S. Synthesis of metal-organic frameworks: A mini review. *Korean J Chem Eng.*, **2013**, *30*, 1667-1680.
- (25) (a) Kitagawa, S.; Matsuda, R. Chemistry of coordination space of porous coordination polymers. *Coord. Chem. Rev.*, **2007**, *251*, 2490-2509. (b) Kitagawa, S.; Uemura, K. Dynamic porous properties of coordination polymers inspired by hydrogen bonds. *Chem Soc Rev*, **2005**, *34*, 109-119. (c) Ghosh, S. K., Zhang, J. P.; Kitagawa, S. Reversible topochemical transformation of a soft crystal of a coordination polymer. *Angew. Chem.*, **2007**, *46*, 7965-7968. (d) Matsuda, R., Kitaura, R., Kitagawa, S., Kubota, Y., Belosludov, R.V., Kobayashi, T. C., Sakamoto, H., Chiba, T., Takata, M., Kawazoe, Y.; Mita, Y. Highly controlled acetylene accommodation in a metal-organic microporous material. *Nature.*, **2005**, *436*, 238-241. (e) Ghosh, S. K., Bureekaew, S.; Kitagawa, S. A Dynamic, Isocyanurate- Functionalized Porous Coordination Polymer. *Angew. Chem. Int. Ed.*, **2008**, *47*, 3403-3406.
- (26) Khlobystov, A. N.; Blake, A. J.; Champness, N. R.; Lemenovskii, D. A.; Majouga, A. G.; Zyk, N. V.; Schröder, M. Supramolecular design of one-dimensional coordination polymers based on silver (I) complexes of aromatic nitrogen-donor ligands. *Coord. Chem. Rev.*, **2001**, *222*, 155-192.

- (27) Kitagawa, S.; Munakata, M. Molecular architecture of copper (I) coordination polymers towards crystal lattice design. *In: Trends Inorganic Chemistry*, **1993**, 3, 437-462.
- (28) Sel, K.; Demirci, S.; Meydan, E.; Yildiz, S.; Ozturk, O. F.; Al-Lohedan, H.; Sahiner, N. Benign Preparation of Metal-Organic Frameworks of Trimesic Acid and Cu, Co or Ni for Potential Sensor Applications. *J. Electron. Mater.*, **2015**, 44, 136-143.
- (29) Kitagawa, S. Metal-organic frameworks (MOFs). *Chem. Soc. Rev.*, **2014**, 43, 5415-5418.
- (30) Gagnon, K. J.; Perry, H. P.; Clearfield, A. Conventional and unconventional metal-organic frameworks based on phosphonate ligands: MOFs and UMOFs. *Chem. Rev.*, **2011**, 112, 1034-1054.
- (31) Lin, Z. J.; Lü, J.; Hong, M.; Cao, R. Metal-organic frameworks based on flexible ligands (FL-MOFs): structures and applications. *Chem. Soc. Rev.*, **2014**, 43, 5867-5895.
- (32) Baca, B. T.; del Castillo, L. F.; Vera-Cruz, P.; Toscano, R. A.; Rodríguez-Hernández, J.; Balmaseda, J. Synthesis, characterization, and crystal structure of two zinc linear dicarboxylates. *Powder Diffr.*, **2016**, 31, 229-232.
- (33) Batten, S. R.; Neville, S. M.; Turner, D. R. Coordination polymers: design, analysis and application: *Royal Society of Chemistry*, **2009**.
- (34) Wang, L.; Yan, Z. H.; Xiao, Z.; Guo, D.; Wang, W.; Yang, Y. Reactant ratiomodulated entangled Cd (II) coordination polymers based on rigid tripodal imidazole ligand and tetrabromoterephthalic acid: interpenetration, interdigitation and self-penetration. *CrystEngComm.*, **2013**, 15, 5552-5560.
- (35) Kan, W. Q.; Ma, J. F.; Liu, Y. Y.; Yang, J. A series of coordination polymers based on 5-(2-carboxybenzyloxy) isophthalic acid and bis (imidazole) ligands: syntheses, topological structures and photoluminescent properties. *CrystEngCommunity.*, **2012**, 14, 2316-2326.
- (36) Li, C.-P.; Chen, J.; Du, M. Mixed-ligand metallosupramolecular complexes with Br_n-terephthalic acid (n = 1 or 4) and a versatile bent dipyriddy tecton: Structural modulation by substituent effect of the ligand and metal ion. *Polyhedron*, **2010**, 29, 463-469.
- (37) Li, C.-P.; Chen, J.; Du, M. Structural diversification and metal-directed assembly of coordination architectures based on tetrabromoterephthalic acid and a bent dipyriddy

- tection 2, 5-bis(4-pyridyl)-1,3,4-oxadiazole. *CrystEngCommunity*, **2010**, *12*, 4392-4402.
- (38) Li, H. H.; Ma, Y. J.; Zhao, Y. Q.; Cui, G. H. Synthesis and characterization of three cobalt (II) coordination polymers with tetrabromoterephthalic acid and flexible bis (benzimidazole) ligands. *Transit. Met. Chem.*, **2015**, *40*, 21-29.
- (39) Zhang, M.; Chen, C.; Wang, Q.; Fu, W.; Huang, K.; Zhou, W. A metal-organic framework functionalized with piperazine exhibiting enhanced CH₄ storage. *J. Mater. Chem. A.*, **2017**, *5*, 349-354.
- (40) Krishnamurthy, G.; Agarwal, S. Room Temperature Synthesis and Characterization of a Zn (II) based Metal-organic Framework with Mixed Ligands, 1, 4-Benzenedicarboxylic Acid and 1-methyle Imidazole. *Proc. Mater. Sci.*, **2014**, *5*, 1258-1265.
- (41) Dey, C.; Kundu, T.; Biswal, B. P.; Mallick, A.; Banerjee, R. Crystalline metal-organic frameworks (MOFs): synthesis, structure and function. *Acta Crystallographica Section B: Structural Science, Crystal Engineering and Materials*, **2014**, *70*, 3-10.
- (42) Tranchemontagne, D. J.; Hunt, J. R.; Yaghi, O. M. Room temperature synthesis of metal-organic frameworks: MOF-5, MOF-74, MOF-177, MOF-199, and IRMOF-0. *Tetrahedron*, **2008**, *64*, 8553-8557.
- (43) Gándara, F.; Furukawa, H.; Lee, S.; Yaghi, O. M. High Methane Storage Capacity in Aluminum Metal-Organic Frameworks. *J. Am. Chem. Soc.*, **2014**, *136*, 5271-5274.
- (44) Cravillon, J.; Münzer, S.; Lohmeier, S. J.; Feldhoff, A.; Huber, K.; Wiebcke, M. Rapid room-temperature synthesis and characterization of nanocrystals of a prototypical zeolitic imidazolate framework. *Chem. Mater.*, **2009**, *21*, 1410-1412.
- (45) Jhung, S. H.; Lee, J. H.; Yoon, J. W.; Serre, C.; Férey, G.; Chang, J. S. Microwave Synthesis of Chromium Terephthalate MIL- 101 and Its Benzene Sorption Ability. *Adv. Mater.*, **2007**, *19*, 121-124.
- (46) Choi, J. S.; Son, W. J.; Kim, J.; Ahn, W. S. Metal-organic framework MOF-5 prepared by microwave heating: factors to be considered. *Microporous Mesoporous Mater.*, **2008**, *116*, 727-731.
- (47) Gedanken, A. Using sonochemistry for the fabrication of nanomaterials. *Ultrason. Sonochem.*, **2004**, *11*, 47-55.
- (48) Stock, N.; Biswas, S. Synthesis of metal-organic frameworks (MOFs): routes to various MOF topologies, morphologies, and composites. *Chem. Rev.*, **2011**, *112*, 933-969.

- (49) Son, W. J.; Kim, J.; Kim, J.; Ahn, W. S. Sonochemical synthesis of MOF-5. *Chem. Commun.*, **2008**, 47, 6336-6338.
- (50) Yang, D. A.; Cho, H. Y.; Kim, J.; Yang, S. T.; Ahn, W. S. CO₂ capture and conversion using Mg-MOF-74 prepared by a sonochemical method. *Energy Environ. Sci.*, **2012**, 5, 6465-6473.
- (51) Cho, H. Y.; Kim, J.; Kim, S. N.; Ahn, W. S. High yield 1-L scale synthesis of ZIF-8 via a sonochemical route. *Microporous Mesoporous Mater.*, **2013**, 169, 180-184.
- (52) Azad, F. N.; Ghaedi, M.; Dashtian, K.; Hajati, S.; Pezeshkpour, V. Ultrasonically assisted hydrothermal synthesis of activated carbon-HKUST-1-MOF hybrid for efficient simultaneous ultrasound-assisted removal of ternary organic dyes and antibacterial investigation: Taguchi optimization. *Ultrasonics Sonochemistry*, **2016**, 31, 383-393.
- (53) Lee, Y. R.; Cho, S. M.; Ahn, W. S.; Lee, C. H.; Lee, K. H.; Cho, W. S. Facile synthesis of an IRMOF-3 membrane on porous Al₂O₃ substrate via a sonochemical route. *Microporous Mesoporous Mater.*, **2015**, 213, 161-168.
- (54) Mueller, U.; Puetter, H.; Hesse, M.; Schubert, M.; Wessel, H.; Huff, J.; Guzmán, M. Method for the controlled storage and release of gases using an electrochemically produced crystalline, porous, organometallic skeleton material: *Google Patents*, **2009**.
- (55) Martinez Joaristi, A.; Juan-Alcañiz, J.; Serra-Crespo, P.; Kapteijn, F.; Gascon, J. Electrochemical synthesis of some archetypical Zn²⁺, Cu²⁺, and Al³⁺ metal organic frameworks. *Cryst. Growth Des.*, **2012**, 12, 3489-3498.
- (56) Pichon, A.; James, S. L. An array-based study of reactivity under solvent-free mechanochemical conditions-insights and trends. *CrystEngComm.*, **2008**, 10, 1839-1847.
- (57) Bilal, M.; Rasheed, T.; Sosa-Hernández, J. E.; Raza, A.; Nabeel, F.; Iqbal, H. M. N. "Hazardous Pollutants in the Water Environment: Occurrence, Monitoring, Fate, Removal Technologies, and Risk Assessment." *Sci. Total Environ.* **2021**, 789, 147620.
- (58) Rathi, B. S.; Kumar, P. S.; Parthasarathy, V.; Gokul, R.; Dharani, R.; Lavanya, R.; Rangasamy, G. Current Research Progress in the Biological Removal of Emerging Contaminants from the Water Environment. *Water Pract. Technol.* **2024**, 19, 3154-3181.
- (59) Li, J.-R.; Kuppler, R. J.; Zhou, H.-C. Selective Gas Adsorption and Separation in Metal-Organic Frameworks. *Chem. Soc. Rev.* **2009**, 38, 1477-1504.

- (60) Li, H.; Eddaoudi, M.; O’Keeffe, M.; Yaghi, O. M. Design and Synthesis of an Exceptionally Stable and Highly Porous Metal-Organic Framework. *Nature* **1999**, *402*, 276-279.
- (61) Li, J.-R.; Sculley, J.; Zhou, H.-C. Metal-Organic Frameworks for Separations. *Chem. Rev.* **2012**, *112*, 869-932.
- (62) Lustig, W. P.; Mukherjee, S.; Rudd, N. D.; Desai, A. V.; Li, J.; Ghosh, S. K. Metal-Organic Frameworks: Functional Luminescent and Photonic Materials for Sensing Applications. *Chem. Soc. Rev.* **2017**, *46*, 3242-3285.
- (63) Li, X.; Surendran Rajasree, S.; Yu, J.; Deria, P. Energy Transfer in Metal-Organic Frameworks for Fluorescence Sensing. *ACS Appl. Mater. Interfaces* **2021**, *13*, 4975-4990.
- (64) Dhakshinamoorthy, A.; Asiri, A. M.; Garcia, H. Metal-Organic Frameworks in Heterogeneous Catalysis: Recent Progress, New Trends, and Future Perspectives. *Chem. Rev.* **2020**, *120*, 8468-8535.
- (65) Zhao, M.; Tong, S. Recent Progress and Perspectives on Metal-Organic Framework-Based Electrode Materials for Metal-Ion Batteries and Supercapacitors. *Energy Fuels* **2024**, *38*, 13796-13818.
- (66) Zhang, S.; Wang, M.; Wang, X.; Song, J.; Yang, X. Electrocatalysis in MOF Films for Flexible Electrochemical Sensing: A Comprehensive Review. *Biosensors* **2024**, *14*, 420.
- (67) Behera, N.; Duan, J.; Jin, W.; Kitagawa, S. The Chemistry and Applications of Flexible Porous Coordination Polymers. *EnergyChem* **2021**, *3*, 100067.
- (68) Liu, J.; Chen, L.; Cui, H.; Zhang, J.; Zhang, L.; Su, C.-Y. Applications of Metal-Organic Frameworks in Heterogeneous Supramolecular Catalysis. *Chem. Soc. Rev.* **2014**, *43*, 6011-6061.
- (69) Li, J.-R.; Sculley, J.; Zhou, H.-C. Metal-Organic Frameworks for Separations. *Chem. Rev.* **2012**, *112*, 869-932.
- (70) Dincă, M.; Long, J. R. High-Enthalpy Hydrogen Adsorption in Cation-Exchanged Variants of the Microporous Metal-Organic Framework $\text{Mn}_3[(\text{Mn}_4\text{Cl})_3(\text{BTT})_8(\text{CH}_3\text{OH})_{10}]_2$. *J. Am. Chem. Soc.* **2007**, *129*, 11172-11176.
- (71) Kreno, L. E.; Leong, K.; Farha, O. K.; Allendorf, M.; Van Duyne, R. P.; Hupp, J. T. Metal-Organic Framework Materials as Chemical Sensors. *Chem. Rev.* **2012**, *112*, 1105-1125.

- (72) Zhou, H.-C.; Long, J. R.; Yaghi, O. M. Introduction to Metal-Organic Frameworks. *Chem. Rev.* **2012**, *112*, 673-674.
- (73) Kreno, L. E.; Leong, K.; Farha, O. K.; Allendorf, M.; Van Duyne, R. P.; Hupp, J. T. Metal-Organic Framework Materials as Chemical Sensors. *Chem. Rev.* **2012**, *112*, 1105-1125.
- (74) Sun, C.-Y.; Qin, C.; Wang, X.-L.; Su, Z.-M. Luminescent MOFs as Sensors for Metal Ions and Small Molecules. *Chem. Soc. Rev.* **2014**, *43*, 5444-5455.
- (75) Dhakshinamoorthy, A.; Asiri, A. M.; Garcia, H. Metal-Organic Frameworks as Multifunctional Materials for Heterogeneous Catalysis and Sensors. *Adv. Sci.* **2018**, *5*, 1700463.
- (76) Wang, Z.; Zhang, H.; Sun, Y. MOF-Based Electronic Devices: Sensing, Memory, Logic, and Neuromorphic Computing. *Chem. Soc. Rev.* **2022**, *51*, 468-492.
- (77) Zhang, X.; Zhao, Y.; Jiang, Z.; Wang, Y.; Chen, Y. Metal-Organic Frameworks for Detection of Explosives and Chemical Warfare Agents. *Coord. Chem. Rev.* **2019**, *388*, 79-106.
- (78) Alyamni, N.; Abot, J. L.; Zestos, A. G. Perspective-Advances in Voltammetric Methods for the Measurement of Biomolecules. *ECS Sensors Plus* **2024**, *3*, 027001.
- (79) Rodushkin, I.; Engström, E.; Stenberg, A.; Baxter, D. C. Determination of Low-Abundance Elements at Ultra-Trace Levels in Urine and Serum by Inductively Coupled Plasma-Sector Field Mass Spectrometry. *Anal. Bioanal. Chem.* **2004**, *380*, 247-257.
- (80) Manousi, N.; Zachariadis, G. A. Development and Validation of an ICP-AES Method for the Determination of Toxic and Nutrient Metals in Candies: Application for the Analysis of Different Samples from the Greek Market. *Appl. Sci.* **2021**, *11*, 10599.
- (81) Lagalante, A. F. Atomic Absorption Spectroscopy: A Tutorial Review. *Appl. Spectrosc. Rev.* **1999**, *34*, 173-189.
- (82) Burts, K.; Plisko, T.; Dmitrenko, M.; Zolotarev, A.; Kuzminova, A.; Bildyukevich, A.; Ermakov, S.; Penkova, A. Novel Thin Film Nanocomposite Membranes Based on Chitosan Succinate Modified with Fe-BTC for Enhanced Pervaporation Dehydration of Isopropanol. *Membranes* **2022**, *12*, 653.
- (83) Dionísio, A. G. G.; de Jesus, A. M. D.; Amais, R. S.; Donati, G. L.; Miranda, K. A.; Guerra, M. B. B.; Pereira-Filho, E. R. Old and New Flavors of Flame (Furnace) Atomic Absorption Spectrometry. *Int. J. Spectrosc.* **2011**, *2011*, 1-12.

- (84) Sun, H.; Qin, Y.; Li, B.; Wu, D. Metal-Organic Framework-Based PET Sensors for Environmental Monitoring of Toxic Gases and Heavy Metals. *Coord. Chem. Rev.* **2023**, *485*, 215108.
- (85) Nguyen, T. T.; Luo, Y.; Huang, L.; Zhao, Y. Tunable ICT Emission in Donor-Acceptor Systems for Environment-Responsive Sensors. *J. Mater. Chem. C* **2022**, *10*, 1068-1076.
- (86) Yuan, L.; Lin, W.; Zheng, K.; He, L.; Huang, W. Fluorescent Probes for Live-Cell and In Vivo Imaging of Reactive Oxygen and Nitrogen Species. *Chem. Soc. Rev.* **2017**, *46*, 4285-4302.
- (87) Guo, X.; Zheng, S.; Liu, J.; Wang, F. Supramolecular Charge-Transfer Complexes in Chemical Sensing and Light Harvesting. *Chem. Rev.* **2023**, *123*, 880-931.
- (88) Wei, Y.; Gao, J.; Han, C.; Dai, J.; Zhang, J. Intermolecular Charge-Transfer Interactions in Organic Photodetectors and Sensors. *Adv. Opt. Mater.* **2021**, *9*, 2002152.
- (89) Xu, Z.; Yoon, J.; Spring, D. R. Fluorescent Chemosensors for Zn^{2+} . *Chem. Soc. Rev.* **2010**, *39*, 1996-2006.
- (90) Nolan, E. M.; Lippard, S. J. Tools and Tactics for the Optical Detection of Mercuric Ion. *Chem. Rev.* **2008**, *108*, 3443-3480.
- (91) Wong, A.; Ghosh, C.; You, Y.; Kim, S. J.; Kim, S. H.; Kim, S. J.; Hong, J. I. A Highly Selective Fluorescent Chemosensor for Cu^{2+} Based on the CHEQ Mechanism. *Org. Lett.* **2003**, *5*, 1123-1126.
- (92) Sahoo, S. K.; Sharma, D.; Bera, R. K.; Crisponi, G.; Callan, J. F. Iron(III) Selective Molecular and Nanosensors. *Chem. Soc. Rev.* **2012**, *41*, 7195-7227.
- (93) Zheng, L.; Wu, S.; Lin, J.; Liu, Y. FRET-Based Fluorescent Probes for Bioimaging and Biosensing. *ACS Appl. Bio Mater.* **2023**, *6*, 1496-1515.
- (94) Wang, M.; Xu, Z.; Du, D.; Lin, Y. Recent Advances in FRET-Based Biosensors for Biomedical Applications. *Biosens. Bioelectron.* **2024**, *238*, 115586.
- (95) Zhang, X.; Zhang, H.; Li, H.; Chen, J. Design and Applications of FRET-Based Nanosensors in Environmental Monitoring. *ACS Sens.* **2023**, *8*, 3301-3312.
- (96) Wang, Y.; Xu, H.; Zhang, C.; Wang, L. Advanced FRET Platforms in Bioanalytical Chemistry: Trends and Perspectives. *Anal. Chem.* **2023**, *95*, 4352-4364.
- (97) Chen, Y.; Gao, Y.; Zhang, Y.; Zhang, H. A Coordination Polymer-Based FRET Sensor for the Selective Detection of Trace Metal Ions. *J. Mater. Chem. B* **2023**, *11*, 3140-3148.

- (98) Chou, P. T.; Martinez, M. L.; Clements, J. H. Excited-State Intramolecular Proton Transfer in 3-Hydroxyflavone and Its Derivatives. *J. Phys. Chem. A* **1997**, 101, 9121-9131.
- (99) Kim, H. M.; Cho, B. R. Small-Molecule Two-Photon Probes for Bioimaging Applications. *Chem. Rev.* **2015**, 115, 501-557.
- (100) Zhao, J.; Ji, S.; Chen, Y.; Guo, H.; Yang, P. Excited State Intramolecular Proton Transfer (ESIPT): From Principal Photophysics to the Development of New Chromophores and Applications in Fluorescent Molecular Probes and Luminescent Materials. *Phys. Chem. Chem. Phys.* **2012**, 14, 8803-8817.
- (101) Sengupta, P. K.; Kasha, M. Excited-State Proton Transfer in 3-Hydroxyflavone and Related Compounds. *Chem. Phys. Lett.* **1979**, 68, 382-385.
- (102) Goswami, S.; Das, S.; Das, A. K.; Zangrando, E. An ESIPT-Based Fluorescent Probe for the Selective Detection of Zn^{2+} in Aqueous Media and Its Application in Live Cell Imaging. *Inorg. Chem.* **2014**, 53, 8763-8769.
- (103) Winnik, F. M. Photophysics of Preassociated Pyrenes in Aqueous Polymer Solutions and in Other Organized Media. *Chem. Rev.* **1993**, 93, 587-614.
- (104) Valeur, B.; Berberan-Santos, M. N. *Molecular Fluorescence: Principles and Applications*; Wiley-VCH: Weinheim, 2012.
- (105) Förster, T. Delocalized Excitation and Excitation Transfer. In *Modern Quantum Chemistry*; Sinanoglu, O., Ed.; Academic Press: New York, 1965; pp 93-137.
- (106) Grabowski, Z. R.; Rotkiewicz, K.; Rettig, W. Structural Changes Accompanying Intramolecular Electron Transfer: Focus on Twisted Intramolecular Charge Transfer States. *Chem. Rev.* **2003**, 103, 3899-4032.
- (107) Smith, J. A.; Brown, R. L.; Johnson, M. T. Fluorescent Sensors for Metal Ions: Advances and Applications. *J. Mater. Chem. C* **2020**, 8, 5230-5241.
- (108) Wang, X.; Gao, Z.; Zhang, W. Mechanistic Insights into Fluorescence Quenching in Metal Ion Sensors. *Dalton Trans.* **2018**, 47, 1564-1572.
- (109) Patel, R.; Kumar, S. Biomedical Applications of Metal Ion Sensing Coordination Polymers. *ACS Appl. Bio Mater.* **2022**, 5, 765-775.
- (110) Agency for Toxic Substances and Disease Registry (ATSDR). *Toxicological Profiles*; U.S. Department of Health and Human Services, Public Health Service: Atlanta, GA, 2007-2022.
- (111) Institute of Medicine (US) Panel on Micronutrients. *Dietary Reference Intakes for Vitamin A, Vitamin K, Arsenic, Boron, Chromium, Copper, Iodine, Iron, Manganese,*

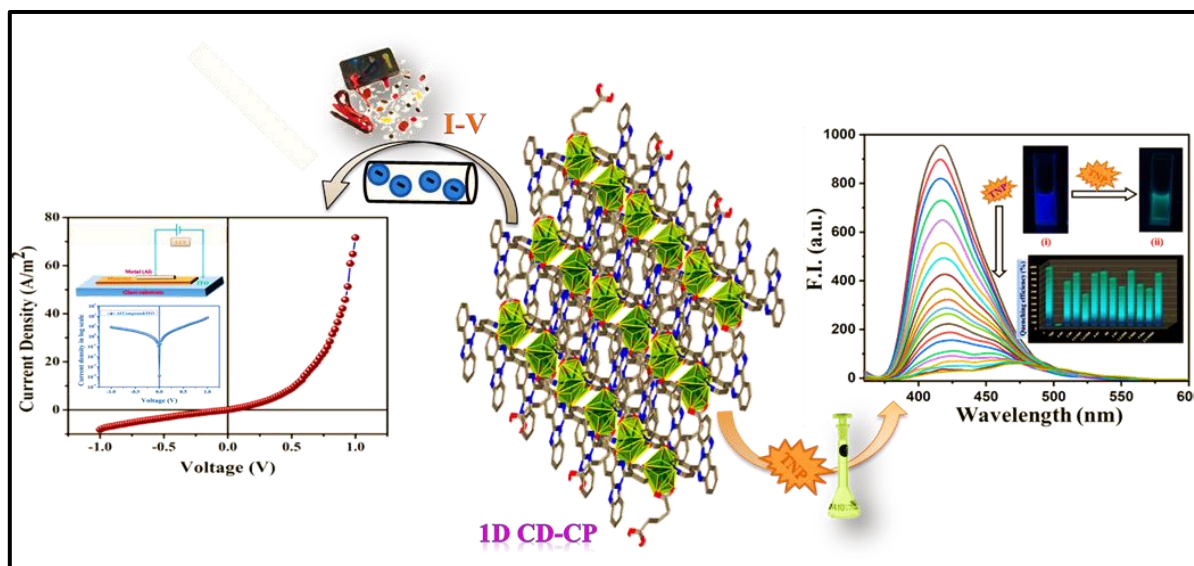
- Molybdenum, Nickel, Silicon, Vanadium, and Zinc*; National Academies Press: Washington, DC, 2001.
- (112) World Health Organization. *Guidelines for Drinking-Water Quality: Fourth Edition Incorporating the First Addendum*; World Health Organization: Geneva, 2017.
- (113) Lee, S.; Park, J. H. Coordination Polymers as Selective Fluorescent Sensors for Aluminum Ions. *Chem. Commun.* **2019**, 55, 1350-1353.
- (114) Chen, Y.; Zhao, L.; Li, H. Selective Detection of Al^{3+} in Aqueous Media Using Luminescent Coordination Polymers. *Sens. Actuators, B* **2021**, 329, 129131.
- (115) Wang, X.; Gao, Z.; Zhang, W. Mechanistic Insights into Fluorescence Quenching in Metal Ion Sensors. *Dalton Trans.* **2018**, 47, 1564-1572.
- (116) Patel, R.; Kumar, S. Biomedical Applications of Metal Ion Sensing Coordination Polymers. *ACS Appl. Bio Mater.* **2022**, 5, 765-775.
- (117) Lv, P.; Cao, Y.; Liu, Z.; Wang, R.; Ye, B.; Li, G. Dual luminescent lanthanide coordination polymers for ratiometric sensing and efficient removal of Hg^{2+} . *Anal. Methods* **2020**, 12, 91-96.
- (118) Rong, J.; Li, L.; Wang, L. and Zhang, W. Bifunctional Luminescent Rare Earth Metal-Organic Frameworks for Highly Sensing Fe^{3+} Ions and TNP. *J. Inorg. Organomet. Polym. Mater.* **2024**, 34, 2676-2687.
- (119) Agency for Toxic Substances and Disease Registry (ATSDR). *Toxicological Profile for Picric Acid (Trinitrophenol)*; U.S. Department of Health and Human Services, 2017.
- (120) Wang, J.; Zhang, L.; Chen, H. Environmental Fate and Toxicity of Nitroaromatic Explosives. *J. Environ. Manage.* **2018**, 213, 261-268.
- (121) Zhao, Y.; Sun, J.; Wang, L. Fluorescent Metal-Organic Frameworks for Sensing Nitroaromatic Explosives. *Chem. Commun.* **2014**, 50, 6279-6282.
- (122) Sun, J.; Zhao, Y.; Wang, L. Fluorescence Quenching of Coordination Polymers for Nitroaromatic Explosive Sensing. *ACS Appl. Mater. Interfaces* **2019**, 11, 20154-20162.
- (123) Liu, Y.; Sun, J.; Zhang, W.; Wang, L. Luminescent Zn(II) Coordination Polymers for Selective Detection of Picric Acid. *Inorg. Chem.* **2017**, 56, 5868-5875.
- (124) Zhou, X.; Liu, Y.; Wang, L. Selective Detection of Picric Acid via Fluorescence Quenching in Coordination Polymers. *Sensors* **2020**, 20, 1012.
- (125) U.S. Environmental Protection Agency (EPA). *Aquatic Toxicity Data for Nitroaromatic Compounds*. 2016.

- (126) National Library of Medicine (NLM). *Hazardous Substances Data Bank: Picric Acid*. 2020.
- (127) Li, X.; Zhao, W.-J.; Zhang, L.; Zhou, X. A New Luminescent Zn(II) Coordination Polymer: Selective Detection of TNP and Enhancement Activity on Sepsis by Regulating the miR-16 Expression in Immune Cells. *Monatsh. Chem.* **2020**, *151*, 1069-1076.
- (128) Zhang, L.; Liu, Y.; Wang, L. Selective and Recyclable Sensing of Aqueous Phase 2,4,6-Trinitrophenol (TNP) Based on Cd(II) Coordination Polymer with Zwitterionic Ligand. *Crystals* **2018**, *8*, 456.
- (129) Kumar, S.; Singh, R.; Gupta, R.; Sharma, S.; Yadav, S.; Kumar, R. Recent Advances in Coordination Polymer-Based Sensors for Detection of Nitroaromatic Compounds. *Coord. Chem. Rev.* **2023**, *470*, 214688.
- (130) Xu, G.; Nie, P.; Dou, H.; Ding, B.; Li, L.; Zhang, X. Exploring metal organic frameworks for energy storage in batteries and supercapacitors. *Mater. Today*. **2017**, *20*, 191-209.
- (131) Dutta, B.; Dey, A.; Sinha, C.; Ray, P. P.; Mir, M. H. Photochemical Structural Transformation of a Linear 1D Coordination Polymer Impacts the Electrical Conductivity. *Inorg. Chem.* **2018**, *57*, 8029-8032.
- (132) Naskar, K.; Maity, S.; Jana, S.; Dutta, B.; Tanaka, S.; Mallick, D.; Akitsu, T.; Sinha, C. Arylazoimidazole Coordinated and Naphthalene-Dicarboxylato Bridged Polymers of Co(II) and Photochromic Zn(II) Complexes. *Cryst. Growth. Des.* **2018**, *18*, 2986-2997.
- (133) Dutta, B.; Jana, R.; Sinha, C.; Ray, P. P.; Mir, M. H. Synthesis of a Cd(II) based 1D coordination polymer by in situ ligand generation and fabrication of a photosensitive electronic device. *Inorg. Chem. Front.* **2018**, *5*, 1998-2005.
- (134) Gomes, W. P.; Cardon, F. Electron energy levels in semiconductor electrochemistry. *Prog. Surf. Sci.* **1982**, *12*, 155-215.
- (135) Sahoo, T.; Kale, P. Work function- based metal-oxide-semiconductor hydrogen sensor and its functionality: A review. *Adv. Mater. Interfaces.* **2021**, *8*, 2100649.
- (136) Mönch, W. Metal-semiconductor contacts: electronic properties. *Surf. Sci.* **1994**, *299*, 928-944.
- (137) Halder, S.; Dey, A.; Bhattacharjee, A.; Ortega-Castro, J.; Frontera, A.; Ray, P. P.; Roy, P. A Cd (II)-based MOF as a photosensitive Schottky diode: experimental and theoretical studies. *Dalton Trans.* **2017**, *46*, 11239-11249.

- (138) Anantharaj, S.; Ede, S. R.; Karthick, K.; Sam Sankar, S.; Sangeetha, K.; Karthik, P. E.; Kundu, S. Precision and Correctness in the Evaluation of Electrocatalytic Water Splitting: Revisiting Activity Parameters with a Critical Assessment. *Energy Environ. Sci.* **2018**, *11*, 744-771.
- (139) Anantharaj, S.; Karthik, P. E.; Subramanian, B.; Kundu, S. Pt Nanoparticle Anchored Molecular Self-Assemblies of DNA: An Extremely Stable and Efficient HER Electrocatalyst with Ultralow Pt Content. *ACS Catal.* **2016**, *6*, 4660-4672.
- (140) Mohammed-Ibrahim, J.; Xiaoming, S. Recent Progress on Earth Abundant Electrocatalysts for Hydrogen Evolution Reaction (HER) in Alkaline Medium to Achieve Efficient Water Splitting-A Review. *J. Energy Chem.* **2019**, *5*, 111-160.
- (141) Wu, H.; Zuo, X.; Wang, S. P.; Yin, J. W.; Zhang, Y. N.; Chen, J. Theoretical and Experimental Design of Pt-Co(OH)₂ Electrocatalyst for Efficient HER Performance in Alkaline Solution. *Prog. Nat. Sci. Mater. Int.* **2019**, *29*, 356-361.
- (142) Saha, J.; Verma, S.; Ball, R.; Subramaniam, C.; Murugavel, R. Compositional Control as the Key for Achieving Highly Efficient OER Electrocatalysis with Cobalt Phosphates Decorated Nanocarbon Florets. *Small* **2020**, *16*, 1907512.
- (143) Ma, Y.; Miao, Y.; Mu, G.; Lin, D.; Xu, C.; Zeng, W.; Xie, F. Highly Enhanced OER Performance by Er-Doped Fe-MOF Nanoarray at Large Current Densities. *Nanomaterials* **2021**, *11*, 1847.
- (144) Zhuang, L.; Ge, L.; Yang, Y.; Li, M.; Jia, Y.; Yao, X.; Zhu, Z. Ultrathin Iron-Cobalt Oxide Nanosheets with Abundant Oxygen Vacancies for the Oxygen Evolution Reaction. *Adv. Mater.* **2017**, *29*, 1606793.
- (145) Liu, J.; Zhu, D.; Ling, T.; Vasileff, A.; Qiao, S. Z. S-NiFe₂O₄ Ultra-Small Nanoparticle Built Nanosheets for Efficient Water Splitting in Alkaline and Neutral pH. *Nano Energy* **2017**, *40*, 264-273.
- (146) Sankar, S. S.; Rathishkumar, A.; Geetha, K.; Kundu, S. Electrospinning as a Tool in Fabricating Hydrated Porous Cobalt Phosphate Fibrous Network as High Rate OER Electrocatalysts in Alkaline and Neutral Media. *Int. J. Hydrogen Energy* **2021**, *46*, 10366-10376.

Chapter 2

In Situ Oxidation of Pyridyl-Dihydrobenzoimidazoquinazoline and the Synthesis of a Highly Luminescent Cd(II) Coordination Polymer: A Promising Candidate for Mutagenic Nitroaromatic Detection and Device Fabrication



Abstract:

Pyridyl-substituted imidazoquinoline, a potent fluorescent framework, is advantageous to architect multifunctional coordination networks for sensing and fabricating emergent electrical conductors. In this work, a Cd(II)-based one-dimensional (1D) coordination polymer (1D CP), $[\text{Cd}(\text{glu})_2(\text{pbiq})_2(\text{H}_2\text{O})]_n$ (**1**), [**H₂glu** = glutaric acid and **pbiq** = 4-(6-(pyridin-4-yl)benzo[4,5]imidazo[1,2-*c*]quinazoline)], has been structurally confirmed by single-crystal X-ray crystallography. The H-bonding and $\pi\cdots\pi$ interactions built a three-dimensional (3D) supramolecular structure that strongly emits at 416 nm in acetonitrile suspension. Potentially intrusive nitroaromatics (NAs) and trinitrophenol (TNP) selectively quench the strong emission of **1**, and the highest quenching is noted in the case of TNP. A detection limit (limit of detection (LOD)) of 1.51×10^{-7} M for TNP is determined. The band gap (3.31 eV) of **1** recognizes semiconducting behavior, and an electronic device is fabricated. The correlation of current vs voltage (*I-V* plot) reveals a substantial non-ohmic electrical conductivity of **1** (Λ : 1.10×10^{-5} S m⁻¹) along with a low energy barrier (Φ_B : 0.69), and the series resistance (R_s) becomes 6.21 k Ω .

2.1 Introduction

Over the past few years, the design strategy is focused on integrating different functional properties in one system of coordination polymer (CP)/metal-organic framework (MOF) toward the design of multifunctional materials ([Chapter 1](#)) for achieving sustainable development goals (SDGs).¹⁻⁴ Multifunctional materials, a sort of smart material, can be activated by stimulating agents (light, heat, magnetic field, mechanical) to induce new challenging property(ies) that have been associated with the change in geometry of the molecular component of the material.^{5,6} The CPs/MOFs have been drawn into fascinating network topologies in a variety of potent applications due to their tunable pores, large surface area, and variable functionality.^{7,8} They can be used in sensing, electrical conductivity manipulation, gas sorption and separation, variable-temperature magnetism, catalysis, drug delivery, etc.⁹⁻²⁰ Out of many properties, the sensing of explosives and manipulation of energy-saving materials have attracted intensive attention in science and engineering fields.^{13,21,22} A great deal of interest is being paid to luminescent frameworks for the detection of ions and molecules.²³⁻²⁶ A country's defense and security is of primary importance when it comes to selective and sensitive molecular sensing. In comparison, luminescent CPs are more useful because of higher structural stability even in strenuous and toxic environment, larger surface area and porosities, and faster response rates than those of molecular sensors.²⁷⁻³¹ Based on the straightforward design approach and structural flexibility, one-dimensional (1D) luminescent CPs are extremely appealing, and such molecules can quickly recognize exogenous analytes because of the better availability of interacting sites with respect to higher-dimensional CPs.^{32,33} Such smooth interactions are extremely significant in terms of selectivity and time to recognition. Moreover, 1D luminescent CPs have the ability to self-assemble into supramolecular aggregates through secondary interactions, which led to better, faster, and smoother performance than their corresponding native form and improvement in thermal and mechanical stability. These supramolecular interactions and aggregation are crucial in the context of sensing study. In this instance, the trans-like disposition of the nitrogen donor ligand has a significant impact on the fishbone-like 1D network, which in turn regulates the photophysical property. Due to the simplicity of the 1D system, all of these structural-electronic effects have been well investigated.

Chemicals are ubiquitous, and their wide adoptions have deleterious repercussions on both the environment and public health. It is becoming more and more important to detect perilous substances like nitroaromatics (NAs) and volatile organic compounds (VOCs), to

safeguard and withstand the sustainability issues as mooted by SDGs. Especially in the case of explosives and mutagenic pollutants like nitroaromatics (NAs) such an accurate, real-time, and rapid detection is required, whether for homeland security, military applications, forensic investigations, or minefield analysis.³⁴⁻³⁸ In industrial explosives, nitroaromatics (NAs) are one of the most common ingredients, and they are found in thousands of unexploded landmines around the globe. There is no doubt that 2,4,6-trinitrophenol (TNP) is one of the most powerful nitroaromatic explosives (NAEs). In fact, it is even stronger than 2,4,6-trinitrotoluene (TNT); in addition to being used in the manufacture of rocket fuels, matches, pyrotechnics, and landmines, it is also used in the dye, pharmaceutical, and textile industries.^{39,40} It has been dumped into the environment through large-scale production and uncontrolled commercial uses and leads to serious negative effects on the balancing of soil or water bodies.⁴¹ Our food system becomes contaminated with nitrophenols when the level of nitrophenols reaches 150 g L^{-1} due to its bioaccumulation, which can have major deadly impacts on living things.^{42,43} Their rates of biomagnification are much higher than the rates of biodegradation/metabolism.⁴⁴ As with other organic pollutants, phenol and its nitro derivatives can cause hematotoxicity, neurotoxicity, as well as carcinogenesis and mutagenesis inside the human body.⁴⁵⁻⁴⁷ Several ailments, including skin rashes, respiratory problems, asphyxiation, etc., are brought by longterm exposure to such substances.⁴⁸⁻⁵⁰

Due to its simplicity, rapid response times, greater selectivity, minimal cost, rapid visual detection, and dualphase compatibility, the use of fluorescence-based sensors attracts a lot of attention in this area.^{26,51} Therefore, it faces a challenge to develop a fluorescent chemosensor capable of detecting nitroaromatic substances efficiently in a green solvent media using straightforward synthetic strategies.

Generally, the CPs do not have very striking electrical properties due to the presence of large numbers of electroinnocent structural components.⁵²⁻⁵⁴ Nonetheless, the literature reports^{55,56} that some of the Zn(II)/Cd(II) CPs have semiconducting band gap and allow smooth charge transportation. Recently, 1D CPs have been developed with spectacular electrical properties that are generating massive interest due to the simplicity of the chain-like structural arrays that seamlessly correlate functionality with applications.^{55,56} In addition, the 1D CPs produce higher-dimensional supramolecular aggregates through various secondary interactions, resulting in improvement of charge transportation due to a combined, “through-bond” and “through-space”, charge passage.^{57,58}

It has, however, been rare to construct highly luminescent one-dimensional CPs with flexible carboxylates for chemical sensing and electronic fabrication.⁵⁹⁻⁶³ Based on all of these aspects, in this work, Cd(II)-coordinated 1D CP (**1**) is synthesized from in situ oxidation of 6-(pyridin-4-yl)-5,6-dihydrobenzo[4,5]imidazo[1,2-*c*]quinazoline linked by flexible glutarate. The structure is established, and theoretical computation has supported the semiconducting band gap. Thus, a Schottky device is constructed and also electrical conductivity (Λ : $1.10 \times 10^{-5} \text{ S m}^{-1}$) is measured. The strong emission of **1** is quenched by 2,4,6-trinitrophenol (TNP), and the limit of detection (LOD) $1.51 \times 10^{-7} \text{ M}$ lies much below the World Health Organization (WHO) recommended threshold limit.

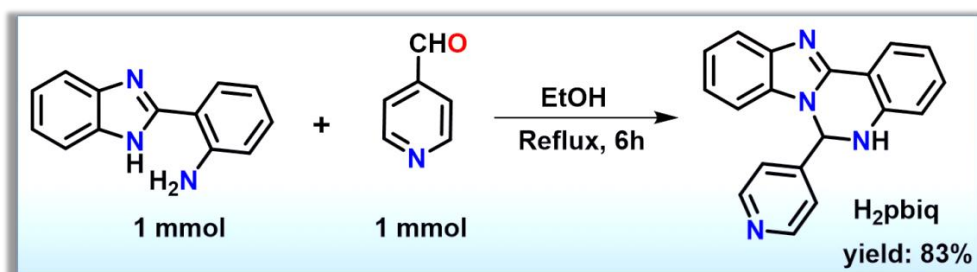
2.2 Experimental Section

2.2.1 Materials and General Methods

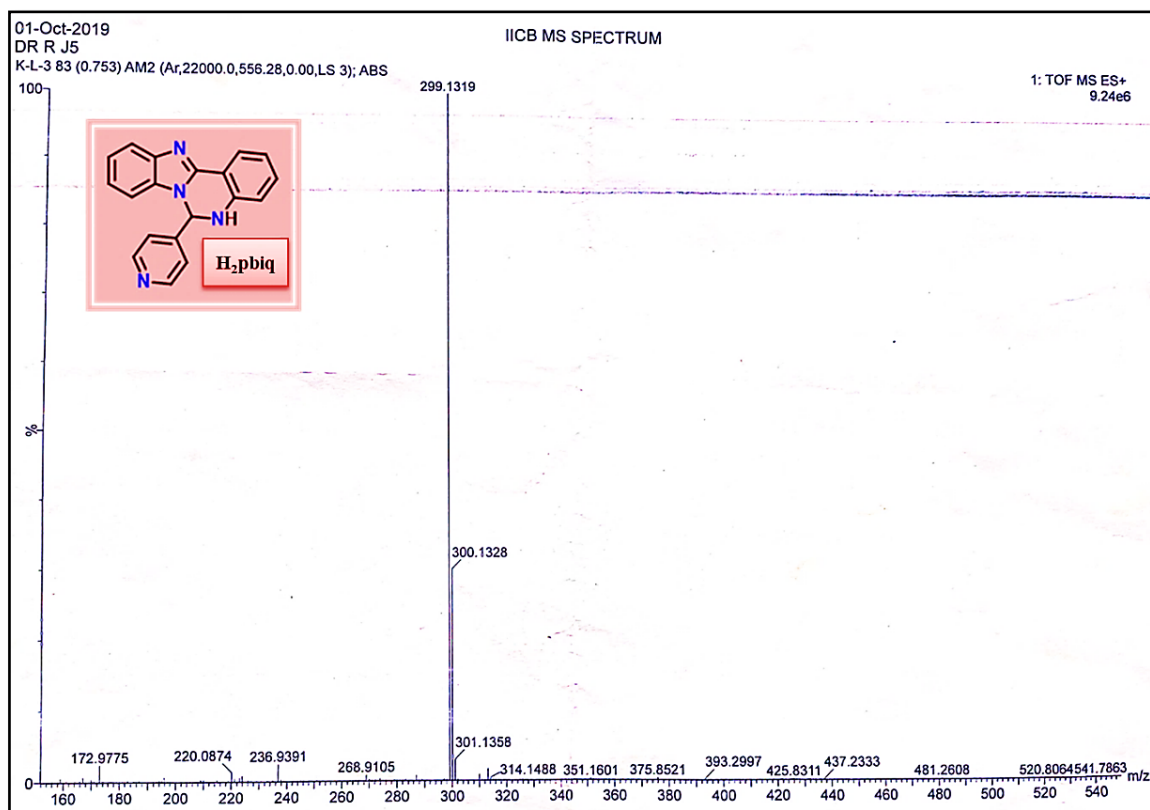
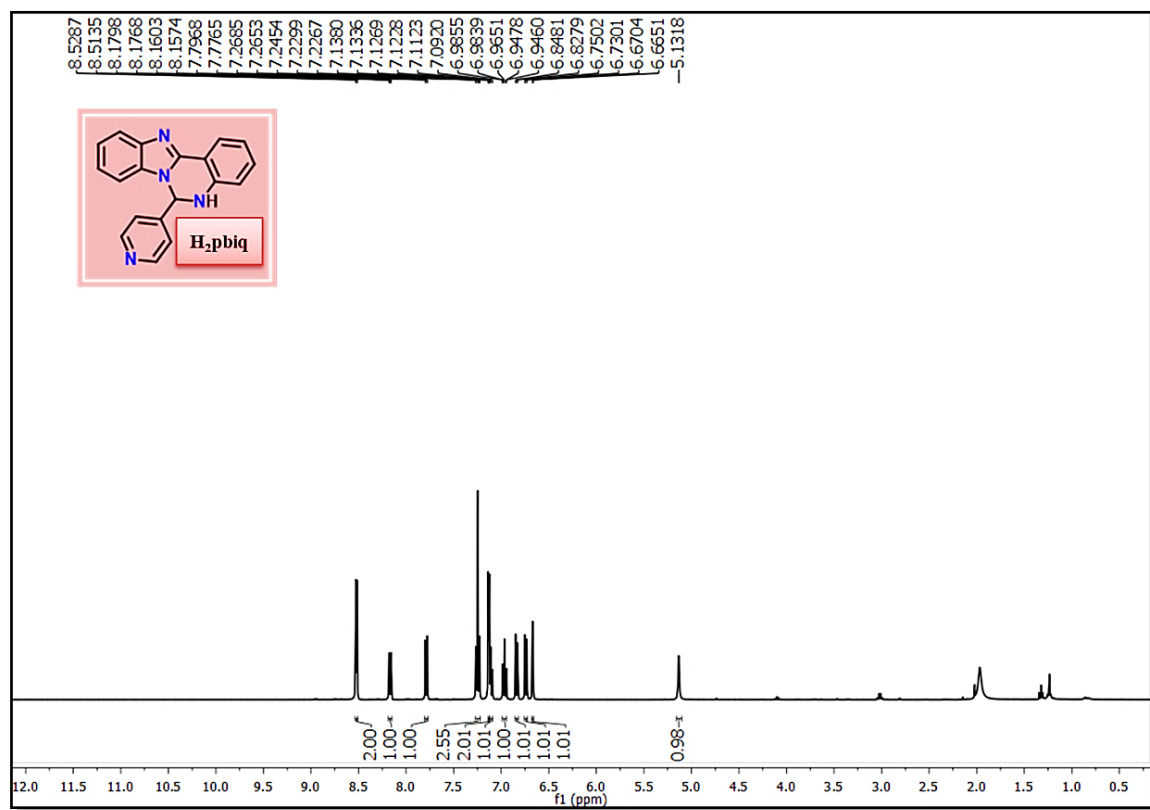
2-(1*H*-benzo[*d*]imidazol-2-yl) aniline and pyridine-4-carbaldehyde were purchased from Sigma-Aldrich. All other organic reagents, inorganic salts and solvents were of the reagent grade, obtained from Spectrochem and Merck, and used without further purification. Plates for thin-layer chromatography (TLC) were used to monitor each reaction (Merck silica gel 60, f_{254}) and column chromatography was carried out utilizing silica gel (100-200 mesh). Tetramethylsilane (TMS) served as the internal standard in ^1H -NMR spectra recorded on a 300 MHz (Bruker-DPX) in CDCl_3 and $\text{DMSO-}d_6$ solvents. ^{13}C NMR spectra were recorded on a 75 MHz (Bruker-DPX) instrument in CDCl_3 and $\text{DMSO-}d_6$ using same internal standard. HRMS (m/z) measurements were taken with an ESI method and a Q-ToF Micro mass spectrometer, respectively. PerkinElmer SPECTRUM II LITA FT-IR was used to capture an infrared spectrum in KBr ($4500\text{-}500 \text{ cm}^{-1}$). The elemental analyzer PerkinElmer 240C was used for the CHN analysis. The thermal stability of the compound as it was manufactured was tested using a PerkinElmer Pyris Diamond TG/DTA instrument at temperature between 30 and 800 °C with a heating rate of 10 °/minute. On a Bruker D8 Advance X-ray diffractometer, ambient temperature X-ray powder diffraction (XRPD) patterns were captured using Cu $K\alpha$ radiation ($\lambda = 1.548 \text{ \AA}$), generated at 40 kV and 40 mA at 2θ range of 5-50°. PerkinElmer Spectrofluorometer model LS55 and PerkinElmer Spectrophotometer Lambda 25 were used, respectively, to record the measurements of the fluorescence and UV-Vis spectra. Measurements of time-correlated single-photon counts were recorded using a HORIBA Jobin-Yvon system for counting single photons over time.

2.2.2 Synthesis of Ligand (**H₂pbiq**)

To an ethanol (5 mL) solution of 2-(1*H*-benzo[*d*]imidazol-2-yl)aniline (209 mg, 1.0 mmol) was added pyridine-4-carbaldehyde (107 mg, 1.0 mmol) and refluxed for several hours. Using a thin-layer chromatography (TLC) test at an interval of 30 min, the reaction was stopped after 6 h, then it was concentrated at a low pressure after being cooled to room temperature. Before being dried over anhydrous Na₂SO₄ and compressed at a reduced pressure, the reaction mixture was separated by column chromatography using ethyl acetate/hexane (3:7, v/v) as the eluent to isolate pure product, 6-(pyridin-4-yl)-5,6-dihydrobenzo[4,5]imidazo[1,2-*c*]quinazoline (**H₂pbiq**) (**Scheme 2.1**). High-resolution mass spectrometry (HRMS) (electrospray ionization (ESI), *m/z*) calcd for C₁₉H₁₅N₄ [M+H]⁺ : 299.1297; found: 299.1319 (**Figure 2.1**); ¹H NMR (400 MHz, CDCl₃): δ 8.52 (d, *J* = 6.08 Hz, 2H), 8.17 (dd, *J*₁ = 7.8 Hz, *J*₂ = 1.2 Hz, 1H), 7.79 (d, *J* = 8.1 Hz, 1H), 7.27-7.23 (m, 2H), 7.14-7.12 (m, 2H), 7.10 (d, *J* = 8.1 Hz, 1H), 6.99-6.95 (m, 1H), 6.83 (d, *J* = 8.1 Hz, 1H), 6.74 (d, *J* = 8.0 Hz, 1H), 6.67 (d, *J* = 2.12 Hz, 1H), 5.13 (s, 1H) (**Figure 2.2**); ¹³C NMR (100 MHz, CDCl₃): δ 150.9, 141.0, 132.7, 132.1, 125.8, 123.3, 123.2, 120.91, 120.9, 119.6, 115.6, 109.6, 68.3 (**Figure 2.3**); IR (neat): *ν*_{max} 2944, 1609, 1515, 1478, 1390, 1290, 1265, 1152, 814, 732 cm⁻¹ (**Figure 2.4**).



Scheme 2.1 Synthesis of 6-(pyridin-4-yl)-5,6-dihydrobenzo[4,5]imidazo[1,2-*c*]quinazoline (**H₂pbiq**).

Figure 2.1 Mass spectrum of H_2pbiq .Figure 2.2 1H -NMR spectroscopy of H_2pbiq .

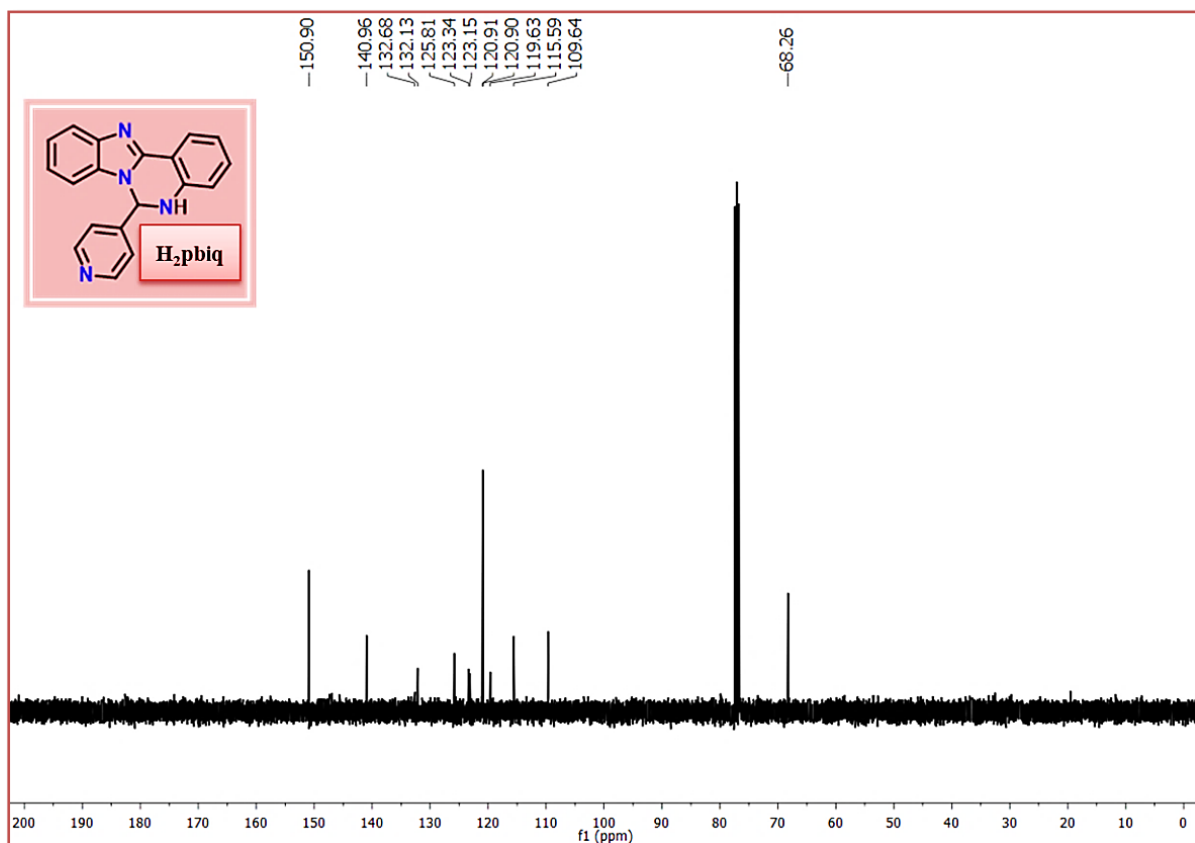


Figure 2.3 ^{13}C -NMR spectroscopy of H_2pbic .

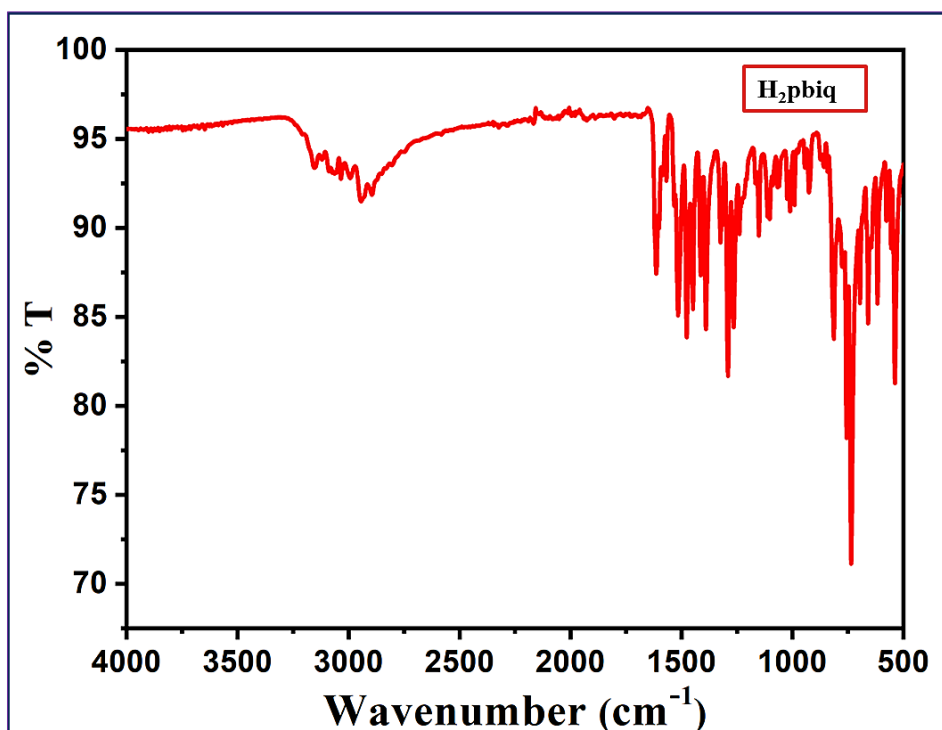
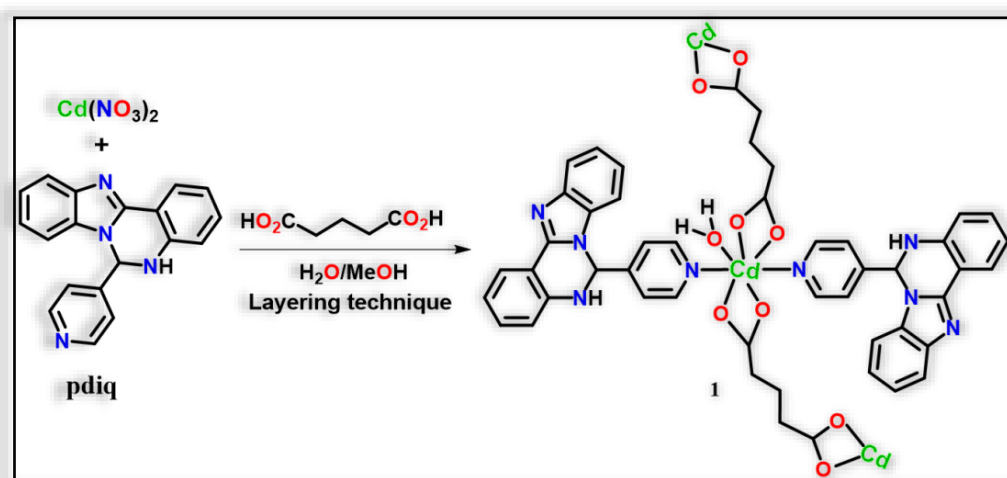


Figure 2.4 IR spectrum of H_2pbic .

2.2.3 Synthesis of $[\text{Cd}(\text{glu})_2(\text{pbiq})_2(\text{H}_2\text{O})]_n$ (1)

To an aqueous solution of $\text{Cd}(\text{NO}_3)_2 \cdot 4\text{H}_2\text{O}$ (61.7 mg, 0.2 mmol), a buffer solution of H_2O and MeOH (1:1 (v/v)) was layered followed by injecting an aqueous (2 mL) solution of **H₂pbiq** (59.6 mg, 0.2 mmol). A neutral solution of glutaric acid (26.4 mg, 0.2 mmol) in EtOH (2 mL) by Et_3N (21 mg, 0.2 mmol) was added slowly to the top layer in this solution and left to dissipate for a few days. After 10 days, block-like yellow crystals of $[\text{Cd}(\text{glu})_2(\text{pbiq})_2(\text{H}_2\text{O})]$ (1) (**Scheme 2.2**) were obtained (98 mg, yield 57.6%). For $\text{C}_{43}\text{H}_{32}\text{CdN}_8\text{O}_5$, the elements calculated (%) were C, 60.53; H, 3.78; N, 13.13; found: C, 60.61; H, 3.74; N 13.19.



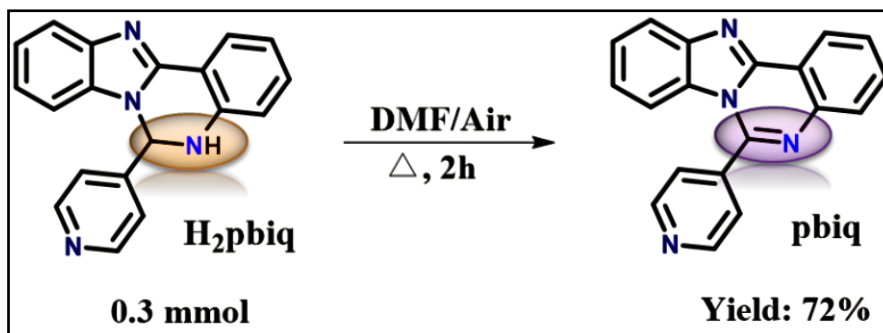
Scheme 2.2 Synthesis of $[\text{Cd}(\text{glu})_2(\text{pbiq})_2(\text{H}_2\text{O})]_n$ (1).

CAUTION! Cd(II) compounds are potentially toxic and poisonous. They are handled carefully following all precautions and have been prepared in small quantities.

2.2.4 Synthesis of 6-(pyridin-4-yl)-benzo[4,5]imidazo[1,2-c]quinazoline (pbiq)

To produce the required heterocycle pbiq, 6-(pyridin-4-yl)-5,6-dihydrobenzo[4,5]imidazo[1,2-c]quinazoline (**H₂pbiq**) (89.4 mg, 0.3 mmol) was dissolved in DMF (3 ml) while air was bubbled through the reaction mixture and then the mixture was refluxed for 2 h. Following the completion of the reaction, the mixture was poured into water (30 ml), and the light yellow compounds were precipitated, filtered off and column chromatography was used to purify the crude product with ethyl acetate/hexane (2:3, v/v) as the eluent, yielding the desired 6-(pyridin-4-yl)-benzo[4,5]imidazo[1,2-c]quinazoline (**pbiq**) (yield: 64.4 mg, 72%) (**Scheme 2.3**). HRMS (ESI, m/z) calcd. for $\text{C}_{19}\text{H}_{13}\text{N}_4$ $[\text{M}+\text{H}]^+$: 297.1140; found: 297.1141 (**Figure 2.5**); ^1H NMR (300 MHz, $\text{DMSO}-d_6$): δ 8.97 (d, $J = 5.91$ Hz, 2H), 8.66 (dd, $J_1 = 7.8$ Hz, $J_2 = 1.05$ Hz, 1H), 7.98 (t, $J = 8.1$ Hz, 2H), 7.93-7.88 (m, 3H),

7.83-7.78 (m, 1H), 7.52-7.47 (m, 1H), 7.24-7.18 (m, 1H), 6.56 (d, $J = 8.4$ Hz, 1H) (Figure 2.6); ^{13}C NMR (100 MHz, $\text{DMSO-}d_6$): δ 151.1, 147.7, 146.7, 144.4, 142.3, 142.0, 132.5, 129.2, 129.1, 128.4, 125.9, 124.3, 123.5, 123.2, 120.2, 118.8, 114.2 (Figure 2.7); IR (neat): ν_{max} 2923, 1624, 1592, 1534, 1444, 1367, 1222, 1154, 961, 825, 742 cm^{-1} (Figure 2.8).



Scheme 2.3 Synthesis of 6-(pyridin-4-yl)-benzo[4,5]imidazo[1,2-*c*]quinazoline (**pbiq**).

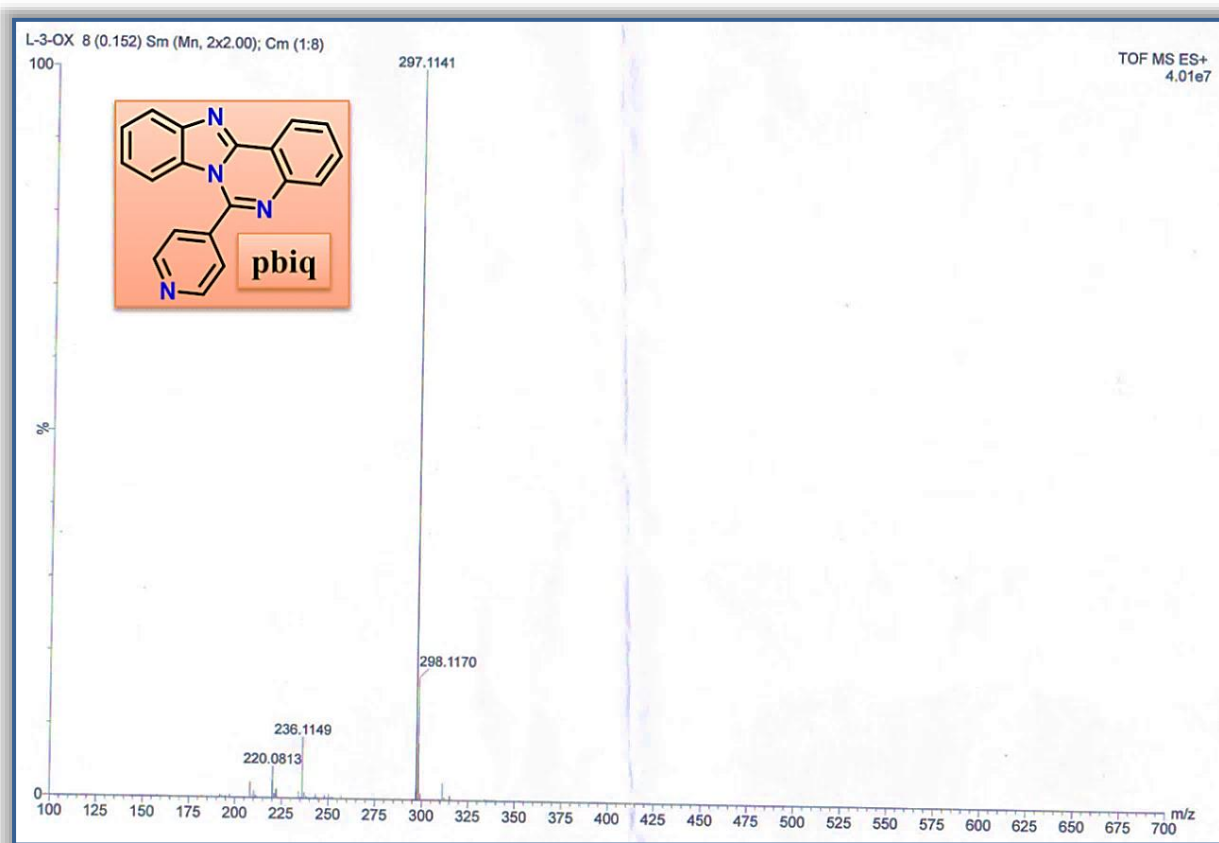


Figure 2.5 Mass spectrum of **pbiq**.

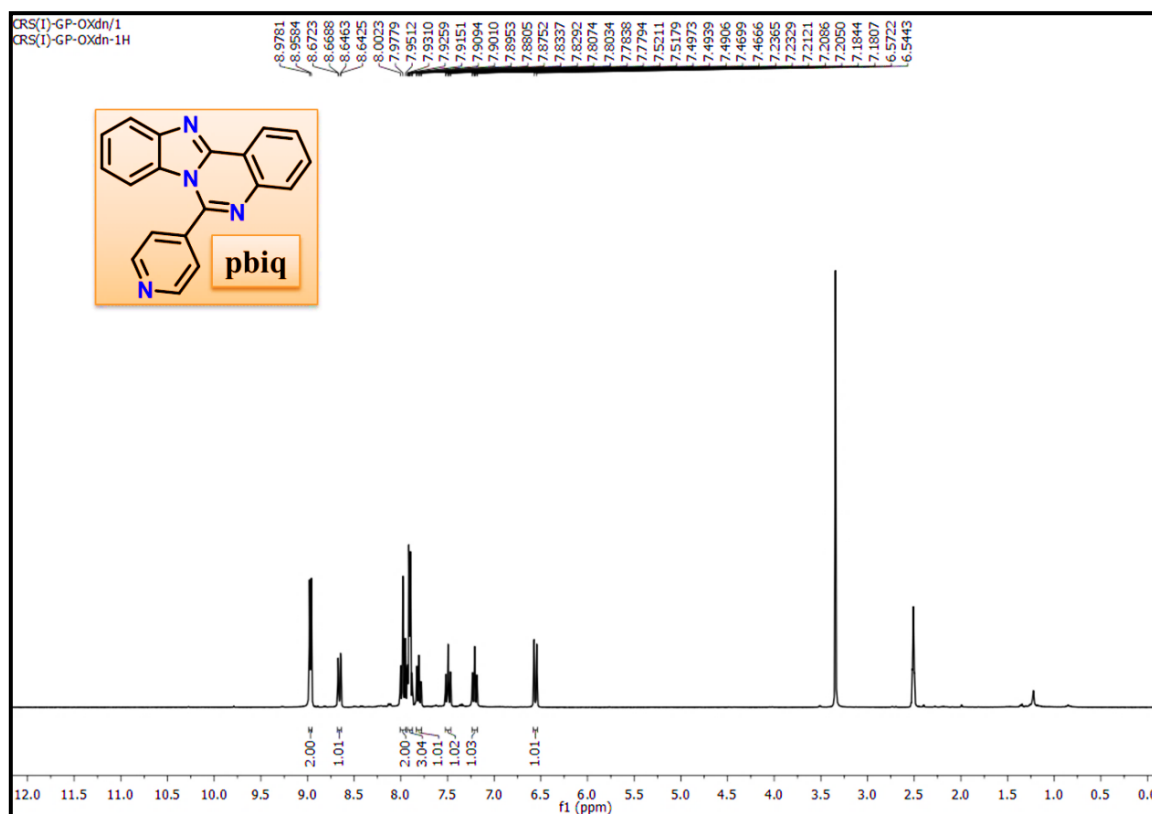


Figure 2.6 ^1H -NMR spectroscopy of pbiq.

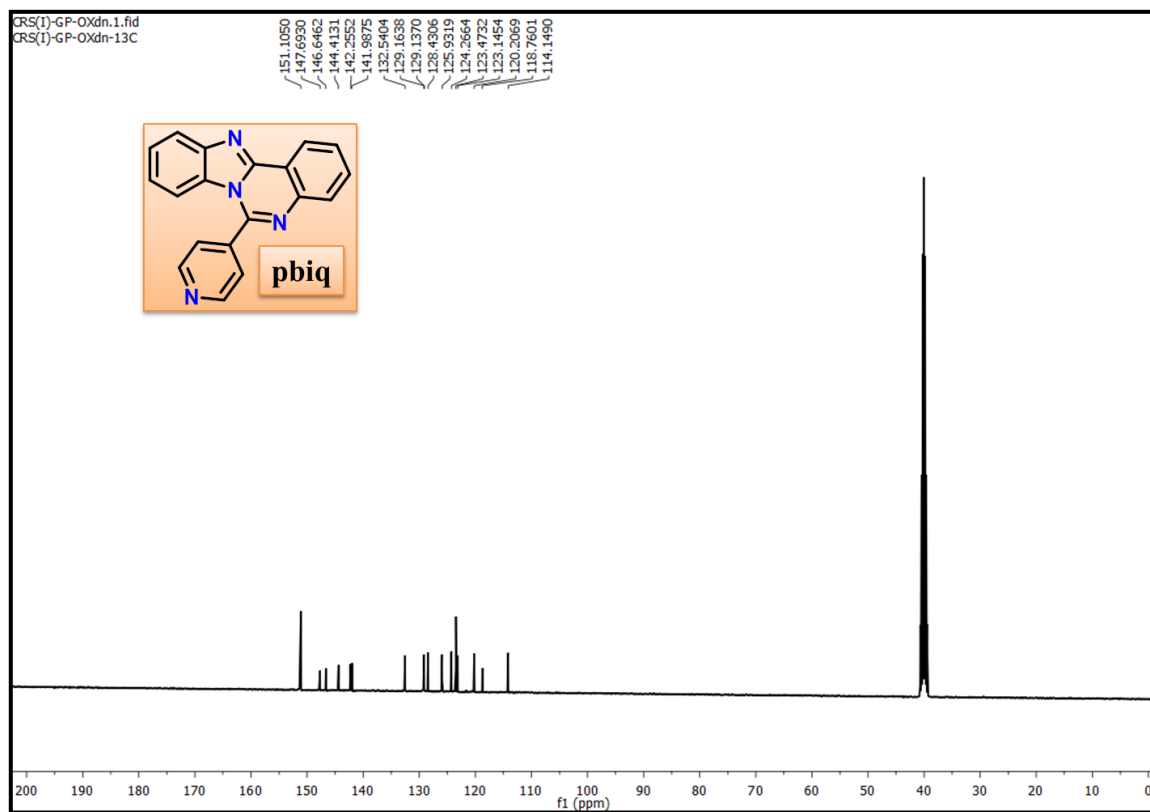


Figure 2.7 ^{13}C -NMR spectroscopy of pbiq.

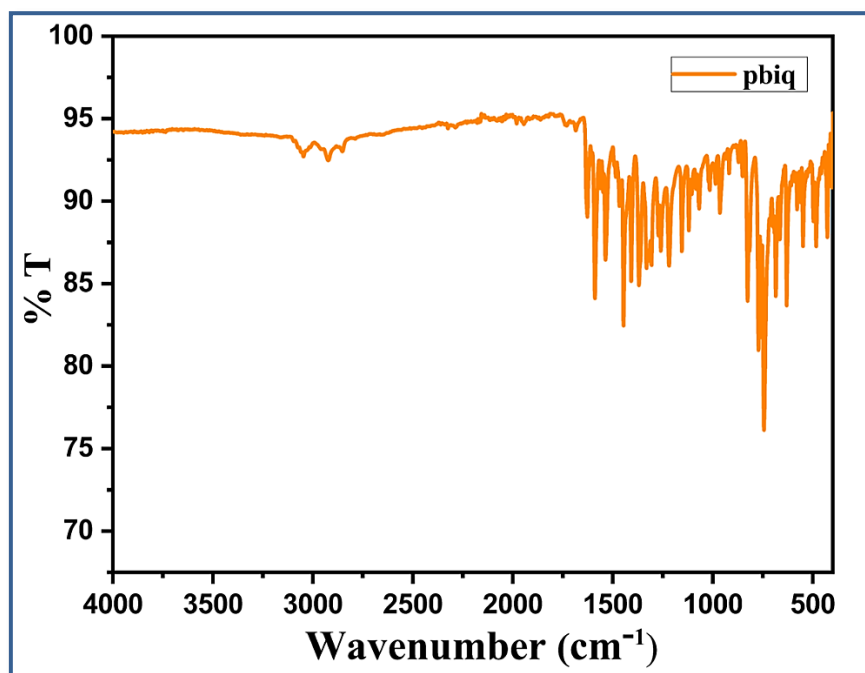


Figure 2.8 IR spectrum of pbiq.

2.2.5 Single-Crystal X-ray Diffraction (SC-XRD)

To measure single crystal X-ray data, a suitable crystal of **1** was sorted after being removed from the mother liquor. The crystal was placed under a polarized optical microscope and covered with paratone oil and mounted using MiteGen loops. SC-XRD data were collected from a Bruker APEX-II diffractometer, equipped with Mo K α radiation and a charge-coupled device (CCD) detector. All reflections were refined by least squares to determine crystal-orientation matrices and cell parameters, and the hkl values tended to be within the range of $-10 \leq h \leq 10$, $-11 \leq k \leq 11$, $-35 \leq l \leq 35$. SADABS⁶⁴ was used to perform the absorption correction, and the information compiled ($I > 2\sigma(I)$) was combined with the SAINT program.⁶⁵ The SHELXL software package, Apex III software suite, and Olex 2 were used to carry out the full-matrix least-squares improvements.⁶⁶ The molecular structure was carried out with SHELXT.⁶⁷ Refinement of the compound's non-H atoms was based on isotropic thermal parameters. Geometric alignment for each hydrogen atom was uniform, and each rode on its parent atom. Table 2.1 provides the crystallographic data of **1**. Additionally, Table 2.2 contains the bond lengths and angles used in this study. 2253510 reflects the CCDC number for **1**.

Table 2.1 Crystal data and refinement parameters for **1**.

Formula	C ₄₃ H ₃₂ CdN ₈ O ₅
CCDC	2253510
Formula weight	854.18
Crystal system	Triclinic
space group	<i>P</i> -1
<i>a</i> (Å)	8.5518 (4)
<i>b</i> (Å)	9.2086 (4)
<i>c</i> (Å)	29.4874 (13)
α (deg)	87.019 (2)
β (deg)	81.794 (1)
γ (deg)	67.557 (2)
<i>V</i> (Å ³)	2124.27 (17)
<i>Z</i>	2
<i>D</i> _{calcd} (g/cm ³)	1.334
μ (mm ⁻¹)	4.547
λ (Å)	1.54178
data[<i>I</i> > 2 σ (<i>I</i>)]/params	7697/510
GOF on <i>F</i> ²	1.049
Final <i>R</i> indices[<i>I</i> > 2 σ (<i>I</i>)] ^{a,b}	<i>R</i> 1 = 0.0695 <i>wR</i> 2 = 0.1920

$$^aR1 = \Sigma||F_o| - |F_c|| / \Sigma|F_o|, ^b wR2 = [\Sigma w(F_o^2 - F_c^2)^2 / \Sigma w(F_o^2)^2]^{1/2}$$

Table 2.2 Selected bond lengths and bond angles in **1**.

Bond length	(Å)	Bond Angles	(°)
Cd(01) - O(00C)	2.441(4)	O(00D) - Cd(01) - C(01O_b)	110.23(17)
Cd(01) - O(005)	2.351(4)	O(00D) - Cd(01) - N(4)	91.75(14)
Cd(01) - O(00D)	2.320(4)	N(4) - Cd(01) - N(5)	179.65(15)
Cd(01) - N(4)	2.352(4)	O(00C) - Cd(01) - O(00B_b)	165.37(14)
Cd(01) - N(5)	2.333(4)	O(00D) - Cd(01) - C(01F)	109.73(15)
Cd(01) - O(00B_b)	2.453(4)	N(5) - Cd(01) - O(00G_b)	94.09(13)
Cd(01) - O(00G_b)	2.338(4)	O(005) - Cd(01) - C(01F)	27.50(14)
		O(00C) - Cd(01) - O(00G_b)	139.75(16)
		O(00C) - Cd(01) - O(00D)	82.81(15)

		N(4) - Cd(01) - C(01O_b)	83.31(15)
		N(4) - Cd(01) - O(00B_b)	84.22(15)
		O(00B_b) - Cd(01) - O(00G_b)	54.18(15)
		O(005) - Cd(01) - O(00C)	54.45(13)
		O(005) - Cd(01) - O(00D)	137.22(13)
		O(005) - Cd(01) - N(4)	88.34(14)
		O(005) - Cd(01) - N(5)	91.94(14)
		O(005) - Cd(01) - O(00B_b)	139.12(14)
		O(00C) - Cd(01) - N(4)	91.75(14)
		O(00C) - Cd(01) - N(5)	88.26(14)

Symmetry Code: a = x, -1+y, z; b = x, 1+y, z

2.2.6 Theoretical calculations

With the GAUSSIAN-09 program package, the geometry of **1** was optimized by DFT (density functional theory) computation technique using Single Crystal Coordinate parameters.⁶⁸ Theoretical computations were conducted using the DFT-B3LYP hybrid functional.⁶⁹ The LanL2MB basis set was used for Cd. To depict all of the various spectral transitions involving low-lying electronic states, the time-dependent density functional theory (TDDFT) was applied.⁷⁰ Finally, in the theoretical computations, the Gauss sum⁷¹ approach was used to analyze the fractional entanglement of the distinct components of the polymeric complex associate with each molecular orbital individually.

2.2.7 Device Fabrication

The prepared material was used in thin film semiconducting devices to describe the material's electrical properties. Technology was used to create a metal-semiconductor (MS) junction using the synthesized material as the semiconductor component of the device and aluminium (Al) as the metal (**Figure 2.9**). An indium tin oxide (ITO) coated glass substrate was thoroughly cleaned with acetone, ethanol, and distilled water being subjected to an ultrasonicator. The substrate was subsequently dried in a N₂ atmosphere. To create a well-distributed, homogenous medium, the synthesized material was dissolved in N,N-dimethylformamide (DMF) solvent and then ultrasonically processed. The prepared material film was then created by spin-coating the dispersion onto the ITO-coated glass substrate that had already been cleaned. The thickness of film (*d*) was measured to one micrometre using a surface profiler. Finally, aluminium metal was deposited onto the film using vacuum coating equipment with electron beam technique (HINDHIVAC) at a base pressure of 10⁻⁶ Torr.

Using a shadow mask the effective diode area (A) was maintained at $7.065 \times 10^{-6} \text{ m}^2$. A thorough examination of the device attributes was done in order to look into the electrical characteristics of the synthesized material.

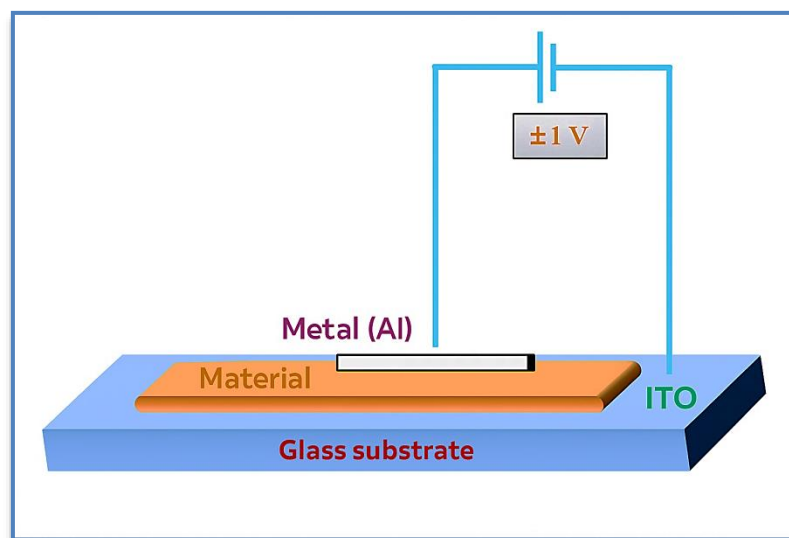


Figure 2.9 Schematic representation of device fabrication.

A Keithley 2635B source metre was used to record the device's current density-voltage (J - V) data for electrical characterization (using two probe method). Every step of the preparations and characterizations was done at room temperature (303K).

2.3 Results and Discussion

2.3.1 Structure of $[\text{Cd}(\text{glu})_2(\text{pbiq})_2(\text{H}_2\text{O})]_n$ (**1**)

Diffusion of Cd^{2+} in aqueous methanol to the solution of 6-(pyridin-4-yl)-5,6-dihydrobenzo[4,5]imidazo[1,2-*c*]quinazoline (**H₂pbiq**) for several days in the presence of a neutral solution of glutaric acid (**H₂glu**) has crystalized Cd-CP (**1**). The single-crystal X-ray structure determination of **1** has revealed that in situ aerial oxidation of **H₂pbiq** to its oxidized form 6-(pyridin-4-yl)benzo[4,5]imidazo[1,2-*c*]quinazoline (**pbiq**) ([Scheme 2.3](#)) has taken place, which subsequently coordinates monodentately to the metal ion (Cd^{2+}) followed by bridging with flexible glutarate (**glu²⁻**) to produce a 1D fishbone-like polymeric architecture. It has been observed that **1** is crystallized in triclinic system, space group $P\bar{1}$, $Z = 2$ and D_{calcd} (g cm^{-3}) = 1.335.

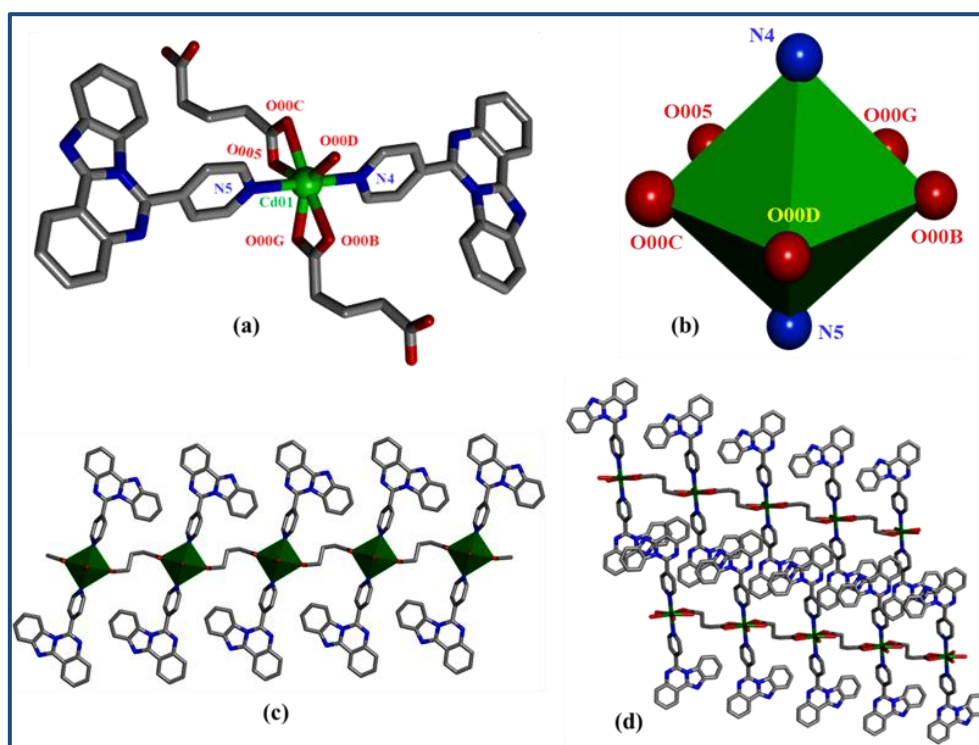


Figure 2.10 (a) Various coordinated arrangements in **1**: a perspective. (b) Coordination polyhedral around the constituting central metal ion. (c) 1D polymeric network fragment in **1**. (d) View of the parallel 1D chains.

It has been observed that **1** is crystallized in triclinic system, space group $P-1$, $Z = 2$ and D_{calcd} (g cm^{-3}) = 1.335. The construction of the asymmetric unit and metal center environment is defined as distorted pentagonal bi-pyramidal CdO_5N_2 (Figure 2.10a,b) coordination sphere. The metal ion, Cd(II), is linked via the bridging glu^{2-} to propagate the 1D chain (Figure 2.10c); the nitrogen donor pbiq has been disposed in the rod-fashion (trans) and acted as monodentate ligand. Other heterocyclic N-donor centers are free from coordination. To fulfill the seventh coordination, one H_2O is coordinated to Cd(II). The Cd-O (Cd01-O005 = 2.351(4), Cd01-O00C = 2.441(4), Cd01-O00D = 2.320(4), Cd01-O00B_b = 2.453(4), Cd01-O00G_b = 2.338(4) Å) and Cd-N bond lengths (Cd01-N4 = 2.352(4), Cd01-N5 = 2.333(4) Å) and bond angles (O005-Cd01-O00C = 54.45(13), O005-Cd01-O00D = 137.22(13), O005-Cd01-N4 = 88.34(14), O005-Cd01-N5 = 91.94(14), N4-Cd01-N5 = 179.65(15), O00C-Cd01-O00D = 82.81(15), N4-Cd01-O00B_b = 84.22(15), O00B_b-Cd01-O00G_b = 84.22(15)).

The 1D chains are assembled through extensive $\pi \cdots \pi$ interaction (3.694 Å) of the imidazolyl motif (N1-C00K-N2-C00L-COOI) (Figure 2.10d) and phenyl ring (C1-C2-C3-C4-C5-C6) to generate higher-dimensional supramolecular aggregate (Figure 2.11a). It is

also important to note that there are significant H-bonding interactions between the pyridyl-H and benzimidazolyl-N, $\text{H00S}\cdots\text{N1}$, 2.519 Å (Figure 2.11b). Hence, this structural assembly may have an influence on charge mobilization and may adjust the electrical properties if a device is fabricated with the polymeric compound.

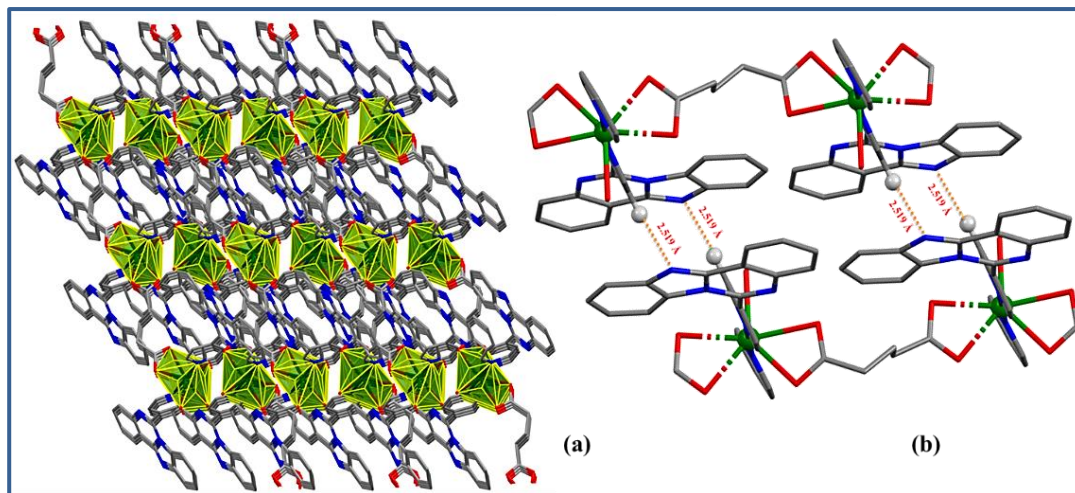


Figure 2.11 (a) Extended supramolecular aggregation of **1**. (b) H-bonding interaction within the network.

2.3.2 Powder X-ray Diffraction (PXRD) and Thermogravimetric Analysis (TGA) Experiment

Powder X-ray diffraction (PXRD) spectrum at room temperature reports the material's overall phase purity. The PXRD pattern of as-synthesized **1** was in perfect agreement with the model created using data from a single crystal, demonstrating decent phase clarity and bulk material uniformity (Figure 2.12).

Thermogravimetric analysis (TGA, 30-800 °C in a N_2 environment) determines the thermostability of **1** up to 269 °C (Figure 2.13). However, there is a mass loss observed at 30-100 °C, which does not relate to the structural architecture as there is no such indication of degradation from molecular counterparts and may infer the loss of surface adsorption of gas molecules. Thus, this small mass (near about 3% at 50 °C) loss is not related to network deviation; PXRD of the heated sample at 50 °C revealed no change in the PXRD pattern (Figure 2.12). Therefore, compound **1** with wide temperature ranges can be advantageous in material applications.

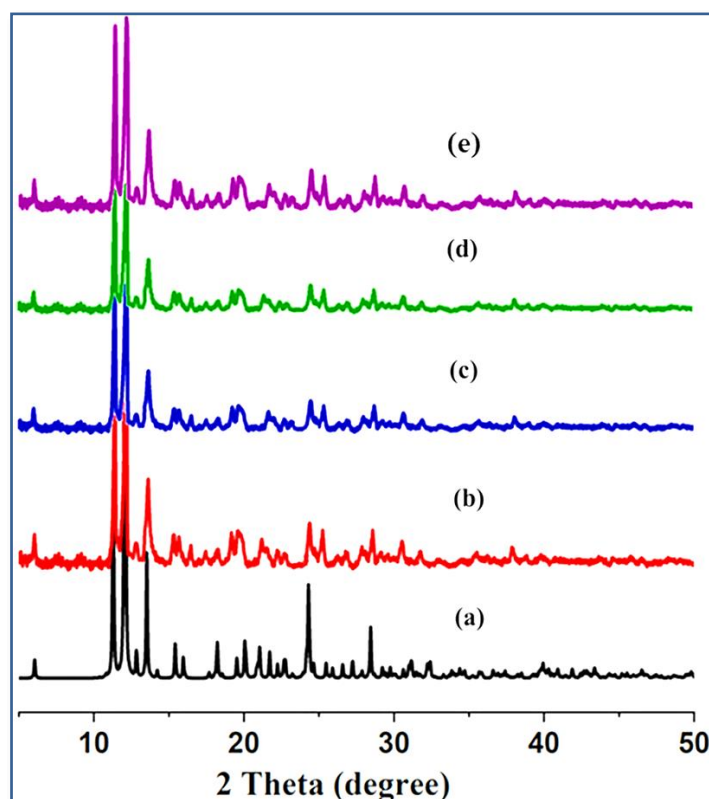


Figure 2.12 PXRD patterns of (a) simulated from the X-ray single crystal structure of **1** (black), (b) as-synthesized compound **1** (red), (c) **1** after prolonged immersion in pH solution (Ph = 4) (royal), (d) **1** after immersion in TNP solution (olive), (e) **1** after heating at 50 °C (purple).

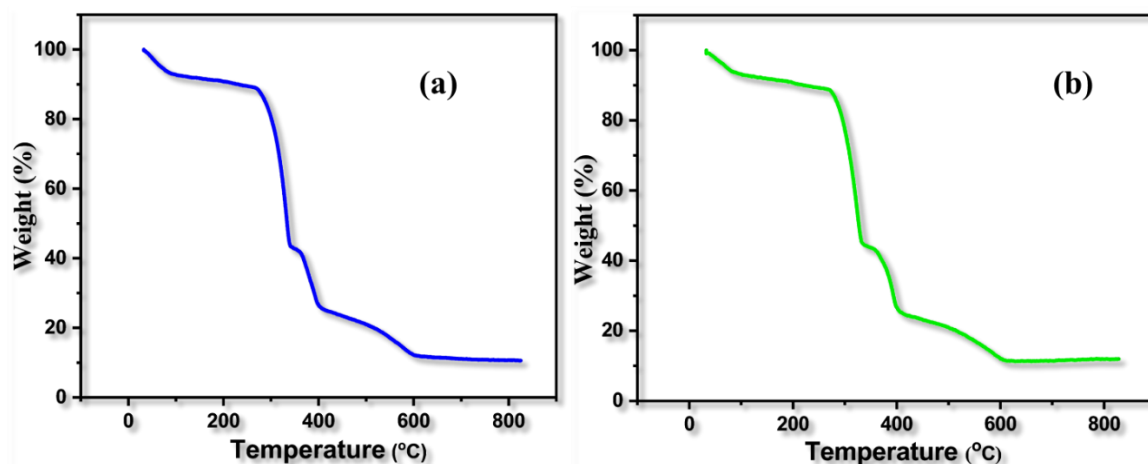


Figure 2.13 TGA analysis of Cd-CP (**1**) (a) before and, (b) after TNP analysis.

2.3.3 Sensing Property toward NAEs

Quinazoline derivatives are fluorescent and have been used for the detection of metal ions.⁷² However, the use of these derivatives for the sensing of nitroaromatic explosives (NAEs) is not so prominent. Acetonitrile suspension of **1** shows the absorption bands at 347

and 287 nm, which correspond to $n-\pi^*$ and $\pi-\pi^*$ transitions, respectively (Figure 2.14), and has been compared with free ligand **pbiq**. In the dispersion phase (acetonitrile) at room temperature (298 K), **1** exhibits blue emission at 417 nm. In contrast, under identical circumstances, the free glutaric acid is nonemissive and **pbiq** is weakly emissive. On coordinating with Cd(II) the substantial fluorescence enhancement may be attributed to the augmentation of rigidity and weakening of vibrational and rotational relaxation of pyridyl-benzoimidazoquinazoline unit.⁷³⁻⁷⁶

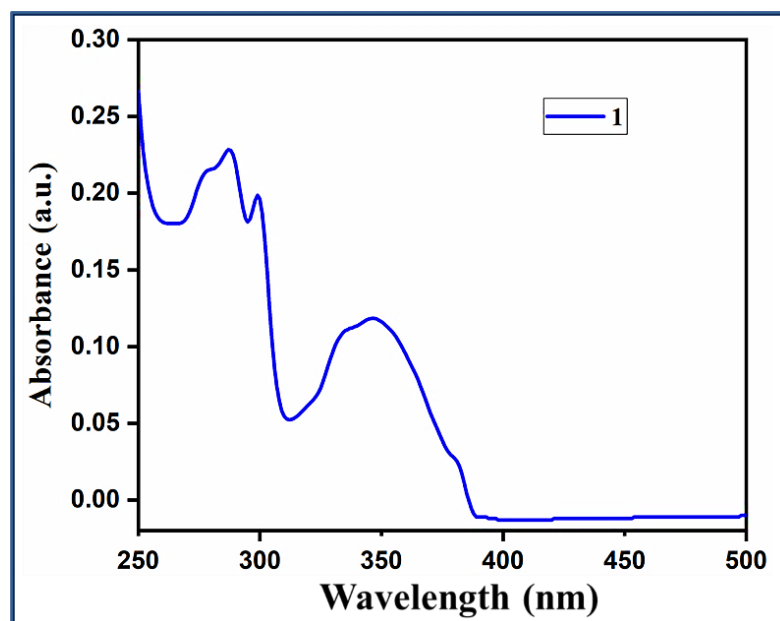


Figure 2.14 UV-Visible spectrum of **1** in acetonitrile.

Different NAEs such as 2,4,6-trinitrophenol (TNP), 4-nitrotoluene (4-NT), 2-nitrophenol (2-NP), 3-nitrobenzoic acid (3-NBA), 1,4-dinitrobenzene (1,4-DNB), 4-nitrophenol (4-NP), nitrobenzene (NB), 4-nitroacetanilide acid (5-NAc), 1,3-dinitrobenzene (1,3-DNB), 3,5-dinitrobenzoic acid (3,5-DNBA), 2,4-dinitrophenol (2,4-DNP), and 2-nitrotoluene (2-NT) have been used to check their influence on the strong emission of acetonitrile-dispersed compound **1**. Upon addition of an equivalent volume of nitroaromatic analytes (38.1 μM) to the solution of **1** (10 μM), fluorescence quenching was perceived at different levels, and the efficiency of the quenching follows the order: TNP > 2,4-DNP > 4-NAc > 2-NT > 3-NBA > 4-NP > NB > 1,4-DNB > 3,5-DNBA > 2-NP > 4-NT > 1,3-DNB. So, TNP shows the highest quenching ability (97.6%) and the highest selectivity to the emission of **1** in the family of NAEs (Figure 2.15a). TNP in suspended acetonitrile solution of **1** exhibits dramatic suppression of emission with a red shift of 60 nm (λ_{em} , 477 nm), in contrast to other NAEs (Figure 2.15b). On considering the contribution of fluorescence

resonance energy transfer (FRET) (Figure 2.16) and photoinduced electron transfer (PET) between the analyte (TNP) and **1**, the mechanism of quenching may be explained.⁷⁷

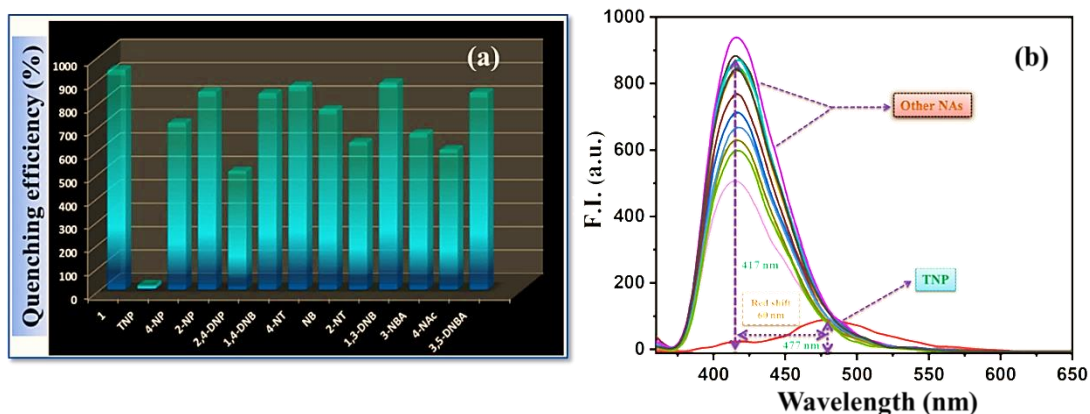


Figure 2.15 (a) NAEs' effectiveness in quenching emission of **1**. (b) Emission spectra of **1** dispersed in ACN medium in presence of different NAs (2,4,6-trinitrophenol (TNP), 4-nitrotoluene (4-NT), 2-nitrophenol (2-NP), 3-nitrobenzoic acid (3-NBA), 1,4-dinitrobenzene (1,4-DNB), 4-nitrophenol (4-NP), nitrobenzene (NB), 4-nitroacetanilide acid (5-NAC), 1,3-dinitrobenzene (1,3-DNB), 3,5-dinitrobenzoic acid (3,5-DNBA), 2,4-dinitrophenol (2,4-DNP) and 2-nitrotoluene (2-NT)).

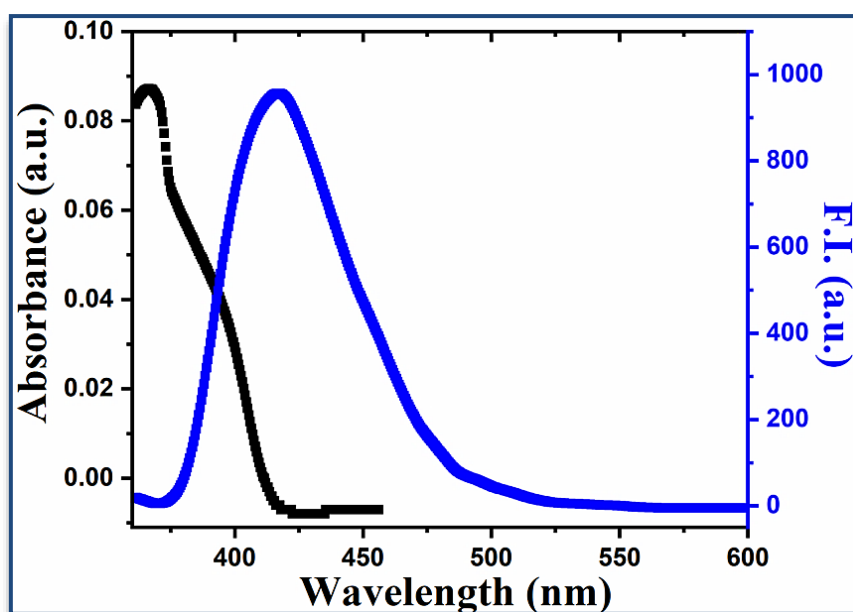


Figure 2.16 Overlapping of absorption spectra of TNP with emission spectra of **1**. The black and blue curve represent the absorption spectra of trinitrophenol (TNP) and the emission spectra of Cd(II)-CP (**1**) in acetonitrile, respectively.

To test the sensing ability of **1**, a TNP solution was progressively added to the acetonitrile suspension of **1** (Figure 2.17a). The intensity of emission gradually decreases up to 38.1 μM , and 97.6% of the initial emission has been quenched. Stern-Volmer plot (S -V plot) ($I_0/I = 1 + K_{\text{SV}} \times [\text{TNP}]$, where I_0 and I are the fluorescence intensities of **1** in the

absence and presence of TNP, respectively, and the molar concentration of TNP is given by [TNP]) determines the Stern-Volmer quenching constant, K_{sv} , $1.06 \times 10^5 \text{ M}^{-1}$.

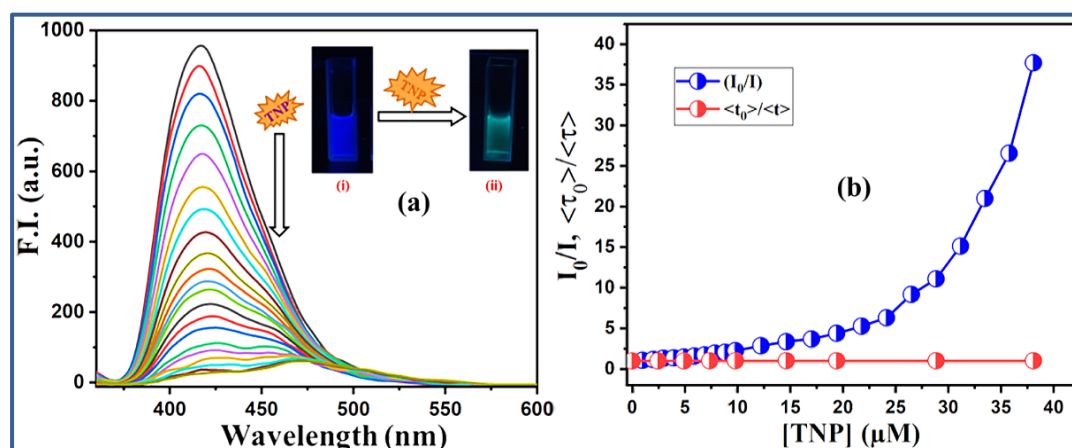


Figure 2.17 (a) Emission spectral feature of **1** (10 μM) disseminated upon addition of TNP solution incrementally in acetonitrile (0-38.1 μM); inset: Fluorescence cuvette images containing suspended acetonitrile solution of **1** under UV light ($\lambda = 365 \text{ nm}$) before TNP addition (i), and after TNP addition (ii). (b) Steady-state (I_0/I , blue) and time-resolved ($\langle \tau_0 \rangle / \langle \tau \rangle$, red) Stern-Volmer plots.

The plot shows upward curvature⁷⁸ (Figure 2.17b), which indicates that TNP acts as both a static and dynamic quencher, and increasing the TNP concentration results in a higher degree of quenching. Based on the linear region of the S-V plot having a smaller concentration of TNP, the K_{sv} value was determined (Figure 2.18a). The limit of detection (LOD), $1.51 \times 10^{-7} \text{ M}$ (Figure 2.18b), is much lower than the United States Environmental Protection Agency (USEPA) recommended value⁷⁹ of 0.1 mg m^{-3} and is comparable with CPs/MOF-based sensing materials to date.^{38,60-63,80}

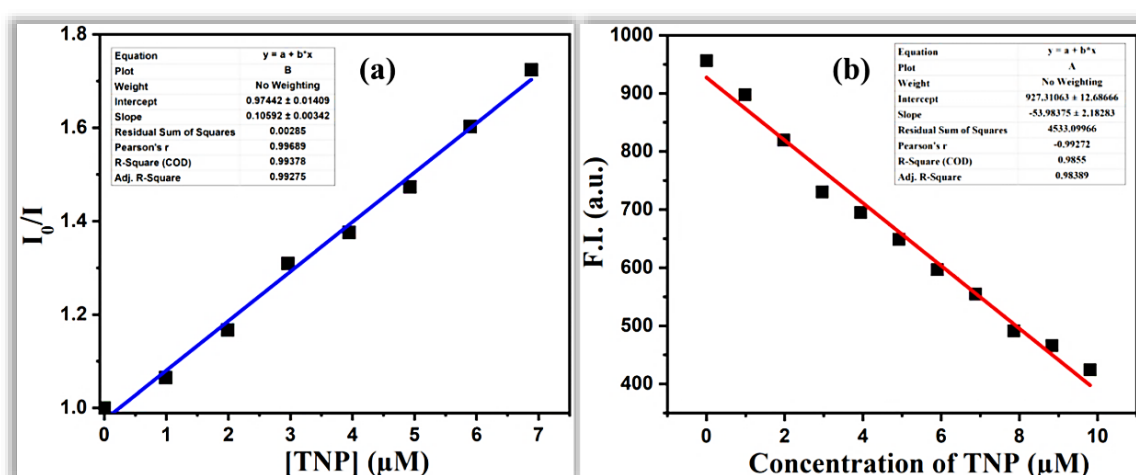


Figure 2.18 (a) Stern-Volmer plot of **1** at lower range of quencher [TNP] (in μM) concentration. (b) The linear dynamic response of **1** for TNP and the determination of the limit of detection (LOD) of TNP.

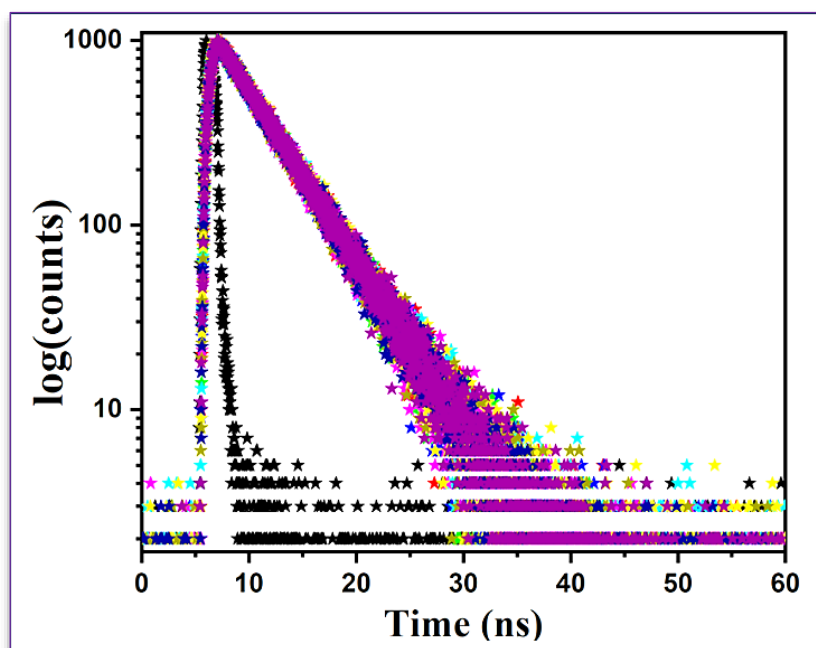
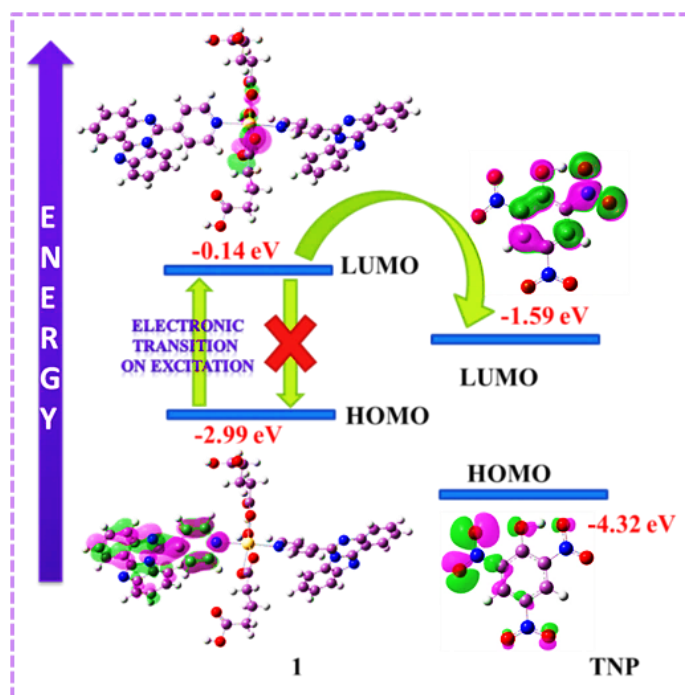


Figure 2.19 Representative fluorescence decay spectra of **1** ($10\ \mu\text{M}$) in the absence and presence of increasing concentration of TNP. Spectra 1-9 corresponds to the TNP concentration $0\ \mu\text{M}$ (red star), $2.47\ \mu\text{M}$ (green star), $4.93\ \mu\text{M}$ (blue star), $7.37\ \mu\text{M}$ (cyan star), $9.80\ \mu\text{M}$ (magenta star), $14.63\ \mu\text{M}$ (yellow star), $19.42\ \mu\text{M}$ (dark yellow star), $28.85\ \mu\text{M}$ (navy star), $38.10\ \mu\text{M}$ (purple star), respectively.

The degradation of the fluorescence lifetime of **1** was studied with continuous addition of TNP, in order to establish a quenching mechanism within this system (**Figure 2.19**). The excited species (**1**^{*}) remains undisturbed with the addition of TNP incrementally, as demonstrated by the fluorescence lifetime decay of **1** and lifetime plot (**Figure 2.17b** and **Table 2.3**). It is observed that the lifetime (τ) of **1** is $4.669\ \text{ns}$, and upon addition of TNP ($2.47\ \mu\text{M}$), the τ remains at $4.662\ \text{ns}$, and even at higher concentration ($38.10\ \mu\text{M}$; $\tau = 4.615\ \text{ns}$), it does not show any significant change in the excited-state stability of the compound. In order to estimate the molecular functions of **1** and TNP, optimal geometries were used. Calculations were made to figure out the associated orbital energies of the lowest unoccupied molecular orbital (LUMO) ($-0.14\ \text{eV}$ for **1**; $-1.59\ \text{eV}$ for TNP) and highest occupied molecular orbital (HOMO) ($-2.99\ \text{eV}$ for **1**; $-4.32\ \text{eV}$ for TNP). It is however noteworthy that the HOMO and LUMO of **1** and LUMO of TNP differ in energy. Consequently, it is possible to transfer energy from the excited state of **1** (**1**^{*}) to the ground state of TNP (**Figure 2.20**).

Table 2.3 Fluorescence lifetime decay parameters of **1** (10 μ M) with incremental addition of TNP.

TNP (μ M)	τ (ns)	CHISQ
0	4.669	1.048066
2.47	4.662	1.069910
4.93	4.656	1.020654
7.37	4.652	0.973620
9.80	4.629	1.039440
14.63	4.636	0.999736
19.42	4.628	1.041390
28.85	4.625	1.023367
38.10	4.615	1.093165

**Figure 2.20** Possible energy transfer between excited state of **1** (**1***) and TNP.

It does not appear that the emissions intensity of **1** has changed; despite the presence of acidic solutions (pH = 2-7) (**Figure 2.21**), suggesting acid-resistant structural integrity. The acid-immersed PXRD pattern of **1** (**Figure 2.12**) reaffirmed the previous finding as well.

According to the experimental observations, it can be stated that acidic conditions are compatible with a stable molecular network. Following TNP sensing, the stability of Cd-CP (**1**) is further examined by TGA and then by PXRD analysis. It is shown that the thermal stability and diffraction pattern remain unaffected, demonstrating the structural endurance of Cd-CP (Figures 2.12 and 2.13).

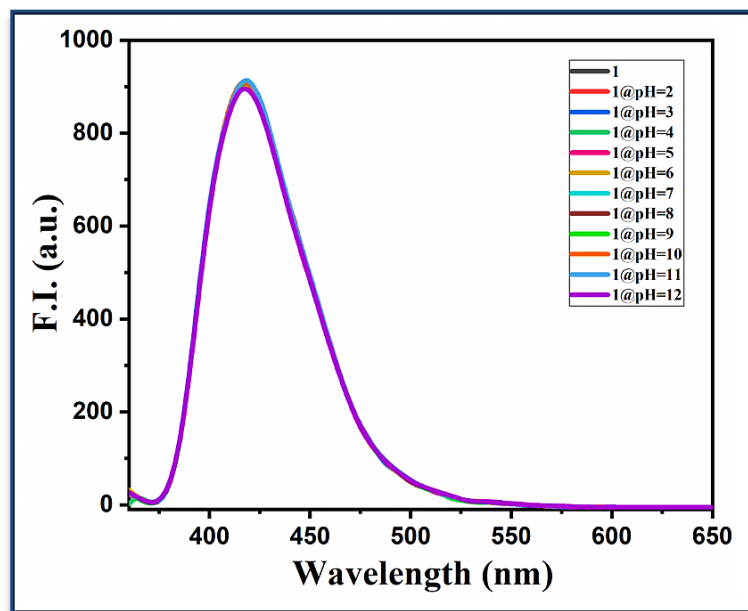


Figure 2.21 Emission spectra of **1** in presence of different PH solutions.

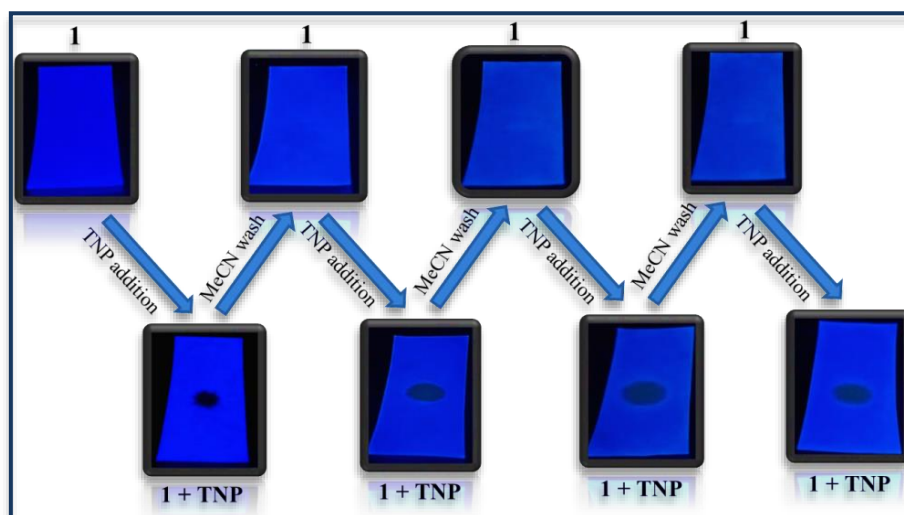


Figure 2.22 Paper strip experiment for recyclability of Cd-CP (**1**) towards TNP sensing.

As part of a lab-to-land application, a straightforward “use-and-throw” technique is constructed in order to explain the experimental finding. A dry paper strip coated with Cd-CP was exposed to a drop of trinitrophenol (TNP) solution, and the resulting photograph was captured with a UV light of wavelength 365 nm. To make the strip reusable, it was dried

under air after being cleaned with acetonitrile (Figure 2.22). According to the study, recyclability up to a wide range of implementations is fairly satisfactory.

2.3.4 Electrical Characterization

The absorption spectrum (250-500 nm) in acetonitrile suspension has been used following Tauc's equation (eq 1) to reckon the direct optical band gap, 3.31 eV (Figure 2.23) (theoretical, 2.85 eV).⁸¹

$$(\alpha h\nu)^2 = c(h\nu - E_g) \dots \dots \dots (1)$$

where α is the coefficient of absorption, E_g is the energy of the optical band gap, h is Planck's constant, ν is the frequency, and c is a constant.

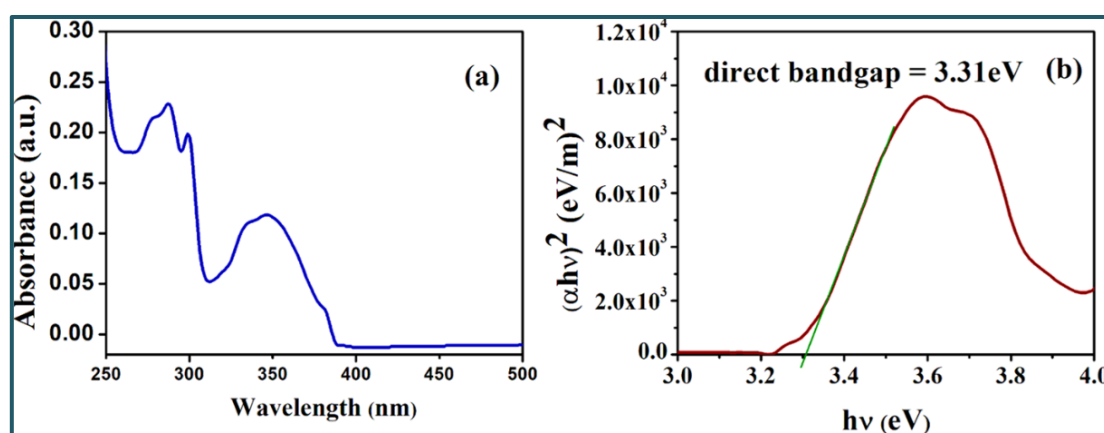


Figure 2.23 (a) UV-Vis absorption spectrum of **1** in acetonitrile. (b) Tauc's plot: illustrates the compound's band gap energy.

The optical band gap, 3.31 eV, insists to design a semiconducting device. To have a better understanding of the charge carrier translocation process within the metal-semiconductor (MS) interface, the J - V curve was drawn, and the space charge limited current (SCLC) theory was applied to gain more insight into the electrical characteristics.⁸²⁻⁸⁴ The cell-like structural arrangement of coordination polymeric compounds transports charges within their construction assembly. The electrical characteristics are further impacted by their steric and mechanical attributes (rigidity or flexibility) of organic connectors. Thus, by switching the linkers from stiff to flexible, the bulk electrical characteristics of such metalcoordinated polymers may be improved. Flexible linkers typically found that the structure may support better charge mobility.^{85,86} In the present material, the nitrogen donor ligand with highly conjugated polyaromatic attachment from both sides of the metal center may act as a hanging passage for "through-space" charge transport within nearby layers. Room temperature and dark-phase electrical property supports the device applicability of the

material in ambient condition. Therefore, considering the current technological aspect, our synthesized material may be potentially applicable for laboratory to land application. Room-temperature J - V plot (Figure 2.24) in dark condition is used to calculate the electrical conductivity to be $1.10 \times 10^{-5} \text{ S m}^{-1}$. The J - V graph of the fabricated thin-film metal-semiconductor (MS) device shows nonlinear rectifying characteristics, which indicates the formation of Schottky barrier with a rectification ratio of 8.75 at the MS junction. J - V data, in particular, are commonly used to compute various Schottky diode (SD) parameters. The main transport mechanism in SDs is therefore widely thought to be pure thermionic emission. In the current scenario, experimental findings from the J - V data may be explained using the following equations (eqs 2 and 3)⁸⁷

$$J = J_{sat} [\exp \frac{\beta}{\eta} V - 1] \dots \dots \dots (2)$$

and

$$J_{sat} = AA^*T^2 \exp(-\beta\phi) \dots \dots \dots (3)$$

Here, at bias V , J is the current density of the diode; η is the ideality factor; $\beta = (q/kT)$ is the inverse thermal voltage; A^* indicates modified Richardson constant; A refers to the area of the diode; and ϕ is a measure of Schottky barrier height (SBH). It is assumed that the modified Richardson constant is $1.206 \times 10^6 \text{ A K}^{-2} \text{ m}^{-2}$.

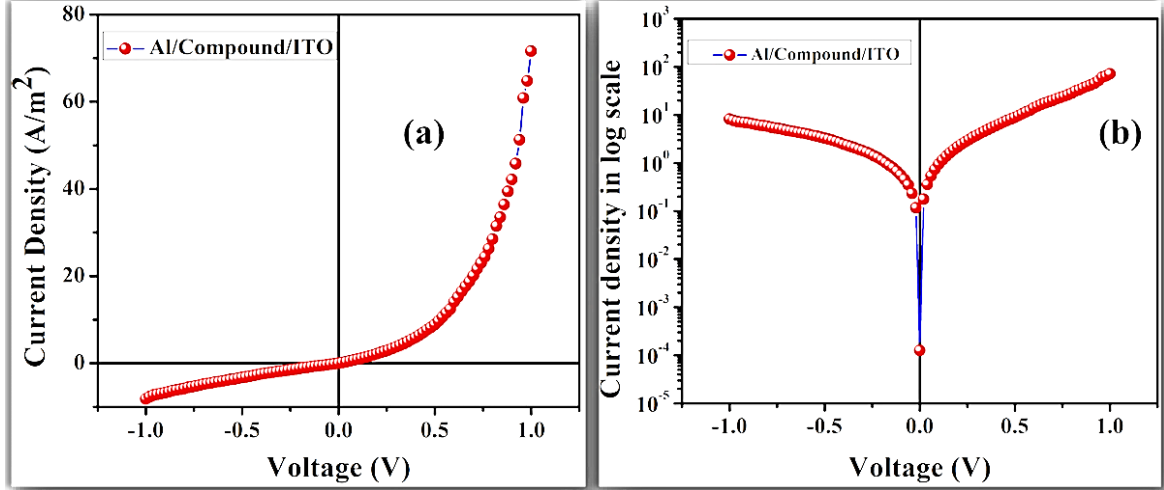


Figure 2.24 Current density vs voltage graph in (a) linear scale and (b) log scale for aluminum (Al)/compound/indium tin oxide (ITO).

The $\ln J$ vs $\ln V$ graph reflects the voltage domain of forward bias (Figure 2.25a), and the linear portion of the plot was fitted in order to better comprehend how the MS interface facilitates charge transportation. The slope in region I is 1, which implies that Ohmic conduction predominates in carrier transport events.⁸⁸ In light of trap-assisted carrier transition, in region II, the slope is 2, exposing the mechanism of space charge limited

conduction (SCLC). A series resistance (eq 4) was taken into account (R_s), and the value of J_{sat} was substituted into eq 2⁸⁹

$$J = AA^*T^2 \exp(-\beta\phi) \left[\exp \frac{\beta}{\eta} (V - IR_s) - 1 \right] \dots \dots \dots (4)$$

Where, the voltage drop is indicated by the term IR_s .

Differentiation of eq 4 as a function of $\ln J$ provides the Cheungs' equation (eq 5):⁹⁰

$$\frac{dV}{d \ln J} = JAR_s + \frac{\eta}{\beta} \dots \dots \dots (5)$$

Using a $dV/d \ln J$ vs J plot, it is possible to calculate the ideality factor and series resistance of an integrated Schottky device. In the J - V characteristics curve, the $dV/d \ln J$ vs J profiles of the diode tend to be linear with regard to the downward curvature zone of forward bias (Figure 2.25b). In this area, series resistance and ideality factor are more significant since the current follows Ohm's law (Table 2.4). The ideality factor frequently fails to match one simply due to the MS junction's inhomogeneity.⁹¹

The current density-dependent function $H(J)$, as defined in the Cheung model, can be expressed as in eq 6.⁹⁰

$$H(J) = V - \frac{\eta}{\beta} \ln \left(\frac{J}{A^*T^2} \right) = JAR_s + \eta \phi \dots \dots \dots (6)$$

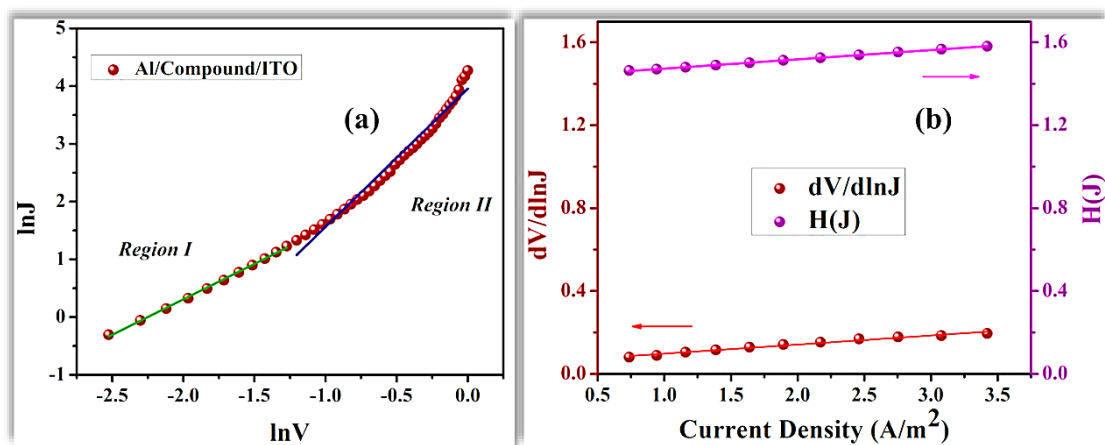


Figure 2.25 (a) $\ln J$ vs $\ln V$ plot for the fabricated device. (b) $dV/d \ln J$ and $H(J)$ vs current density graph for Al/compound/ITO structure.

Table 2.4 Device parameters based on the synthesized material for schottky diodes.

Rectification ratio	Conductivity ($S m^{-1}$)	Ideality factor	Barrier height (eV)	R_s from $dV/d \ln J$ ($k\Omega$)	R_s from $H(J)$ ($k\Omega$)
8.75	1.10×10^{-5}	2.06	0.693	6.21	6.34

By analyzing the $H(J)$ vs J graph, the Schottky barrier height of the device can be determined (Figure 2.25b). Like the $dV/d\ln J$ vs J plot, these data indicate uniformity in the minimal potential area. As determined by the $H(J)$ vs J plot, Table 2.4 reflects the barrier height (ϕ) and series resistance (R_s). The series resistance (R_s) was derived using two different approaches, and the values were almost comparable (6.21 and 6.34 k Ω , Table 2.4). In addition to surface features, the metal-to-semiconductor contact's caliber was considered to be of significant importance.⁹²

2.4 Conclusions

Pyridinyl-dihydrobenzoimidazoquinazoline is air-oxidized during complex formation with Cd(II) in the presence of glutaric acid and has synthesized a highly luminous 1D [Cd-(glu)₂(pbic)₂(H₂O)]_n. The strong emission is selectively quenched by nitroaromatic explosives (NAEs) and the highest quenching efficiency is seen for TNP with a detection limit of 1.51×10^{-7} M. The energy transfer mechanism, FRET and PET, is shown to be effective for the quenching process including both static and dynamic quenching in response to elevated analyte concentrations. The lower-dimensional, 1D CP shows spectacular electrical conductivity (Λ : 1.10×10^{-5} S m⁻¹) in the semiconducting regime as suggested by the experimental band gap (3.31 eV) and flexible linkers typically found in the structure to support better charge mobility, which may be due to the self-assembly of 1D chains. This approach offers a possible method for improving CPs potential in molecular sensing and semiconducting device fabrications.

2.5 References

- (1) Tranchemontagne, D. J.; Mendoza-Cortés, J. L.; O’Keeffe, M.; Yaghi, O. M. Secondary building units, nets and bonding in the chemistry of metal-organic frameworks. *Chem. Soc. Rev.* **2009**, 38, 1257-1283.
- (2) Lee, C. Y.; Bae, Y. S.; Jeong, N. C.; Farha, O. K.; Sarjeant, A. A.; Stern, C. L.; Nickias, P.; Snurr, R. Q.; Hupp, J. T.; Nguyen, S. T. Kinetic separation of propene and propane in metal-organic frameworks: controlling diffusion rates in plate-shaped crystals via tuning of pore apertures and crystallite aspect ratios. *J. Am. Chem. Soc.* **2011**, 133, 5228-5231.

- (3) Li, F. L.; Wang, P.; Huang, X.; Young, D. J.; Wang, H. F.; Braunstein, P.; Lang, J. P. Large-scale, bottom-up synthesis of binary metal-organic framework nanosheets for efficient water oxidation. *Angew. Chem.* **2019**, *131*, 7125-7130.
- (4) Liu, C. Y.; Chen, X. R.; Chen, H. X.; Niu, Z.; Hirao, H.; Braunstein, P.; Lang, J. P. Ultrafast luminescent light-up guest detection based on the lock of the host molecular vibration. *J. Am. Chem. Soc.* **2020**, *142*, 6690-6697.
- (5) Yang, Z. Y.; Sang, X.; Liu, D.; Li, Q. Y.; Lang, F.; Abrahams, B. F.; Hou, H.; Braunstein, P.; Lang, J. P. Photopolymerization-Driven Macroscopic Mechanical Motions of a Composite Film Containing a Vinyl Coordination Polymer. *Angew. Chem., Int. Ed.* **2023**, *135*, No. e202302429.
- (6) Wang, M. F.; Mi, Y.; Hu, F. L.; Hirao, H.; Niu, Z.; Braunstein, P.; Lang, J. P. Controllable multiple-step configuration transformations in a thermal/photoinduced reaction. *Nat. Commun.* **2022**, *13*, No. 2847.
- (7) Eddaoudi, M.; Moler, D. B.; Li, H.; Chen, B.; Reineke, T. M.; O’Keeffe, M.; Yaghi, O. M. Assembly of metal-organic frameworks from large organic and inorganic secondary building units: new examples and simplifying principles for complex structures. *Acc. Chem. Res.* **2001**, *34*, 319-330.
- (8) Wang, C.; Liu, D.; Lin, W. Metal-organic frameworks as a tunable platform for designing functional molecular materials. *J. Am. Chem. Soc.* **2013**, *135*, 13222-13234.
- (9) Kreno, L. E.; Leong, K.; Farha, O. K.; Allendorf, M.; Van Duyne, R. P.; Hupp, J. T. Metal-organic framework materials as chemical sensors. *Chem. Rev.* **2012**, *112*, 1105-1125.
- (10) Cui, Y.; Yue, Y.; Qian, G.; Chen, B. Luminescent functional metal-organic frameworks. *Chem. Rev.* **2012**, *112*, 1126-1162.
- (11) Wang, F.; Wang, Y. T.; Yu, H.; Chen, J. X.; Gao, B. B.; Lang, J. P. One unique 1D silver (I)-bromide-thiol coordination polymer used for highly efficient chemiresistive sensing of ammonia and amines in water. *Inorg. Chem.* **2016**, *55*, 9417-9423.
- (12) Ren, X. Y.; Lu, L. H. Luminescent nanoscale metal-organic frameworks for chemical sensing. *Chin. Chem. Lett.* **2015**, *26*, 1439-1445.
- (13) Xie, L. S.; Skorupskii, G.; Dincă, M. Electrically conductive metal-organic frameworks. *Chem. Rev.* **2020**, *120*, 8536-8580.
- (14) Li, J. R.; Kuppler, R. J.; Zhou, H. C. Selective gas adsorption and separation in metal-organic frameworks. *Chem. Soc. Rev.* **2009**, *38*, 1477-1504.

- (15) Murray, L. J.; Dincă, M.; Long, J. R. Hydrogen storage in metalorganic frameworks. *Chem. Soc. Rev.* **2009**, 38, 1294-1314.
- (16) Kurmoo, M. Magnetic metal-organic frameworks. *Chem. Soc. Rev.* **2009**, 38, 1353-1379.
- (17) Lee, J.; Farha, O. K.; Roberts, J.; Scheidt, K. A.; Nguyen, S. T.; Hupp, J. T. Metal organic framework materials as catalysts. *Chem. Soc. Rev.* **2009**, 38, 1450-1459.
- (18) Liu, J.; Chen, L.; Cui, H.; Zhang, J.; Zhang, L.; Su, C. Y. Applications of metal-organic frameworks in heterogeneous supramolecular catalysis. *Chem. Soc. Rev.* **2014**, 43, 6011-6061.
- (19) Taylor-Pashow, K. M. L.; Rocca, J. D.; Xie, Z. G.; Tran, S.; Lin, W. Post synthetic Modifications of Iron-Carboxylate Nanoscale Metal-Organic Frameworks for Imaging and Drug Delivery. *J. Am. Chem. Soc.* **2009**, 131, 14261-14263.
- (20) Horcajada, P.; Chalati, T.; Serre, C.; Gillet, B.; Sebrie, C.; Baati, T.; Eubank, J. F.; Heurtaux, D.; Clayette, P.; Kreuz, C.; Chang, J. S.; Hwang, Y. K.; Marsaud, V.; Bories, Y.-N.; Cynober, L.; Gil, S.; Ferey, G.; Couvreur, P.; Gref, R. Porous metal-organic framework nanoscale carriers as a potential platform for drug delivery and imaging. *Nat. Mater.* **2010**, 9, 172-178.
- (21) Wang, X. P.; Han, L. L.; Wang, Z.; Guo, L. Y.; Sun, D. Microporous Cd (II) metal-organic framework as fluorescent sensor for nitroaromatic explosives at the sub-ppm level. *J. Mol. Struct.* **2016**, 1107, 1-6.
- (22) Guo, L. Y.; Su, H. F.; Kurmoo, M.; Wang, X. P.; Zhao, Q. Q.; Lin, S. C.; Tung, C. H.; Sun, D.; Zheng, L. S. Multifunctional tripledecker inverse 12-metallacrown-4 sandwiching halides. *ACS Appl. Mater. Interfaces* **2017**, 9, 19980-19987.
- (23) Chen, B.; Xiang, S.; Qian, G. Metal-Organic Frameworks with Functional Pores for Recognition of Small Molecules. *Acc. Chem. Res.* **2010**, 43, 1115-1124.
- (24) Cui, Y.; Chen, B.; Qian, G. Lanthanide metal-organic frameworks for luminescent sensing and light-emitting applications. *Coord. Chem. Rev.* **2014**, 273-274, 76-86.
- (25) Müller-Buschbaum, K.; Beuerle, F.; Feldmann, C. MOF based luminescence tuning and chemical/physical sensing. *Microporous Mesoporous Mater.* **2015**, 216, 171-199.
- (26) Hu, Z.; Deibert, B. J.; Li, J. Luminescent metal-organic frameworks for chemical sensing and explosive detection. *Chem. Soc. Rev.* **2014**, 43, 5815-5840.
- (27) Tulskey, E. G.; Long, J. R. Dimensional reduction: a practical formalism for manipulating solid structures. *Chem. Mater.* **2001**, 13, 1149-1166.

- (28) Stock, N.; Biswas, S. Synthesis of metal-organic frameworks (MOFs): routes to various mof topologies, morphologies, and composites. *Chem. Rev.* **2012**, *112*, 933-969.
- (29) Li, M.; Li, D.; O'Kee, M.; Yaghi, O. M. Topological Analysis of Metal-Organic Frameworks with Polytopic Linkers and/or Multiple Building Units and the Minimal Transitivity Principle. *Chem. Rev.* **2014**, *114*, 1343-1370.
- (30) Chen, W. M.; Meng, X. L.; Zhuang, G. L.; Wang, Z.; Kurmoo, M.; Zhao, Q. Q.; Wang, X. P.; Shan, B.; Tung, C. H.; Sun, D. A superior fluorescent sensor for Al^{3+} and UO_2^{2+} based on a Co (II) metal-organic framework with exposed pyrimidyl Lewis base sites. *J. Mater. Chem. A* **2017**, *5*, 13079-13085.
- (31) Sheng, K.; Lu, H.; Sun, A.; Wang, Y.; Liu, Y.; Chen, F.; Bian, W.; Li, Y.; Kuang, R.; Sun, D. A naked-eye colorimetric sensor for chloroform. *Chin. Chem. Lett.* **2019**, *30*, 895-898.
- (32) Rossetti, A.; Lippi, M.; Marti-Rujas, J.; Sacchetti, A.; Cametti, M. Highly dynamic and tunable behavior of 1D coordination polymers based on the bispidine ligand. *Chem.-Eur. J.* **2018**, *24*, 19368-19372.
- (33) Leong, W. L.; Vittal, J. J. One-dimensional coordination polymers: complexity and diversity in structures, properties, and applications. *Chem. Rev.* **2011**, *111*, 688-764.
- (34) Toal, S. J.; Trogler, W. C. Polymer sensors for nitroaromatic explosives detection. *J. Mater. Chem.* **2006**, *16*, 2871-2883.
- (35) Senesac, L.; Thundat, T. G. Nanosensors for trace explosive detection. *Mater. Today* **2008**, *11*, 28-36.
- (36) Salinas, Y.; Martinez-Mañez, R.; Marcos, M. D.; Sancenon, F.; Costero, A. M.; Parra, M.; Gil, S. Optical chemosensors and reagents to detect explosives. *Chem. Soc. Rev.* **2012**, *41*, 1261-1296.
- (37) Germain, M. E.; Knapp, M. J. Optical explosives detection: from color changes to fluorescence turn-on. *Chem. Soc. Rev.* **2009**, *38*, 2543-2555.
- (38) Nagarkar, S. S.; Desai, A. V.; Ghosh, S. K. A fluorescent metalorganic framework for highly selective detection of nitro explosives in the aqueous phase. *Chem. Commun.* **2014**, *50*, 8915-8918.
- (39) Venkatramaiah, N.; Kumar, S.; Patil, S. Fluoranthene based fluorescent chemosensors for detection of explosive nitroaromatics. *Chem. Commun.* **2012**, *48*, 5007-5009.

- (40) Thorne, P. G.; Jenkins, T. F. A Field Method for Quantifying Ammonium Picrate and Picric Acid in Soil. *Field Anal. Chem. Technol.* **1997**, *1*, 165-170.
- (41) He, G.; Peng, H.; Liu, T.; Yang, M.; Zhang, Y.; Fang, Y. A novel picric acid film sensor via combination of the surface enrichment effect of chitosan films and the aggregation-induced emission effect of siloles. *J. Mater. Chem.* **2009**, *19*, 7347-7353.
- (42) Wasi, S.; Tabrez, S.; Ahmad, M. Toxicological effects of major environmental pollutants: an overview. *Environ. Monit. Assess.* **2013**, *185*, 2585-2593.
- (43) Kuo, D. T. F.; Rattner, B. A.; Martenson, S. C.; Letcher, R.; Fernie, K. J.; Treu, G.; Deutsch, M.; Johnson, M. S.; Deglin, S.; Embry, M. A critical review of bioaccumulation and biotransformation of organic chemicals in birds. *Rev. Environ. Contam. Toxicol.* **2022**, *260*, No. 6.
- (44) USEPA. *Ambient Water Quality Criteria for Nitrophenol*; U.S. Environmental Protection Agency: Washington, DC, 1980.
- (45) Michalowicz, J.; Duda, W. Phenols-Sources and Toxicity. *Pol. J. Environ. Stud.* **2007**, *16*, 347-362.
- (46) Thorne, P. G.; Jenkins, T. F. A field method for quantifying ammonium picrate and picric acid in soil. *Field Anal. Chem. Technol.* **1997**, *1*, 165-170.
- (47) Wollin, K. M.; Dieter, H. H. Toxicological Guidelines for Monocyclic Nitro-, Amino- and Aminonitroaromatics, Nitramines, and Nitrate Esters in Drinking Water. *Arch. Environ. Contam. Toxicol.* **2005**, *49*, 18-26.
- (48) Tang, Z.; Chen, H.; Zhang, Y.; Zheng, B.; Zhang, S.; Cheng, P. Functional two-dimensional coordination polymer exhibiting luminescence detection of nitroaromatics. *Cryst. Growth Des.* **2019**, *19*, 1172-1182.
- (49) Abuzalat, O.; Wong, D.; Park, S. S.; Kim, S. Highly selective and sensitive fluorescent zeolitic imidazole frameworks sensor for nitroaromatic explosive detection. *Nanoscale* **2020**, *12*, 13523-13530.
- (50) Maiti, K.; Mahapatra, A. K.; Gangopadhyay, A.; Maji, R.; Mondal, S.; Ali, S. S.; Das, S.; Sarkar, R.; Datta, P.; Mandal, D. Simple bithiocarbonohydrazone as a sensitive, selective, colorimetric, and ratiometric fluorescent chemosensor for picric acids. *ACS Omega* **2017**, *2*, 1583-1593.
- (51) Rachuri, Y.; Parmar, B.; Bisht, K. K.; Suresh, E. Mixed ligand two dimensional Cd(II)/Ni(II) metal organic frameworks containing dicarboxylate and tripodal N-

- donor ligands: Cd(II) MOF is an efficient luminescent sensor for detection of picric acid in aqueous media. *Dalton Trans.* **2016**, 45, 7881-7892.
- (52) Sun, L.; Campbell, M. G.; Dincă, M. Electrically conductive porous metal-organic frameworks. *Angew. Chem., Int. Ed.* **2016**, 55, 3566-3579.
- (53) Stavila, V.; Talin, A. A.; Allendorf, M. D. MOF-based electronic and opto-electronic devices. *Chem. Soc. Rev.* **2014**, 43, 5994-6010.
- (54) Ahmed, F.; Datta, J.; Dutta, B.; Naskar, K.; Sinha, C.; Alam, S. M.; Kundu, S.; Ray, P. P.; Mir, M. H. Cation dependent charge transport in linear dicarboxylate based isotypical 1D coordination polymers. *RSC Adv.* **2017**, 7, 10369-10375.
- (55) Ahmed, F.; Dutta, B.; Mir, M. H. Electrically conductive 1D coordination polymers: design strategies and controlling factors. *Dalton Trans.* **2021**, 50, 29-38.
- (56) Liu, J.; Zhou, W.; Liu, J.; Howard, I.; Kilibarda, G.; Schlabach, S.; Couprie, D.; Addicoat, M.; Yoneda, S.; Tsutsui, Y.; Sakurai, T.; et al. Photoinduced Charge-Carrier Generation in Epitaxial MOF Thin Films: High Efficiency as a Result of an Indirect Electronic Band Gap. *Angew. Chem., Int. Ed.* **2015**, 54, 7441-7445.
- (57) Ahmed, F.; Datta, J.; Sarkar, S.; Dutta, B.; Jana, A. D.; Ray, P. P.; Mir, M. H. Water tetramer confinement and photosensitive Schottky behavior of a 2D coordination polymer. *ChemistrySelect* **2018**, 3, 6985-6991.
- (58) Dutta, B.; Jana, R.; Sinha, C.; Ray, P. P.; Mir, M. H. Synthesis of a Cd (II) based 1D coordination polymer by in situ ligand generation and fabrication of a photosensitive electronic device. *Inorg. Chem. Front.* **2018**, 5, 1998-2005.
- (59) Ahmed, F.; Halder, S.; Dutta, B.; Islam, S.; Sen, C.; Kundu, S.; Sinha, C.; Ray, P. P.; Mir, M. H. Synthesis and structural characterization of a Cu (II)-based 1D coordination polymer and its application in Schottky devices. *New J. Chem.* **2017**, 41, 11317-11323.
- (60) Ghorai, P.; Dey, A.; Hazra, A.; Dutta, B.; Brandão, P.; Ray, P. P.; Banerjee, P.; Saha, A. Cd(II) Based Coordination Polymer Series: Fascinating Structures, Efficient Semiconductors, and Promising Nitro Aromatic Sensing. *Cryst. Growth Des.* **2019**, 19, 6431-6447.
- (61) Dutta, B.; Hazra, A.; Dey, A.; Sinha, C.; Ray, P. P.; Banerjee, P.; Mir, M. H. Construction of a Succinate-Bridged Cd(II)-Based Two-Dimensional Coordination Polymer for Efficient Optoelectronic Device Fabrication and Explosive Sensing Application. *Cryst. Growth Des.* **2020**, 20, 765-776.

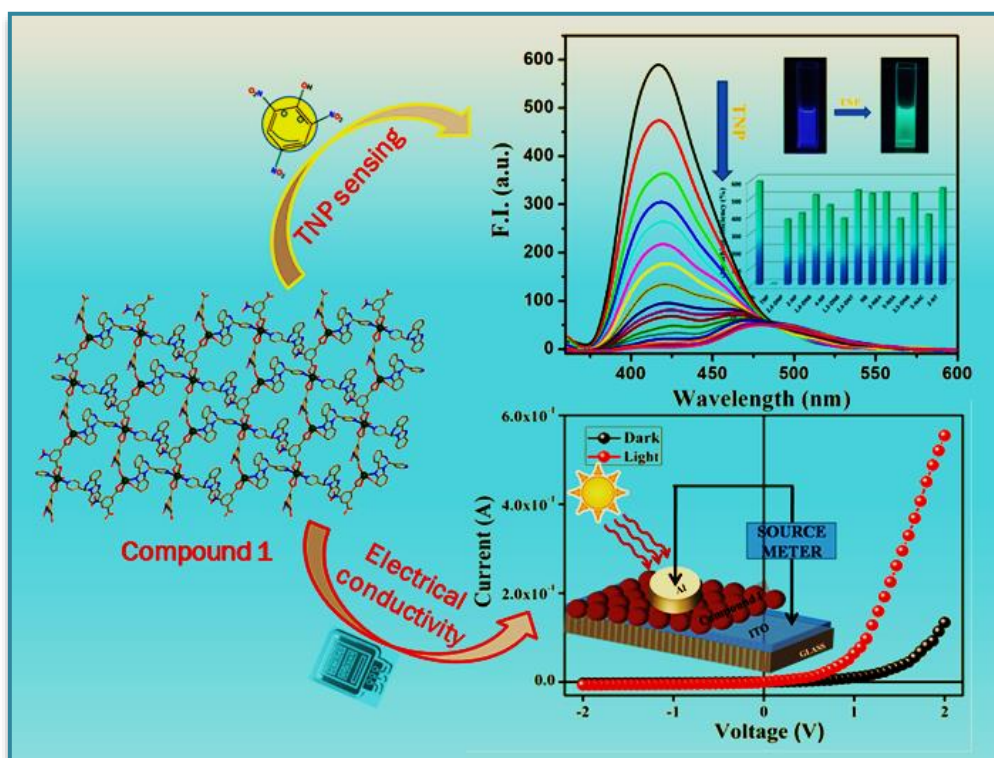
- (62) Bairy, G.; Dey, A.; Dutta, B.; Ray, P. P.; Sinha, C. 2D Cd (II)-MOF of Pyridyl-Imidazoquinazoline: Structure, Luminescence, and Selective Detection of TNP and Fabrication of Semiconducting Devices. *Cryst. Growth Des.* **2022**, 22, 3138-3147.
- (63) Bairy, G.; Dey, A.; Dutta, B.; Maity, S.; Sinha, C. Rational synthesis of a pyridyl-imidazoquinazoline based multifunctional 3D Zn (ii)-MOF: structure, luminescence, selective and sensitive detection of Al^{3+} and TNP, and its semiconducting device application. *Dalton Trans.* **2022**, 51, 13749-13761.
- (64) SADABS. *Bruker AXS Area Detector Scaling and Absorption Correction*; Bruker AXS Inc.: Madison, WI, 2014.
- (65) *SMART and SAINT*; Bruker AXS Inc.: Madison, WI, 1998.
- (66) Bourhis, L. J.; Dolomanov, O. V.; Gildea, R. J.; Howard, J. A.; Puschmann, H. The anatomy of a comprehensive constrained, restrained refinement program for the modern computing environment-Olex2 dissected. *Acta Crystallogr., Sect. A: Found. Adv.* **2015**, 71, 59-75.
- (67) Sheldrick, G. M. SHELXT-Integrated space-group and crystalstructure determination. *Acta Crystallogr., Sect. A: Found. Adv.* **2015**, 71, 3-8.
- (68) Frisch, M. J.; Trucks, G. W.; Schlegel, H. B.; Scuseria, G. E.; Robb, M. A.; Cheeseman, J. R.; Scalmani, G.; Barone, V.; Mennucci, B.; Petersson, G. A.; Nakatsuji, H.; Caricato, M.; Li, X.; Hratchian, H. P.; Izmaylov, A. F.; Bloino, J.; Zheng, G.; Sonnenberg, J. L.; Hada, M.; Ehara, M.; Toyota, K.; Fukuda, R.; Hasegawa, J.; Ishida, M.; Nakajima, T.; Honda, Y.; Kitao, O.; Nakai, H.; Vreven, T.; Montgomery, J. A., Jr.; Peralta, J. E.; Ogliaro, F. M.; Bearpark, J.; Heyd, J.; Brothers, E.; Kudin, K. N.; Staroverov, V. N.; Kobayashi, R.; Normand, J.; Raghavachari, K.; Rendell, A.; Burant, J. C.; Iyengar, S. S.; Tomasi, J.; Cossi, M.; Rega, N.; Millam, J. M.; Klene, M.; Yazyev, O.; Austin, A. J.; Cammi, R.; Pomelli, C.; Ochterski, J. W.; Martin, R. L.; Morokuma, K.; Zakrzewski, V. G.; Salvador, G. A. P.; Dannenberg, J. J.; Dapprich, S.; Daniels, A. D.; Farkas, Ö.; Foresman, J. B.; Ortiz, J. V.; Cioslowski, J.; Fox, D. J. *Gaussian 09*, revision D.01; Gaussian, Inc.: Wallingford, CT, 2009.
- (69) Becke, A. D. Density-Functional Thermochemistry. III. The Role of Exact Exchange. *J. Chem. Phys.* **1993**, 98, 5648-5652.
- (70) Stratmann, R. E.; Scuseria, G. E.; Frisch, M. J. An efficient implementation of time-dependent density-functional theory for the calculation of excitation energies of large molecules. *J. Chem. Phys.* **1998**, 109, 8218-8224.

- (71) O'Boyle, N. M.; Tenderholt, A. L.; Langner, K. M. Cclib: a Library for Package-independent Computational Chemistry Algorithms. *J. Comput. Chem.* **2008**, 29, 839-845.
- (72) Pandey, R.; Yadav, M.; Shahid, M.; Misra, A.; Pandey, D. S. Design and synthesis of fluorescent 6-aryl [1, 2-c] quinazolines serving as selective and sensitive 'on-off' chemosensor for Hg²⁺ in aqueous media. *Tetrahedron Lett.* **2012**, 53, 3550-3555.
- (73) Kaur, N.; Kaur, B. Recent development in anthracene possessing chemosensors for cations and anions. *Microchem. J.* **2020**, 158, No. 105131.
- (74) Che, Y.; Yang, X.; Zang, L. Ultrasensitive fluorescent sensing of Hg²⁺ through metal coordination-induced molecular aggregation. *Chem. Commun.* **2008**, 12, 1413-1415.
- (75) Dutta, B.; Jana, R.; Bhanja, A. K.; Ray, P. P.; Sinha, C.; Mir, M. H. Supramolecular aggregate of Cadmium (II)-based one-dimensional coordination polymer for device fabrication and sensor application. *Inorg. Chem.* **2019**, 58, 2686-2694.
- (76) Yao, S. L.; Tian, X. M.; Li, L. Q.; Liu, S. J.; Zheng, T. F.; Chen, Y. Q.; Zhang, D. S.; Chen, J. L.; Wen, H. R.; Hu, T. L. A Cd^{II}-Based Metal-Organic Framework with pcu Topology as Turn-On Fluorescent Sensor for Al³⁺. *Chem.-Asian J.* **2019**, 14, 3648-3654.
- (77) Asha, K. S.; Bhattacharyya, K.; Mandal, S. Discriminative detection of nitro aromatic explosives by a luminescent metal-organic framework. *J. Mater. Chem. C* **2014**, 2, 10073-10081.
- (78) Keizer, J. Nonlinear Fluorescence Quenching and the Origin of Positive Curvature in Stern-Volmer Plots. *J. Am. Chem. Soc.* **1983**, 105, 1494-1498.
- (79) U.S. EPA. *Provisional Peer-Reviewed Toxicity Values for Picric Acid and Ammonium Picrate*, EPA/690/R-20/008F; U.S. Environmental Protection Agency: Washington, DC, 2020.
- (80) Nagarkar, S. S.; Joarder, B.; Chaudhari, A. K.; Mukherjee, S.; Ghosh, S. K. Highly Selective Detection of Nitro Explosives by a Luminescent Metal-Organic Framework. *Angew. Chem., Int. Ed.* **2013**, 52, 2881-2885.
- (81) Das, P.; Pal, B.; Das, M.; Sil, S.; Das, D.; Layek, A.; Ray, P. P. Findings of inhomogeneity in barrier height of Schottky junction Al/rGO-SnO₂ having anomaly in theoretical and experimental value of Richardson constant: A Gaussian approach. *Results Phys.* **2022**, 42, No. 105996.
- (82) Zhang, P.; Ang, Y. S.; Garner, A. L.; Valfells, Á.; Luginsland, J. W.; Ang, L. K. Space-charge limited current in nanodiodes: Ballistic, collisional, and dynamical effects. *J. Appl. Phys.* **2021**, 129, No. 100902.

- (83) Zhao, C.; Yi, J.; Wang, L.; Lu, G.; Huang, H.; Kim, H. K.; Yu, H.; Xie, C.; You, P.; Lu, G.; Qiu, M.; et al. An improved performance of all polymer solar cells enabled by sequential processing via nonhalogenated solvents. *Nano Energy* **2022**, *104*, No. 107872.
- (84) Dutta, B.; Halder, S. Fabrication of Schottky Barrier Diodes Utilizing Schiff Base Compounds and Metal Complexes with Schiff Base Ligands. *ChemistrySelect* **2023**, *8*, No. e20230158.
- (85) Naskar, K.; Dey, A.; Dutta, B.; Ahmed, F.; Sen, C.; Mir, M. H.; Roy, P. P.; Sinha, C. Intercatenated coordination polymers (ICPs) of carboxylato bridged Zn (II)-isoniazid and their electrical conductivity. *Cryst. Growth Des.* **2017**, *17*, 3267-3276.
- (86) Dutta, B.; Datta, J.; Maity, S.; Sinha, C.; Sun, D.; Ray, P. P.; Mir, M. H. Electrical property and Schottky behavior of a flexible Schiff-base compound: X-ray structure and stabilization of 1D water chain. *Phys. Chem. Chem. Phys.* **2018**, *20*, 24744-24749.
- (87) Das, P.; Pal, B.; Datta, J.; Das, M.; Sil, S.; Ray, P. P. Improved charge transport properties of graphene incorporated tin oxide based Schottky diode over pure one. *J. Phys. Chem. Solids* **2021**, *148*, No. 109706.
- (88) Das, M.; Das, P.; Datta, J.; Das, D.; Acharya, S.; Ray, P. P. Improved device performance of rod like ZnO in a Schottky type photosensor compared to particle like ZnO: Analysis of charge transport. *Mater. Sci. Semicond. Process.* **2021**, *130*, No. 105799.
- (89) Helal, H.; Benamara, Z.; Perez, B. G.; Kacha, A. H.; Rabehi, A.; Wederni, M. A.; Mourad, S.; Khirouni, K.; Monier, G.; Robert-Goumet, C. A new model of thermionic emission mechanism for nonideal Schottky contacts and a method of extracting electrical parameters. *Eur. Phys. J. Plus* **2020**, *135*, No. 895.
- (90) Cheung, S. K.; Cheung, N. W. Extraction of Schottky diode parameters from forward current-voltage characteristics. *Appl. Phys. Lett.* **1986**, *49*, 85-87.
- (91) Das, P.; Majumdar, S.; Dey, A.; Mandal, S.; Mondal, A.; Chakrabarty, S.; Ray, P. P.; Dey, B. 4, 4'-Bipyridine-based Ni(ii)-metallogel for fabricating a photo-responsive Schottky barrier diode device. *New J. Chem.* **2021**, *45*, 15920-15927.
- (92) Naaz, S.; Das, P.; Khan, S.; Dutta, B.; Maity, S.; Ghosh, P.; Ray, P. P.; Mir, M. H. Fabrication of a halopyridine appended Co(ii) based 1D coordination polymer for efficient charge transportation. *Polyhedron* **2021**, *201*, No. 115159.

Chapter 3

2D Cd(II)-MOF of Pyridyl-Imidazoquinazoline: Structure, Luminescence, and Selective Detection of TNP and Fabrication of Semiconducting Devices



Abstract:

Pyridyl-substituted imidazoquinolines are highly fluorescent probes and are useful for the design of smart materials. A hitherto unknown pyridylimidazoquinazoline-coordinated two-dimensional (2D)-Cd(II)-MOF $\{[\text{Cd}_2(5\text{-nip})_2(\text{pdiq})_2(\text{H}_2\text{O})_2(\text{CH}_3\text{OH})]\cdot\text{H}_2\text{O}\}_n$ (CP **1**), [H_2nip = 5-nitroisophthalic acid and **pdiq** = 6-(pyridin-4-yl)-5,6-dihydrobenzo[4,5]imidazo[1,2-*c*]quinazoline] has been designed and structurally confirmed by single-crystal X-ray crystallography. The presence of $\text{C-H}\cdots\pi$ and $\pi\cdots\pi$ interactions in CP **1** makes it a three-dimensional (3D) supramolecular structure. The excellent luminescent behavior of CP **1** is selectively quenched by trinitrophenol (TNP) even in the presence of potentially intrusive nitroaromatic explosives (NAEs). A limit of detection (LOD) of 2.75×10^{-7} M for TNP is achieved ($3\sigma/m$). In addition, the CP **1** displays electrical conductivity on an electronic device with the metal-semiconductor (MS) junction. Current *vs* voltage (*I-V* plot) correlation reveals the substantial enhancement of electrical conductivity upon illumination (Λ : $1.12 \times 10^{-3} \text{ S m}^{-1}$ (dark), $6.33 \times 10^{-3} \text{ S m}^{-1}$ (light)) along with a decrease in energy barrier (Φ_{B} : 0.53 (dark), 0.42 (light)). The plots of $\log V$ *vs* $\log I$ show a non-Ohmic feature at a higher voltage ($\log V \geq 0$) both in the dark and the light phase, which is the characteristic of a Schottky diode barrier (SDB).

3.1 Introduction

The field of porous coordination polymers (PCPs) or metal-organic frameworks (MOFs) has been of immense interest (Chapters 1 & 2) for the last two decades owing to their high porosity and extraordinary crystallinity.¹ Due to the tunable pore size, large surface area, and variable functionality, intriguing network topologies of PCPs have attracted attention in the field of potent applications such as catalysis, gas sorption and separation, magnetism in variable temperatures, drug delivery, sensing, electrical conductivity, etc.²⁻¹² The choice of the metal center, bridging organics, and/or capping groups/ligands define the structural motif of MOFs, whereas temperature, pressure, solvent, pH of the medium and counteranion of the metal salt, etc. represent the different dimensionalities within the MOFs. Both the π -electron-rich organic ligand and aromatic polycarboxylate as building blocks have been widely used to impart luminescent properties to the products. Among MOFs, luminescent frameworks are of great choice of interest to detect ions/molecules.¹³⁻¹⁹ In the field of selective and sensitive molecular sensing, the detection of explosives is of paramount importance, considering the defense and security purposes of a country. The structural stability, size, porosity, surface area, etc., of luminescent MOFs make them more attractive and effective over luminescent molecules because they increase sensitivity, decrease the limit of detection (LOD), increase the rate of response, and reduce the response time.²⁰⁻²⁵ Two-dimensional (2D)-MOFs (metal-organic frameworks) have potential advantages over one-dimensional (1D) and three-dimensional (3D)-MOFs due to their more exposed dynamic sites, higher sensitivity, faster response time, better stability, and ultralow limit of detection for sensing applications.²⁶

Nitroaromatic explosives (NAEs), major constituents of explosive materials, are used in land mines, high-explosive shells and armed devices, etc.²⁷ Among various NAEs, 2,4,6-trinitrophenol (TNP) prevails, being even stronger than its well-known counterpart 2,4,6-trinitrotoluene (TNT), and has been broadly used in aniline synthesis, oxidative metal etching, fireworks, matches, and rocket fuels as well as in leather, pharmaceutical, and dye industries.^{28,29} During mass production and indiscriminate commercial uses, it is released into the environment and causes serious health issues.³⁰⁻³² Similarly, TNP is widely used as NAEs in devastating terror attacks, which ultimately turn out to be fatal to human civilization. Therefore, a selective, sensitive, safe, economic, environmentally benign, and rapid detection method of TNP is of great importance and highly desired.

In this regard, the fluorescence-based sensing method triggers intensive attention owing to its simple operational method, high selectivity and sensitivity, instantaneous response time, and low cost.^{14,33} Therefore, the design of a fluorescent chemosensor for the efficient detection of NAEs, especially working in a green solvent medium with simplified synthetic procedures, is a challenging goal for the scientific community.

Owing to the recent progression from laboratory to field application in the field of energy-saving materials, the application of photoconductive molecules has attracted enormous attention.^{12,34-36} The CPs with bridging dicarboxylate moieties are of current interest as they bring metal centers as close as possible for easy flow of electrons. The appropriate combination of auxiliary links can affect the electrical conduction properties and semiconductor performance of the material. The semiconducting materials exhibiting nonlinear rectifying nature in the metal-semiconductor (MS) junction can be utilized in the fabrication of the Schottky devices.^{37,38} The photoresponsive Schottky diode behavior³⁹ is of current interest to tackle the energy crisis in this century. Tauc's plot is used to calculate the band gap and aims to figure out how the material behaves while it is semiconducting. Secondary interactions between conjugated electron-rich aromatic moieties have been shown to dramatically enhance charge mobility across the material's structure. The structural, chemical, and thermal stability of these materials encouraged researchers to employ them in the realm of semiconductors in this regard. Keeping this in mind, we have designed a number of CPs⁴⁰⁻⁴⁴ that have electrical conductivity and are suitable for the manufacture of active electronic devices.

During the past few years, a series of MOF-based fluorescent sensors¹³⁻¹⁹ have been reported for the detection of NAEs, but the use of 2D MOF in the fabrication of electronic devices as well as chemical sensors has not been explored much.^{26,38,44} Herein, we have fabricated, for the first time, a highly fluorescent 2D Cd(II)-MOF (metal-organic framework), CP **1**, which is assembled by a heterocyclic ligand, 6-(pyridin-4-yl)-5,6-dihydrobenzo[4,5]imidazo[1,2-*c*]quinazoline (**pdiq**) and a bridging linker, 5-nitroisophthalate (5-nip). CP **1** is highly selective toward the detection of TNP even in the presence of other contending NAEs, which indicates that CP **1** can serve as an excellent selective and sensitive chemosensor. More interestingly, the CP **1** exhibits electrical conductivity in the semiconducting regime as confirmed by an experimental band gap (3.2 eV). Electrical characterization reveals that the CP **1** shows substantial enhancement of the electrical

conductivity upon irradiation ($6.33 \times 10^{-3} \text{ S m}^{-1}$) compared to the dark phase conductance ($1.12 \times 10^{-3} \text{ S m}^{-1}$).

In this work, we have reported the dual application of a 2D CP to photosensitive conductivity and selective TNP sensing. The chemistry of such a unique molecular network system is of boundless attention to synthetic chemists as a consequence of the stimulating structural feature in pyridyl-imidazoquinazoline scaffold; in fact, this type of ligand is quite elusive in the field of coordination polymers. This result exhibits that photocurrent can be converted many times repeatedly without deterioration of the on/off ratio and might find applications in photoswitching electronic devices. Thus, the unique characteristic property is exceptional and represents an important footstep toward the use of synthesized materials in optoelectronics and photovoltaics in this energy crisis era. In addition, the selective sensing of TNP is also an important aspect in view of environmental and health issues as well as security concerns. The steady-state Stern-Volmer plot displays an upward curvature, signifying the concurrence of static and dynamic quenching with TNP, and/or the extent of quenching is great at a higher concentration.

3.2 Experimental Section

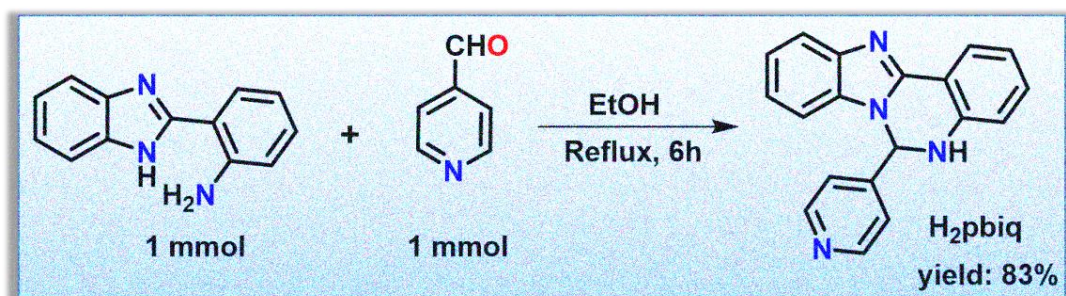
3.2.1 Materials and General Methods

Unless otherwise stated, all of the commercial reagents, solvents, and inorganic salts were reagent grade and were purchased from Spectrochem and Merck and used without further purification. 2-(1*H*-Benzo[*d*]imidazol-2-yl) aniline and isonicotinaldehyde were purchased from Sigma-Aldrich. All reactions were monitored with thin-layer chromatography (TLC) plates (Merck silica gel 60, f_{254}). Column chromatography was done using silica gel (100-200 mesh). ^1H NMR spectra were collected on 300 MHz (Bruker DPX) and 400 MHz spectrometers (JEOL JNMECZ400S/L1) in CDCl_3 and $\text{DMSO}-d_6$ solvents using tetramethylsilane (TMS) as the internal standard. ^{13}C NMR spectra were obtained on 75 MHz (Bruker D8 high-resolution mass spectrometry PX) and 100 MHz spectrometers (JEOL JNMECZ400S/L1) in CDCl_3 and $\text{DMSO}-d_6$ solvents using tetramethylsilane (TMS) as the internal standard. High-resolution mass spectrometry (HRMS) (m/z) was measured using electrospray ionization (ESI) techniques and a Q-ToF Micro mass spectrometer. The infrared spectrum in KBr ($4500\text{-}500 \text{ cm}^{-1}$) was recorded using a PerkinElmer Fourier transform infrared (FT-IR) Spectrum RX1 spectrometer. For CHN analysis, a PerkinElmer 240C elemental analyzer instrument was utilized. A PerkinElmer Pyris Diamond thermogravimetry/differential

thermal analysis (TG/DTA) instrument was exploited to test the thermal stability of the as-synthesized compound at a temperature range between 30 and 800 °C and a heating rate of 10 °C min⁻¹. Ambient temperature X-ray powder diffraction (XRPD) patterns were recorded on a Bruker D8 ADVANCE X-ray diffractometer using Cu K α radiation ($\lambda = 1.548 \text{ \AA}$) produced at 40 kV and 40 mA at a 2θ range of 5-50°. The fluorescence and ultraviolet-visible (UV-Vis) spectra were recorded on a PerkinElmer spectrofluorimeter model LS55 and a PerkinElmer Spectrophotometer LAMBDA 25, respectively. Time-correlated single-photon counting measurements were conducted using a HORIBA Jobin-Yvon setup for time-resolved single-photon counting.

3.2.2 Synthesis of Ligand (pdiq)

The synthesis was carried out following the literature method.⁴⁵ A mixture of 2-(1*H*-benzo[*d*]-imidazol-2-yl) aniline (209 mg, 1.0 mmol) and isonicotinaldehyde (107 mg, 1.0 mmol) was taken in a round-bottom flask in ethanol (10.0 mL) and refluxed for 6 h. After completion of the reaction as indicated by TLC, the reaction mixture was cooled down to ambient temperature and concentrated under reduced pressure. Further, the reaction mixture was diluted with ethyl acetate and dried over anhydrous Na₂SO₄ and concentrated under reduced pressure. The crude product was purified by column chromatography using ethyl acetate/hexane (7:3, v/v) as an eluent to afford the desired 6-(pyridin-4-yl)-5,6-dihydrobenzo[4,5]imidazo[1,2-*c*]quinazoline (**pdiq**) (Scheme 3.1). HRMS (ESI, *m/z*) calcd. for C₁₉H₁₅N₄ [M+H]⁺: 299.1297; found: 299.1319 (Figure 3.1); ¹H NMR (400 MHz, CDCl₃): δ 8.52 (d, *J* = 6.08 Hz, 2H), 8.17 (dd, *J*₁ = 7.8 Hz, *J*₂ = 1.2 Hz, 1H), 7.79 (d, *J* = 8.1 Hz, 1H), 7.27-7.23 (m, 2H), 7.14-7.12 (m, 2H), 7.10 (d, *J* = 8.1 Hz, 1H), 6.99-6.95 (m, 1H), 6.83 (d, *J* = 8.1 Hz, 1H), 6.74 (d, *J* = 8.0 Hz, 1H), 6.67 (d, *J* = 2.12 Hz, 1H), 5.13 (s, 1H) (Figure 3.2); ¹³C NMR (100 MHz, CDCl₃): δ 150.9, 141.0, 132.7, 132.1, 125.8, 123.3, 123.2, 120.91, 120.9, 119.6, 115.6, 109.6, 68.3 (Figure 3.3).



Scheme 3.1 Synthesis of 6-(pyridin-4-yl)-5,6-dihydrobenzo[4,5]imidazo[1,2-*c*]quinazoline (**pdiq**).

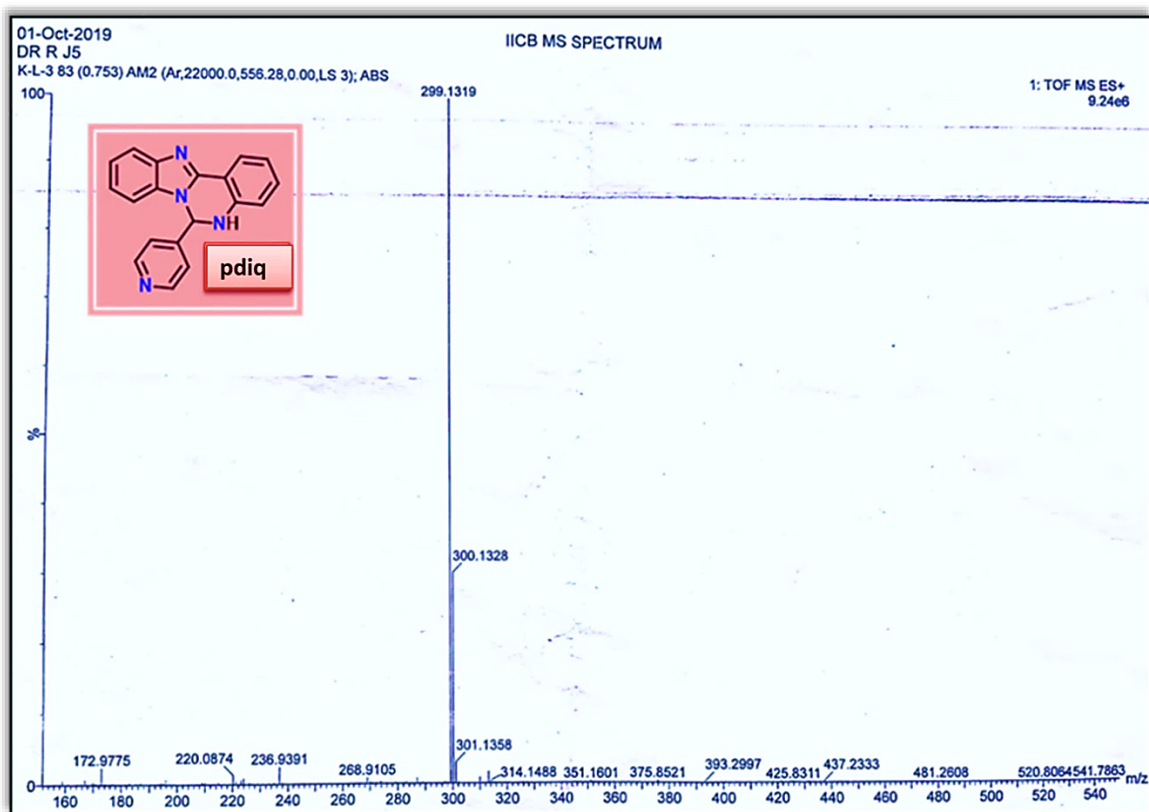


Figure 3.1 Mass spectrum of **pdiq**.

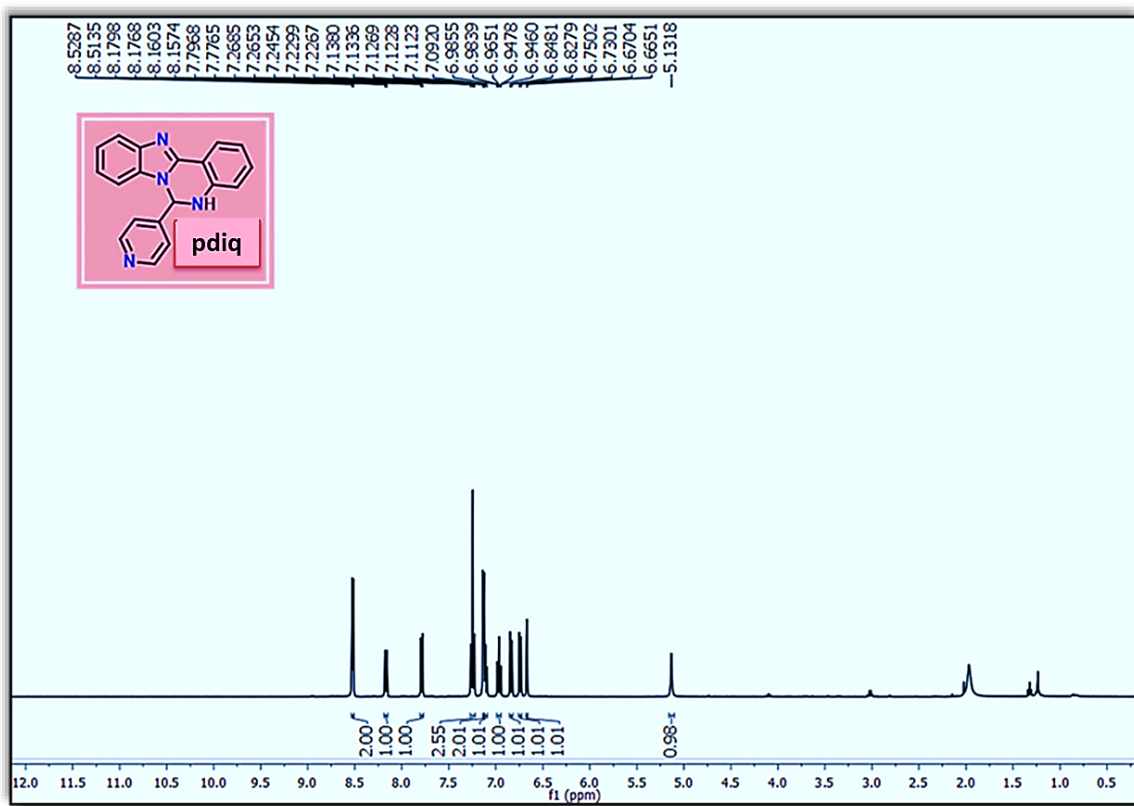


Figure 3.2 ¹H-NMR spectroscopy of **pdiq**.

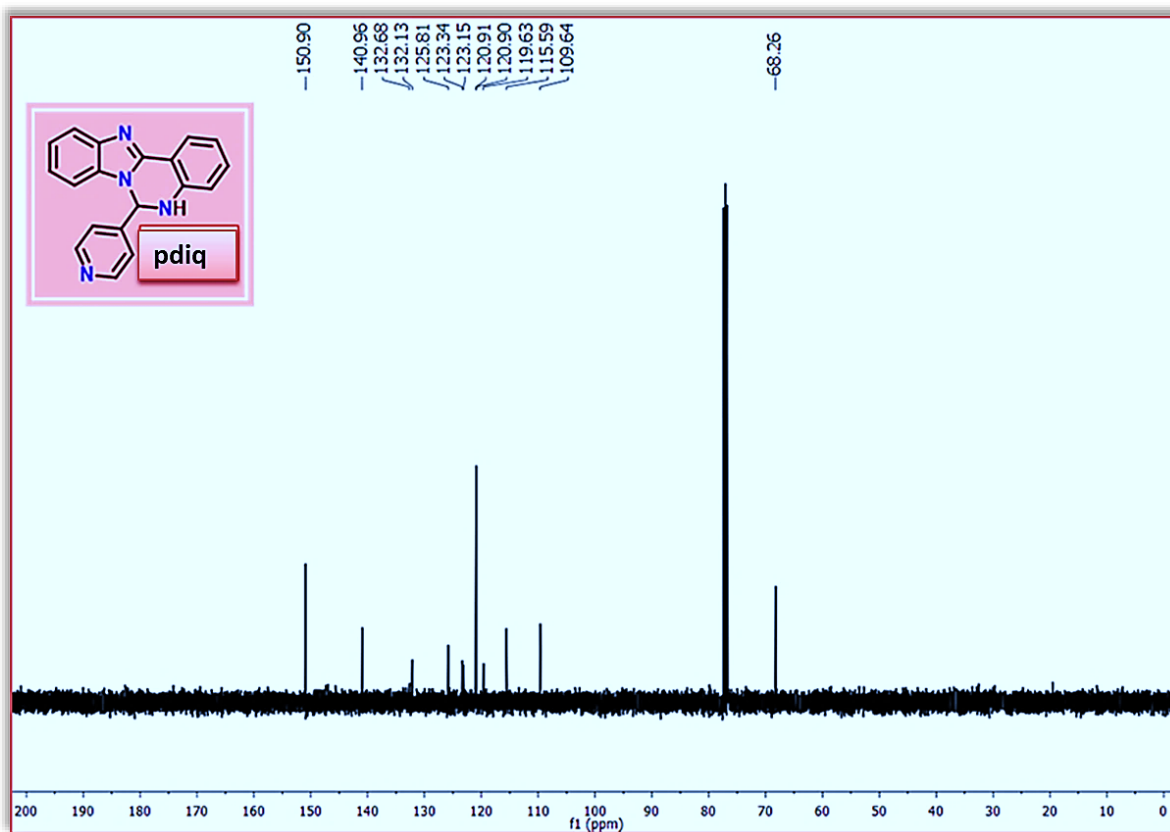
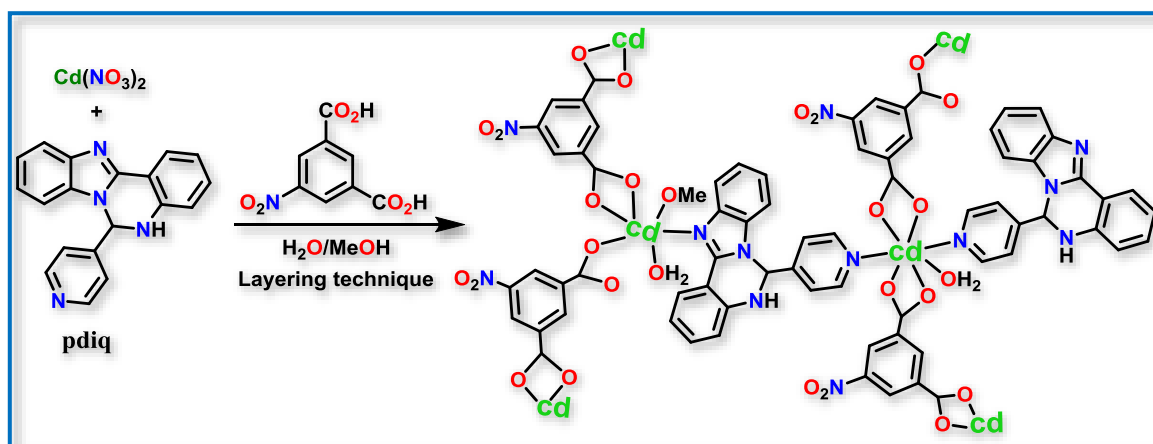


Figure 3.3 ^{13}C -NMR spectroscopy of **pdiq**.

3.2.3 Synthesis of $[\text{Cd}_2(5\text{-nip})_2(\text{pdiq})_2(\text{H}_2\text{O})_2(\text{CH}_3\text{OH})]\cdot\text{H}_2\text{O}$ (CP 1)

A solution of **pdiq** (59.6 mg, 0.2 mmol) in MeOH (2 mL) was slowly and carefully layered into a solution of $\text{Cd}(\text{NO}_3)_2\cdot 4\text{H}_2\text{O}$ (61.7 mg, 0.2 mmol) in H_2O (2 mL) using a buffer solution of MeOH and H_2O (2 mL of a 1:1 (v/v)). It was then layered with a solution of 5-nitroisophthalic acid (42 mg, 0.2 mmol), neutralized with Et_3N (21 mg, 0.2 mmol) in 2 mL of EtOH. It was then allowed to diffuse for a few days. The yellow-colored block-shaped crystals of $[\text{Cd}_2(5\text{-nip})_2(\text{pdiq})_2(\text{H}_2\text{O})_2(\text{CH}_3\text{OH})]\cdot\text{H}_2\text{O}$ (CP 1) (Scheme 3.2) were obtained after five days (164 mg, yield 62%). For $\text{C}_{55}\text{H}_{42}\text{Cd}_2\text{N}_{10}\text{O}_{16}$, the elements calculated (%) were C 49.90, H 3.20, N 10.58; the elements found were C 49.87, H 3.17, N 10.61.



Scheme 3.2 Synthesis of $[\text{Cd}_2(5\text{-nip})_2(\text{pdiq})_2(\text{H}_2\text{O})_2(\text{CH}_3\text{OH})]\cdot\text{H}_2\text{O}$ (CP 1).

3.2.4 General X-ray Crystallography

The single crystal of CP **1** was collected from the mother liquid and transferred to oil and further mounted for measuring the single-crystal X-ray data. The diffraction was estimated with a Bruker SMART APEX II diffractometer attached to a graphite monochromatic Mo K α radiation source ($\lambda = 0.71073 \text{ \AA}$) at 293 K. The crystal-orientation matrices and unit cell parameters were estimated from the least-square refinements of all reflections, and the hkl values were in the range of $-14 \leq h \leq 14$, $-16 \leq k \leq 16$, and $-20 \leq l \leq 20$. The collected data ($I > 2\sigma(I)$) were integrated using the SAINT program,⁴⁶ and the absorption correction was carried out by SADABS.⁴⁷ Using SHELX-97,⁴⁸ the molecular structure of the single crystal of CP **1** was determined. Anisotropic thermal parameters were used for the refinement of non-hydrogen atoms of the compound. There was an exact geometric alignment of the hydrogen atoms, and each hydrogen atom was constrained to ride on its parent atom. Crystallographic data of CP **1** are given in **Tables 3.1** and **3.2**, including the bond lengths and angles. The CCDC number for CP **1** is **2114983**.

Table 3.1 Crystal data and refinement parameters for CP **1**.

Formula	$\text{C}_{55}\text{H}_{42}\text{Cd}_2\text{N}_{10}\text{O}_{16}$
CCDC	2114983
Formula weight	1323.81
Crystal system	Triclinic
space group	$P-1$
a (Å)	12.304 (1)
b (Å)	13.8559 (11)
c (Å)	17.3618 (13)

α (deg)	100.869 (2)
β (deg)	102.572 (2)
γ (deg)	106.520 (2)
V (Å ³)	2668.6 (4)
Z	2
D_{calcd} (g/cm ³)	1.648
μ (mm ⁻¹)	0.879
λ (Å)	0.71073
data[$I > 2\sigma(I)$]/params	8760/769
GOF on F^2	1.073
Final R indices[$I > 2\sigma(I)$] ^{a,b}	$RI = 0.0399$ $wR2 = 0.0985$

$$^a R1 = \Sigma ||F_o| - |F_c|| / \Sigma |F_o|, \quad ^b wR2 = [\Sigma w(F_o^2 - F_c^2)^2 / \Sigma w(F_o^2)^2]^{1/2}$$

Table 3.2 Selected bond lengths and bond angles in CP 1.

Bond length	(Å)	Bond Angles	(°)
Cd(1) - O(12)	2.312(5)	O(10) - Cd(2) - N(5)	87.36(12)
Cd(1) - O(7_b)	2.389(4)	N(4) - Cd(2) - N(5)	176.66(13)
Cd(2) - O(11)	2.288(4)	Cd(2) - O(10) - C(20)	94.9(3)
Cd(2) - O(4_a)	2.418(3)	O(14) - Cd(1) - N(6)	118.51(13)
Cd(1) - O(14)	2.200(3)	O(9) - Cd(2) - O(10)	54.08(11)
Cd(1) - O(8_b)	2.360(3)	O(12) - Cd(1) - O(14)	88.10(17)
Cd(2) - N(4)	2.342(4)	O(9) - Cd(2) - O(11)	89.24(14)
Cd(1) - N(6)	2.289(4)	O(10) - Cd(2) - O(11)	142.85(15)
Cd(2) - O(10)	2.344(3)	O(12) - Cd(1) - N(6)	85.10(16)
Cd(2) - O(3_a)	2.485(4)	O(12) - Cd(1) - O(8_b)	87.73(16)
		C(27) - O(7) - Cd(1_c)	91.0(3)
		O(14) - Cd(1) - C(27_b)	107.11(15)
		O(12) - Cd(1) - O(7_b)	111.87(16)
		O(7_b) - Cd(1) - C(27_b)	27.39(14)
		N(4) - Cd(2) - O(3_a)	90.30(12)
		N(5) - Cd(2) - O(3_a)	89.96(12)
		O(14) - Cd(1) - O(8_b)	131.64(13)
		O(15) - Cd(1) - C(27_b)	92.01(14)

Symmetry Code: a = -1+x, y, z; b = 1+x, y, z; c = -x, 2-y, 2-z; d = 1-x, 2-y, 2-z.

3.2.5 Theoretical Calculations

The optimized geometry of CP **1** was established using density functional theory (DFT) with the GAUSSIAN-09 program package.⁴⁹ The DFT-B3LYP⁵⁰ hybrid theoretical functional was employed throughout the calculations. For all of the elements, the LanL2DZ basis set was employed. The X-ray coordinates of CP **1** were used in the computation process. The time-dependent density functional theory (TDDFT)⁵¹⁻⁵³ was used to illustrate all of the distinct low-lying electronic transitions in the spectra. For the purpose of analyzing the fractional entanglement of the different individual components in the polymeric compound to each molecular orbital, the Gauss sum⁵⁴ technique was used in the last step of the theoretical calculations.

3.2.6 Device Fabrication

To perform the electrical analysis of our synthesized material we have developed multiple metal-semiconductor (MS) junction devices with the sandwich-like configuration of ITO/CP **1**/Al (Figure 3.4). To fabricate the MS junction devices, thin film of as-synthesized CP **1** was grown on pre-cleaned ITO coated glass substrate by doctors blade method. Here we used aluminium, deposited on a plain glass slide in the Vacuum Coating Unit under pressure 10^{-6} Torr as metal electrode.

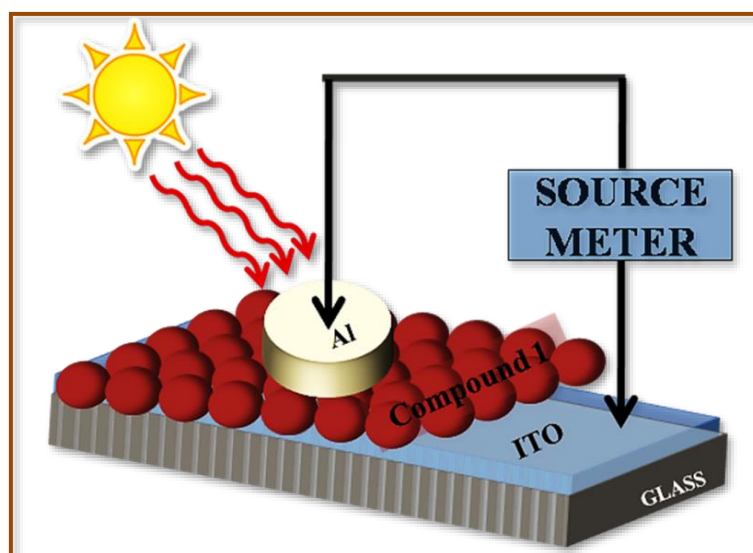


Figure 3.4 Schematic representation of device fabrication.

Using Sourcemeter made by Keithley (model no: 2635B) and adopting two-probe technique, the current-voltage (I - V) characteristics of the devices was measured to analyze the electrical properties. All the device fabrication and measurements were carried out at room temperature and under ambient conditions.

3.3 Results and Discussion

3.3.1 Structure of $[\text{Cd}_2(\text{5-nip})_2(\text{pdiq})_2(\text{H}_2\text{O})_2(\text{CH}_3\text{OH})]\cdot\text{H}_2\text{O}$ (CP 1)

The CP 1 is crystallized in a triclinic crystal system of space group $P-1$. The asymmetric unit is constituted of two metal centers (Cd1 and Cd2); the coordination atmosphere around these nodes is quite different (Figure 3.5a). Cd1 is hexacoordinated, CdO_5N unit, having a distorted octahedral geometry with five oxygen atoms (three oxygen atoms from dicarboxylic acid and two oxygen atoms from solvent molecules, H_2O and CH_3OH) and N-coordination from the pyridinyl-N group (Cd1-N6, 2.289(4) Å) of the adjacent motif. In this unit, one 5-nip is chelated to Cd(II) (Cd1-O7 = 2.389(4), Cd1-O8 = 2.360(3) Å) and another 5-nip is monocoordinated (Cd1-O14 = 2.200(3) Å); on the other hand, one water molecule (Cd1-O12 = 2.312(5) Å), one methanol (Cd1-O15 = 2.349(4) Å), and one pyridinyl-N of pdiq are appended with the Cd1 metal node. Again, Cd2 lies in the center of a hepta-coordination distorted pentagonal bipyramid CdO_5N_2 unit, having a distorted pentagon with five oxygen atoms (four oxygen atoms joined from chelated dicarboxylate, Cd2-O3 = 2.485(4), Cd2-O4 = 2.418(3), Cd2-O9 = 2.470(3), Cd2-O10 = 2.344(3) Å) and one oxygen from H_2O (Cd2-O11 = 2.288(4) Å) and two axial nitrogen coordination from pyridinyl-N (Cd2-N4 = 2.342(4), Cd2-N5 = 2.319(4) Å).

Both 5-nip and pdiq serve as bridging motifs, and each of them propagates to constitute a 1D structure and simultaneously the 2D network (Figure 3.5b). Two adjacent Cd centers, Cd1 and Cd2, are separated by 10.007 Å when bridged through 5-nip, and pdiq separates the two metal centers by 10.491 Å.

A number of hydrogen bonds and $\pi\cdots\pi$ interactions are there in the molecular assembly to constitute 3D supramolecular arrangement. The potential hydrogen bonds are N3-H3 \cdots O3 = 2.16, N7-H7 \cdots N2 = 2.32, O00F-H100 \cdots O4 = 2.10, O00F-H101 \cdots O8 = 2.13, O11-H102 \cdots O9 = 1.93, and O11-H103 \cdots O00F = 1.97 Å. The extensive $\pi\cdots\pi$ interactions are observed between Cg8 (C14-C15-C16-C17-C18-C19) and Cg9 (C21-C22-C23-C24-C25-C26), corresponding to a distance of 3.791 Å; similarly, the interaction distance of Cg1 (N1-C7-N2-C14-C19) and Cg9 (C21-C22-C23-C24-C25-C26) is 3.742 Å (Figure 3.5c). The C-H $\cdots\pi$ interactions (C028-H02B \cdots Cg7 (C8-C9-C10-C11-C12-C13) = 2.81 Å and C44-H44 \cdots Cg6 (N5-C29-C30-C31-C32-C33)) are employed for the fabrication of extended supramolecular aggregates (Figure 3.5d).

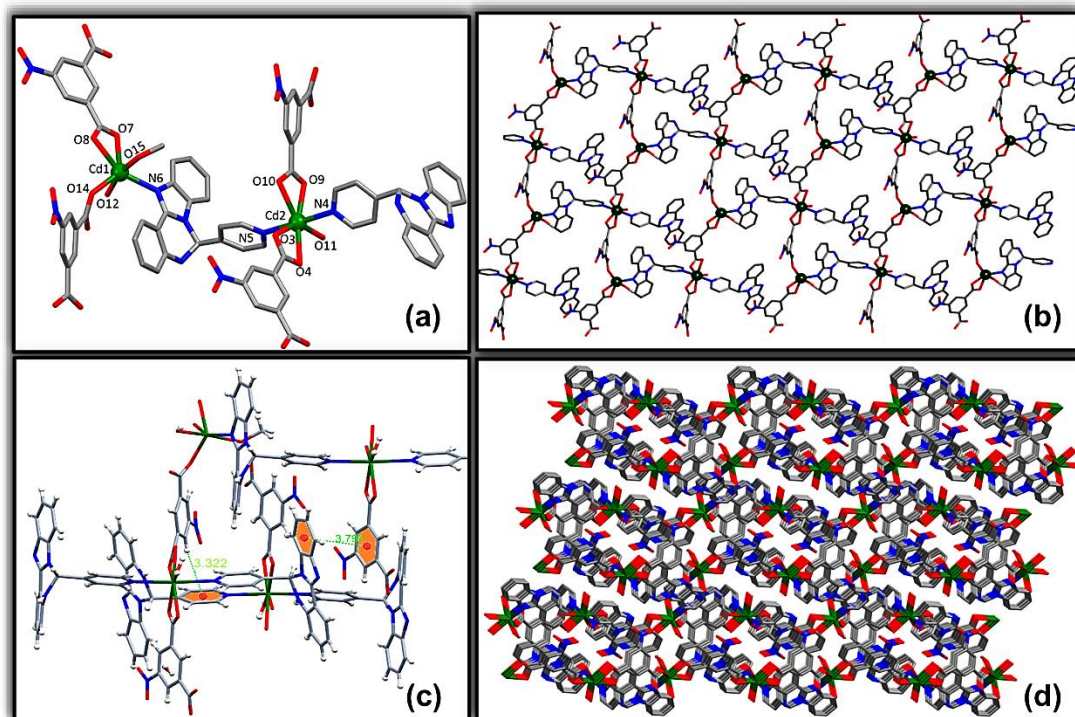


Figure 3.5 (a) Perspective view of the repeating dimeric unit of CP **1** showing different coordination arrangements around the metal centers. (b) View of 2D net constructed through 5-nip and **pdiq**. (c) $\pi\cdots\pi$ and $\text{C-H}\cdots\pi$ interactions play a pivotal role in forming a network. (d) Extended 3D supramolecular aggregate of CP **1** along the b-axis.

3.3.2 PXRD and TGA Analysis

To determine the phase purity of the bulk material, CP **1**, powder X-ray diffraction (PXRD) analysis was performed at room temperature. The PXRD pattern of the as-synthesized crystalline powder CP **1** was in good agreement with the simulated one from the single-crystal data, indicating the high range of phase purity and consistency of the bulk material (**Figure 3.6**). Thermogravimetric analysis (TGA) was measured to verify the thermal stability of CP **1**, temperatures within the range of 30–800 °C in a N_2 atmosphere. A weight loss of 1.23% was observed in the temperature range of 95–105 °C, mainly due to the loss of one noncoordinated water molecule. According to TGA analysis, CP **1** is stable up to 305 °C (**Figure 3.7**). Considering its wide range of thermal stability, the compound can be of benefit in material applications.

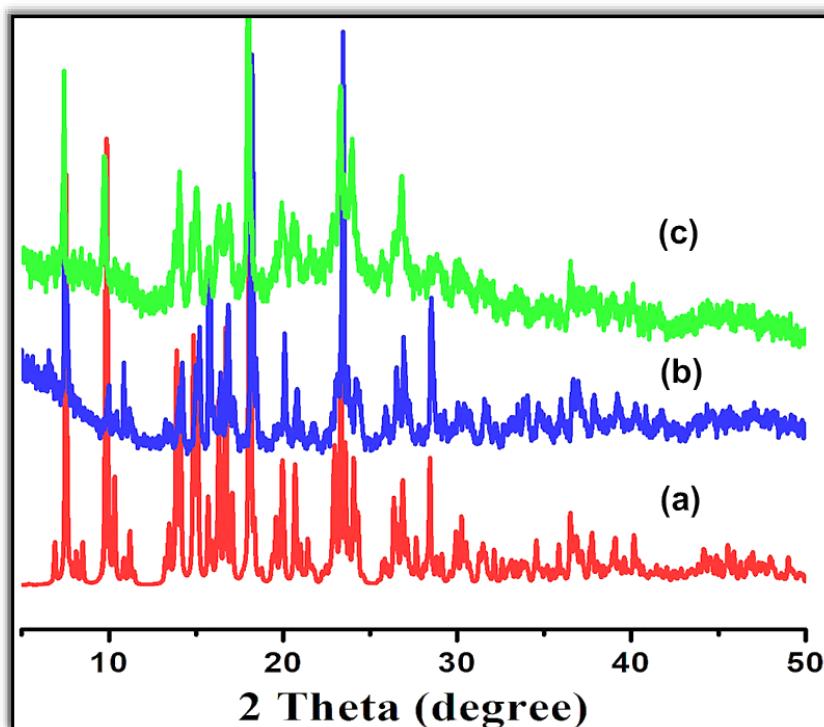


Figure 3.6 PXRD patterns of (a) simulated from the X-ray single structure of CP 1 (red), (b) as-synthesized CP 1 (blue) and (c) CP 1 after the prolonged immersed in lower pH solution (pH = 4) (green).

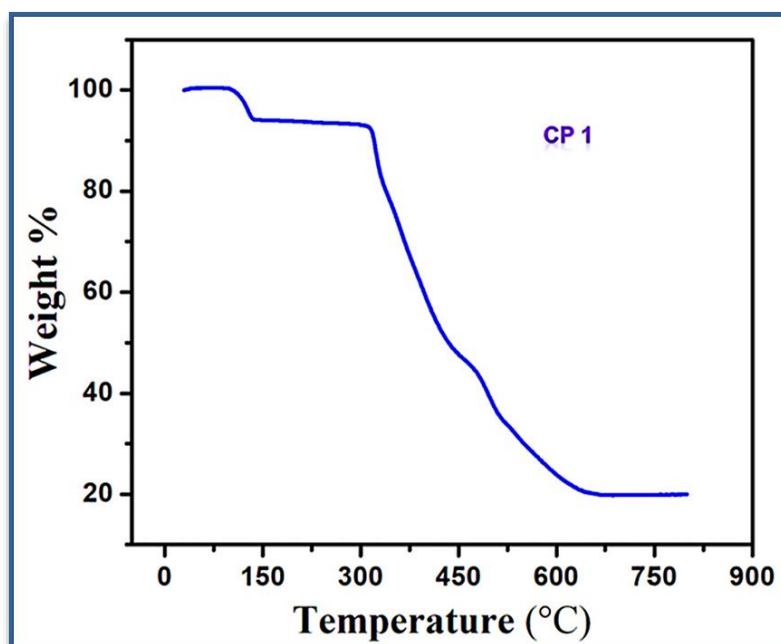


Figure 3.7 TGA plot of CP 1.

3.3.3 Sensing Property towards NAEs

As shown in **Figure 3.8a**, CP 1 dispersed in acetonitrile has an absorption band at 350 nm, while the ligands pdiq and 5-nip show absorption at 347 and 250 nm, respectively. Upon

excitation at 380 nm in the dispersion phase (acetonitrile), CP **1** shows a strong blue emission at 416 nm and a calculated quantum yield (ϕ_f) of 0.0024 at room temperature. Free ligands **pdiq** and 5-nip are weakly emissive under identical conditions in acetonitrile. The strong fluorescence intensity may be attributed to the enhancement of rigidity and the π -conjugacy of the ligand, pyridyl-imidazoquinazoline, upon coordination to Cd^{2+} . To investigate the fluorescence sensing ability of various NAEs, such as 2,4,6-trinitrophenol (TNP) or picric acid (PA), 2,4-dinitrophenol (2,4-DNP), 2-nitrophenol (2-NP), 1,4-dinitrobenzene (1,4-DNB), 4-nitrophenol (4-NP), 1,3-dinitrobenzene (1,3-DNB), 2,4-dinitrotoluene (2,4-DNT), nitrobenzene (NB), 3-nitrobenzoic acid (3-NBA), 5-nitrosalicylic acid (5-NSA), 3,5-dinitrobenzoic acid (3,5-DNBA), 5-nitroacetanilide, and 2-nitrotoluene (2-NT), they were injected to the well-dispersed suspension of CP **1** in acetonitrile medium. Different extents of fluorescence quenching were observed upon addition of an equal amount of nitroaromatic analytes (38.1 μM) to the suspension of CP **1** (10 μM), and the quenching efficiency follows the order $\text{TNP(PA)} > 2,4\text{-DNP} > 1,3\text{-DNB} > 5\text{-NSA} > 5\text{-nitroacetanilide} > 2\text{-NP} > 4\text{-NP} > 1,4\text{-DNB} > \text{NB} > 3,5\text{-DNBA} > 3\text{-NBA} > 2,4\text{-DNT} > 2\text{-NT}$. The highest quenching (99.2%) of initial emission of CP **1** toward TNP makes it much more selective than any other NAEs (Figure 3.8b), with a quantum yield of $\phi_f = 0.36$. and a limit of detection ($3\sigma/k$ method) of 0.27 μM . Upon light absorption of TNP in acetonitrile suspension of CP **1** at 380 nm shows a drastic quenching of emission and is red-shifted by 64 nm (λ_{em} , 480 nm) (Figure 3.9a) compared to other NAEs. The quenching may be explained via the combination of fluorescence resonance energy transfer (FRET) (Figure 3.9b) and photoinduced electron transfer (PET) between the analyte (TNP) and CP **1**.⁵⁵

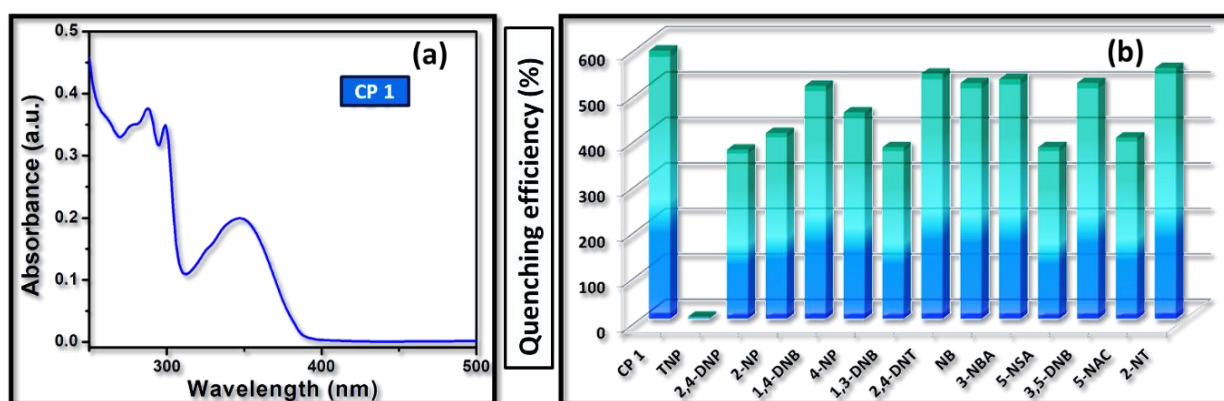


Figure 3.8 (a) UV-Visible spectrum of CP **1** in acetonitrile. (b) Quenching efficiency of epNACs toward the emission of CP **1**.

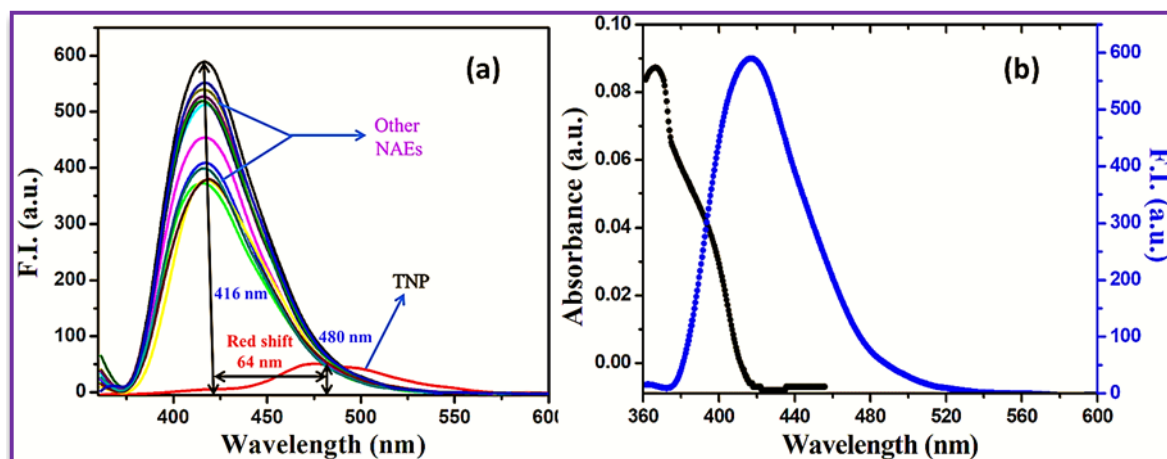


Figure 3.9 (a) Emission spectra of CP **1** dispersed in ACN medium in presence of different NAEs. (b) Overlapping of absorption spectra of TNP with emission spectra of CP **1**.

To further interpret the sensing ability of CP **1** toward TNP, the fluorescence titration experiments were performed by the gradual addition of a TNP solution into a suspension of acetonitrile (**Figure 3.10a**). The emission intensity gradually decreases, and a 99.2% quenching of initial emission was observed when the concentration of TNP was increased to $38.1 \mu\text{M}$ and a limit of detection ($3\sigma/k$ method) of $0.27 \mu\text{M}$ was also observed (**Figure 3.10b**). Relative quenching curves were quantitatively studied using the Stern-Volmer equation (S-V plot): $(I_0/I) = 1 + K_{\text{SV}} \times [\text{TNP}]$, where I_0 and I indicate the fluorescence intensity of CP **1** in the absence and presence of TNP, respectively, $[\text{TNP}]$ represents the molar concentration of TNP, and K_{SV} ($1.4 \times 10^5 \text{ M}^{-1}$, **Figure 3.10c**) is the Stern-Volmer quenching constant. The Stern-Volmer plot exhibits an upward curvature (**Figure 3.10d**),⁵⁶ which suggests the concurrence of static and dynamic quenching with TNP, and the extent of quenching is high at a higher concentration of TNP. The K_{SV} value was calculated from the linear portion of the S-V plot (**Figure 3.10c**) at a lower concentration of TNP and it is found to be the highest value reported^{32,38,44,55,57-60} so far for MOF-based sensor materials.

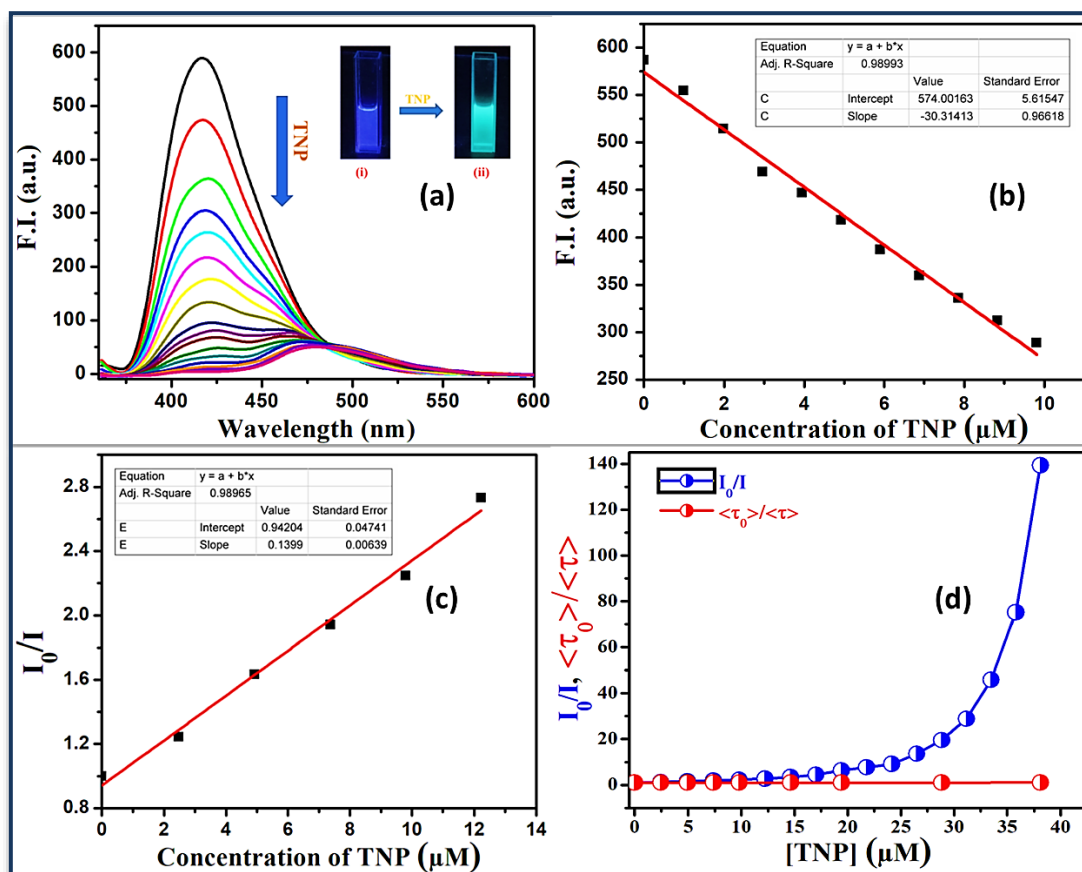


Figure 3.10 (a) Emission spectra of CP **1** (10 μM) dispersed in acetonitrile upon the incremental addition of TNP solution (0–38.1 μM). Inset: photographs of fluorescence cuvettes containing acetonitrile suspensions of the compound under UV light ($\lambda = 365\text{ nm}$) before TNP addition (i) and UV light after TNP addition (ii). (b) The linear dynamic response of CP **1** for TNP and the determination of the limit of detection (LOD) of TNP. (c) Stern-Volmer plot of CP **1** at lower range of quencher [TNP] (in μM) concentration. (d) Steady-state (I_0/I , blue) and time-resolved ($\langle\tau_0\rangle/\langle\tau\rangle$, red) Stern-Volmer plots.

To establish the quenching mechanism prevailing in this system, the fluorescence lifetime decay of CP **1** was performed with the gradual addition of TNP (Figure 3.11). The lifetime plot (Figure 3.10d; Table 3.3) clearly exhibits that the excited species (CP **1**^{*}) is preformed and does not perturb with the incremental addition of TNP. To support the fluorescence quenching, the MOs of CP **1** and TNP were computed using optimized geometries. The relative orbital energies of the HOMO (−5.79 eV for CP **1**; −8.80 eV for TNP) and lowest unoccupied molecular orbital (LUMO) (−3.63 eV for CP **1**; −4.85 eV for TNP) were calculated. The energy difference in the highest occupied molecular orbital (HOMO) of CP **1** and TNP was much larger (3.01 eV) than that for LUMOs (1.22 eV). Hence, the energy transfer is accessible from the excited state of CP **1** to the ground state of TNP (Figure 3.12).⁶¹ The fluorescence intensity of CP **1** remains unaltered even in an acidic medium (pH =

2-7), (Figure 3.13) which induces structural endurance in acidic conditions. The PXRD of material obtained after immersion in a low pH solution (3.5-5.5) for 4 h gives a pattern similar to the as-synthesized compound (Figure 3.5). Therefore, during TNP sensing, the structural architecture of the framework remains unchanged.

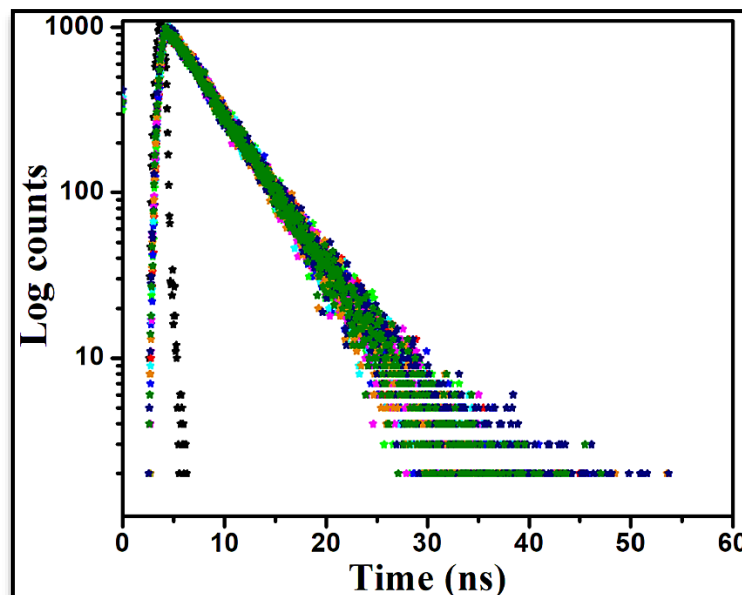


Figure 3.11 Representative fluorescence decay spectra of CP **1** (10 μM) in the absence and presence of increasing concentration of TNP. Spectra 1-9 corresponds to the TNP concentration 0 μM (red circle), 2.47 μM (green star), 4.93 μM (blue star), 7.37 μM (cyan blue star), 9.80 μM (pink star), 14.63 μM (orange star), 19.42 μM (wine star), 28.85 μM (navy star), 38.10 μM (olive star), respectively.

Table 3.3 Fluorescence lifetime decay parameters of CP **1** (10 μM) with gradual addition of TNP.

TNP (μM)	τ (ns)	CHISQ
0	4.67	1.116974
2.47	4.58	1.084677
4.93	4.55	1.056476
7.37	4.57	0.9527653
9.80	4.58	1.018855
14.63	4.54	1.056809
19.42	4.60	1.095134
28.85	4.58	1.086315
38.10	4.50	1.037778

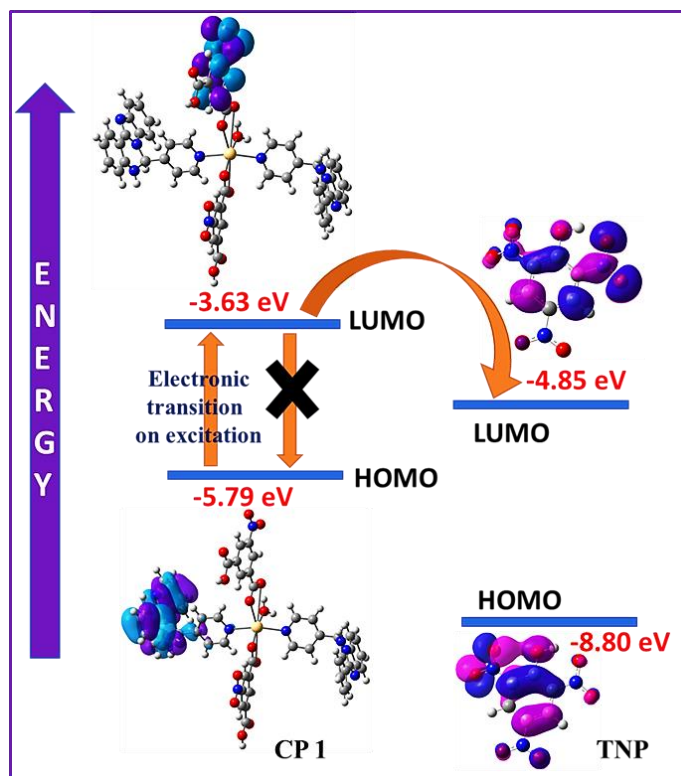


Figure 3.12 Possibility of energy transfer between the excited state of CP 1 (CP 1*) and TNP.

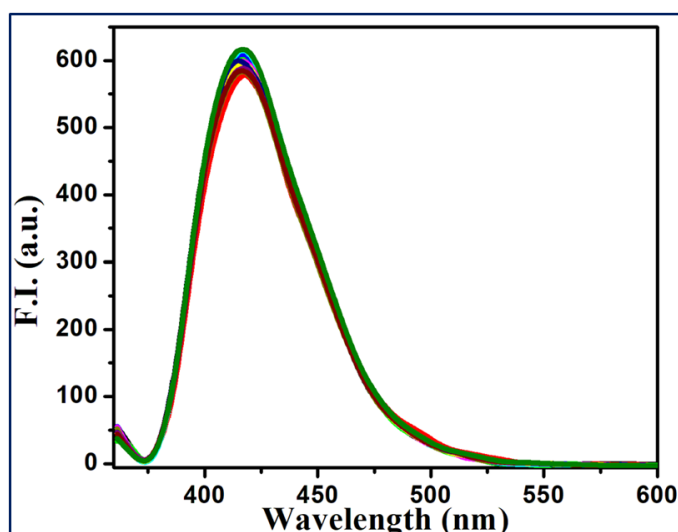


Figure 3.13 Emission spectra of CP 1 in presence of different PH solutions.

3.3.4 Optical Characterization

The absorbance property of synthesized CP 1 has been studied by UV-Vis spectroscopy (Inset of [Figure 3.14](#)). The spectrum has been analysed within 300-700 nm. Employing [eq 1](#) (Tauc equation), estimation of optical band gap was done ([Figure 3.14](#)):⁶²

$$(\alpha h\nu)^2 = A(h\nu - E_g) \dots \dots \dots (1)$$

where, α , E_g , h , and ν have their typical notation. In this equation, there is an electron transition dependent constant ' n ' and another constant ' A ' which has value 1 for the ideal case. The band gaps (Optical) (E_g) for direct transition have been estimated as 3.2 eV for our synthesized CP 1. The optical band gap may suggest the semiconducting behavior of the compound.

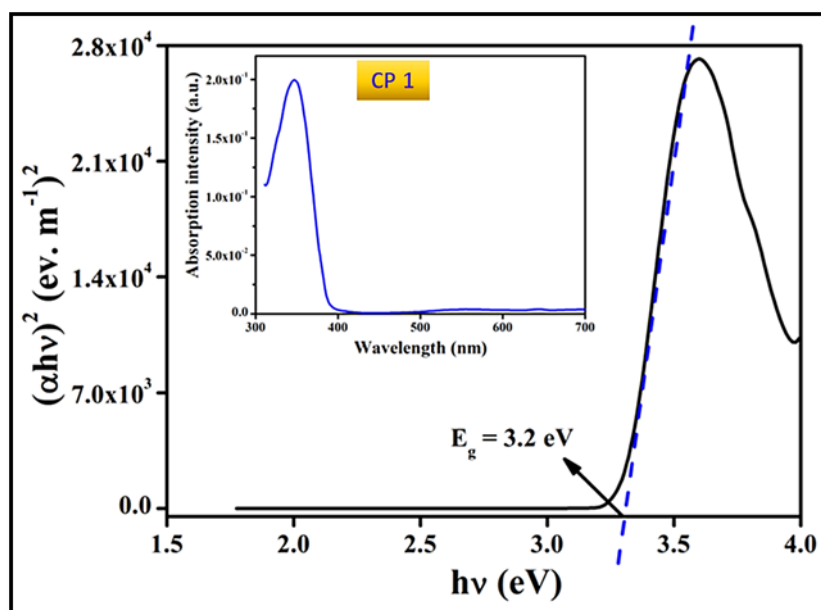


Figure 3.14 Tauc's plots for CP 1 and (inset) UV-Vis absorption spectra.

3.3.5 Electrical Properties of a Schottky Device

Metal-semiconductor (MS) junction thin-film device of CP 1 has been fabricated⁶³, and the I - V plot, with and without irradiation, is presented in **Figure 3.15**. Under the dark condition, the electrical conductivity was $1.12 \times 10^{-3} \text{ S m}^{-1}$, and upon illumination (AM 1.5G photoirradiation), the conductivity increased to $6.33 \times 10^{-3} \text{ S m}^{-1}$. This enhancement of conductivity upon irradiation condition may be due to the easy transport of charge through the band conduction mechanism and the lowering of the energy barrier of the compound.⁶⁴ The conductivity depends on the illuminated light density and wavelength. To investigate the photoconductivity of our device, we tested it under light sources with different wavelengths. Specifically, we used a UV light source with a wavelength of 310 nm and a visible light source with a wavelength of 700 nm. Under 310 nm illumination, the conductivity was measured to be $2.81 \times 10^{-3} \text{ S m}^{-1}$, while under 700 nm illumination, the conductivity increased to $6.33 \times 10^{-3} \text{ S m}^{-1}$. All measurements were carried out under identical experimental conditions. These results indicate that the conductivity under 700 nm light is

nearly twice as high as that under 310 nm light. The I - V curves for both conditions are presented in Figure 3.16a.

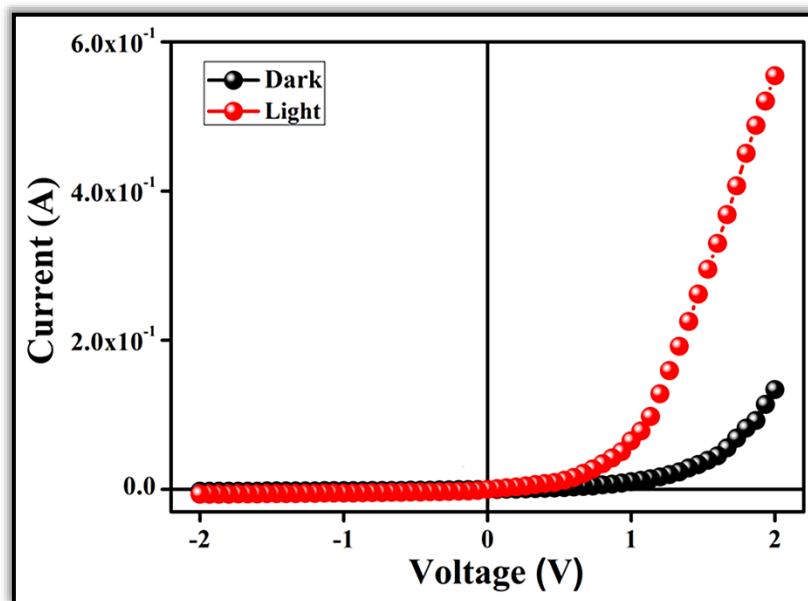


Figure 3.15 I - V characteristic curve under dark and photoillumination conditions.

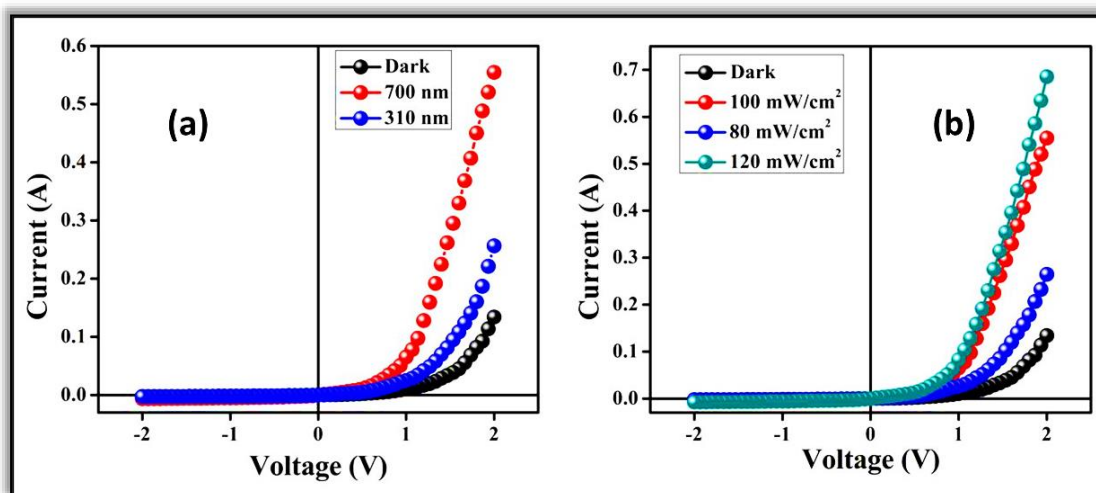


Figure 3.16 I - V characteristic curves recorded under varying illumination conditions: (a) using light sources of different wavelengths, and (b) under varying light intensities.

To gain deeper insight into the photoconductive response, additional measurements were carried out under varying light intensities of 80, 100 (AM1.5G standard), and 120 mW/cm^2 , with all intensities precisely calibrated using photodiodes at the measurement point. The device exhibited conductivities of 2.81×10^{-3} , 7.64×10^{-3} , and $6.33 \times 10^{-3} \text{ S m}^{-1}$, respectively (Figure 3.16b). The results demonstrate a clear correlation between light intensity and conductivity, which can be attributed to the increased generation of photo-induced charge carriers at higher illumination levels. However, further increase in intensity

beyond 120 mW/cm² was avoided, as excessive irradiance can lead to thermal instability in the material due to heat accumulation.

The *I-V* graphs of the fabricated thin-film MS device show nonlinear rectifying characteristics, which are typical for the Schottky barrier diode (SBD). Under dark conditions, the SBD's rectification ratio (I_{on}/I_{off}) at ± 2 V was 55.15, and upon light irradiation, it increased to 86.95. An irradiated condition produces a larger current, demonstrating the photosensitivity by a factor ~ 4 for the device. The *I-V* characteristics of the MS device have been further analyzed with the help of thermionic emission theory. Hence, Cheung's model has been used to evaluate the device parameters.^{62,65-67}

$$I = I_0 \exp\left(\frac{qV}{\eta kT}\right) \left[1 - \exp\left(\frac{-qV}{\eta kT}\right)\right] \dots \dots \dots (2)$$

$$I_0 = AA^*T^2 \exp\left(\frac{-q\phi_B}{kT}\right) \dots \dots \dots (3)$$

where I_0 , k , T , V , A , η and A^* stands for saturation current, electronic charge, Boltzmann constant, temperature in Kelvin, forward bias voltage, effective diode area, ideality factor and effective Richardson constant, respectively. The effective Richardson constant was considered as 32 AK⁻² cm⁻² for the fabricated devices.

The series resistance, ideality factor and barrier potential height was also determined by using eqs 4 to 6, which was extracted from Cheung's idea,^{65,66}

$$\frac{dV}{d(\ln I)} = \left(\frac{\eta kT}{q}\right) + IR_S \dots \dots \dots (4)$$

$$H(I) = V - \left(\frac{\eta kT}{q}\right) \ln\left(\frac{I}{AA^*T^2}\right) \dots \dots \dots (5)$$

$$H(I) = IR_S + \eta \phi_B \dots \dots \dots (6)$$

The plot of $dV/d\ln I$ vs I (Figure 3.17a) calculates the ideality factor (η) 2.89 without illumination and 2.12 with illumination (Table 3.4). The deviation of η from the ideal value, 1, can be attributed to the presence of inhomogeneities and the occurrence of interface defect states and/or series resistance at the junction of Schottky.^{68,69} Thus, the recombination of fewer amounts of charge carriers at the interface may improve the homogeneity in the light irradiation condition than in the dark condition.⁶⁵ The energy barrier, Φ_B , is calculated from the intercept of the $H(I)$ vs I plot (Figure 3.17b). Upon light irradiation, Φ_B decreases, and the slope gives the series resistance (R_s) of the device (Table 3.4). The decrease in R_s for the device under light irradiation designates their potential application in optoelectronic devices. The $\log I$ vs $\log V$ plot (Figure 3.17c) helps to explain the transport mechanism at the Schottky junction; it shows two different regions (regions I and II) with different slopes for

the devices under the dark and light phases. The slope close to 1 in region I indicates $V \propto I$ (ohmic regime), whereas region II has a slope close to 2, which indicates a regime dominated by space charge limited current (SCLC).^{62,70} In region II, the number of background electrons is higher than the electrons in region I, and the interjected electrons are distributed in the total region, giving rise to a field dominated by space charge. Hence, the current in this region (region II) is supervised by the SCLC.^{62,70} The effective carrier mobility (μ_{eff}) can be computed utilizing the Mott-Gurney equation (eq 7) in the SCLC model with the high voltage data of the I vs V^2 plot (Figure 3.17d).^{62,67,70}

$$I = \frac{9\mu_{eff}\epsilon_0\epsilon_r A}{8} \left(\frac{V^2}{d^3} \right) \dots \dots \dots (7)$$

where, I , μ_{eff} , ϵ_r , and ϵ_0 are the current, the effective mobility, the relative dielectric constant and the free space permittivity of the material, respectively.

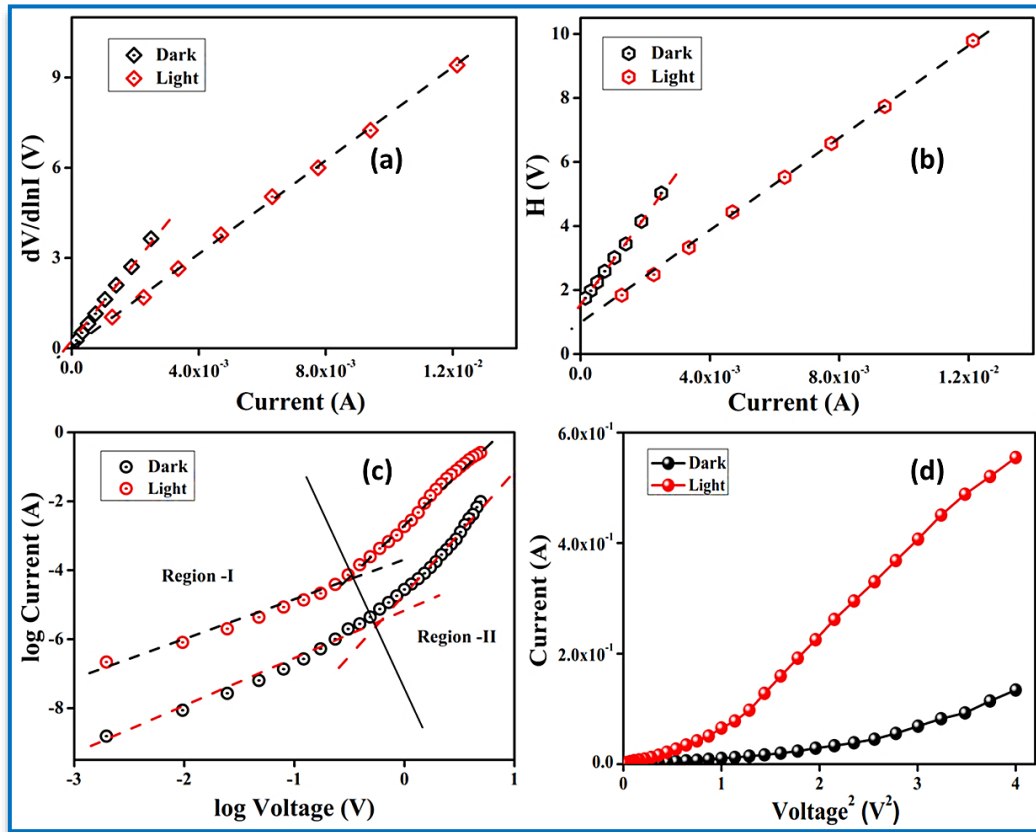


Figure 3.17 (a) $dV/d\ln I$ vs I curve with and without illumination. (b) H vs I curves with and without illumination. (c) $\log I$ vs $\log V$ curves with and without illumination. (d) I vs V^2 curves with and without illumination.

The relative dielectric constant of the material (ϵ_r) can be calculated from the saturation region of the capacitance vs frequency (in log scale) curve at higher frequency with the equation given below:⁶²

$$\varepsilon_r = \frac{1}{\varepsilon_0} \cdot \frac{C d}{A} \dots\dots\dots(8)$$

where, C , d , and A are the capacitance at saturation, the thickness of the film ($\sim 1 \mu\text{m}$) and the device area, respectively. With this formula, we obtain ε_r values of 6.02×10^{-2} for our synthesized CP 1 (Figure 3.18).

To study the charge transport behaviour through the junction, the transit time (τ) and diffusion length (L_D) are determined using eq 9 from the slope of the I vs V plot in the SCLC region (region II).⁶⁷

$$\tau = \frac{9\varepsilon_0\varepsilon_r A}{8d} \left(\frac{V}{I} \right) \dots\dots\dots(9)$$

$$\mu_{eff} = \frac{qD}{kT} \dots\dots\dots(10)$$

$$L_D = \sqrt{2D\tau} \dots\dots\dots(11)$$

where, D stands for diffusion coefficient that can be determined using Einstein-Smoluchowski equation (eq 10).

Table 3.4. Schottky device parameters of CP 1 based SBD.

Condition	On/Off Ratio	Conductivity (S.m ⁻¹)	Photosensitivity	Ideality factor	Barrier height (eV)	R_s From $dV/d\ln I$ (Ω)	R_s from H (Ω)
Dark	55.15	1.12×10^{-3}	4.13	2.89	0.53	1428.68	1392.91
Light	86.95	6.33×10^{-3}		2.12	0.42	771.45	733.05

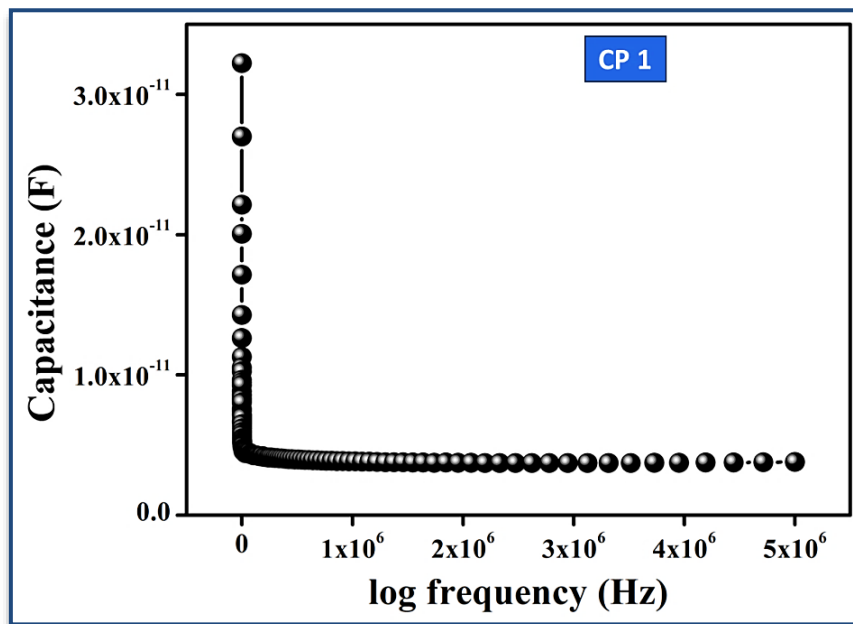


Figure 3.18 Capacitance vs frequency graph for the determination of the dielectric constant.

Table 3.5 Charge-conducting parameters of the CP **1**-based thin-film device.

Condition	ϵ_r	μ_{eff} ($\text{m}^2\text{V}^{-1}\text{s}^{-1}$)	τ (sec)	$\mu_{eff}\tau$ (m^2V^{-1})	D	L_D (m)
Dark	6.02×10^{-2}	12.06×10^{-3}	2.46×10^{-11}	2.97×10^{-13}	3.11×10^{-4}	1.24×10^{-7}
Light		38.64×10^{-3}	8.69×10^{-12}	3.35×10^{-13}	9.96×10^{-4}	1.32×10^{-7}

Using the diffusion length of the charge carriers (L_D), the device performance is measured. A complete analysis of the parameters assessed in the SCLC region demonstrates that the charge transport properties of the material are enhanced upon irradiation with light (Table 3.5). The diode parameters of the fabricated thin-film device demonstrate much-enhanced charge transfer kinetics after light irradiation. As a consequence, such materials could have a bright future in gadget development.

3.4 Conclusion

Pyridinyl-imidazoquinazoline-coordinated highly luminescent 2D Cd(II)-MOF, $\{[\text{Cd}_2(5\text{-nip})_2(\text{pd}i\text{q})_2(\text{H}_2\text{O})_2(\text{CH}_3\text{OH})] \cdot \text{H}_2\text{O}\}_n$ (CP **1**), has been structurally characterized. Due to its high fluorogenic nature, this compound has been utilized for the selective detection of 2,4,6-trinitrophenol (TNP) out of 13 electron-deficient NAEs, and the detection limit is as low as $0.27 \mu\text{M}$, which is in good agreement with reported Cd-MOF sensors in acidic pH (3.5-5.5) medium. Both the theoretical and experimental findings are in favor of the energy transfer mechanism (FRET and PET) for the quenching process. The dynamic quenching at a higher analyte concentration (due to upward curvature) is noted. The improved electrical conductivity of 2D Cd(II)-MOF during light irradiation in the semiconductor area as confirmed by the experimental band gap (3.2 eV) and higher mobility in the network could be attributed to its lower barrier height and series resistance.

3.5 References

- (1) Tranchemontagne, D. J.; Mendoza-Cortés, J. L.; O’Keeffe, M.; Yaghi, O. M. Secondary building units, nets and bonding in the chemistry of metal-organic frameworks. *Chem. Soc. Rev.* **2009**, 38, 1257-1283.
- (2) Liu, J.; Chen, L.; Cui, H.; Zhang, J.; Zhang, L.; Su, C. Y. Applications of metal-organic frameworks in heterogeneous supramolecular catalysis. *Chem. Soc. Rev.* **2014**, 43, 6011-6061.

- (3) Xu, Z.; Han, L.-L.; Zhuang, G.-L.; Bai, J.; Sun, D. In Situ Construction of Three Anion-Dependent Cu(I) Coordination Networks as Promising Heterogeneous Catalysts for Azide-Alkyne “Click” Reactions. *Inorg. Chem.* **2015**, *54*, 4737-4743.
- (4) Li, J. R.; Kuppler, R. J.; Zhou, H. C. Selective gas adsorption and separation in metal-organic frameworks. *Chem. Soc. Rev.* **2009**, *38*, 1477-1504.
- (5) Kurmoo, M. Magnetic metal-organic frameworks. *Chem. Soc. Rev.* **2009**, *38*, 1353-1379.
- (6) Taylor-Pashow, K. M. L.; Rocca, J. D.; Xie, Z. G.; Tran, S.; Lin, W. Postsynthetic Modifications of Iron-Carboxylate Nanoscale Metal-Organic Frameworks for Imaging and Drug Delivery. *J. Am. Chem. Soc.* **2009**, *131*, 14261-14263.
- (7) Horcajada, P.; Chalati, T.; Serre, C.; Gillet, B.; Sebrie, C.; Baati, T.; Eubank, J. F.; Heurtaux, D.; Clayette, P.; Kreuz, C.; Chang, J. S.; Hwang, Y. K.; Marsaud, V.; Bories, Y.-N.; Cynober, L.; Gil, S.; Férey, G.; Couvreur, P.; Gref, R. Porous metal-organic framework nanoscale carriers as a potential platform for drug delivery and imaging. *Nat. Mater.* **2010**, *9*, 172-178.
- (8) Panda, T.; Kundu, T.; Banerjee, R. Structural isomerism leading to variable proton conductivity in Indium(III) Isophthalic acid based frameworks. *Chem. Commun.* **2013**, *49*, 6197-6199.
- (9) Samanta, D.; Mukherjee, P. S. Structural diversity in multinuclear Pd (II) assemblies that show low-humidity proton conduction. *Chem. -Eur. J.* **2014**, *20*, 5649-5656.
- (10) Kreno, L. E.; Leong, K.; Farha, O. K.; Allendorf, M.; Van Duyne, R. P.; Hupp, J. T. Metal-organic framework materials as chemical sensors. *Chem. Rev.* **2012**, *112*, 1105-1125.
- (11) Xie, L. S.; Skorupskii, G.; Dincă, M. Electrically conductive metal-organic frameworks. *Chem. Rev.* **2020**, *120*, 8536-8580.
- (12) Ahmed, F.; Dutta, B.; Mir, M. H. Electrically conductive 1D coordination polymers: design strategies and controlling factors. *Dalton Trans.* **2021**, *50*, 29-38.
- (13) Müller-Buschbaum, K.; Beuerle, F.; Feldmann, C. MOF based luminescence tuning and chemical/physical sensing. *Microporous Mesoporous Mater.* **2015**, *216*, 171-199.
- (14) Hu, Z.; Deibert, B. J.; Li, J. Luminescent metal-organic frameworks for chemical sensing and explosive detection. *Chem. Soc. Rev.* **2014**, *43*, 5815-5840.
- (15) Allendorf, M. D.; Bauer, C. A.; Bhakta, R. K.; Houk, R. J. T. Luminescent metal-organic frameworks. *Chem. Soc. Rev.* **2009**, *38*, 1330-1352.

- (16) Cui, Y.; Yue, Y.; Qian, G.; Chen, B. Luminescent Functional Metal-Organic Frameworks. *Chem. Rev.* **2012**, *112*, 1126-1162.
- (17) Kreno, L. E.; Leong, K.; Farha, O. K.; Allendorf, M.; Van Duyne, R. P.; Hupp, J. T. Metal-Organic Framework Materials as Chemical Sensors. *Chem. Rev.* **2012**, *112*, 1105-1125.
- (18) Cui, Y.; Chen, B.; Qian, G. Lanthanide metal-organic frameworks for luminescent sensing and light-emitting applications. *Coord. Chem. Rev.* **2014**, *273-274*, 76-86.
- (19) Chen, B.; Xiang, S.; Qian, G. Metal-Organic Frameworks with Functional Pores for Recognition of Small Molecules. *Acc. Chem. Res.* **2010**, *43*, 1115-1124.
- (20) Li, M.; Li, D.; O'Kee, M.; Yaghi, O. M. Topological Analysis of Metal-Organic Frameworks with Polytopic Linkers and/or Multiple Building Units and the Minimal Transitivity Principle. *Chem. Rev.* **2014**, *114*, 1343-1370.
- (21) Natarajan, S.; Mahata, P. Metal-organic framework structureshow closely are they related to classical inorganic structures? *Chem. Soc. Rev.* **2009**, *38*, 2304-2318.
- (22) Kartha, K. K.; Babu, S. S.; Srinivasan, S.; Ajayaghosh, A. Attogram sensing of trinitrotoluene with a self-assembled molecular gelator. *J. Am. Chem. Soc.* **2012**, *134*, 4834-4841.
- (23) Ding, Y. J.; Li, T.; Hong, X. J.; Zhu, L. C.; Cai, Y. P.; Zhu, S. M.; Yu, S. J. Construction of four 3d-4f heterometallic pillar-layered frameworks containing left- and right-handed helical chains and a I⁻ chemosensor. *CrystEngComm* **2015**, *17*, 3945-3952.
- (24) SK, M.; Biswas, S. A thiadiazole-functionalized Zr(IV)-based metal organic framework as a highly fluorescent probe for the selective detection of picric acid. *CrystEngComm* **2016**, *18*, 3104-3113.
- (25) Guo, X.-Y.; Zhao, F.; Liu, J.-J.; Liu, Z.-L.; Wang, Y.-Q. An ultrastable Zinc(II)-organic framework as a recyclable multiresponsive luminescent sensor for Cr(III), Cr(VI) and 4-nitrophenol in the aqueous phase with high selectivity and sensitivity. *J. Mater. Chem. A* **2017**, *5*, 20035-20043.
- (26) Li, Z.; Zhan, D.; Saeed, A.; Zhao, N.; Wang, J.; Xu, W.; Liu, J. Fluoride sensing performance of fluorescent NH₂-MIL-53(Al): 2D nanosheets vs. 3D bulk. *Dalton Trans.* **2021**, *50*, 8540-8548.

- (27) He, G.; Peng, H.; Liu, T.; Yang, M.; Zhang, Y.; Fang, Y. A novel picric acid film sensor via combination of the surface enrichment effect of chitosan films and the aggregation-induced emission effect of siloles. *J. Mater. Chem.* **2009**, *19*, 7347-7353.
- (28) Venkatramaiah, N.; Kumar, S.; Patil, S. Fluoranthene based fluorescent chemosensors for detection of explosive nitroaromatics. *Chem. Commun.* **2012**, *48*, 5007-5009.
- (29) Thorne, P. G.; Jenkins, T. F. A Field Method for Quantifying Ammonium Picrate and Picric Acid in Soil. *Field Anal. Chem. Technol.* **1997**, *1*, 165-170.
- (30) Mantha, R.; Taylor, K. E.; Biswas, N.; Bewtra, J. K. A Continuous System for Fe0 Reduction of Nitrobenzene in Synthetic Wastewater. *Environ. Sci. Technol.* **2001**, *35*, 3231-3236.
- (31) Marvin-Sikkema, F. D.; de Bont, J. A. M. Degradation of nitroaromatic compounds by microorganisms. *Appl. Microbiol. Biotechnol.* **1994**, *42*, 499-507.
- (32) Xiao, J.-D.; Qiu, L.-G.; Ke, F.; Yuan, Y.-P.; Xu, G.-S.; Wang, Y.-M.; Jiang, X. Rapid synthesis of nanoscale terbium-based metalorganic frameworks by a combined ultrasound-vapour phase diffusion method for highly selective sensing of picric acid. *J. Mater. Chem. A* **2013**, *1*, 8745-8752.
- (33) Rachuri, Y.; Parmar, B.; Bisht, K. K.; Suresh, E. Mixed ligand two dimensional Cd(II)/Ni(II) metal organic frameworks containing dicarboxylate and tripodal N-donor ligands: Cd(II) MOF is an efficient luminescent sensor for detection of picric acid in aqueous media. *Dalton Trans.* **2016**, *45*, 7881-7892.
- (34) Sun, L.; Campbell, M. G.; Dincă, M. Electrically Conductive Porous Metal-Organic Frameworks. *Angew. Chem., Int. Ed.* **2016**, *55*, 3566-3579.
- (35) Liu, H.; Wang, Y.; Qin, Z.; Liu, D.; Xu, H.; Dong, H.; Hu, W. Electrically conductive coordination polymers for electronic and optoelectronic device applications. *J. Phys. Chem. Lett.* **2021**, *12*, 1612-1630.
- (36) Miner, E. M.; Fukushima, T.; Sheberla, D.; Sun, L.; Surendranath, Y.; Dincă, M. Electrochemical oxygen reduction catalysed by Ni₃(hexaiminotriphenylene)₂. *Nat. Commun.* **2016**, *7*, No. 10942.
- (37) Dutta, B.; Jana, R.; Sinha, C.; Ray, P. P.; Mir, M. H. Synthesis of a Cd(II) based 1D coordination polymer by in situ ligand generation and fabrication of a photosensitive electronic device. *Inorg. Chem. Front.* **2018**, *5*, 1998-2005.
- (38) Ghorai, P.; Dey, A.; Hazra, A.; Dutta, B.; Brandão, P.; Ray, P. P.; Banerjee, P.; Saha, A. Cd(II) Based Coordination Polymer Series: Fascinating Structures, Efficient

- Semiconductors, and Promising Nitro Aromatic Sensing. *Cryst. Growth Des.* **2019**, *19*, 6431-6447.
- (39) Ahmed, F.; Dutta, B.; Mir, M. H. Electrically conductive 1D coordination polymers: design strategies and controlling factors. *Dalton Trans.* **2021**, *50*, 29-38.
 - (40) Naskar, K.; Dey, A.; Dutta, B.; Ahmed, F.; Sen, C.; Mir, M. H.; Roy, P. P.; Sinha, C. Intercatenated coordination polymers (ICPs) of carboxylato bridged Zn (II)-isoniazid and their electrical conductivity. *Cryst. Growth Des.* **2017**, *17*, 3267-3276.
 - (41) Naskar, K.; Sil, S.; Sahu, N.; Dutta, B.; Slawin, A. M. Z.; Roy, P. P.; Sinha, C. Enhancement of Electrical Conductivity due to Structural Distortion from Linear to Nonlinear Dicarboxylato-Bridged Zn(II) 1D-Coordination Polymers. *Cryst. Growth Des.* **2019**, *19*, 2632-2641.
 - (42) Jana, S.; Jana, R.; Sil, S.; Dutta, B.; Sato, H.; Roy, P. P.; Datta, A.; Akitsu, T.; Sinha, C. Influence of Axial Linkers on Polymerization in Paddle-Wheel Cu(II) Coordination Polymers for the Application of Optoelectronics Devices. *Cryst. Growth Des.* **2019**, *19*, 6283-6290.
 - (43) Dutta, B.; Dey, A.; Sinha, C.; Ray, P. P.; Mir, M. H. Photochemical Structural Transformation of a Linear 1D Coordination Polymer Impacts the Electrical Conductivity. *Inorg. Chem.* **2018**, *57*, 8029-8032.
 - (44) Dutta, B.; Hazra, A.; Dey, A.; Sinha, C.; Ray, P. P.; Banerjee, P.; Mir, M. H. Construction of a Succinate-Bridged Cd(II)-Based Two-Dimensional Coordination Polymer for Efficient Optoelectronic Device Fabrication and Explosive Sensing Application. *Cryst. Growth Des.* **2020**, *20*, 765-776.
 - (45) Kumar, A.; Pandey, R.; Kumar, A.; Pandey, D. S. Pyridylphenyl appended imidazoquinazoline based ratiometric fluorescence “turn on” chemosensor for Hg²⁺ and Al³⁺ in aqueous media. *RSC Adv.* **2014**, *4*, 55967-55970.
 - (46) *SMART and SAINT*, Bruker AXS Inc.: Madison, WI, 1998.
 - (47) *SADABS. Bruker AXS Area Detector Scaling and Absorption Correction*, Bruker AXS Inc.: Madison, WI, 2014.
 - (48) Sheldrick, G. M. A short history of SHELX. *Acta Crystallogr., Sect. A: Found. Crystallogr.* **2008**, *64*, 112-122.
 - (49) Frisch, M. J.; Trucks, G. W.; Schlegel, H. B.; Scuseria, G. E.; Robb, M. A.; Cheeseman, J. R.; Scalmani, G.; Barone, V.; Mennucci, B.; Petersson, G. A.; Nakatsuji, H.; Caricato, M.; Li, X.; Hratchian, H. P.; Izmaylov, A. F.; Bloino, J.;

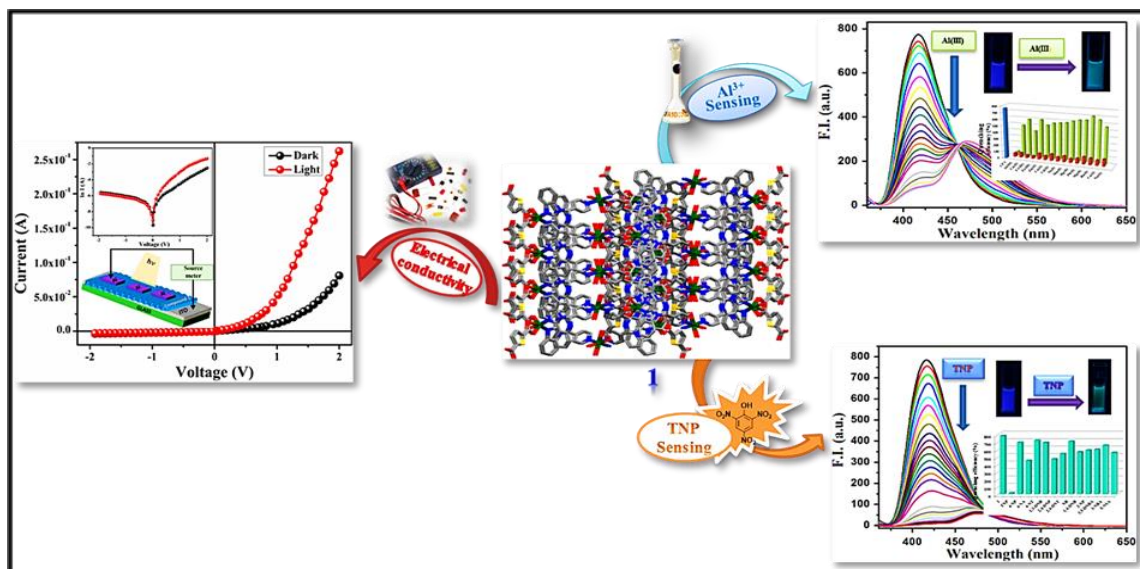
- Zheng, G.; Sonnenberg, J. L.; Hada, M.; Ehara, M.; Toyota, K.; Fukuda, R.; Hasegawa, J.; Ishida, M.; Nakajima, T.; Honda, Y.; Kitao, O.; Nakai, H.; Vreven, T.; Montgomery, J. A., Jr.; Peralta, J. E.; Ogliaro, F. M.; Bearpark, J.; Heyd, J.; Brothers, E.; Kudin, K. N.; Staroverov, V. N.; Kobayashi, R.; Normand, J.; Raghavachari, K.; Rendell, A.; Burant, J. C.; Iyengar, S. S.; Tomasi, J.; Cossi, M.; Rega, N.; Millam, J. M.; Klene, M.; Yazyev, O.; Austin, A. J.; Cammi, R.; Pomelli, C.; Ochterski, J. W.; Martin, R. L.; Morokuma, K.; Zakrzewski, V. G.; Salvador, G. A. P.; Dannenberg, J. J.; Dapprich, S.; Daniels, A. D.; Farkas, Ö.; Foresman, J. B.; Ortiz, J. V.; Cioslowski, J.; Fox, D. J. *Gaussian 09*, Revision D.01, Gaussian, Inc.: Wallingford, CT, 2009.
- (50) Becke, A. D. Density-Functional Thermochemistry. III. The Role of Exact Exchange. *J. Chem. Phys.* **1993**, 98, 5648-5652.
- (51) Bauernschmitt, R.; Ahlrichs, R. Treatment of electronic excitations within the adiabatic approximation of time dependent density functional theory. *Chem. Phys. Lett.* **1996**, 256, 454-464.
- (52) Stratmann, R. E.; Scuseria, G. E.; Frisch, M. J. An efficient implementation of time-dependent density-functional theory for the calculation of excitation energies of large molecules. *J. Chem. Phys.* **1998**, 109, 8218-8224.
- (53) Casida, M. E.; Jamorski, C.; Casida, K. C.; Salahub, D. R. Molecular excitation energies to high-lying bound states from time dependent density-functional response theory: Characterization and correction of the time-dependent local density approximation ionization threshold. *J. Chem. Phys.* **1998**, 108, 4439-4449.
- (54) O'Boyle, N. M.; Tenderholt, A. L.; Langner, K. M. CcLib: a Library for Package-independent Computational Chemistry Algorithms. *J. Comput. Chem.* **2008**, 29, 839-845.
- (55) Asha, K. S.; Bhattacharyya, K.; Mandal, S. Discriminative detection of nitro aromatic explosives by a luminescent metal-organic framework. *J. Mater. Chem. C* **2014**, 2, 10073-10081.
- (56) Keizer, J. Nonlinear Fluorescence Quenching and the Origin of Positive Curvature in Stern-Volmer Plots. *J. Am. Chem. Soc.* **1983**, 105, 1494-1498.
- (57) Nagarkar, S. S.; Desai, A. V.; Ghosh, S. K. A fluorescent metalorganic framework for highly selective detection of nitro explosives in the aqueous phase. *Chem. Commun.* **2014**, 50, 8915-8918.

- (58) Nagarkar, S. S.; Joarder, B.; Chaudhari, A. K.; Mukherjee, S.; Ghosh, S. K. Highly Selective Detection of Nitro Explosives by a Luminescent Metal-Organic Framework. *Angew. Chem., Int. Ed.* **2013**, *52*, 2881-2885.
- (59) Song, X. Z.; Song, S. Y.; Zhao, S. N.; Hao, Z. M.; Zhu, M.; Meng, X.; Wu, L. L.; Zhang, H. Single-Crystal-to-Single-Crystal transformation of a europium (III) metal-organic framework producing a multi-responsive luminescent sensor. *J. Adv. Funct. Mater.* **2014**, *24*, 4034-4041.
- (60) Buragohain, A.; Yousufuddin, M.; Sarma, M.; Biswas, S. 3D luminescent amide-functionalized cadmium tetrazolate framework for selective detection of 2, 4, 6-trinitrophenol. *Cryst. Growth Des.* **2016**, *16*, 842-851.
- (61) Ghosh, D.; Dutta, U.; Haque, A.; Mordvinova, N. E.; Lebedev, O. I.; Pal, K.; Gayen, A.; Seikh, M. M.; Mahata, P. Ultra-high sensitivity of luminescent ZnCr₂O₄ nanoparticles toward nitroaromatic explosives sensing. *Dalton Trans.* **2018**, *47*, 5011-5018.
- (62) Dey, A.; Middy, S.; Jana, R.; Das, M.; Datta, J.; Layek, A.; Ray, P. P. Light Induced Charge Transport Property Analysis of Nanostructured ZnS Based Schottky Diode. *J. Mater. Sci. Mater. Electron.* **2016**, *27*, 6325-6335.
- (63) Roy, S.; Halder, S.; Dey, A.; Harms, K.; Ray, P. P.; Chattopadhyay, S. Representation of a photosensitive Schottky barrier diode made with hetero-dinuclear cobalt(III)/sodium building blocks. *New J. Chem.* **2020**, *44*, 1285-1293.
- (64) Konar, S.; Dey, A.; Choudhury, S. R.; Das, K.; Chatterjee, S.; Ray, P. P.; Mukhopadhyay, S.; et al. Two Zinc (II)-Based Metal Complexes of New Pyrimidine Derived Ligand: Anion-Dependent Structural Variations and Charge Transport Property Analysis. *J. Phys. Chem. C* **2018**, *122*, 8724-8734.
- (65) Rhoderick, E. H. *Metal Semiconductors Contacts*; Oxford University Press: Oxford, 1978.
- (66) Cheung, S. K.; Cheung, N. W. Extraction of Schottky diode parameters from forward current-voltage characteristics. *Appl. Phys. Lett.* **1986**, *49*, 85-87.
- (67) Dey, A.; Layek, A.; Roychowdhury, A.; Das, M.; Datta, J.; Middy, S.; Das, D.; Ray, P. P. Investigation of Charge Transport Properties in Less Defective Nanostructured ZnO Based Schottky Diode. *RSC Adv.* **2015**, *5*, 36560-36567.
- (68) Gupta, R. K.; Yakuphanoglu, F. Photoconductive Schottky diode based on Al/p-Si/SnS₂/Ag for optical sensor applications. *Sol. Energy* **2012**, *86*, 1539-1545.

- (69) Miao, X.; Tongay, S.; Petterson, M. K.; Berke, K.; Rinzler, A. G.; Appleton, B. R.; Hebard, A. F. High Efficiency Graphene Solar Cells by Chemical Doping. *Nano Lett.* **2012**, *12*, 2745-2750.
- (70) Blom, P. W. M.; de Jong, M. J. M.; van Munster, M. G. Electricfield and temperature dependence of the hole mobility in poly(pphenylenevinylene). *Phys. Rev. B* **1997**, *55*, R656-R659.

Chapter 4

Rational synthesis of a pyridyl-imidazoquinazoline based multifunctional 3D Zn(II)-MOF: structure, luminescence, selective and sensitive detection of Al^{3+} and TNP, and its semiconducting device application



Abstract:

In the age of sustainable development, the exploration of multifunctional materials is of high priority due to their economic benefits and environmental suitability. A stable luminescent coordination polymer, $[\text{Zn}_2(\text{tdc})_4(\text{pdiq})_3]$ (**1**), (**pdiq** = pyridyl-imidazoquinazoline; H_2tdc = 2,5-thiophenedicarboxylic acid) has been prepared and structurally confirmed by single-crystal X-ray diffraction analysis. The 3D framework consists of a distorted octahedral geometry with a ZnO_4N_2 coordination sphere where four carboxylato-O donations come from two tdc^{2-} as bridging ligands and two pyridyl-Ns come from two **pdiq**. The $\pi\cdots\pi$ interactions between the imidazolium and phenyl groups bestow robustness on the architecture. The compound is chemically stable to water, shows tolerance to acid/base aqueous solutions (pH = 2-12), and is stable to the impact of organic solvents. The high dispersibility of Zn-MOF (**1**) in acetonitrile may enhance the fluorescence intensity compared to that in water, which prompted fluorescence measurements in the former solvent and it is used for the efficient and selective turn-off ratiometric sensing of Al^{3+} ions (LOD, 1.39×10^{-7} M). In addition, the fluorescence emission of **1** is instantly quenched by trinitrophenol (TNP) and the LOD is 1.54×10^{-7} M. The Tauc's plot is used to measure the semiconducting band gap (3.33 eV) and the electrical conductivity is significantly increased upon illumination (Λ : $1.14 \times 10^{-3} \text{ S m}^{-1}$ (dark), $5.35 \times 10^{-3} \text{ S m}^{-1}$ (light)) and the energy barrier declines marginally (FB: 0.57 (dark), 0.49 (light)). Transit time (τ) and diffusion length (L_D) at the quasi-Fermi level were analyzed to offer information on the charge transport mechanism of the compound. The better performance on photo-irradiation signifies the enhanced charge transfer kinetics of a Zn-MOF coated thin-film device (**TFD 1**), which encourages its application in semiconductor devices.

4.1 Introduction

With reference to discussion in previous chapters (**Chapters 1-3**), it is imperative that the tremendous importance of Coordination polymers (CPs) or Metal-Organic Frameworks (MOFs) has greatly influenced the current scientific research. Novelty of the materials are due to their intriguing architectures, stability, flexibility and versatile applications.^{1,2} Metal-organic frameworks (MOFs), as a kind of ordered porous hybrid material, have attracted extensive attention in gas storage and separation, molecular magnetism, ion exchange, electrical conductivity, sensing, catalysis and drug delivery.³⁻¹⁶ MOFs have been widely engineered to have robust structures and chemical stability by incorporating both appropriate π -electron-rich organic ligands and inorganic secondary building units (SBUs).¹⁷⁻²⁰ In recent years, luminescent MOFs (LMOFs) have attracted a lot of attention due to their high selectivity, sensitivity, rapid response, and reversibility as chemical sensors.²¹⁻²⁵ It is possible to adjust the luminescent properties by picking different metal clusters, and selecting N, O, or S recognition sites, and post-synthesizing modified organic motifs. Sensors based on CPs/MOFs generally detect by either increasing (turning on) or decreasing (turning off) their luminescence intensity at a single wavelength. Ratiometric luminescent sensors, on the other hand, emit dual wavelengths, and their detections are not easily affected by internal instrumental factors such as voltage fluctuations, light-shielding, or changes in sensor concentration, making them better suited to potential applications.²⁶⁻²⁹ CPs/MOFs showing ratiometric luminescent sensing are very limited; mostly lanthanide metals ($\text{Ln} = \text{Eu}^{3+}, \text{Tb}^{3+}$) are very prominent and there are very few transition metals showing this aspect.³⁰⁻³³ In this context, the synthesis of such materials of transition or non-transition metal ions has received a major challenge, but as yet, very few ratiometric luminescent TM-MOF (TM = transition metal) sensors have been used with luminescence ablation.³⁴

Aluminum is the third most abundant metal found in the earth's crust, and it is extensively used in the packaging of food, drugs and various types of utensils in daily use and electrical conducting materials for modern life.³⁵⁻³⁸ Due to indiscriminate human activities, the accumulation of a high concentration of Al^{3+} can be perceived in the environment and in the human body which breaches the maximum intake of 3-10 mg as per World Health Organization (WHO) guidelines.^{39,40} The uncontrolled increase in Al^{3+} in the human body has several adverse neurodegenerative effects on health, causing Parkinson's and Alzheimer's diseases, myopathy along with osteomalacia, anemia, and decreased liver and kidney

function.⁴¹⁻⁴⁴ Therefore the selective, sensitive and rapid quantification of Al^{3+} ions in drinking water, food, and beverages is of great importance and much anticipated.

With the increase in the use of nitroaromatics (NA) as an explosive for terrorist activities, government forensic and criminal investigation departments need rapid, easy, simple and cheap detection processes.^{45,46} 2,4,6-Trinitrophenol (TNP, popularly known as picric acid) is one of the most potent NAs, even stronger than its well-known counterpart 2,4,6-trinitrotoluene (TNT), and is widely used in the preparation of fireworks and dyes, in leather and pharmaceutical industries, and for the manufacture of rocket fuels.^{47,48} In addition, the release of this hazardous material into the environment contaminates water and soil, and causes severe environmental pollution and several health issues.⁴⁹⁻⁵² Therefore, the facile and selective detection of TNP is in high demand for civilian safety and environmental remediation. In this regard, the fluorescence-based sensing method has emerged as one of the most upcoming tools in recent years for the detection of metal ions and NAs, because of its simple operational technique, rapid response time, low cost, high selectivity and sensitivity, and expedient visual detection as well as dual compatibility in solid and solution phases.^{53,54} Therefore, the manifestation of a new fluorescent chemosensor in the form of MOFs for the selective, sensitive and efficient detection of metal ions and NAs, particularly working in green media with simplified synthetic procedures, still remains a challenge.

‘Energy’ is the key term in modern civilization, and for sustainable development the global search for alternative renewable energy sources is a particular focus in governmental budgets and scientific objectives. To date, many inorganic, organic and hybrid materials and their fabricated devices have shown their suitability.⁵⁵⁻⁵⁷ In every case, charge transportation is a prodigious concern; the variability of conditions, such as high temperature, state of the materials, structural diversity and the presence of secondary interactions plays a pivotal role in this aspect. And hence the judicious selection of molecular constituents is also highly dependent on charge mobility. Among the reported materials, MOFs or CPs are coming from such a place that their structural architecture can easily be tuned and through which their electronic property has been improved.⁵⁸⁻⁶⁰ In order to meet these requirements, a number of CPs have been designed that can be made into active electronic devices and possess electrical conductivity.⁶¹⁻⁶⁴

The correct fusion of basic functionality and luminescence characteristics can result in the development of a multifunctional MOF with diverse properties, such as the ratiometric and selective detection of Al^{3+} ions and TNP, and fabrication into semiconducting devices.

Until now, examples of MOFs with such an all-in-one function have yet to be explored.^{65,66} We therefore consider the aforementioned challenges as our reason for utilizing a single framework for multiple applications and have developed a 3D Zn(II)-MOF derived from a novel heterocyclic ligand, 6-(pyridin-4-yl)-5,6-dihydrobenzo[4,5]imidazo[1,2-*c*]quinazoline (**pdig**), and a bridging linker, 2,5-thiophene dicarboxylate (2,5-H₂tdc). Zn-MOF (**1**) has been used as a dual sensor for Al³⁺ and TNP through fluorescence quenching in acetonitrile. Interestingly, the electrical conductivity of a device fabricated from **1** (**TFD 1**) was enhanced on light irradiation and the details are discussed in this work.

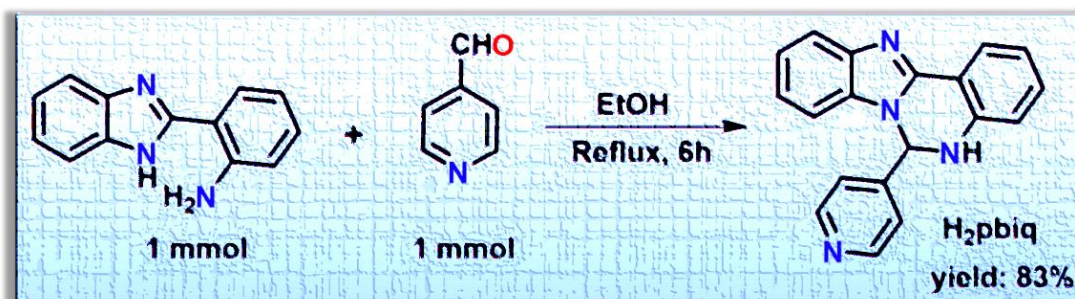
4.2 Experimental Section

4.2.1 Materials and Methods

The reagents, inorganic metal salts and solvents were reagent grade and were purchased from Merck and Spectrochem, and used without further purification. 2-(1*H*-Benzo[*d*]imidazol-2-yl) aniline and 2,5-thiophenedicarboxylic acid were purchased from Sigma-Aldrich. Thin layer chromatography (TLC) plates (Merck silica gel 60, f₂₅₄) were used to monitor the reaction. Silica gel (100-200 mesh) was used to perform column chromatography. 300 MHz (Bruker-DPX) and 400 MHz (JEOL-JNM-ECZ400S/L1) NMR instruments were utilized to depict ¹H-NMR spectra in CDCl₃ and DMSO-*d*₆ media and tetramethylsilane (TMS) was used as an internal standard. A 100 MHz (JEOL-JNM-ECZ400S/L1) NMR instrument was utilized to illustrate ¹³C-NMR spectra in CDCl₃. HRMS (*m/z*) was measured using the ESI technique with a Q-ToF Micro mass spectrometer. PerkinElmer FT-IR Spectrum RX1 spectrometer was used to record the infrared spectrum (4000-500 cm⁻¹). For CHN analysis, a PerkinElmer 240C elemental analyzer was utilized. A PerkinElmer Pyris Diamond TG/DTA instrument was exploited to test the thermal stability of the as-synthesized compound in a temperature range between 30 °C and 800 °C at a heating rate of 10 °C min⁻¹. Ambient temperature X-Ray powder diffraction (XRPD) patterns were recorded on a Bruker D8 Advance X-ray diffractometer using Cu Kα radiation (λ = 1.548 Å) produced at 40 kV and 40 mA in a 2θ range of 5-50°. The fluorescence and UV-Vis spectra were drawn on a PerkinElmer spectrofluorometer model LS55 and a PerkinElmer Lambda 25 spectrophotometer, respectively. The time-resolved single-photon counting measurements were performed using a time-correlated single-photon counting setup from HORIBA Jobin-Yvon.

4.2.2 Synthesis of Ligand (pdiq)

To synthesize the desired ligand **pdiq**, a mixture of 2-(1*H*-benzo[*d*]imidazol-2-yl)aniline (209 mg, 1.0 mmol) and isonicotinaldehyde (107 mg, 1.0 mmol) was taken in a round-bottom flask. To this reaction mixture, absolute ethanol (10.0 mL) was added and allowed to reflux for 6 h. After completion of the reaction as indicated by TLC, the reaction mixture was cooled to ambient temperature and the volume was reduced using a rotary evaporator. Then the reaction mixture was diluted with ethyl acetate and dried over anhydrous Na₂SO₄ and the volume was further reduced using a rotary evaporator. Column chromatography was done to purify the crude product using ethyl acetate/hexane (7 : 3, v/v) as eluent, to afford the desired 6-(pyridin-4-yl)-5,6-dihydrobenzo[4,5]imidazo[1,2-*c*]quinazoline (**pdiq**) (**Scheme 4.1**). HRMS (ESI, *m/z*) calcd. for C₁₉H₁₅N₄ [M+H]⁺: 299.1297; found: 299.1319 (**Figure 4.1**); ¹H NMR (400 MHz, CDCl₃): δ 8.52 (d, *J* = 6.08 Hz, 2H), 8.17 (dd, *J*₁ = 7.8 Hz, *J*₂ = 1.2 Hz, 1H), 7.79 (d, *J* = 8.1 Hz, 1H), 7.27-7.23 (m, 2H), 7.14-7.12 (m, 2H), 7.10 (d, *J* = 8.1 Hz, 1H), 6.99-6.95 (m, 1H), 6.83 (d, *J* = 8.1 Hz, 1H), 6.74 (d, *J* = 8.0 Hz, 1H), 6.67 (d, *J* = 2.12 Hz, 1H), 5.13 (s, 1H) (**Figure 4.2**); ¹³C NMR (100 MHz, CDCl₃): δ 150.9, 141.0, 132.7, 132.1, 125.8, 123.3, 123.2, 120.91, 120.9, 119.6, 115.6, 109.6, 68.3 (**Figure 4.3**).



Scheme 4.1 Synthesis of 6-(pyridin-4-yl)-5,6-dihydrobenzo[4,5]imidazo[1,2-*c*]quinazoline (**pdiq**).

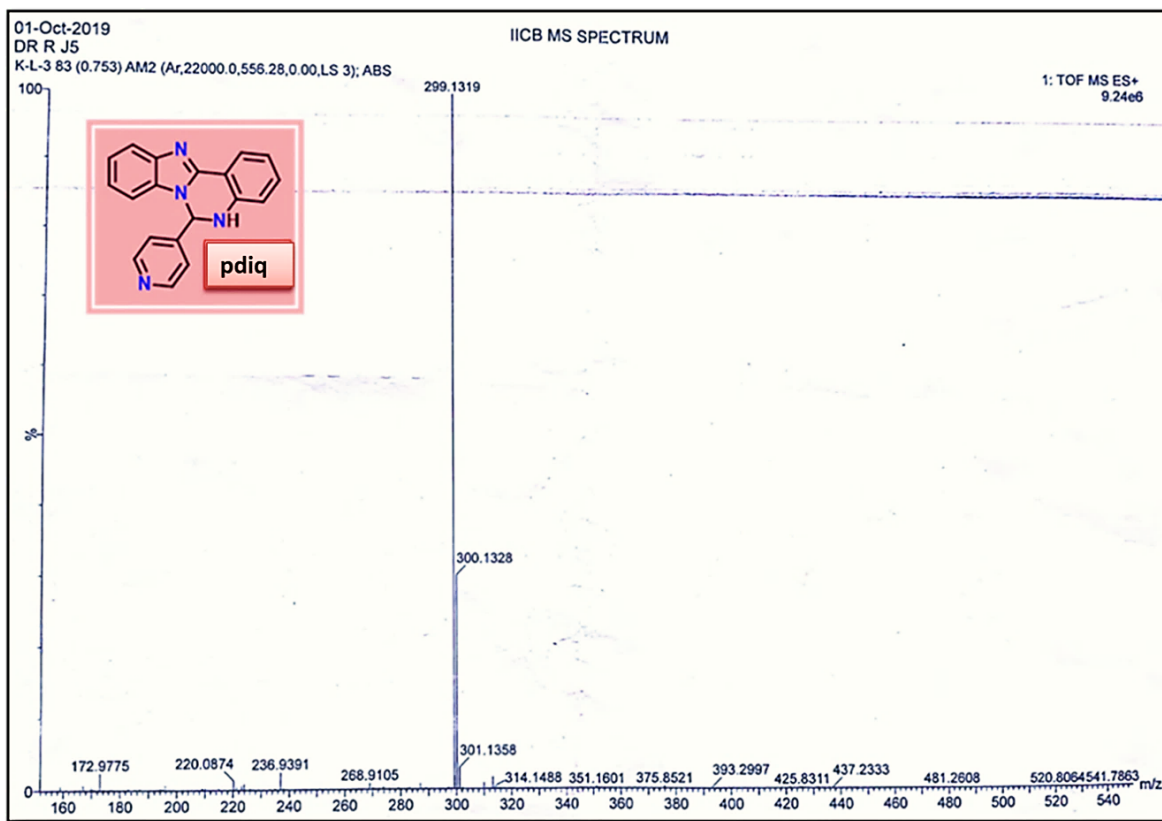


Figure 4.1 Mass spectrum of **pdiq**.

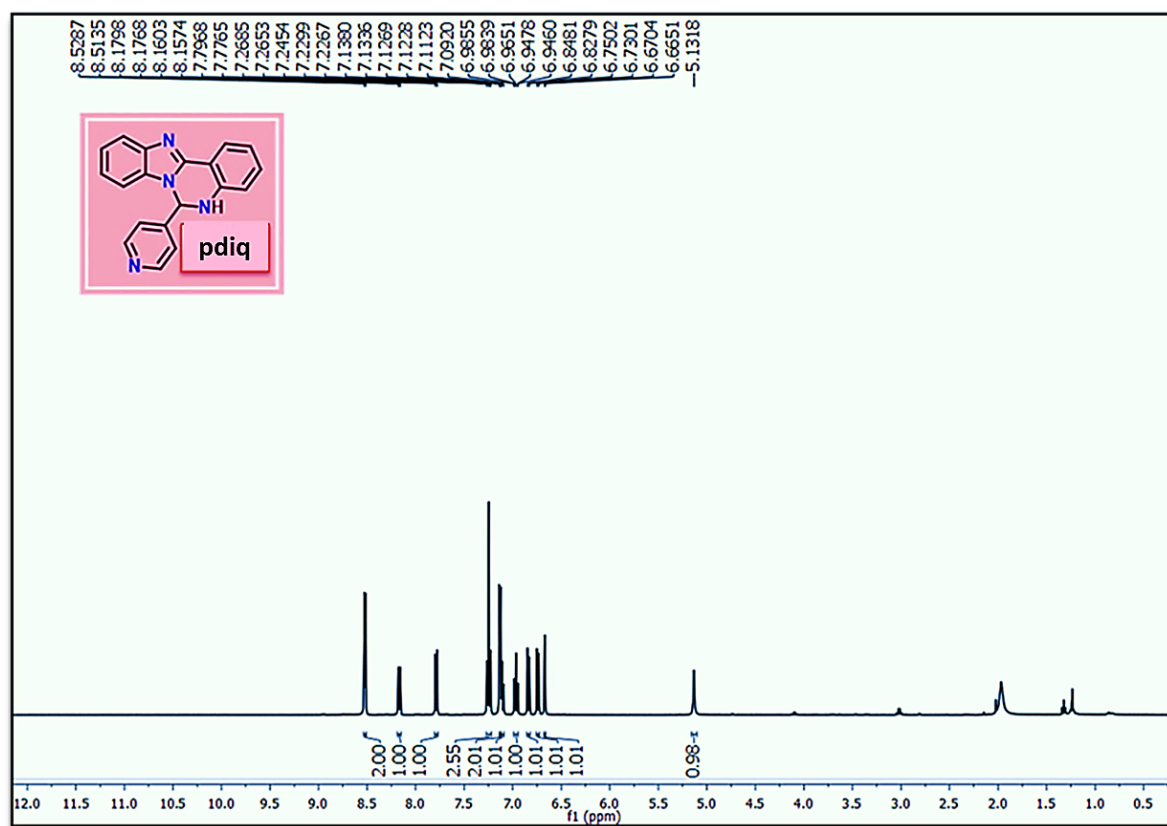


Figure 4.2 ¹H-NMR spectroscopy of **pdiq**.

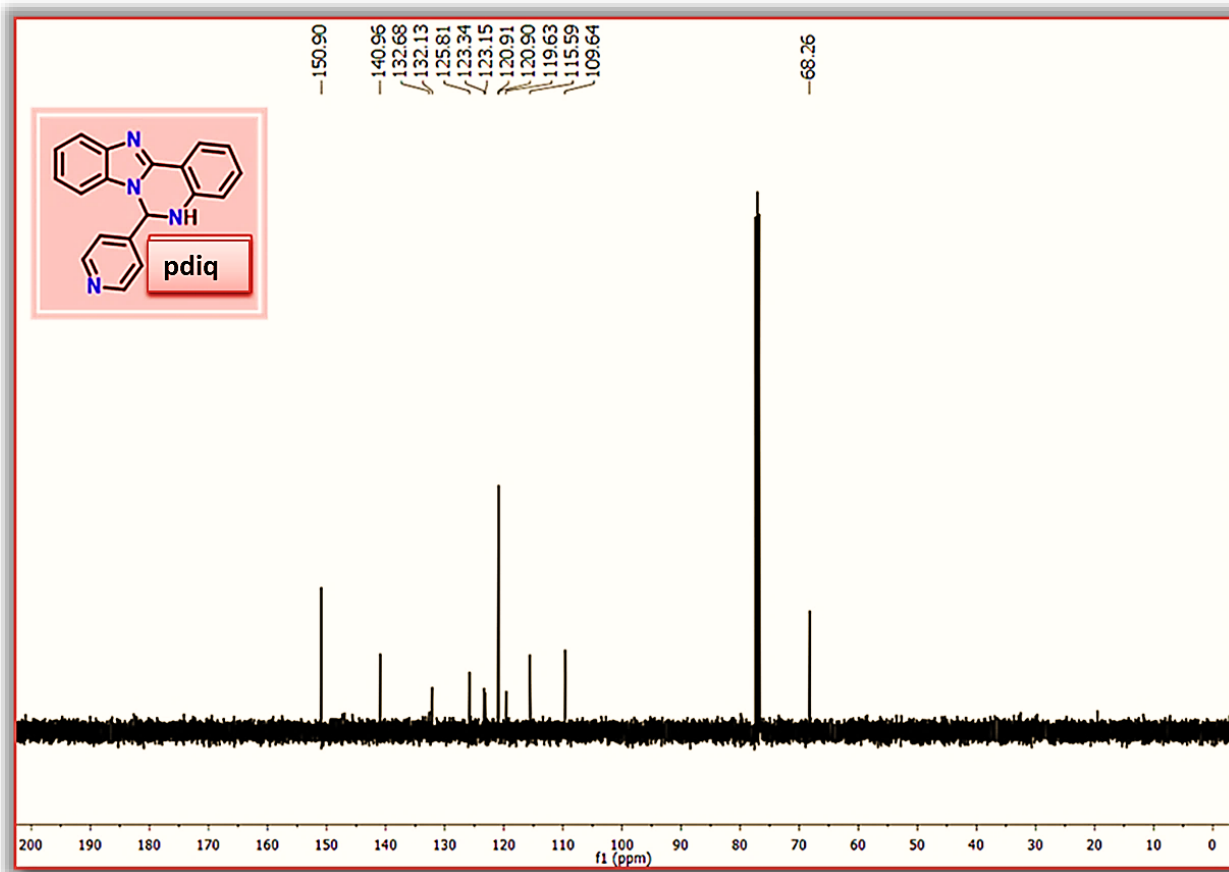
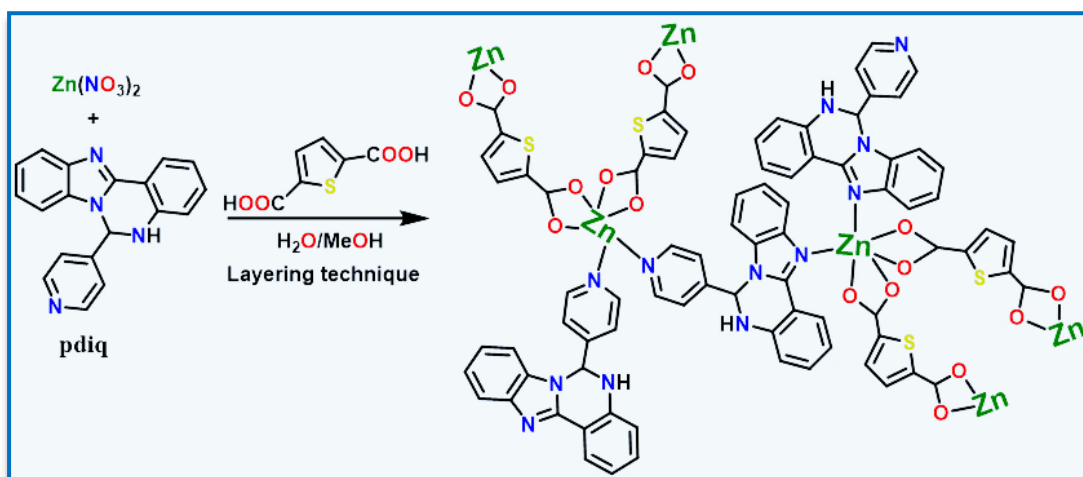


Figure 4.3 ^{13}C -NMR spectroscopy of **pdiq**.

4.2.3 Synthesis of $[\text{Zn}_2(\text{tdc})_4(\text{pdiq})_3]$ (**1**)

A solution of **pdiq** (59.6 mg, 0.2 mmol) in MeOH (2 mL) was slowly and carefully layered into a solution of $\text{Zn}(\text{NO}_3)_2 \cdot 6\text{H}_2\text{O}$ (61.7 mg, 0.2 mmol) in H_2O (2 mL) using 2 mL of a 1 : 1 (v/v) buffer solution of MeOH and H_2O . Then a solution of 2,5-thiophenedicarboxylic acid (42 mg, 0.2 mmol) neutralized with Et_3N (21 mg, 0.2 mmol) in 2 mL EtOH was layered upon it. It was then allowed to diffuse for a few days. The yellow-colored block-shaped crystal of $[\text{Zn}_2(\text{tdc})_4(\text{pdiq})_3]$ (**1**) (Scheme 4.2) was obtained after five days (164 mg, yield 62%). Elemental analysis (%) calculated for $\text{C}_{81}\text{H}_{58}\text{N}_{12}\text{O}_{16}\text{S}_4\text{Zn}_2$: C, 56.67; H, 3.39; N, 11.90; found: C, 56.74; H, 3.37; N 11.95.

Scheme 4.2 Synthesis of $[Zn_2(tdc)_4(pdiq)_3]$ (**1**).

4.2.4 General X-ray Crystallography

A single crystal of **1** was isolated from the solution, immersed in oil and mounted on a goniometer head to collect the X-ray data. A Bruker SMART APEX II CCD diffractometer combined with a graphite-monochromated Mo $K\alpha$ radiation source ($\lambda = 0.71073 \text{ \AA}$) at 273 K was used. The matrices for crystal-orientation and the parameters labeling the unit cell were assessed from the least-square refinements of all reflections and the hkl values were in the range of $-13 \leq h \leq 13$, $-37 \leq k \leq 37$, $-68 \leq l \leq 68$. The crystallographic data (Table 4.1) were processed with the SAINT program,⁶⁷ and were used for integration ($I > 2\sigma(I)$) and absorption correction was carried out using SADABS.⁶⁸ The single-crystal molecular structure was solved with the help of SHELXT 2014/5 and refinement was done using Olex2 1.5-dev.⁶⁹⁻⁷¹ Anisotropic thermal parameters are very convenient to refine the non-hydrogen atoms of the compound. The hydrogen atoms were perfectly positioned and were forced to ride on the parent atoms in their geometrically perfect positions. The selected bond lengths and bond angles are labeled in **1** (Table 4.2). CCDC number for **1**: 2162910.

Table 4.1 Crystal data and refinement parameters for **1**.

Formula	$C_{25}H_{16}N_4O_4SZn$
CCDC	2162910
Formula weight	533.87
Crystal system	Orthorhombic
space group	' $F d d'$ '
a (Å)	11.4312 (13)
b (Å)	31.433 (4)
c (Å)	57.919 (6)

α (deg)	90
β (deg)	90
γ (deg)	90
V (Å ³)	20811 (4)
Z	32
D_{calcd} (g/cm ³)	1.363
μ (mm ⁻¹)	1.061
λ (Å)	0.71073
data[$I > 2\sigma(I)$]/params	4587/369
GOF on F^2	1.1344
Final R indices[$I > 2\sigma(I)$] ^{a,b}	$R1 = 0.0623$, $wR2 = 0.2169$

$$^a R1 = \Sigma ||F_o| - |F_c|| / \Sigma |F_o|, ^b wR2 = [\Sigma w(F_o^2 - F_c^2)^2 / \Sigma w(F_o^2)^2]^{1/2}$$

Table 4.2 Selected bond lengths and bond angles in **1**.

Bond length	(Å)	Bond Angles	(°)
Zn(1) - O(1)	2.010(7)	O(2) - Zn(1) - O(2)y	86.10(19)
Zn(1) - O(2)	2.530(6)	N(3) - Zn(1) - O(2)y	85.82(19)
Zn(1) - N(3)	2.088(5)	O(1)y - Zn(1) - N(3)y	114.1(3)
Zn(1) - O(1)y	2.010(7)	O(3) - Zn(2) - O(3)s	81.67(18)
Zn(1) - O(2)y	2.530(6)	O(3) - Zn(2) - N(4)w	152.1(2)
Zn(1) - N(3)y	2.088(5)	O(4) - Zn(2) - N(4)t	105.3(2)
Zn(2) - O(3)	2.555(6)	O(3)s - Zn(2) - N(4)t	152.1(2)
Zn(2) - O(4)	2.006(8)	O(4)s - Zn(2) - N(4)w	105.3(2)
Zn(2) - O(3)s	2.555(6)	O(1) - Zn(1) - O(1)y	123.2(3)
Zn(2) - O(4)s	2.006(8)	O(2) - Zn(1) - N(3)	168.9(2)
Zn(2) - N(4)t	2.061(4)	N(3) - Zn(1) - N(3)y	103.17(19)
Zn(2) - N(4)w	2.061(4)	O(2)y - Zn(1) - N(3)y	168.9(2)
Bond Angles	(°)	O(3) - Zn(2) - O(4)s	95.3(2)
O(1) - Zn(1) - O(2)y	81.3(2)	O(4) - Zn(2) - O(3)s	95.3(2)
O(2) - Zn(1) - O(1)y	81.3(2)	O(4) - Zn(2) - N(4)w	97.9(2)
N(3) - Zn(1) - O(1)y	100.6(2)	O(3)s - Zn(2) - N(4)w	94.49(17)
O(1)y - Zn(1) - O(2)y	57.0(3)	N(4)t - Zn(2) - N(4)w	101.02(17)
O(3) - Zn(2) - O(4)	55.4(3)	Zn(2) - O(3) - C(25)	78.0(5)
O(3) - Zn(2) - N(4)t	94.49(17)	Zn(1) - N(3) - C(3)	131.6(5)
O(4) - Zn(2) - O(4)s	143.3(3)	Zn(1) - O(1) - C(20)	103.1(6)

O(3)s - Zn(2) - O(4)s	55.4(3)	Zn(2) - O(4) - C(25)	104.4(6)
O(4)s - Zn(2) - N(4)t	97.9(2)	Zn(1) - N(3) - C(9)	122.8(4)
Zn(1) - O(2) - C(20)	79.6(5)	C(17) - N(4) - Zn(2)g	124.6(4)
C(18) - N(4) - Zn(2)g	118.7(3)	O(1) - Zn(1) - O(2)	57.0(3)
O(1) - Zn(1) - N(3)	114.1(3)		
O(1) - Zn(1) - N(3)y	100.6(2)		

Symmetry Code: g = -1/4+x, 1-y, -1/4+z; y = 3/4-x, 3/4-y, z; s = 7/4-x, y, 3/4-z; t = 3/2-x, 1-y, 1/2-z; w = 1/4+x, 1-y, 1/4+z.

4.2.5 Theoretical Calculations

The optimized geometry of **1** was established with the help of density functional theory (DFT) using the GAUSSIAN-09 program package.⁷² All the essential theoretical calculations were achieved using the hybrid DFT-B3LYP function.⁷³ All the elements of the model were based on the LanL2DZ basis set. X-ray coordinates for a single crystal were taken for **1**. To depict different low-lying electronic transitions in the spectra, time-dependent density functional theory (TDDFT) calculations were performed.⁷⁴⁻⁷⁶ The Gauss sum⁷⁷ method was employed to consider the fractional entanglement of different individual components present in the polymeric compound for each molecular orbital.

4.2.6 Device Fabrication

In this study, multiple metal-semiconductor (MS) junction devices were fabricated in ITO/synthesized **1**/Al sandwich structure to perform the electrical study (**Figure 4.4**). In this regard, well dispersion of the synthesized complexes were made in N,N-dimethyl formamide (DMF) by mixing and sonicated the right proportion (25 mg/ml) of the complex in a vial. This freshly prepared stable dispersion of the compound was deposited on the top of the ITO coated glass substrate by spun firstly at 600 rpm for 5 min and thereafter at 900 rpm for another 5 min with the help of SCU 2700 spin coating unit. Afterward, the as-deposited thin film was dried in a vacuum oven at 80 °C for several minutes to evaporate the solvent part fully. Here we used aluminium as metal electrode, which was deposited using Vacuum Coating Unit on the active layer of the devices by maintaining the effective area as $7.065 \times 10^{-2} \text{ cm}^2$ with shadow mask. Using Sourcemeater made by Keithley (model no: 2401), the current-voltage (*I-V*) characteristics of the devices was measured to analyze the electrical properties. All the device fabrication and measurements were carried out at room temperature and under ambient conditions.

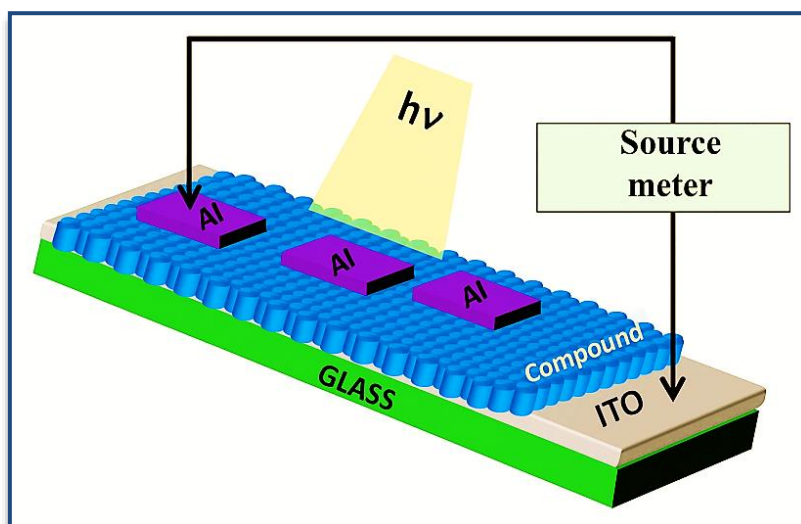


Figure 4.4 Schematic representation of device fabrication.

4.3 Results and Discussion

4.3.1 Structural Description of $[\text{Zn}_2(\text{tdc})_4(\text{pdiq})_3]$ (**1**)

A single crystal of **1** crystallizes in the orthorhombic crystal system with space group $Fddd$, a centro-symmetric compound. The asymmetric unit contains two Zn(II) metal centers (Zn1 and Zn2) with different coordination atmospheres (**Figure 4.5a**). Both the metal centers constitute a distorted octahedral geometry with a ZnO_4N_2 unit; for Zn1, the metal ion is chelated with two dicarboxylato moieties from tdc^{2-} anions and two imidazolium nitrogen atoms of **pdiq** are coordinated in monodentate fashion to generate such a system ($\text{Zn1-O1} = 2.010(7)$, $\text{Zn1-O2} = 2.530(6)$, $\text{Zn1-N3} = 2.088(5)$). On the other hand, the Zn2 metal node has been ligated through the pyridyl-Ns of **pdiq** moieties in a similar monodentate manner and the coordination of O-atoms remains the same ($\text{Zn2-O3} = 2.555(6)$, $\text{Zn2-O4} = 2.006(8)$, $\text{Zn2-N4t} = 2.061(4)$). There is a possibility around the metal nodes to construct two different network structures with the periodical attachments of tdc^{2-} and **pdiq** (**Figure 4.5b**). A spiral ribbon-like portion has appeared within the structural system. This 2D network undergoes 3D assembly with the continuous coordination of constituted ligands as well as accessible aqua molecules within the crystal host (**Figure 4.5c**). Some secondary interactions are there to build the robust molecular architecture; the extensive $\pi \cdots \pi$ interactions have been adapted within the imidazolium rings ($\text{Cg2} = \text{N2-C3-N3-C9-C14}$) with a separation of 3.883 \AA and phenyl rings ($\text{Cg6} = \text{C2-C4-C5-C6-C7-C8}$ and $\text{Cg7} = \text{C9-C10-C11-C12-C13-C14}$) with a separation of 4.062 \AA from **pdiq**.

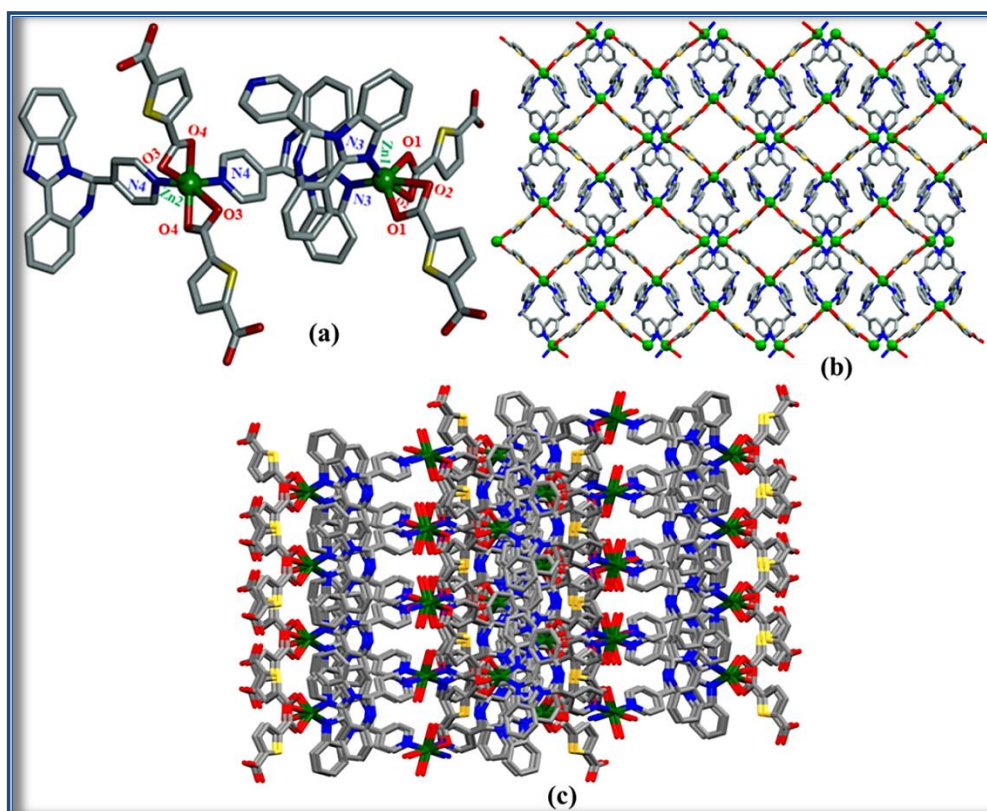


Figure 4.5 (a) Perspective view of the different coordination arrangements around the metal centers of **1**. (b) A view of the 2D network built with **tdc**²⁻ and **pdiq**. (c) View of the 3D assembly in a capped sticks model.

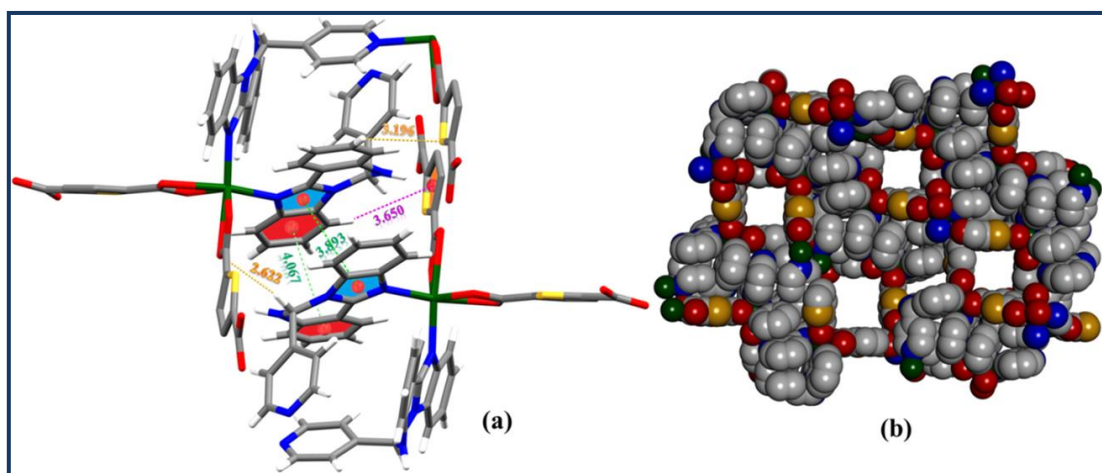


Figure 4.6 (a) A view of $\pi \cdots \pi$, C-H $\cdots \pi$ and H-bonding interactions within the network. (b) Space filled model of **1**.

Non-classical hydrogen bonding has been constituted (C1-H1a \cdots O2, 2.649 Å) and significant C-H $\cdots \pi$ interactions (C13-H13 \cdots Cg1 (S1-C21A-C22A-C23A-C24A), 3.664 Å) also exist (**Figure 4.6a**). Therefore, the generated supramolecular assembly has adopted a strong, stable and flexible molecular architecture (**Figure 4.6b**).

4.3.2 PXRD and TGA Analysis

Powder X-ray diffraction (PXRD) investigation was performed at ambient temperature to assess the phase purity of the bulk material of **1**. Based on the simulated single-crystal data it seems that the PXRD pattern of **1** is in good agreement with that of the synthesized powder, and the extensive uniformity of the bulk material indicates high purity of phases (Figure 4.7). The stability of **1** in acid/base was also checked in the pH range of 2-12 followed by PXRD and it was observed that the diffraction pattern remains unaltered, proving the structural durability of Zn-MOF (Figure 4.7). To examine the thermal stability, thermogravimetric analysis (TGA) of **1** was performed under a dry N₂ atmosphere at temperatures ranging from 30 °C to 800 °C. Compound **1** is thermally stable up to about 320 °C (Figure 4.8), which makes the compound useful in material design.

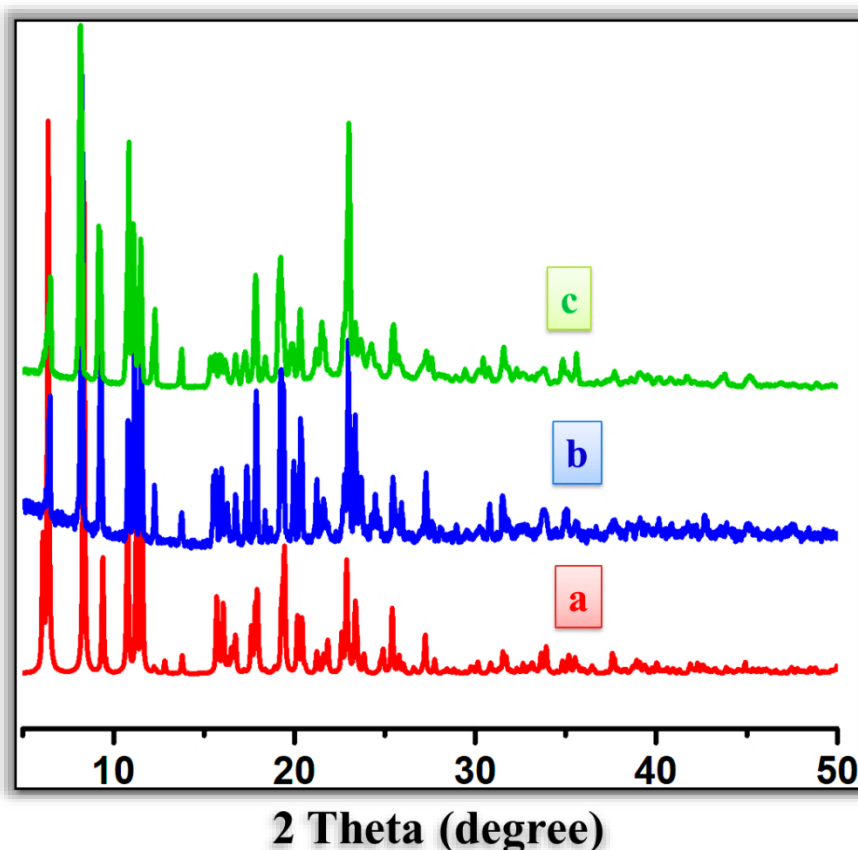


Figure 4.7 PXRD patterns of (a) simulated from the X-ray single structure of **1** (red), (b) as-synthesized **1** (blue) and (c) **1** after the prolonged immersed in lower pH solution (pH = 4) (green).

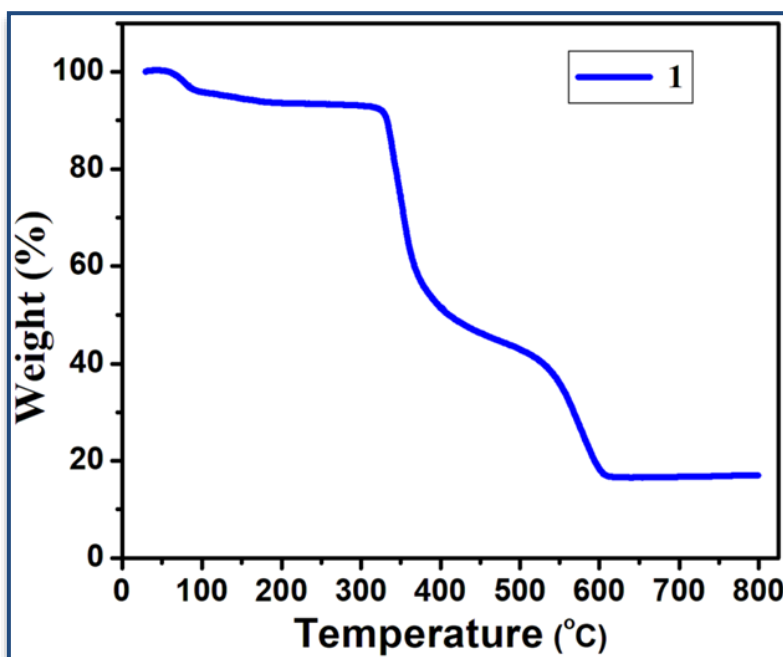


Figure 4.8 TGA plot of **1**.

4.3.3 Photoluminescence Properties

The photoluminescence of MOF is greatly influenced by the orientation of its conjugated organic ligands. A MOF containing metal ions such as Zn(II) (d^{10}) attached to a polytopic organic ligand (like **pdiq**) involving a π -conjugated moiety can exhibit strong luminescence properties. Compound **1** was dispersed in acetonitrile at ambient temperature and the absorption spectrum shows an intense transition at 350 nm (Figure 4.9) while the free ligand **pdiq** shows absorption at 347 nm.

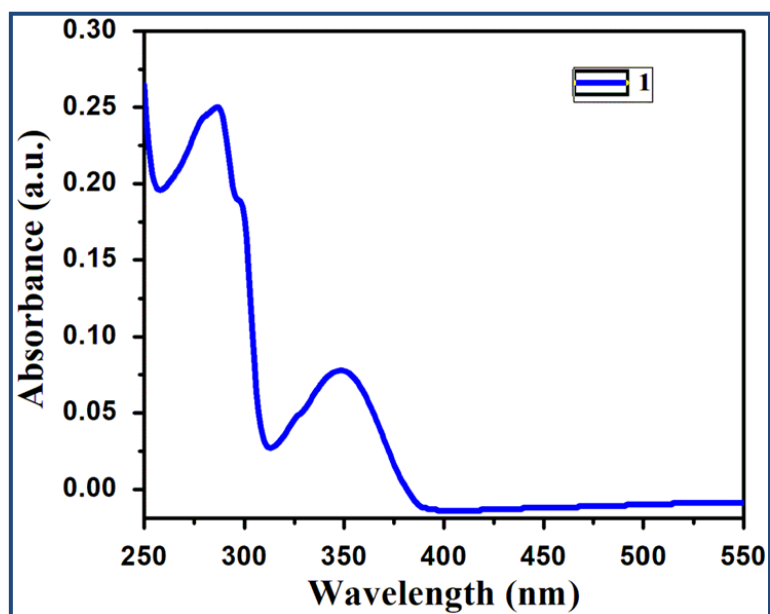


Figure 4.9 UV-Visible spectrum of **1** in acetonitrile.

Therefore, the absorption band at 350 nm is considered a ligand-centered transition. A strong blue emission at 416 nm by **1** is observed upon irradiation at 380 nm in the solution phase (acetonitrile) while free ligand **pdiq** is weakly emissive under identical conditions. The strong fluorescence intensity is attributed to an intraligand transition. Additionally, coordination of the metal center (Zn^{2+}) with the ligand (**pdiq**) can result in increased rigidity of the system, thus reducing nonradiative decay.^{78,79}

4.3.4 Ratiometric Fluorescence Sensing of Al^{3+}

A well-dispersed suspension of **1** in acetonitrile was used to examine its metal ion sensing efficacy by mixing with a solution of different metal ions (Zn^{2+} , Cd^{2+} , Co^{2+} , Ni^{2+} , Mn^{2+} , Hg^{2+} , Cr^{3+} , Fe^{3+} , Al^{3+} , Cu^{2+} , Pb^{2+} , Na^+ , Ca^{2+} , Mg^{2+} , and Ba^{2+}). Acetonitrile belongs to the yellow list (MSDS) but, considering the better dispersibility of Zn-MOF (**1**) than in water and hence the higher intensity of absorption and luminescence spectra, the former is used as a solvent in the spectroscopic experiments. The luminescence intensity of **1** at 416 nm was insignificantly perturbed on adding different metal ions (Figure 4.10a). However, in the case of Al^{3+} , the initial emission intensity of **1** is decreased (416 nm) and a new emission band is generated (472 nm) (Figure 4.10b). The reason is unclear at this stage; however, it is assumed that in Zn-MOF, the π -conjugated polytopic ligand, **pdiq**, may interact with Lewis acidic Al^{3+} or TNP, inducing self-assembly which may cause through space conjugation and may assist in red shifting of the spectral band along with quenching. For the design of effective sensors, selectivity is crucial, and we demonstrated that **1** is selectively sensitive to Al^{3+} by performing competitive photoluminescence experiments.

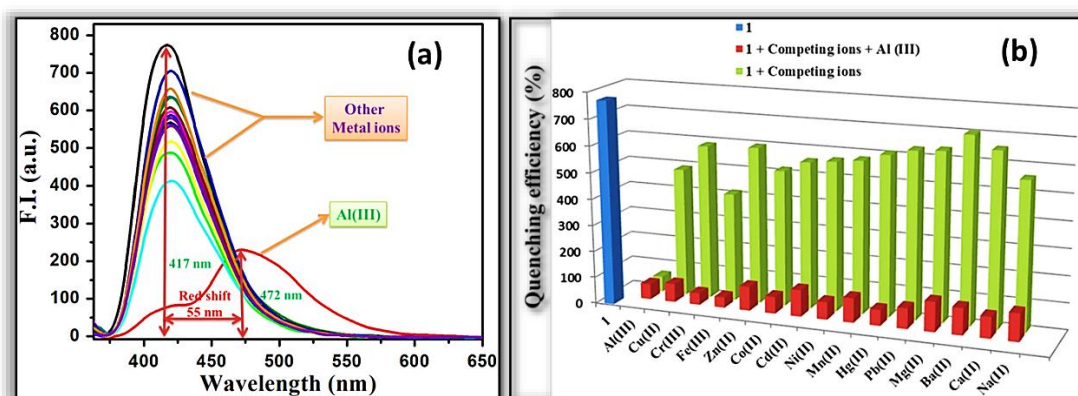


Figure 4.10 (a) Emission spectra of **1** dispersed in CH_3CN in presence of different metal ions. (b) Quenching efficacy of different metal ions toward the emission of **1**.

Besides, we studied the UV-Vis absorption spectra of **1** upon the addition of solutions of different cations. The absorption wavelength remained more or less unshifted; only in the

case of Al^{3+} did the acetonitrile suspension of **1** show a significant red shifting of the band to 380 nm (**Figure 4.11a**). There was no remarkable change in the emission of **1** in the presence of various metal ions with a concentration of $38.1 \mu\text{M}$ in the absence of Al^{3+} ions (**Figure 4.10a**). However, the subsequent addition of Al^{3+} ions dramatically quenched the fluorescence, confirming that **1** was independent of competing metal ions in its ability to detect Al^{3+} in acetonitrile. The CIE coordinates also substantiate the observation (**Figure 4.11b**). In order to assess the interaction between **1** and Al^{3+} ions, we performed an absorbance spectroscopic titration. A decrease in the absorption band across 350 nm was observed with incremental addition of Al^{3+} to the suspension of **1**, with the generation of two isosbestic points at 313 and 367 nm, and new bands at 280 and 380 nm were generated (**Figure 4.11c**).

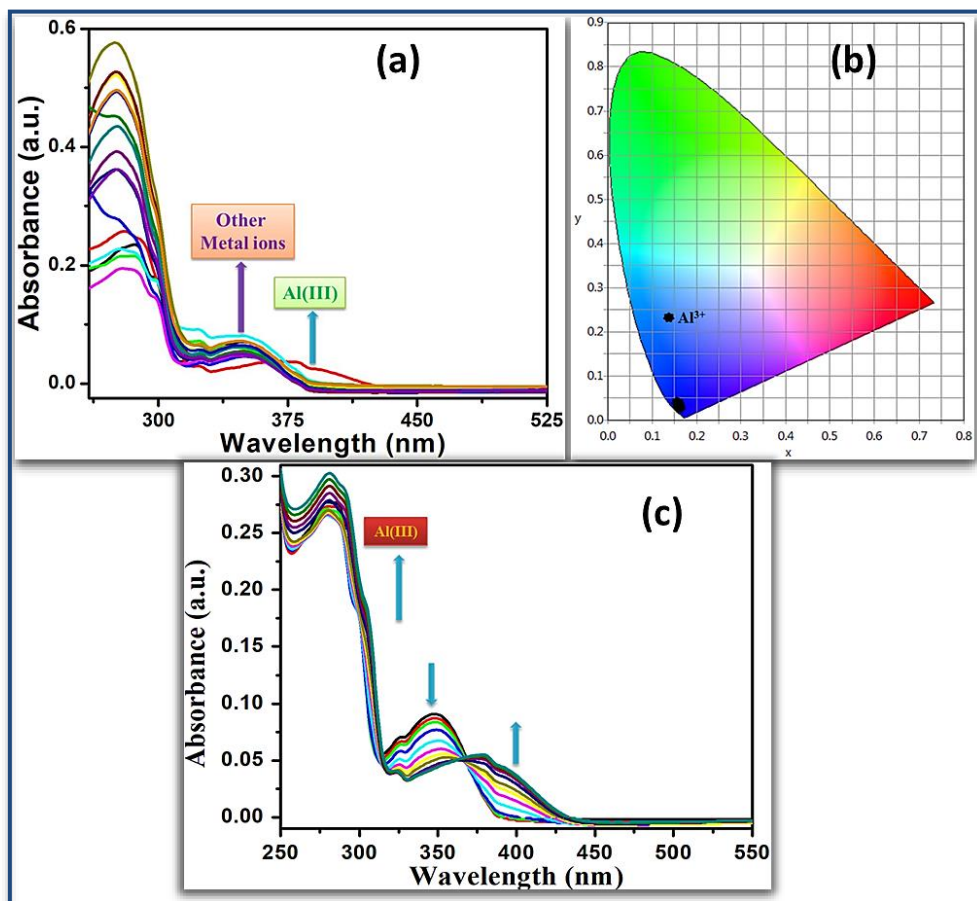


Figure 4.11 (a) Absorption spectra of **1** dispersed in CH_3CN in presence of different metal ions. (b) CIE coordinates of **1** with different metal ions. (c) Absorption spectra of **1** ($10 \mu\text{M}$) in acetonitrile upon the incremental addition of Al^{3+} (0- $38.1 \mu\text{M}$).

To evaluate the sensitivity, the fluorescence intensity of **1** was measured upon the gradual addition of Al^{3+} solution (**Figure 4.12a**). A gradual decrease in luminescence intensity at 417 nm was observed when the concentration of Al^{3+} increased, but a new band

was observed at 472 nm at the same time. Al^{3+} has CIE coordinates of (0.1454, 0.2301), which indicate that the suspension exhibits cyan emission, in contrast with that of the other cations (Figure 4.12b). This finding was also corroborated by optical images of suspensions irradiated by a 365 nm UV lamp (inset of Figure 4.12a).

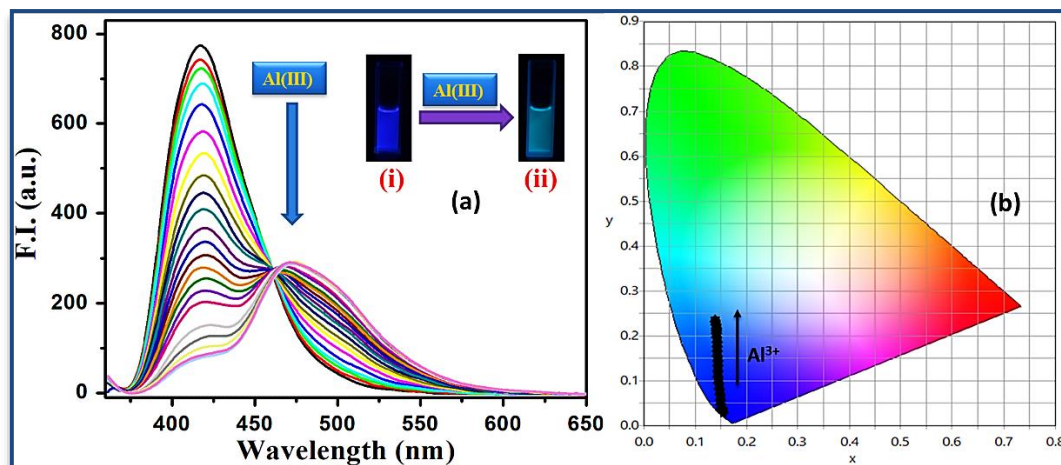


Figure 4.12 (a) Luminescence spectra of **1** (10 μM) in acetonitrile upon the incremental addition of Al^{3+} (0-38.1 μM); inset: fluorescence images of cuvettes filled with acetonitrile suspensions of **1** under UV light ($\lambda = 365 \text{ nm}$) before Al^{3+} addition (i) and after Al^{3+} addition (ii). (b) CIE chromaticity diagram of **1** in acetonitrile with different concentrations of Al^{3+} .

To determine the fluorescent quenching efficiency, the Stern-Volmer plot: $I/I_0 = 1 + K_{\text{sv}}[Q]$, where I_0 and I represent the fluorescence intensities before and after adding Al^{3+} and $[Q]$ represents the molar concentration of the analyte (Al^{3+}), was used to calculate K_{sv} ($4.0 \times 10^4 \text{ M}^{-1}$, Figure 4.13a) (the Stern-Volmer quenching constant). The plot is linear ($R^2 = 0.935$) over the lower concentration range (up to 4.0 μM). The limit of detection ($3\sigma/k$ method) was calculated and found to be 0.139 μM (Figure 4.13b). This observed value of the limit of detection is much lower ($\sim 1/53$ times) than the value (7.41 μM) recommended by the US EPA and FDA for bottled drinking water. This value was also comparable with previous MOF-based sensor materials.^{34,80-84}

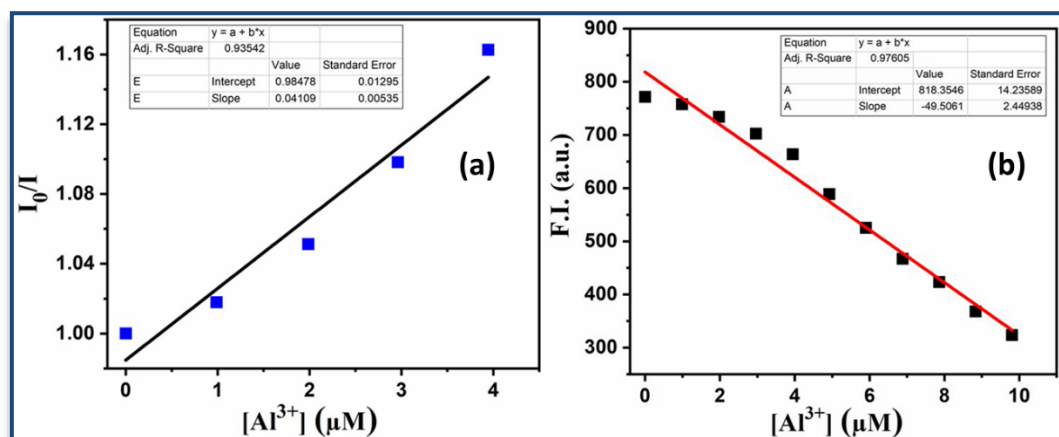


Figure 4.13 (a) Stern-Volmer plot of **1** at lower range of quencher [Al(III)] (in μM) concentration. (b) The linear dynamic response of **1** for Al(III) and the determination of the limit of detection (LOD) of Al(III).

To establish the fluorescence quenching mechanism, the absorption spectra were collected by adding Al^{3+} to an acetonitrile solution of **1**. No apparent absorption of Al^{3+} at 350 nm was found in the solution; therefore, the UV irradiation does not result in quenching due to competitive absorption. Also, the Al^{3+} absorption band shows no overlap with the excitation band of **1**, so it cannot be a case of resonance energy transfer.⁸⁵ In this way, it is possible to explain the quenching of the emission of **1** by Al^{3+} through a collisional process with the framework of **1**. To gain insights into the binding of Al^{3+} ions with the framework of **1**, ^1H -NMR titration was carried out with the incremental addition of Al^{3+} in $\text{DMSO}-d_6$ medium (Figure 4.14). As a result of electronic interactions between the analyte and sensor material, it is possible for the density of electrons to diffuse significantly. Due to the deshielding of aromatic protons, the NMR peaks are broadened and shifted towards higher δ -values.

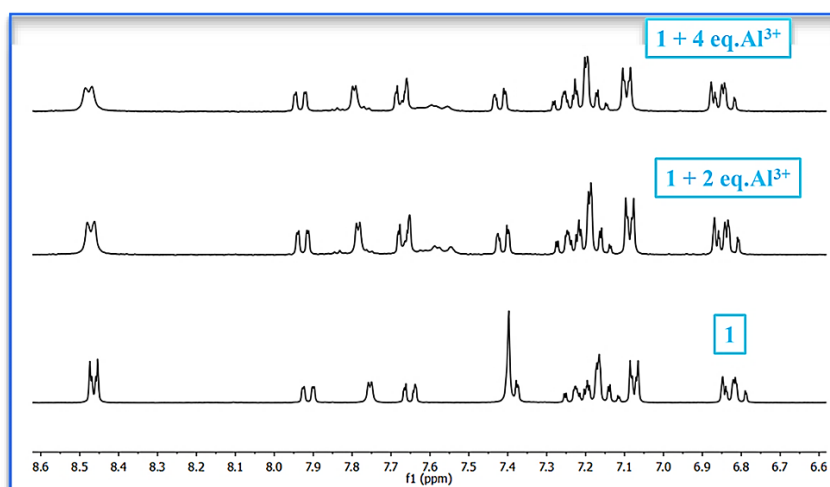


Figure 4.14 ^1H -NMR titration between **1** and Al^{3+} in $\text{DMSO}-d_6$ medium.

To investigate the prevailing interaction, the time-resolved fluorescence spectra were recorded in the absence of and with the incremental addition of Al^{3+} to the solution of **1**. Determining the fluorescence decay profile reveals its monoexponential nature (**Figure 4.15** and **Table 4.3**), and its associated lifetime (τ) gradually decreases from 4.58 ns in acetonitrile solution to 3.57 ns with the successive addition of Al^{3+} solution, which is imperative to some interaction between these components.

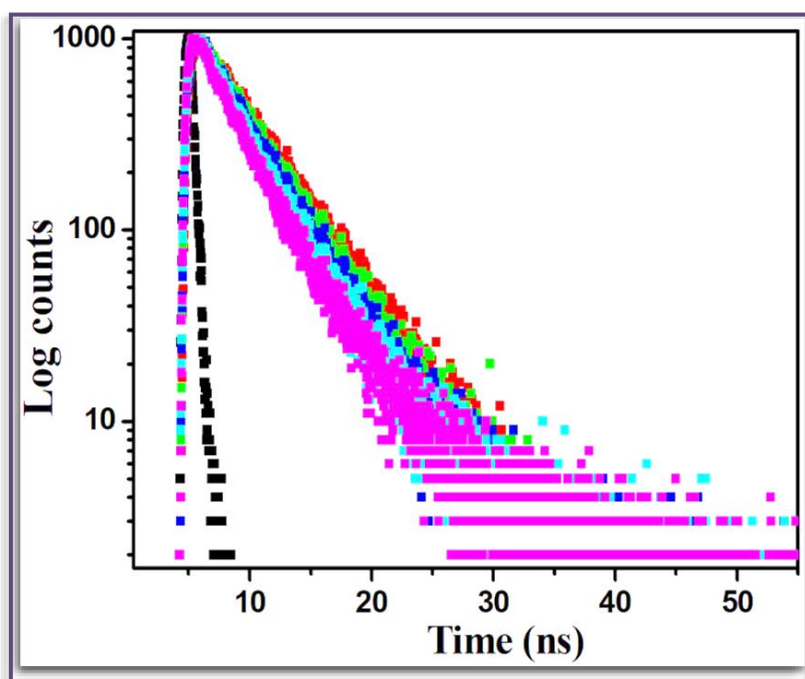


Figure 4.15 Representative fluorescence decay spectra of **1** (10 μM) in the absence and presence of an increasing concentration of Al(III) . Spectra 1-5 corresponds to the Al(III) concentration 0 μM (red square), 9.80 μM (green square), 19.42 μM (blue square), 28.85 μM (cyan square), 38.10 μM (magenta square), respectively.

Table 4.3 Fluorescence Lifetime Decay Parameters of **1** (10 μM) with the Gradual Addition of Al(III) .

$\text{Al(III)} (\mu\text{M})$	$\tau (\text{ns})$	CHISQ
0	4.58	1.168835
9.80	4.21	1.17219
19.42	3.97	1.247764
28.85	3.69	1.215121
38.10	3.57	1.233064

The experimental observation was extended to fabricate a simple ‘use-and-throw’ technology as a part of laboratory-to-land application. A Zn-MOF coated dry paper strip was prepared and subjected to a drop of Al^{3+} solution; the image so formed was captured under a 365 nm UV lamp. This used strip was then washed with acetonitrile, dried under air, and was used a second time. The cycle was continued repetitively (Figure 4.16). From the study, the recyclability is quite satisfactory for long-term enactment.

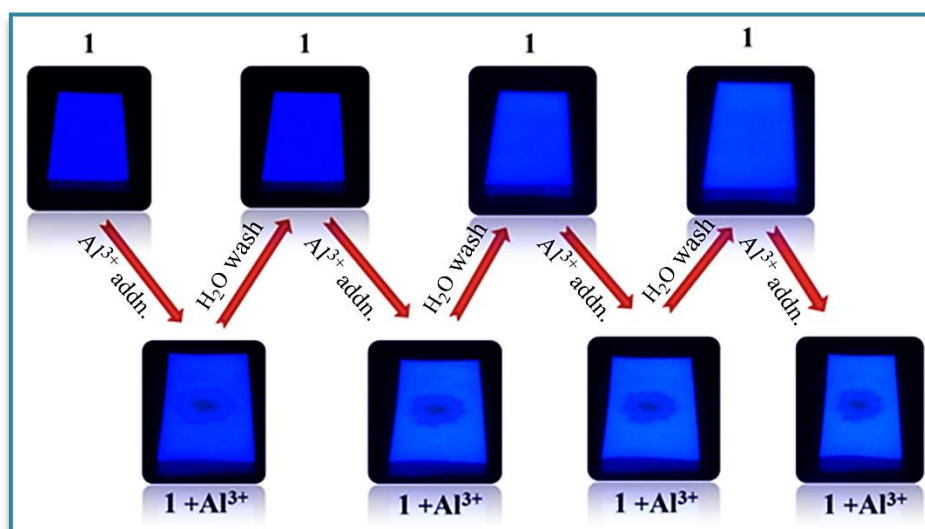


Figure 4.16 Paper strip experiment for recyclability of Zn-MOF (**1**) towards Al^{3+} sensing.

4.3.5 Sensing of Nitroaromatics (NAs)

In a search for the efficiency of fluorophore **1** in the service of mankind we found its suitability for the sensing of nitroaromatics (NAs). NA analytes (38.1 μM), such as picric acid (PA), 2,4,6-trinitrophenol (TNP), 4-nitrophenol (4-NP), 2-nitrophenol (2-NP), 2,4-dinitrophenol (2,4-DNP), nitrobenzene (NB), 1,3-dinitrobenzene (1,3-DNB), 1,4-dinitrobenzene (1,4-DNB), 4-nitrotoluene (4-NT), 2,4-dinitrotoluene (2,4-DNT), 4-nitroaniline (4-NA), 3-nitrobenzoic acid (3-NBA), 5-nitrosalicylic acid (5-NSA), or 3,5-dinitrobenzoic acid (3,5-DNBA), were injected into a well-dispersed suspension of **1** (10 μM) in acetonitrile media and the observed fluorescence quenching efficiency follows the order: $\text{TNP} > 4\text{-NA} > 2,4\text{-DNP} > 2,4\text{-DNT} > 5\text{-NSA} > 1,4\text{-DNB} > 2\text{-NP} > 3,5\text{-DNBA} > 3\text{-NBA} > 1,3\text{-DNB} > 4\text{-NP} > \text{NB} > 4\text{-NT}$. The highest quenching rate (97.8%) is detected for TNP (Figure 4.17a). A continuous decrease in luminescence intensity at 417 nm was observed with increasing concentration of TNP, along with the generation of a new band at 479 nm (Figure 4.17b). The quenching phenomena may be considered via a combination of PET (photoinduced electron transfer) and FRET (fluorescence resonance energy transfer) (Figure 4.17c) between the analyte (TNP) and **1**.⁸⁶ The Stern-Volmer plot is linear up to 20 μM of

[TNP] and then shows upward deviation (Figure 4.17d), which indicates that, with increasing concentration of quencher, both static and dynamic quenching processes are operating.⁸⁷

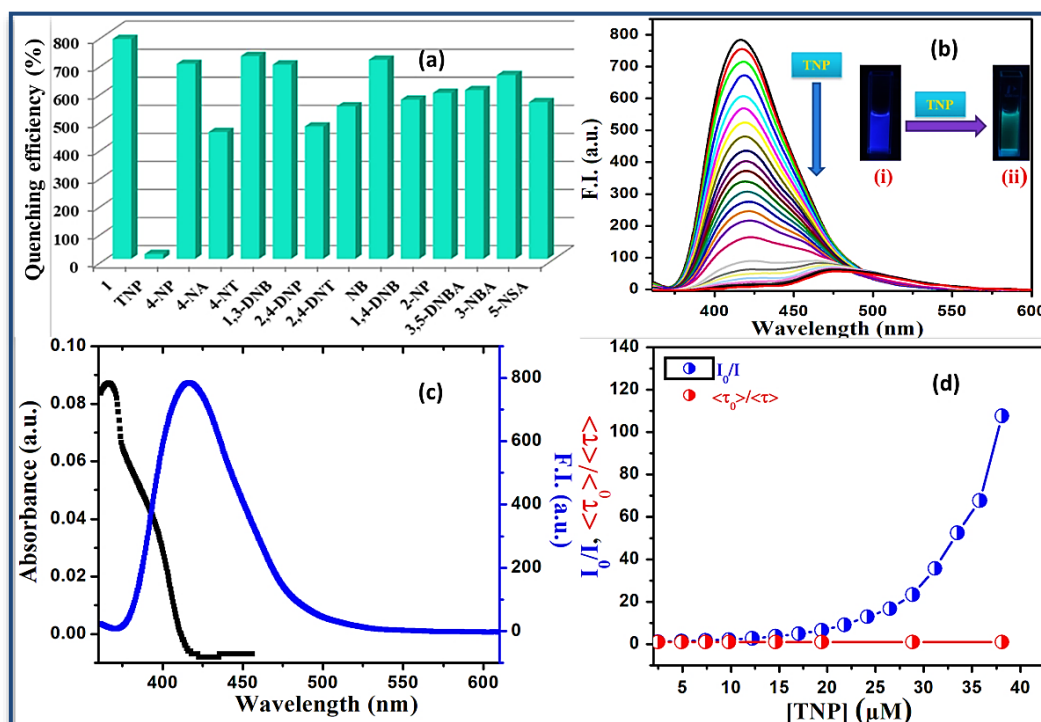


Figure 4.17 (a) Quenching efficiency of NAs toward the emission of **1**. (b) Luminescence spectra of **1** (10 μM) in acetonitrile upon the incremental addition of TNP solution (0-38.1 μM); inset: fluorescence images of cuvettes filled with acetonitrile suspensions of **1** under UV light ($\lambda = 365$ nm) before TNP addition (i) and after TNP addition (ii). (c) Overlapping of absorption spectra of TNP with emission spectra of **1**. (d) Steady-state (I_0/I , blue) and time-resolved ($\langle\tau_0\rangle/\langle\tau\rangle$, red) Stern-Volmer plots.

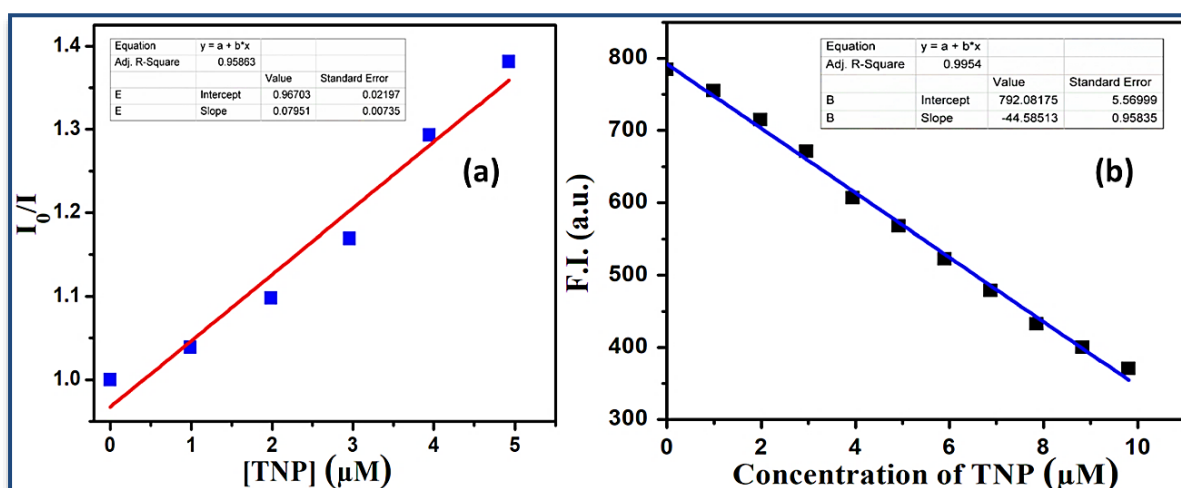


Figure 4.18 (a) Stern-Volmer plot of **1** at lower range of quencher [TNP] (in μM) concentration. (b) The linear dynamic response of **1** for TNP and the determination of the limit of detection (LOD) of TNP.

At lower TNP concentrations, K_{sv} is $0.8 \times 10^5 \text{ M}^{-1}$ (the linear section of the S-V plot (Figure 4.18a) and this is one of the highest values for MOF-based sensor materials reported so far.^{65,66,86,88-91} Moreover, it exhibits excellent sensitivity for detecting analytes at extremely low concentrations, with a limit of detection (LOD) of $1.54 \times 10^{-7} \text{ M}$ (Figure 4.18b). The progressive addition of TNP was followed in the time-resolved instrument to evaluate the lifetime of the composite $[1+\text{Al}^{3+}]$ and it was observed that the fluorescence lifespan of **1** remained unchanged with the progressive addition of TNP (Figure 4.19, Table 4.4). Thus, the presence of a static quenching mechanism is inferred, and the amount of quenching is considerable at higher TNP concentrations.

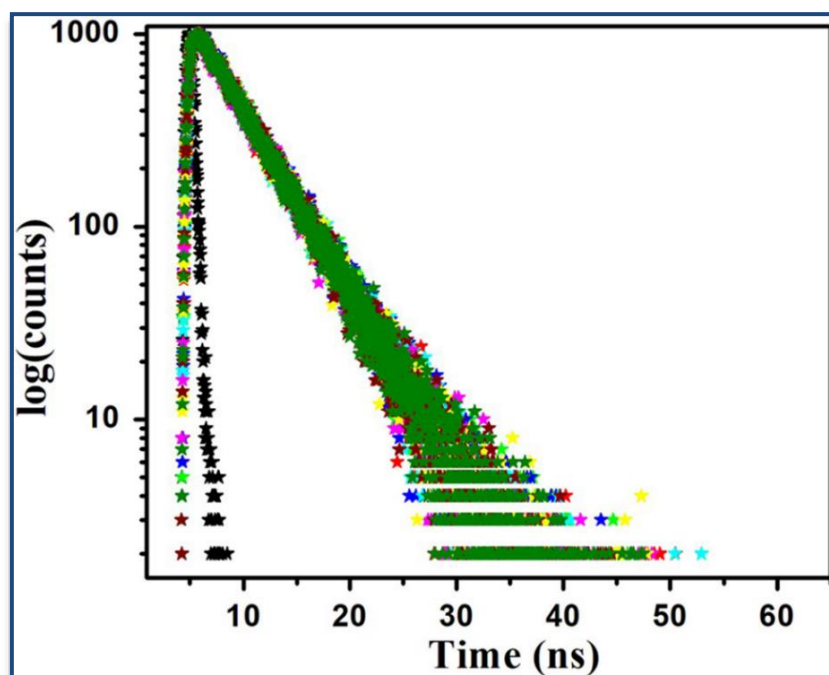


Figure 4.19 Representative fluorescence decay spectra of **1** ($10 \mu\text{M}$) in the absence and presence of increasing concentration of TNP. Spectra 1-9 corresponds to the TNP concentration $0 \mu\text{M}$ (red star), $2.47 \mu\text{M}$ (green star), $4.93 \mu\text{M}$ (blue star), $7.37 \mu\text{M}$ (cyan star), $9.80 \mu\text{M}$ (magenta star), $14.63 \mu\text{M}$ (yellow star), $19.42 \mu\text{M}$ (wine star), $28.85 \mu\text{M}$ (navy star), $38.10 \mu\text{M}$ (olive star), respectively.

Table 4.4 Fluorescence lifetime decay parameters of **1** ($10 \mu\text{M}$) with gradual addition of TNP.

TNP (μM)	τ (ns)	CHISQ
0	4.67	1.245963
2.47	4.60	1.214508
4.93	4.57	1.237810
7.37	4.61	1.178241
9.80	4.57	1.231402

14.63	4.59	1.283751
19.42	4.58	1.187734
28.85	4.55	1.275290
38.10	4.55	1.275290

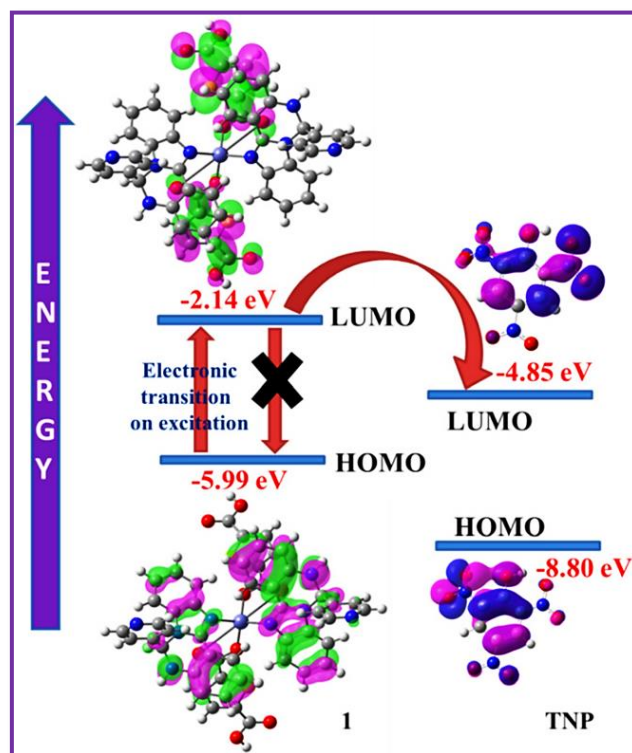


Figure 4.20 Energy transfer quenching mechanism: a possible pathway.

The MOs of **1** and TNP were estimated from optimized geometries to aid the fluorescence quenching. The relative orbital energies of the HOMO (-5.99 eV for **1**; -8.80 eV for TNP) and the LUMO (-2.14 eV for **1**; -4.85 eV for TNP) show that the HOMOs of **1** and TNP have a substantially higher energy difference (2.81 eV) than the LUMOs (2.71 eV). As a result, energy may be transferred from the excited state of **1** to the ground state of TNP (Figure 4.20).⁶⁶

Even in the presence of several lower pH solutions (pH = 2-7) (Figure 4.21), the emission intensity of **1** remains unchanged, which implies structural durability under acidic conditions. The PXRD pattern of the material produced after 4 h of immersion in a low pH solution (3.5-5.5) is identical to that of the untreated compound (Figure 4.7). Based on these experimental findings, it is inferred that the molecular network is stable even under acidic conditions; the framework's architectural integrity remains intact throughout TNP sensing.

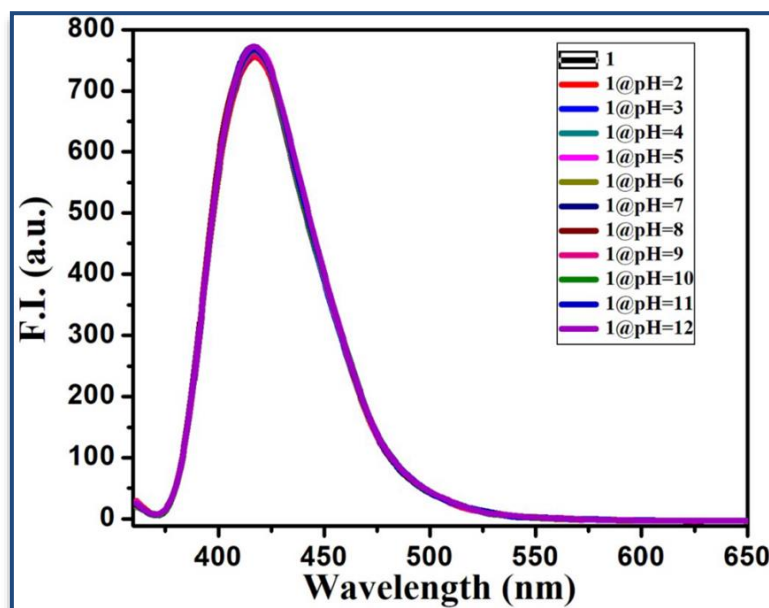


Figure 4.21 Emission spectra of **1** in presence of different pH solutions.

4.3.6 Optical Characterization

The optical band gap (E_g) was calculated using Tauc's equation (eq 1).⁹²

$$(\alpha h\nu) = A(h\nu - E_g)^n \dots \dots \dots (1)$$

where α , E_g , h and ν stands for absorption coefficient, band gap, Planck's constant and frequency of light. The exponent ' n ' is the electron transition processes dependent constant. 'A' is a constant which is considered as 1 for ideal case. To calculate the direct optical bandgap the value of the exponent ' n ' in the above equation has been considered as $n = \frac{1}{2}$.⁹² By extrapolating the linear region of the plot $(\alpha h\nu)^2$ vs. $h\nu$ to $\alpha = 0$ absorption, the values of optical direct band gap (E_g) have been calculated as 3.33 eV for produced compound **1** (Figure 4.22).

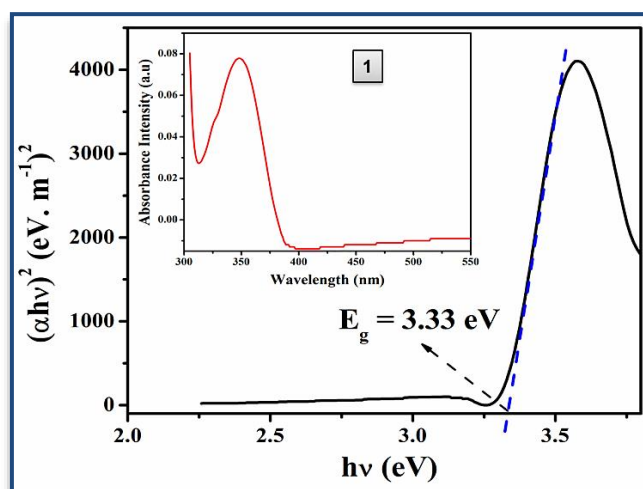


Figure 4.22 Optical band gap (E_g) and UV-Vis absorption spectra (inset) for **1**.

4.3.7 Electrical Characterization

Synthesized compound **1** belongs to the semiconductor family. A thin film device consisting of metal (Al)-semiconductor (synthesized compound) (MS) junction (**TFD 1**) has been fabricated.⁶⁶ The I - V plot (**Figure 4.23**) of the device was recorded at room temperature (26 °C) in the absence of light and also in the presence of photo-irradiation (intensity of light was $\sim 100 \text{ mW cm}^{-2}$) at an applied bias voltage sequentially within the limit of $\pm 2 \text{ V}$ to investigate its electrical properties. The calculated electrical conductivity was $11.40 \times 10^{-4} \text{ S m}^{-1}$ in the dark and after exposure to light, the conductivity had improved to $53.50 \times 10^{-4} \text{ S m}^{-1}$. The considerable improvement (nearly 5 times) in conductivity upon light irradiation may be explained by “hopping transport” between isolated molecules or coordination centers and these charge transfer transitions in the molecules facilitate intramolecular charge separation.⁹³

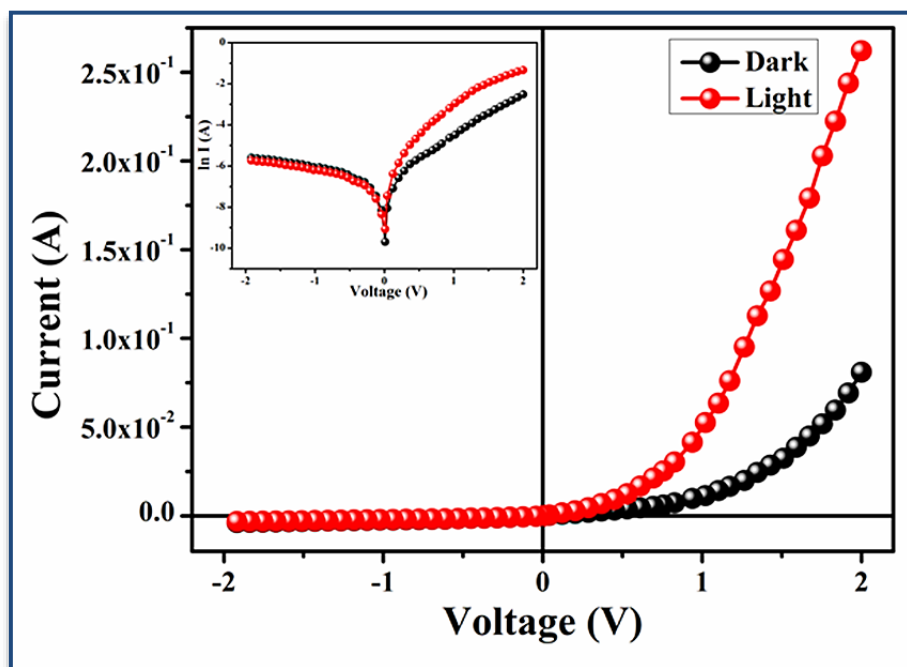


Figure 4.23 I - V characteristic curve under dark and photoillumination conditions.

The nonlinear I - V plots show rectifying behavior under both dark and photo illumination conditions. The current-voltage characteristic of **TFD 1** shows the formation of a Schottky barrier diode (SBD) at the Al/compound interface. The rectification ratios ($I_{\text{on}}/I_{\text{off}}$) at $\pm 2 \text{ V}$ were found to be 21.68 (dark) and 81.42 (light) for **TFD 1**. The larger current from the characteristic curve under irradiation conditions establishes that **TFD 1** is photo-responsive, which has been estimated as 3.24 for **TFD 1**. Further analysis of the I - V characteristic for **TFD 1** was performed by thermionic emission theory. Important diode parameters were also extracted by employing Cheung's method.^{92,94-96}

$$I = I_0 \exp\left(\frac{qV}{\eta kT}\right) \left[1 - \exp\left(\frac{-qV}{\eta kT}\right)\right] \dots\dots\dots (2)$$

$$I_0 = AA^*T^2 \exp\left(\frac{-q\phi_B}{kT}\right) \dots\dots\dots (3)$$

where, I_0 , k , T , V , A , η and A^* stands for saturation current, electronic charge, Boltzmann constant, temperature in Kelvin, forward bias voltage, effective diode area, ideality factor and effective Richardson constant, respectively. The effective diode area has been estimated as $7.065 \times 10^{-2} \text{ cm}^2$ and the effective Richardson constant has been considered as $32 \text{ AK}^{-2} \text{ cm}^{-2}$ for all the devices.

The ideality factor (η) for **TFD 1** under both conditions was calculated from the intercept of $dV/d \ln I$ vs I plot (**Figure 4.24a**). On the other hand, the series resistance (R_s) of the devices was calculated from the slope of this plot. **Table 4.5** lists the values of the ideality factors of **TFD 1** in dark and light. The series resistance, ideality factor and barrier potential height was also determined by using equations 4 to 6, which was extracted from Cheung's idea,^{95,96}

$$\frac{dV}{d(\ln I)} = \left(\frac{\eta kT}{q}\right) + IR_s \dots\dots\dots (4)$$

$$H(I) = V - \left(\frac{\eta kT}{q}\right) \ln\left(\frac{I}{AA^*T^2}\right) \dots\dots\dots (5)$$

$$H(I) = IR_s + \eta \phi_B \dots\dots\dots (6)$$

The values of the ideality factor (η) were estimated as 2.66 (dark) and 1.96 (light) for **TFD 1**. The deviation from the ideal value (~ 1) indicates the inhomogeneities in the Schottky barrier height and the presence of interface states as well as series resistance at the junction.^{97,98} It is noteworthy that the ideality factors of **TFD 1** decrease upon light irradiation. This indicates lower numbers of recombined charge carriers at the interface, and the formation of better homogeneity at the barrier of Schottky junctions.⁹² It may therefore be concluded that **TFD 1** possesses better barrier homogeneity, i.e. less carrier recombination at the junction, when photo-irradiated.

The barrier height (ϕ_B), estimated from the intercept of $H(I)$ vs current plot (**Figure 4.24b** and **Table 4.5**), decreases upon exposure to light (0.57 (dark), 0.49 (light)), as does the ideality factor (η) (2.66 (dark), 1.96 (light)) (**eq 6**). The reason for this reduction is probably the formation of photo-induced charge transporters and their gathering in the vicinity of the conduction band. The decrease in series resistance (R_s : 813.83 (dark), 490.86 (light)) upon irradiation indicates the potential utility of the complex-based devices in optoelectronics.

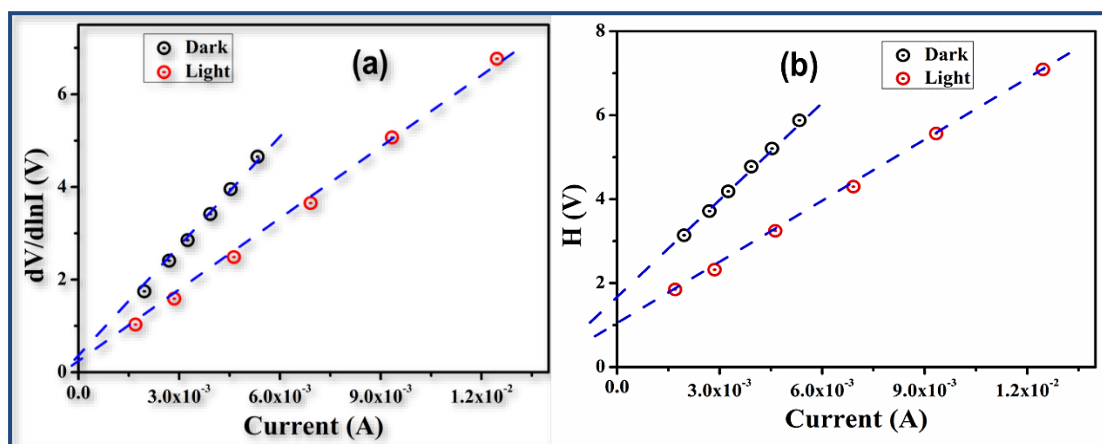


Figure 4.24 (a) A plot of $dV/d\ln I$ vs I curves with and without illumination. (b) H vs I curves for TFD 1 in dark and light.

The plots of $\ln I$ vs $\ln V$ are more straightforward for examining the impact of light on the device (TFD 1) (Figure 4.25a). Two different slopes can clearly be observed and may be marked as regions I and II. The slope, ~ 1 for region-I indicates the ohmic regime and follows $I \propto V$. The value of the slope is about 2 in region-II and follows $I \propto V^2$ (Figure 4.25a). This may be considered a trap-free space charge limited current (SCLC) regime.^{92,99} If the background carriers are fewer than the injected carriers, a space charge field is generated by the spreading of the injected carriers. This space charge field controls the currents and hence the current is called a space charge limited current or SCLC.^{92,99} The Mott-Gurney equation may be used to estimate the effective carrier mobility from the higher voltage section of the I vs V^2 plot (Figure 4.25b):^{92,96,99}

$$I = \frac{9\mu_{eff}\epsilon_0\epsilon_r A}{8} \left(\frac{V^2}{d^3} \right) \dots \dots \dots (7)$$

where ϵ_0 , ϵ_r , μ_{eff} and I indicate the permittivity of free space, relative dielectric constant of the synthesized material, effective mobility and current, respectively.

The dielectric constant of the material (ϵ_r) can be calculated from the saturation region of the capacitance vs. frequency curve at higher frequency with the equation given below:⁹²

$$\epsilon_r = \frac{1}{\epsilon_0} \cdot \frac{C d}{A} \dots \dots \dots (8)$$

where, C , d , and A are the capacitance at saturation, the thickness of the film ($\sim 1 \mu\text{m}$) and the device area, respectively. With this formula, we obtain ϵ_r values of 6.02×10^{-2} for our synthesized compound 1.

Table 4.5 Schottky Device Parameters of **TFD 1**

Condition	On/Off	Conductivity (S.m ⁻¹)	Photo sensitivity	Ideality factor	Barrier height (eV)	R _S from dV/dlnI (Ω)	R _S from H (Ω)
Dark	21.68	11.40 × 10 ⁻⁴	3.24	2.66	0.57	857.62	813.83
Light	81.42	53.50 × 10 ⁻⁴		1.96	0.49	535.39	490.86

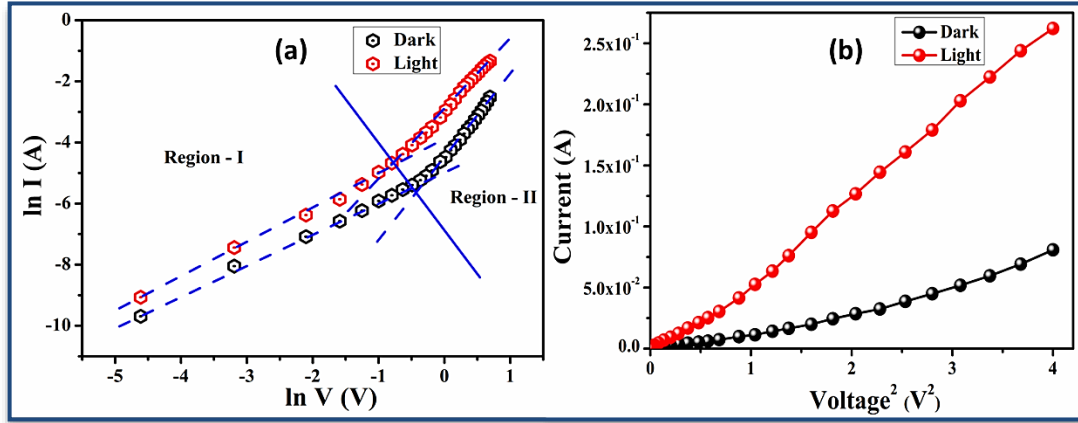


Figure 4.25 (a) $\ln I$ vs $\ln V$ curves for **TFD 1** under dark and irradiation conditions. (b) I vs V^2 curves for **TFD 1** with and without illumination.

The capacitance vs frequency plot at a constant bias potential (**Figure 4.26**) was used to measure the relative dielectric constant,¹⁰⁰ which was estimated as 3.66×10^{-1} for **TFD 1**. The estimated transit time (τ) and diffusion length (L_D) are also helpful for analyzing charge transport across the junction. The slope of the SCLC region (region-II) in a logarithmic representation of the forward current-voltage curve (**Figure 4.25a**) was used to evaluate τ from eq 9.⁹²

$$\tau = \frac{9\epsilon_0\epsilon_r A}{8d} \left(\frac{V}{I} \right) \dots \dots \dots (9)$$

$$\mu_{eff} = \frac{qD}{kT} \dots \dots \dots (10)$$

$$L_D = \sqrt{2D\tau} \dots \dots \dots (11)$$

where, D stands for diffusion coefficient that can be determined using Einstein-Smoluchowski equation (eq 10).⁶²

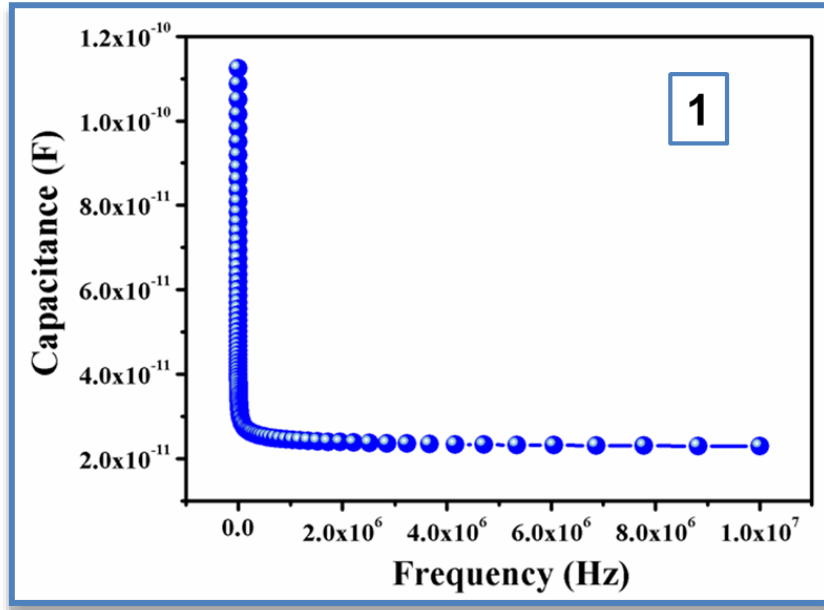


Figure 4.26 Capacitance vs Frequency graph of TFD 1.

Table 4.5 Charge Conducting Parameters of TFD 1.

Condition	ϵ_r	μ_{eff} ($\text{m}^2\text{V}^{-1}\text{s}^{-1}$)	τ (sec)	$\mu_{eff}\tau$	D	L_D (m)
Dark	3.66×10^{-1}	9.01×10^{-4}	3.65×10^{-10}	3.29×10^{-13}	2.32×10^{-5}	1.30×10^{-7}
Light		4.89×10^{-3}	1.14×10^{-10}	5.56×10^{-13}	1.26×10^{-4}	1.69×10^{-7}

The diffusion length (L_D ; eq 11) of the charge carriers plays an influential role in device performance when a metal semiconductor junction is formed. The charge transport properties of the material are improved after light exposure. This is indicated by all the parameters estimated in the SCLC region (Table 4.5). A higher transport rate under irradiation is implied from the higher mobility. On the other hand, on photoirradiation, the numbers of charge carriers are also increased. As the diffusion length is increased under illumination, the charge carriers may travel a longer path before being recombined. This ultimately enhances the current. The better performance on photo-irradiation signifies the enhanced charge transfer kinetics of TFD 1, which is encouraging for its application in semiconductor devices.

4.4 Conclusions

In conclusion, we have developed a π -electron-rich rigid heterocyclic moiety containing multiple coordinating sites for the construction of novel frameworks. Herein, we report the first structural characterization of a 3D Zn-MOF, $[\text{Zn}_2(\text{tdc})_4(\text{pdiq})_3]$ based upon pyridinyl imidazoquinazoline. It is noteworthy that the 3D Zn-MOF is a multiresponsive chemosensor, showing high selectivity and sensitivity towards the detection of Al^{3+} and TNP with detection limits of 0.139 and 0.154 μM , respectively. It is possible that the interactions between the heterocyclic-N of the imidazoquinazoline rings and the Al^{3+} ions may facilitate a more efficient transition from the ligand to Zn^{2+} ions, leading to a turn-off ratiometric luminescence. In the same way, an electron and resonance energy transfer between the CPs and the analyte was determined to be the possible fluorescence quenching mechanism of NAs. The band gap (3.33 eV (experimental), 3.85 eV (DFT computation)) in the 3D framework exhibits substantial enhancement of electrical conductivity upon exposure to light, and higher mobility in the network could be attributed to its lower barrier height and series resistance. Thus, this work offers a promising approach for designing a dual-functional CP sensor for both Al^{3+} ions and NAs, and for fabricating optoelectronic devices.

4.5 References

- (1) Zhou, H. C.; Long, J. R.; Yaghi, O. M. Introduction to metal-organic frameworks. *Chem. Rev.* **2012**, *112*, 673-674.
- (2) Zhou, H. C. Joe.; Kitagawa, S. Metal-Organic Frameworks (MOFs). *Chem. Soc. Rev.* **2014**, *43*, 5415-5418.
- (3) Li, J. R.; Kuppler, R. J.; Zhou, H. C. Selective gas adsorption and separation in metal-organic frameworks. *Chem. Soc. Rev.* **2009**, *38*, 1477-1504.
- (4) Murray, L. J.; Dincă, M.; Long, J. R. Hydrogen storage in metal-organic frameworks. *Chem. Soc. Rev.* **2009**, *38*, 1294-1314.
- (5) Kurmoo, M. Magnetic metal-organic frameworks. *Chem. Soc. Rev.* **2009**, *38*, 1353-1379.
- (6) Hoskins, B. F.; Robson, R. Design and construction of a new class of scaffolding-like materials comprising infinite polymeric frameworks of 3D-linked molecular rods. A reappraisal of the zinc cyanide and cadmium cyanide structures and the synthesis and structure of the diamond-related frameworks $[\text{N}(\text{CH}_3)_4][\text{Cu}^{\text{I}}\text{Zn}^{\text{II}}(\text{CN})_4]$ and

- $\text{Cu}^{\text{I}}[4,4',4'',4''']\text{-tetracyanotetraphenylmethane}]\text{BF}_4 \cdot x\text{C}_6\text{H}_5\text{NO}_2$. *J. Am. Chem. Soc.* **1990**, *112*, 1546-1554.
- (7) Xie, L. S.; Skorupskii, G.; Dincă, M. Electrically conductive metal-organic frameworks. *Chem. Rev.* **2020**, *120*, 8536-8580.
 - (8) Ahmed, F.; Dutta, B.; Mir, M. H. Electrically conductive 1D coordination polymers: design strategies and controlling factors. *Dalton Trans.* **2021**, *50*, 29-38.
 - (9) Panda, T.; Kundu, T.; Banerjee, R. Structural isomerism leading to variable proton conductivity in Indium(III) Isophthalic acid based frameworks. *Chem. Commun.* **2013**, *49*, 6197-6199.
 - (10) Samanta, D.; Mukherjee, P. S. Structural diversity in multinuclear Pd (II) assemblies that show low-humidity proton conduction. *Chem. -Eur. J.* **2014**, *20*, 5649-5656.
 - (11) Kreno, L. E.; Leong, K.; Farha, O. K.; Allendorf, M.; Van Duyne, R. P.; Hupp, J. T. Metal-organic framework materials as chemical sensors. *Chem. Rev.* **2012**, *112*, 1105-1125.
 - (12) Cui, Y.; Yue, Y.; Qian, G.; Chen, B. Luminescent functional metal-organic frameworks. *Chem. Rev.* **2012**, *112*, 1126-1162.
 - (13) Lee, J.; Farha, O. K.; Roberts, J.; Scheidt, K. A.; Nguyen, S. T.; Hupp, J. T. Metal-organic framework materials as catalysts. *Chem. Soc. Rev.* **2009**, *38*, 1450-1459.
 - (14) Liu, J.; Chen, L.; Cui, H.; Zhang, J.; Zhang, L.; Su, C. Y. Applications of metal-organic frameworks in heterogeneous supramolecular catalysis. *Chem. Soc. Rev.* **2014**, *43*, 6011-6061.
 - (15) Taylor-Pashow, K. M. L.; Rocca, J. D.; Xie, Z. G.; Tran, S.; Lin, W. Postsynthetic Modifications of Iron-Carboxylate Nanoscale Metal-Organic Frameworks for Imaging and Drug Delivery. *J. Am. Chem. Soc.* **2009**, *131*, 14261-14263.
 - (16) Horcajada, P.; Chalati, T.; Serre, C.; Gillet, B.; Sebrie, C.; Baati, T.; Eubank, J. F.; Heurtaux, D.; Clayette, P.; Kreuz, C.; Chang, J. S.; Hwang, Y. K.; Marsaud, V.; Bories, Y.-N.; Cynober, L.; Gil, S.; Férey, G.; Couvreur, P.; Gref, R. Porous metal-organic framework nanoscale carriers as a potential platform for drug delivery and imaging. *Nat. Mater.* **2010**, *9*, 172-178.
 - (17) Eddaoudi, M.; Moler, D. B.; Li, H.; Chen, B.; Reineke, T. M.; O'Keeffe, M.; Yaghi, O. M. Assembly of metal-organic frameworks from large organic and inorganic secondary building units: new examples and simplifying principles for complex structures. *Acc. Chem. Res.* **2001**, *34*, 319-330.

- (18) Moulton, B.; Zaworotko, M. J. From molecules to crystal engineering: supramolecular isomerism and polymorphism in network solids. *Chem. Rev.* **2001**, *101*, 1629-1658.
- (19) Tulsy, E. G.; Long, J. R. Dimensional reduction: a practical formalism for manipulating solid structures. *Chem. Mater.* **2001**, *13*, 1149-1166.
- (20) Stock, N.; Biswas, S. Synthesis of metal-organic frameworks (MOFs): routes to various mof topologies, morphologies, and composites, *Chem. Rev.* **2011**, *112*, 933-969.
- (21) Allendorf, M. D.; Bauer, C. A.; Bhakta, R. K.; Houk, R. J. T. Luminescent metal-organic frameworks. *Chem. Soc. Rev.* **2009**, *38*, 1330-1352.
- (22) Chen, B.; Xiang, S.; Qian, G. Metal-Organic Frameworks with Functional Pores for Recognition of Small Molecules. *Acc. Chem. Res.* **2010**, *43*, 1115-1124.
- (23) Kreno, L. E.; Leong, K.; Farha, O. K.; Allendorf, M.; Van Duyne, R. P.; Hupp, J. T. Metal-Organic Framework Materials as Chemical Sensors. *Chem. Rev.* **2012**, *112*, 1105-1125.
- (24) Cui, Y.; Chen, B.; Qian, G. Lanthanide metal-organic frameworks for luminescent sensing and light-emitting applications. *Coord. Chem. Rev.* **2014**, *273*, 76-86.
- (25) Müller-Buschbaum, K.; Beuerle, F.; Feldmann, C. MOF based luminescence tuning and chemical/physical sensing. *Microporous Mesoporous Mater.* **2015**, *216*, 171-199.
- (26) Mehta, P. K.; Hwang, G. W.; Park, J.; Lee, K. H. Highly sensitive ratiometric fluorescent detection of Indium(III) using fluorescent probe based on phosphoserine as a receptor. *Anal. Chem.* **2018**, *90*, 11256-11264.
- (27) Chen, D. M.; Sun, C. X.; Peng, Y.; Zhang, N. N.; Si, H. H.; Liu, C. S.; Du, M. Ratiometric fluorescence sensing and colorimetric decoding methanol by a bimetallic lanthanide-organic framework. *Sens. Actuators, B* **2018**, *265*, 104-109.
- (28) Liu, W.; Dai, X.; Wang, Y. L.; Song, L. P.; Zhang, L. J.; Zhang, D.; Xie, J.; Chen, L.; Wu, J. D.; Wang, J. Q.; Chai, Z. F.; Wang, S. Ratiometric monitoring of thorium contamination in natural water using a dual-emission luminescent europium organic framework. *Environ. Sci. Technol.* **2019**, *53*, 332-341.
- (29) Yoo, J.; Ryu, U. J.; Kwon, W.; Choi, K. M. A multi-dye containing MOF for the ratiometric detection and simultaneous removal of $\text{Cr}_2\text{O}_7^{2-}$ in the presence of interfering ions. *Sens. Actuators, B* **2019**, *283*, 426-433.

- (30) Li, L.; Cheng, J. H.; Liu, Z. P.; Song, L.; You, Y. J.; Zhou, X. H.; Huang, W. Ratiometric luminescent sensor of picric acid based on the dual emission mixed-lanthanide coordination polymer. *ACS Appl. Mater. Interfaces* **2018**, *10*, 44109-44115.
- (31) Dai, Y.; Zhang, J. J.; Liu, S. Q.; Zhou, H. J.; Sun, Y. J.; Pan, Y. Z.; Ni, J.; Yang, J. S. A trichromatic and white-light-emitting MOF composite for multi-dimensional and multi-response ratiometric luminescent sensing. *Chem. - Eur. J.* **2018**, *24*, 9555-9564.
- (32) Wang, X. R.; Huang, Z.; Du, J.; Wang, X. Z.; Gu, N.; Tian, X.; Li, Y.; Liu, Y. Y.; Huo, J. Z.; Ding, B. Hydrothermal preparation of five rare-earth (Re = Dy, Gd, Ho, Pr, and Sm) luminescent cluster-based coordination materials: the first MOFs-based ratiometric fluorescent sensor for Lysine and bifunctional sensing platform for Insulin and Al^{3+} . *Inorg. Chem.* **2018**, *57*, 12885-12899.
- (33) Wu, Z. F.; Tan, B.; Gong, L. K.; Zhang, X.; Wang, H.; Fang, Y.; Hei, X. Z.; Zhang, Z. Z.; Zhang, G. Y.; Huang, X. Y.; Li, J. A Cu^{I} modified Mg-coordination polymer as a ratiometric fluorescent probe for toxic thiol Molecules. *J. Mater. Chem. C* **2018**, *6*, 13367-13374.
- (34) Yu, Y. E.; Wang, Y.; Yan, H.; Lu, J.; Liu, H.; Li, Y.; Wang, S.; Li, D.; Dou, J.; Yang, L.; Zhou, Z. Multiresponsive Luminescent Sensitivities of a 3D Cd-CP with Visual Turn-on and Ratiometric Sensing toward Al^{3+} and Cr^{3+} as Well as Turn-off Sensing toward Fe^{3+} . *Inorg. Chem.* **2020**, *59*, 3828-3837.
- (35) Al- Ashmawy, M. A. Prevalence and public health significance of aluminum residues in milk and some dairy products. *J. Food Sci.* **2011**, *76*, T73-T76.
- (36) Gui, S.; Huang, Y.; Hu, F.; Jin, Y.; Zhang, G.; Yan, L.; Zhang, D.; Zhao, R. Fluorescence turn-on chemosensor for highly selective and sensitive detection and bioimaging of Al^{3+} in living cells based on ion-induced aggregation. *Anal chem.* **2015**, *87*, 1470-1474.
- (37) Reinke, C. M.; Breitzkreutz, J.; Leuenberger, H.; Aluminium in over-the-counter drugs. *Drug Saf.* **2003**, *26*, 1011-1025.
- (38) Wang, G. Q.; Zhao, Y. H.; Hao, Y. F. Friction stir welding of high-strength aerospace aluminum alloy and application in rocket tank manufacturing, *J. Mater. Sci. Technol.* **2018**, *34*, 73-91.
- (39) Krejpcio, Z.; Wojciak, R.W. The influence of Al^{3+} ions on pepsin and trypsin activity in vitro, *Polish J. Environ. Stud.* **2002**, *3*, 251-254.

- (40) Barcelo, J.; Poschenrieder, C. Fast root growth responses, root exudates, and internal detoxification as clues to the mechanisms of aluminium toxicity and resistance: a review. *Environ. Exp. Bot.* **2002**, 48, 75-92.
- (41) Good, P. F.; Olanow, C. W.; Perl, D. P. Neuromelanin-containing neurons of the substantia nigra accumulate iron and aluminum in Parkinson's disease: a LAMMA study. *Brain Res.* **1992**, 593, 343-346.
- (42) Fasman, G. D. Aluminum and Alzheimer's disease: model studies. *Coord. Chem. Rev.* **1996**, 149, 125-165.
- (43) Berthon, G.; Aluminium speciation in relation to aluminium bioavailability, metabolism and toxicity, *Coord. Chem. Rev.* **2002**, 228, 319-341.
- (44) Burwen, D. R.; Olsen, S. M.; Bland, L. A.; Arduino, M. J.; Reid, M. H.; Jarvis, W. R. Epidemic aluminum intoxication in hemodialysis patients traced to use of an aluminum pump. *Kidney Int.* **1995**, 48, 469-474.
- (45) Germain, M. E.; Knapp, M. J. Optical explosives detection: from color changes to fluorescence turn-on. *Chem. Soc. Rev.* **2009**, 38, 2543-2555.
- (46) Thomas III, S. W.; Joly, G. D.; Swager, T. M. Chemical Sensors Based on Amplifying Fluorescent Conjugated Polymers. *Chem. Rev.* **2007**, 107, 1339-1386.
- (47) Thorne, P. G.; Jenkins, T. F. A Field Method for Quantifying Ammonium Picrate and Picric Acid in Soil. *Field Anal. Chem. Technol.* **1997**, 1, 165-170.
- (48) Chahal, M. K.; Sankar, M. 1,8-Naphthyridine-based fluorescent receptors for picric acid detection in aqueous media, *Anal. Methods* **2015**, 7, 10272-10279.
- (49) Marvin-Sikkema, F. D.; de Bont, J. A. M. Degradation of nitroaromatic compounds by microorganisms. *Appl. Microbiol. Biotechnol.* **1994**, 42, 499-507.
- (50) Mantha, R.; Taylor, K. E.; Biswas, N.; Bewtra, J. K. A Continuous System for Fe⁰ Reduction of Nitrobenzene in Synthetic Wastewater. *Environ. Sci. Technol.* **2001**, 35, 3231-3236.
- (51) Xiao, J.-D.; Qiu, L.-G.; Ke, F.; Yuan, Y.-P.; Xu, G.-S.; Wang, Y.-M.; Jiang, X. Rapid synthesis of nanoscale terbium-based metal-organic frameworks by a combined ultrasound-vapour phase diffusion method for highly selective sensing of picric acid. *J. Mater. Chem. A* **2013**, 1, 8745-8752.
- (52) Mukherjee, S.; Desai, A. V.; Manna, B.; Inamdar, A. I.; Ghosh, S. K. *Cryst. Growth Des.* **2015**, 15, 4627-4634.

- (53) Hu, Z.; Deibert, B. J.; Li, J. Luminescent metal-organic frameworks for chemical sensing and explosive detection. *Chem. Soc. Rev.* **2014**, *43*, 5815-5840.
- (54) Rachuri, Y.; Parmar, B.; Bisht, K. K.; Suresh, E. Mixed ligand two dimensional Cd(II)/Ni(II) metal organic frameworks containing dicarboxylate and tripodal N-donor ligands: Cd(II) MOF is an efficient luminescent sensor for detection of picric acid in aqueous media. *Dalton Trans.* **2016**, *45*, 7881-7892.
- (55) Miner, E. M.; Fukushima, T.; Sheberla, D.; Sun, L.; Surendranath, Y.; Dincă, M. Electrochemical oxygen reduction catalysed by Ni₃(hexaiminotriphenylene)₂. *Nat. Commun.* **2016**, *7*, 1-7.
- (56) Sun, L.; Campbell, M. G.; Dinca, M. Electrically Conductive Porous Metal-Organic Frameworks. *Angew. Chem. Int. Ed.* **2016**, *55*, 3566-3579.
- (57) Liu, H.; Wang, Y.; Qin, Z.; Liu, D.; Xu, H.; Dong, H.; Hu, W. Electrically conductive coordination polymers for electronic and optoelectronic device applications. *J. Phys. Chem. Lett.* **2021**, *12*, 1612-1630.
- (58) Dutta, B.; Jana, R.; Sinha, C.; Ray, P. P.; Mir, M. H. Synthesis of a Cd (II) based 1D coordination polymer by in situ ligand generation and fabrication of a photosensitive electronic device. *Inorg. Chem. Front.* **2018**, *5*, 1998-2005.
- (59) Ghorai, P.; Dey, A.; Hazra, A.; Dutta, B.; Brandão, P.; Ray, P. P.; Banerjee, P.; Saha, A. Cd(II) Based Coordination Polymer Series: Fascinating Structures, Efficient Semiconductors, and Promising Nitro Aromatic Sensing. *Cryst. Growth Des.* **2019**, *19*, 6431-6447.
- (60) Ahmed, F.; Dutta, B.; Mir, M. H. Electrically conductive 1D coordination polymers: design strategies and controlling factors. *Dalton Trans.* **2021**, *50*, 29-38.
- (61) Naskar, K.; Dey, A.; Dutta, B.; Ahmed, F.; Sen, C.; Mir, M. H.; Roy, P. P.; Sinha, C. Intercatenated coordination polymers (ICPs) of carboxylato bridged Zn (II)-isoniazid and their electrical conductivity. *Crystal. Growth Design.* **2017**, *17*, 3267-3276.
- (62) Naskar, K.; Sil, S.; Sahu, N.; Dutta, B.; Slawin, A. M. Z.; Roy, P. P.; Sinha, C. Enhancement of Electrical Conductivity due to Structural Distortion from Linear to Nonlinear Dicarboxylato-Bridged Zn(II) 1D-Coordination Polymers. *Cryst. Growth Des.* **2019**, *19*, 2632-2641.
- (63) Jana, S.; Jana, R.; Sil, S.; Dutta, B.; Sato, H.; Roy, P. P.; Datta, A.; Akitsu, T.; Sinha, C. Influence of Axial Linkers on Polymerization in Paddle-Wheel Cu(II)

- Coordination Polymers for the Application of Optoelectronics Devices. *Cryst. Growth Des.* **2019**, *19*, 6283-6290.
- (64) Dutta, B.; Dey, A.; Sinha, C.; Ray, P. P.; Mir, M. H. Photochemical Structural Transformation of a Linear 1D Coordination Polymer Impacts the Electrical Conductivity. *Inorg. Chem.* **2018**, *57*, 8029-8032.
- (65) Dutta, B.; Hazra, A.; Dey, A.; Sinha, C.; Ray, P. P.; Banerjee, P.; Mir, M. H. Construction of a Succinate-Bridged Cd(II)-Based Two-Dimensional Coordination Polymer for Efficient Optoelectronic Device Fabrication and Explosive Sensing Application. *Cryst. Growth Des.* **2020**, *20*, 765-776.
- (66) Bairy, G.; Dey, A.; Dutta, B.; Ray, P. P.; Sinha, C. 2D Cd (II)-MOF of Pyridyl-Imidazoquinazoline: Structure, Luminescence, and Selective Detection of TNP and Fabrication of Semiconducting Devices. *Cryst. Growth Des.* **2022**, *22*, 3138-3147.
- (67) *SMART and SAINT*; Bruker AXS Inc.: Madison, WI, 1998.
- (68) *SADABS. Bruker AXS area detector scaling and absorption correction*; Bruker AXS Inc.: Madison, WI, 2014.
- (69) Sheldrick, G. M. A short history of SHELX. *Acta Crystallogr., Sect. A: Found. Crystallogr.* **2008**, *64*, 112-122.
- (70) Dolomanov, O. V.; Bourhis, L. J.; Gildea, R. J.; Howard, J. A. K.; Puschmann, H. OLEX2: A Complete Structure Solution, Refinement and Analysis Program. *J. Appl. Crystallogr.* **2009**, *42*, 339-341.
- (71) Bourhis, L. J.; Dolomanov, O. V.; Gildea, R. J.; Howard, J. A. K.; Puschmann, H. The Anatomy of a Comprehensive Constrained, Restrained Refinement Program for the Modern Computing Environment-Olex2 Dissected. *Acta Crystallogr., Sect. A: Found. Adv.* **2015**, *71*, 59-75.
- (72) Frisch, M. J.; Trucks, G. W.; Schlegel, H. B.; Scuseria, G. E.; Robb, M. A.; Cheeseman, J. R.; Scalmani, G.; Barone, V.; Mennucci, B.; Petersson, G. A.; Nakatsuji, H.; Caricato, M.; Li, X.; Hratchian, H. P.; Izmaylov, A. F.; Bloino, J.; Zheng, G.; Sonnenberg, J. L.; Hada, M.; Ehara, M.; Toyota, K.; Fukuda, R.; Hasegawa, J.; Ishida, M.; Nakajima, T.; Honda, Y.; Kitao, O.; Nakai, H.; Vreven, T.; Montgomery, J. A., Jr.; Peralta, J. E.; Ogliaro, F. M.; Bearpark, J.; Heyd, J.; Brothers, E.; Kudin, K. N.; Staroverov, V. N.; Kobayashi, R.; Normand, J.; Raghavachari, K.; Rendell, A.; Burant, J. C.; Iyengar, S. S.; Tomasi, J.; Cossi, M.; Rega, N.; Millam, J. M.; Klene, M.; Yazyev, O.; Austin, A. J.; Cammi, R.; Pomelli, C.; Ochterski, J. W.;

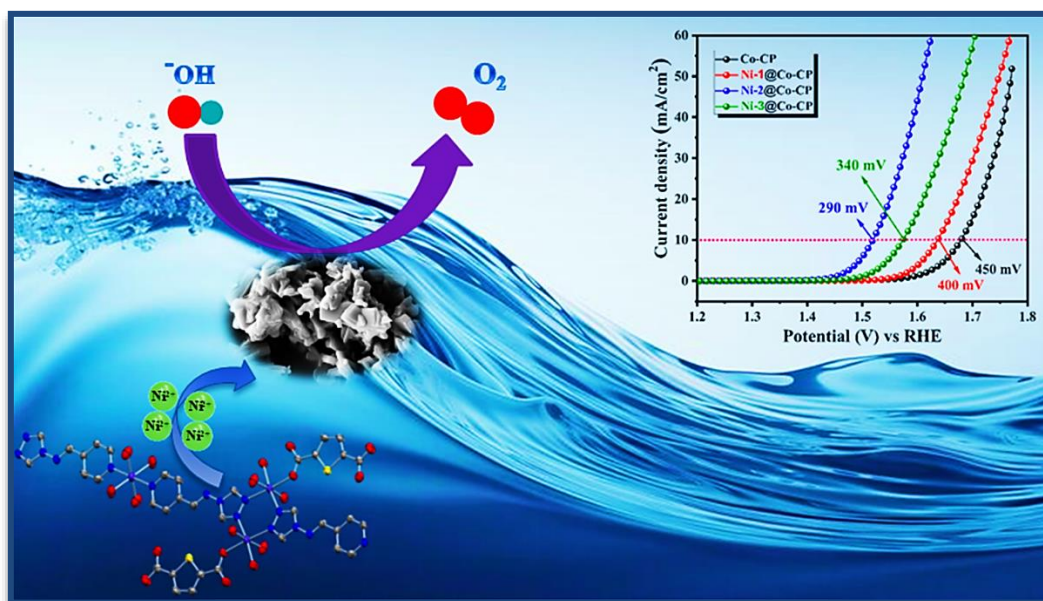
- Martin, R. L.; Morokuma, K.; Zakrzewski, V. G.; Salvador, G. A. P.; Dannenberg, J. J.; Dapprich, S.; Daniels, A. D.; Farkas, Ö.; Foresman, J. B.; Ortiz, J. V.; Cioslowski, J.; Fox, D. J. *Gaussian 09, revision D.01*; Gaussian, Inc.: Wallingford, CT, 2009.
- (73) Becke, A. D. Density-Functional Thermochemistry. III. The Role of Exact Exchange. *J. Chem. Phys.* **1993**, *98*, 5648-5652.
- (74) Bauernschmitt, R.; Ahlrichs, R. Treatment of electronic excitations within the adiabatic approximation of time dependent density functional theory. *Chem. Phys. Lett.* **1996**, *256*, 454-464.
- (75) Stratmann, R. E.; Scuseria, G. E.; Frisch, M. J. An efficient implementation of time-dependent density-functional theory for the calculation of excitation energies of large molecules. *J. Chem. Phys.* **1998**, *109*, 8218-8224.
- (76) Casida, M. E.; Jamorski, C.; Casida, K. C.; Salahub, D. R. Molecular excitation energies to high-lying bound states from time-dependent density-functional response theory: Characterization and correction of the time-dependent local density approximation ionization threshold. *J. Chem. Phys.* **1998**, *108*, 4439-4449.
- (77) O'Boyle, N. M.; Tenderholt, A. L.; Langner, K. M. CcLib: a Library for Package-independent Computational Chemistry Algorithms. *J. Comput. Chem.* **2008**, *29*, 839-845.
- (78) Bai, H. Y.; Ma, J. F.; Yang, J.; Liu, Y. Y.; Ma, J. C. Effect of anions on the self-assembly of Cd (II)-containing coordination polymers based on a novel flexible tetrakis (imidazole) ligand. *Cryst. Growth Des.* **2010**, *10*, 995-1016.
- (79) Zhu, Q. L.; Shen, C. J.; Tan, C. H.; Sheng, T. L.; Hua, S. M.; Wu, X. T. Bright blue emissions with temperature-dependent quantum yields from microporous metal-organic frameworks. *Chem. Commun.* **2012**, *48*, 531-533.
- (80) Zhang, X.; Luo, X.; Zhang, N.; Wu, J.; Huang, Y. Q. A highly selective and sensitive Zn(II) coordination polymer luminescent sensor for Al³⁺ and NACs in the aqueous phase. *Inorg. Chem. Front.* **2017**, *4*, 1888-1894.
- (81) Li, W. X.; Gu, J. H.; Li, H. X.; Dai, M.; Young, D. J.; Li, H. Y.; Lang, J. P. Post-synthetic modification of a two-dimensional metal-organic framework via photodimerization enables highly selective luminescent sensing of aluminum (III). *Inorg. Chem.* **2018**, *57*, 13453-13460.

- (82) Qiao, Y.; Li, Z.; Yu, M. H.; Chang, Z.; Bu, X. H. A metal-organic framework featuring highly sensitive fluorescence sensing for Al^{3+} ions. *CrystEngComm*. **2021**, 23, 8087-8092.
- (83) Wang, S. T.; Zheng, X.; Zhang, S. H.; Li, G.; Xiao, Y. A study of GUPT-2, a water-stable zinc-based metal-organic framework as a highly selective and sensitive fluorescent sensor in the detection of Al^{3+} and Fe^{3+} ions. *CrystEngComm*. **2021**, 23, 4059-4068.
- (84) Chand, S.; Verma, G.; Pal, A.; Pal, S. C.; Ma, S.; Das, M. C. Porous Anionic Co(II) Metal-Organic Framework, with a High Density of Amino Groups, as a Superior Luminescent Sensor for Turn- on Al(III) Detection. *Chem. -Eur. J.* **2021**, 27, 11804-11810.
- (85) Hou, B. L.; Tian, D.; Liu, J.; Dong, L. Z.; Li, S. L.; Li, D. S.; Lan, Y. Q. A Water-Stable Metal-Organic Framework for Highly Sensitive and Selective Sensing of Fe^{3+} Ion. *Inorg. Chem.* **2016**, 55, 10580-10586.
- (86) Asha, K. S.; Bhattacharyya, K.; Mandal, S. Discriminative detection of nitro aromatic explosives by a luminescent metal-organic framework. *J. Mater. Chem. C* **2014**, 2, 10073-10081.
- (87) Keizer, J. Nonlinear Fluorescence Quenching and the Origin of Positive Curvature in Stern-Volmer Plots. *J. Am. Chem. Soc.* **1983**, 105, 1494-1498.
- (88) Nagarkar, S. S.; Desai, A. V.; Ghosh, S. K. A fluorescent metal-organic framework for highly selective detection of nitro explosives in the aqueous phase. *Chem. Commun.* **2014**, 50, 8915-8918.
- (89) Nagarkar, S. S.; Joarder, B.; Chaudhari, A. K.; Mukherjee, S.; Ghosh, S. K. Highly Selective Detection of Nitro Explosives by a Luminescent Metal-Organic Framework. *Angew. Chem. Int. Ed.* **2013**, 52, 2881-2885.
- (90) Song, X. Z.; Song, S. Y.; Zhao, S. N.; Hao, Z. M.; Zhu, M.; Meng, X.; Wu, L. L.; Zhang, H. Single-Crystal-to-Single-Crystal transformation of a europium (III) metal-organic framework producing a multi- responsive luminescent sensor. *J. Adv. Funct. Mater.* **2014**, 24, 4034-4041.
- (91) Buragohain, A.; Yousufuddin, M.; Sarma, M.; Biswas, S. 3D luminescent amide-functionalized cadmium tetrazolate framework for selective detection of 2, 4, 6-trinitrophenol. *Cryst. Growth Des.* **2016**, 16, 842-851.

- (92) Dey, A.; Middy, S.; Jana, R.; Das, M.; Datta, J.; Layek, A.; Ray, P. P. Light Induced Charge Transport Property Analysis of Nanostructured ZnS Based Schottky Diode. *J. Mater. Sci. Mater. Electron.* **2016**, 27, 6325-6335.
- (93) Konar, S.; Dey, A.; Choudhury, S. R.; Das, K.; Chatterjee, S.; Ray, P. P.; Mukhopadhyay, S. Two Zinc (II)-Based Metal Complexes of New Pyrimidine Derived Ligand: Anion-Dependent Structural Variations and Charge Transport Property Analysis. *J. Phys. Chem. C* **2018**, 122, 8724-8734.
- (94) Rhoderick, E. H. *Metal Semiconductors Contacts*. Oxford University Press, Oxford. 1978.
- (95) Cheung, S. K.; Cheung, N. W. Extraction of Schottky diode parameters from forward current-voltage characteristics. *Appl. Phys. Lett.* **1986**, 49, 85-87.
- (96) Dey, A.; Layek, A.; Roychowdhury, A.; Das, M.; Datta, J.; Middy, S.; Das, D.; Ray, P. P. Investigation of Charge Transport Properties in Less Defective Nanostructured ZnO Based Schottky Diode. *RSC Adv.* **2015**, 5, 36560-36567.
- (97) Gupta, R. K.; Yakuphanoglu, F. Photoconductive Schottky diode based on Al/p-Si/SnS₂/Ag for optical sensor applications. *Sol. Energy* **2012**, 86, 1539-1545.
- (98) Miao, X.; Tongay, S.; Petterson, M. K.; Berke, K.; Rinzler, A. G.; Appleton, B. R.; Hebard, A. F. High Efficiency Graphene Solar Cells by Chemical Doping. *Nano Lett.* **2012**, 12, 2745- 2750.
- (99) Blom, P. W. M.; de Jong, M. J. M.; van Munster, M. G. Electric-field and temperature dependence of the hole mobility in poly(p-phenylenevinylene). *Phys. Rev. B* **1997**, 55, R656-R659.
- (100) Dey, A.; Ray, S. K. Analysis of Photoresponse and Charge Transport Properties of Hydrothermally Synthesized ZnSe Nanoparticle Based Schottky Device. *Int. J. Adv. Sci. Eng.* **2020**, 6, S2-1-S2-6.

Chapter 5

Triazolyl-pyridylimine bridging 1D Co(II) redox coordination polymer and its Ni-composite: Structure, surface characterisation and application in the water splitting reaction



Abstract:

Energy crisis is the deadly signal to the modern society. Paradigm shift of energy generation towards non-carbon sources has been a notable surge in research dedicated to the advancement of electrocatalytic H₂ generation reactions. To search for new materials towards the solution of energy crisis and to regulate C-precipitation as a part of Sustainable Development Goals (SDGs) the use of Coordination polymers have appeared as an emergent field due to their consistent porosity and the presence of coordinatively unsaturated metal sites. These materials attribute their remarkable resilience and effectiveness as oxygen evolution reaction (OER) catalysts. In this work, a Co(II)-based redox-active coordination polymer (Co-CP) is synthesised using (*E*)-*N*-(pyridin-4-ylmethylene)-4*H*-1,2,4-triazol-4-amine (pmta) as unsymmetric bridging agent and end capping carboxylate-O coordination by 2,5-thiophenedicarboxylate (tda²⁻). The Co-CP participates in electrocatalytic OER in alkaline medium. Incorporating Ni²⁺ at varying concentration into Co-CP has successfully synthesized Ni@Co-CP composites which have been demonstrated to enhance the electrocatalytic activities. The optimized catalyst, Ni-2@Co-CP (0.75:1 molar ratio of NiCl₂·6H₂O and Co-CP), is amorphous and demonstrates exceptional electrocatalytic efficiency for the OER, with a 290 mV overpotential at 10 mA/cm² current density, 35 mV/dec Tafel slope of and 6.97 Ω charge transfer resistance, as determined by electrochemical impedance spectroscopy (EIS). The design of extraneous metal ion incorporation in the CP framework could be promising candidates for various energy-related applications beyond OER, potentially leading to advancements in energy conversion and storage technologies.

5.1 Introduction

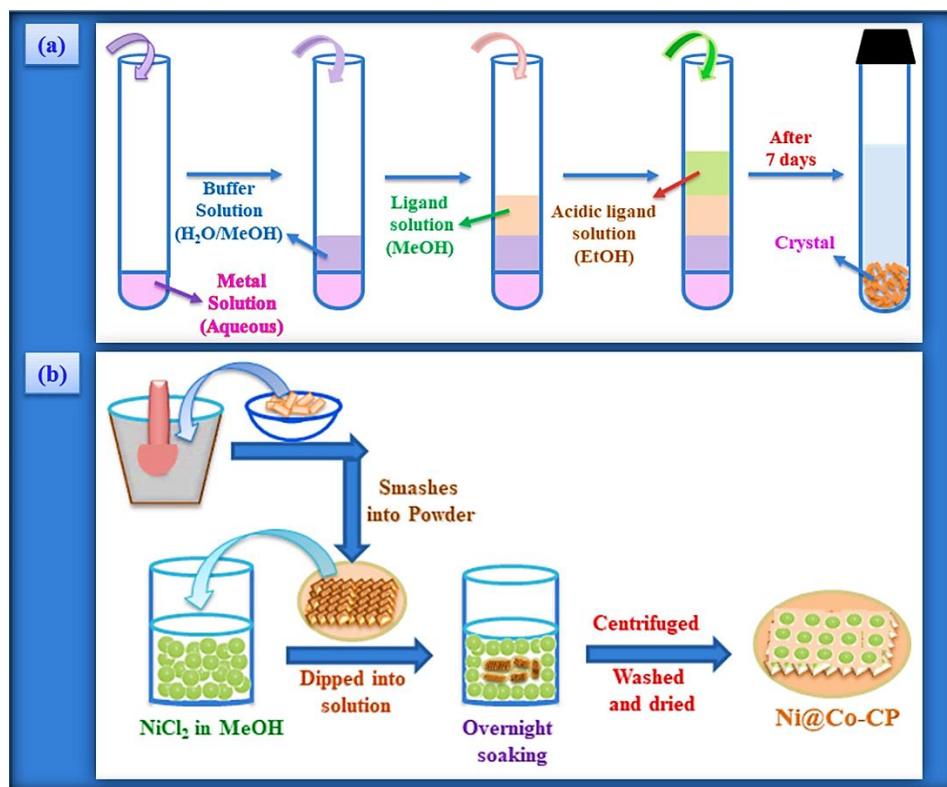
The growing global appetite for energy, and the on-going environmental threat, demands for the development of efficient, sustainable, and zero-carbon emission technologies.¹⁻³ Photoelectrochemical water splitting is a green energy sources for H₂ evolution reaction (HER) and is economically and technologically more facile than solar and wind power.⁴⁻⁸ In the realm of electrolytic water splitting technology the oxygen evolution reaction (OER) is performed on the anode side and the cathode is responsible for the hydrogen evolution reaction (HER).⁹⁻¹¹ The process of OER at the anode is notably slower in kinetics than HER, primarily because OER involves 4e⁻ transfer process ($4\text{OH}^- \rightarrow \text{O}_2 + 2\text{H}_2\text{O} + 4\text{e}^-$) while HER needs 2e⁻ transfer ($2\text{H}^+ + 2\text{e}^- \rightarrow \text{H}_2$) technique.¹²⁻¹⁵ The OER is associated with a considerable kinetic barrier, which adversely affects the electrode efficiency and results in elevated overpotentials.¹⁶⁻¹⁸ Thus, the OER is inherently more intricate and proceeds at a slower pace, and demands a higher overpotential, which severely restricts its overall conversion efficiency. To date, noble metal oxides, particularly RuO₂/IrO₂, are viewed as the forefront materials for effective electrocatalysts in the context of OER.^{19,20} However, several factors conspire to limit the widespread use of noble metals such as, scarcity in nature, exorbitant cost, and their susceptibility to slow degradation when exposed to alkaline environments. It is imperative to pursue innovative alternatives that can serve as earth-abundant, cost-effective and efficient electrocatalysts for the OER, potentially replacing noble metal oxides.

Recently, diverse transition metal oxides, sulphides, hydroxides, selenides, phosphides and mixed metal composites have shown noteworthy performance in the OER catalysis.²¹⁻²⁹ However, their meagre conductivity window, structural instability in strong alkaline medium, and fast surface corrosion impact on the catalytic activity.³⁰ In the realm of electrochemical water splitting reactions, Coordination Polymers/Metal-Organic Frameworks (CPS/MOFs) act as excellent alternatives (**Chapters 1-4**). The CPs/MOFs having large surface areas, adjustable pore sizes, the abundance of metal active sites, and exceptional design flexibility³¹⁻³⁶ facilitate swift mass transport of reactants and products, potential multimetallic composite facility, synergism in the functional property, monodispersity in the catalytic activity where metal nodes are protected by the organic environment from the exogenous irritating environments over traditional inorganic or organic materials.³⁷⁻⁴⁰

Cobalt-based materials, particularly cobalt coordination polymers (Co-CPs), have recently become a focal point in catalysis research, owing to their substantial surface area, low hydrogen binding energy, and the remarkable catalytic activity.⁴¹⁻⁴⁵ Therefore, an

effective approach involves the straightforward synthesis of meticulously structured cobalt-based coordination polymers (Co-CPs), and employ them as a substrate to generate high-performance electrocatalytic materials. The latest research has revealed that, heterometallic polycentric amorphous composites exhibit greater electrocatalytic activity.⁴⁶⁻⁴⁹ Theoretical and experimental findings have revealed that bimetallic centres can effectively adsorb active radical intermediates like $\cdot\text{H}$, $\cdot\text{OH}$, $\cdot\text{O}$, and $\cdot\text{OOH}$, and may promote the electrocatalytic processes. Recently, the consideration of coordination frameworks with active bimetallic nodes shows exceptional electrocatalytic behaviour.⁵⁰⁻⁵²

Herein, we have synthesized a 1D coordination polymer composed of a trinuclear cobalt-based redox-active synthon, $[\text{Co}_3(\text{pmta})_2(\text{tda})_2(\text{H}_2\text{O})_8(\text{OH})_2] \cdot x\text{H}_2\text{O}$ (Co-CP) (Scheme 5.1a) (CCDC: 2441349) using (E)-N-(pyridin-4-ylmethylene)-4H-1,2,4-triazol-4-amine as a bridging motif and 2,5-thiophenedicarboxylate as stop-end coordinating agent. The structure has been decisively verified by the Single Crystal X-Ray Diffraction analysis. The presence of hanging $-\text{COO}$ group has mooted us to fabricate Ni^{2+} -impregnated composites in different ratios (molar ratio of $\text{NiCl}_2 \cdot 6\text{H}_2\text{O}$: Co-CP; Ni-1@Co-CP, Ni-2@Co-CP and Ni-3@Co-CP), through the liquid phase surface adsorption technique (Scheme 5.1b) by loading different amount of Ni^{2+} . The OER activity of the materials has been examined in the 1 M KOH electrolyte solution. In the realm of catalyst development, Ni-2@Co-CP demonstrates exemplary performance in OER, marked by an overpotential 290 mV and current density 10 mA/cm^2 . This is further characterized by a Tafel slope 35 mV/dec and a charge transfer resistance 6.97 Ω , as assessed through detailed electrochemical impedance spectroscopy (EIS) analysis. Furthermore, chronoamperometry study demonstrates its long-standing stability and durability indicating its considerable promise as a dependable OER catalyst in water-splitting applications. In accordance with these findings, the integration of Ni metal into the Co-network substantially boosts the OER efficiency, suggesting their potential as a viable option for the advancement of sustainable electrochemical energy conversion technologies.



Scheme 1. Schematic presentation of the synthesis of (a) Co-CP and (b) Ni@Co-CP.

5.2 Experimental Section

5.2.1 Materials and General Methods

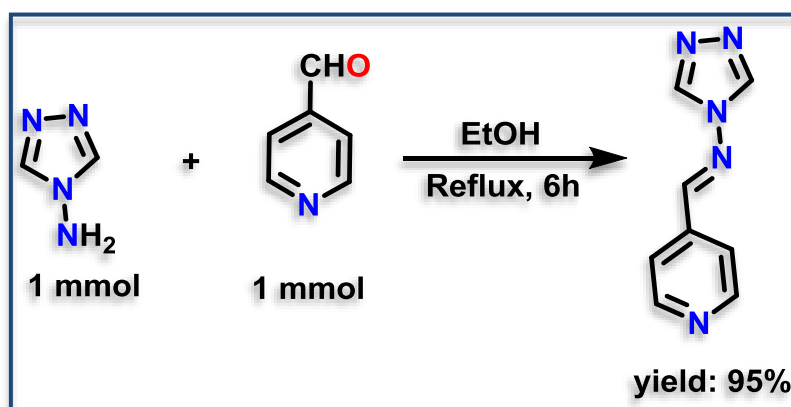
4*H*-1,2,4-triazol-4-amine and Pyridine-4-carbaldehyde were purchased from Sigma-Aldrich. $\text{Co}(\text{NO}_3)_2 \cdot 6\text{H}_2\text{O}$ and $\text{NiCl}_2 \cdot 6\text{H}_2\text{O}$ were purchased from Spectrochem Pvt. Ltd., India. All other organic reagents and solvents were of the reagent grade, obtained from Spectrochem and Merck, and used without further purification. Deionized water (DI) is used throughout this work.

Tetramethylsilane (TMS) served as the internal standard in ^1H -NMR spectra recorded on a 300 MHz (Bruker-DPX) in $\text{DMSO}-d_6$ solvents. ^{13}C -NMR spectra were recorded on a 75 MHz (Bruker-DPX) instrument in $\text{DMSO}-d_6$ using same internal standard. HRMS (m/z) measurements were taken with an ESI method and a Q-ToF Micro mass spectrometer, respectively. PerkinElmer SPECTRUM II LITA FT-IR was used to capture an infrared spectrum in KBr ($4500\text{--}500\text{ cm}^{-1}$). The elemental analyzer PerkinElmer 240C was used for the CHN analysis. The thermal stability of the compound as it was manufactured was tested using a PerkinElmer Pyris Diamond TG/DTA instrument at temperature between 30 and 800°C with a heating rate of $10^\circ/\text{minute}$. The as-prepared samples are initially subjected to XRD analysis with a scanning rate of 10° min^{-1} in the 2θ range $5\text{--}55^\circ$ using a Bruker X-ray powder

diffractometer (XRD) with Cu K α radiation ($\lambda = 0.154$ nm). The morphology of the catalysts was characterized with FE-SEM instrument (SUPRA 55VP Carl Zeiss) with a separate EDS detector connected to that instrument. Energy Dispersive X-ray Spectroscopy (EDS) analysis was done with the assistance of FE-SEM instrument. X-ray photoelectron spectroscopic (XPS) analysis was performed using a Theta Probe AR-XPS system (Thermo Fisher Scientific, UK). HR-TEM, (TecnaiTM G2 TF20) working at an accelerating voltage of 200 kV and by Talos F-200-S with HAADF elemental mapping.

5.2.2 Preparation of Pyridin-4-ylmethylene-[1,2,4]triazol-4-yl-amine (pmta)

The ligand, **pmta**, was synthesised following published procedure⁵³ with some modification as detailed below. A mixture of 4*H*-1,2,4-triazol-4-amine (84 mg, 1.0 mmol) and Pyridine-4-carbaldehyde (107 mg, 1.0 mmol) were mixed and pasted with absolute ethanol (2 mL) and then mixed with additional ethanol (8 mL) and refluxed for 12 h. The TLC was carried out with constant interval to check the reaction status. The solution was then slowly cooled down to ambient temperature and then evaporated in the rotary evaporation technique. A white solid was collected, washed thoroughly with diethyl ether and dried in air and the dry yield of Pyridin-4-ylmethylene-[1,2,4]triazol-4-yl-amine (**pmta**) was 95% (165 mg) (Scheme 5.2). MP: 170 °C; HRMS (ESI, *m/z*) calculated for C₈H₈N₅ [M+H]⁺: 174.0780; found: 174.0785 (Figure 5.1); ¹H-NMR (300 MHz, DMSO-*d*₆): δ 9.21 (s, 2H), 9.15 (s, 1H), 8.80 (d, *J* = 5.8 Hz, 2H), 7.77 (d, *J* = 5.7 Hz, 2H), (Figure 5.2); ¹³C-NMR (100 MHz, DMSO-*d*₆): δ 166.9, 150.7, 150.6, 141.7, 121.9 (Figure 5.3).



Scheme 5.2 Schematic representation for the synthesis of pyridin-4-ylmethylene-[1,2,4]triazol-4-yl-amine (**pmta**).

Chapter 5: Triazolyl-pyridyliminewater splitting reaction

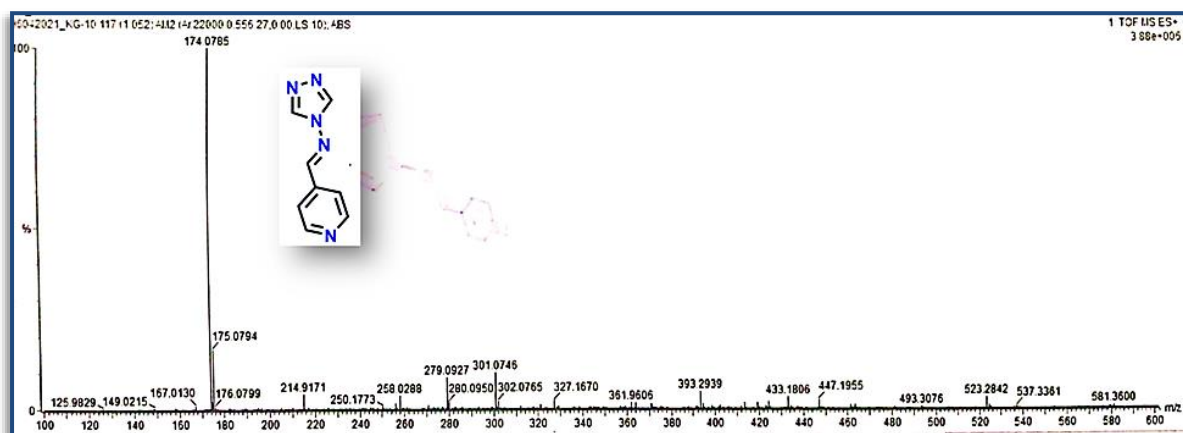


Figure 5.1 Mass spectrum of pmta.

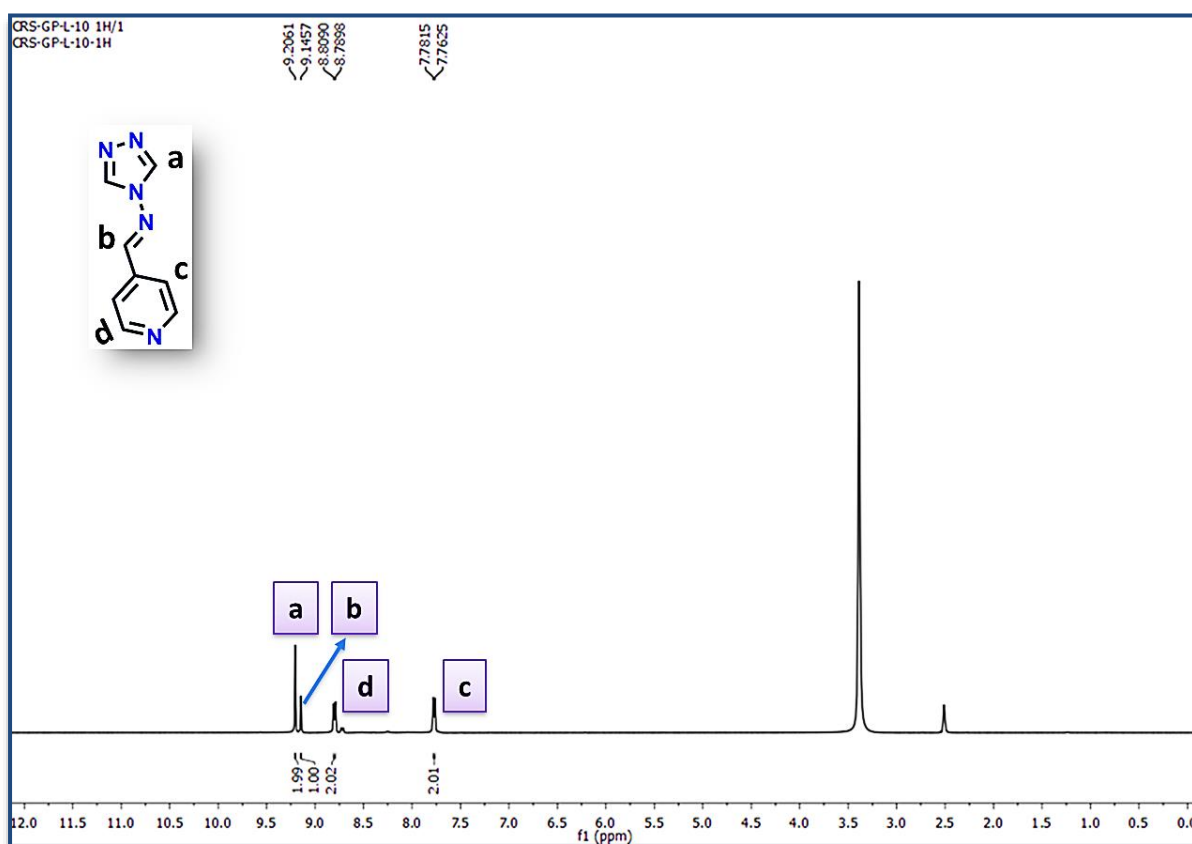


Figure 5.2 ¹H-NMR spectroscopy of pmta.

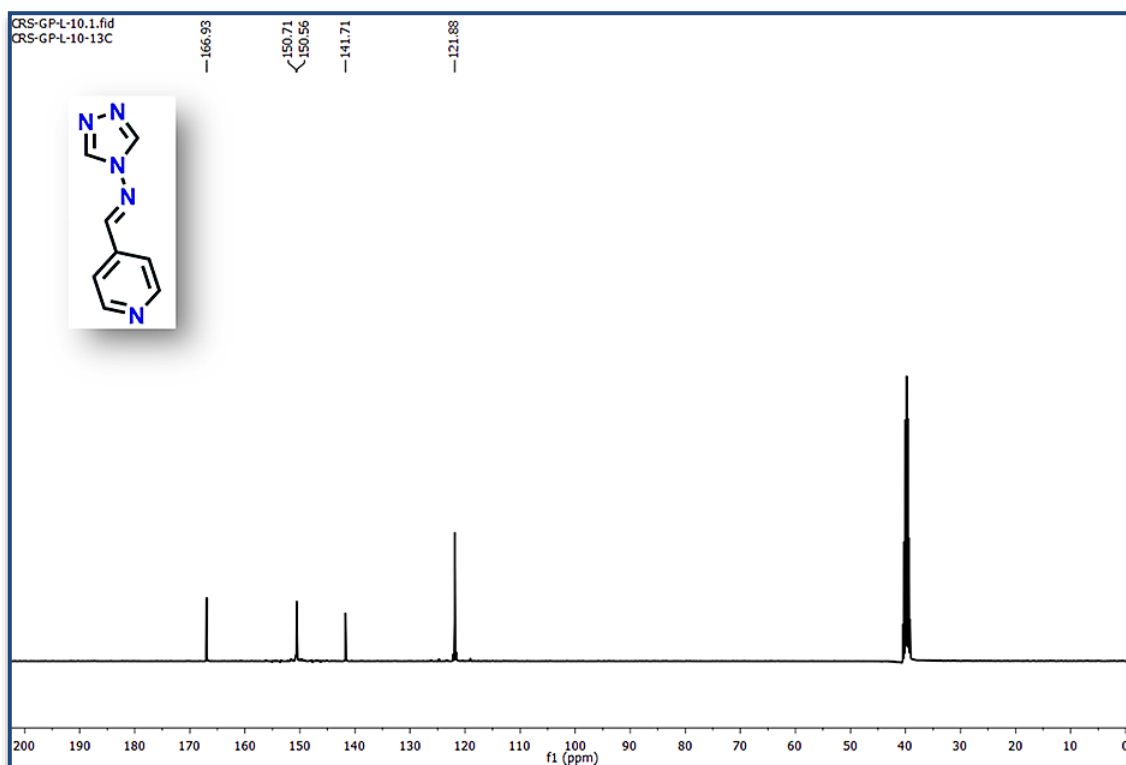
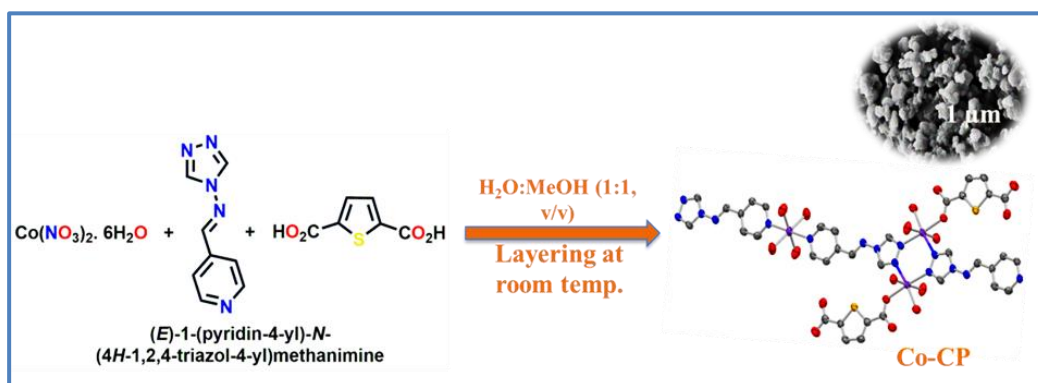


Figure 5.3 ^{13}C -NMR spectroscopy of pmta.

5.2.3 Synthesis of $\{[\text{Co}_3(\text{pmta})_2(\text{tda})_2(\text{H}_2\text{O})_8(\text{OH})_2]\cdot x\text{H}_2\text{O}\}_n$ (Co-CP)

To the aqueous solution (2 mL) of $\text{Co}(\text{NO}_3)_2\cdot 6\text{H}_2\text{O}$ (58.2 mg, 0.2 mmol) water-methanol (1:1 v/v; 2 mL) was slowly layered as a buffer layer. Methanol solution (2 mL) of **pmta** (34.6 mg, 0.2 mmol) was slowly then added over the buffer layer followed by a solution of 2,5-thiophenedicarboxylic acid (**H₂tda**; 34.4 mg, 0.2 mmol) in ethanol (2 mL) and subsequently neutralized with Et_3N (42 mg, 0.4 mmol). The whole mixture was then permitted to diffuse at rest. A brown block shaped crystals were deposited after a week on the surface of the tube; these were carefully separated and air dried (yield: 128 mg, 53.2%) (**Scheme 5.3**). Microanalytical data of Co-CP: C, 27.94; H, 4.52; N, 11.64. Found: C, 27.98; H, 4.55; N, 11.71%.



Scheme 5.3 Schematic representation for the synthesis of $\{[\text{Co}_3(\text{pmta})_2(2,5\text{-tda})_2(\text{H}_2\text{O})_8(\text{OH})_2]\cdot x\text{H}_2\text{O}\}_n$ (Co-CP).

5.2.4 Preparation of Ni@Co-CP Composites

To methanol solution of $\text{NiCl}_2 \cdot 6\text{H}_2\text{O}$ (Set-1: 12 mg, 0.05 mmol; Set-2, 18 mg, 0.075 mmol; Set-3, 24 mg, 0.1 mmol) the crystals of Co-CP (108 mg, 0.1 mmol in each Set) was suspended for 12 h at rest (Table 5.1, Figure 5.4). A light bluish precipitate of Ni@Co-CP was collected (Set-1, Ni-1@Co-CP; Set-2, Ni-2@Co-CP; Set-3, Ni-3@Co-CP). It was then thoroughly washed by methanol and air dried in oven (60 °C) for a period of 6 h.

Table 5.1 A compilation of components utilized in various catalysts.

	Co-CP	$\text{NiCl}_2 \cdot 6\text{H}_2\text{O}$
Co-CP	0.1 mmol	0
Ni-1@Co-CP	0.1 mmol	0.05 mmol
Ni-2@Co-CP	0.1 mmol	0.075 mmol
Ni-3@Co-CP	0.1 mmol	0.1 mmol

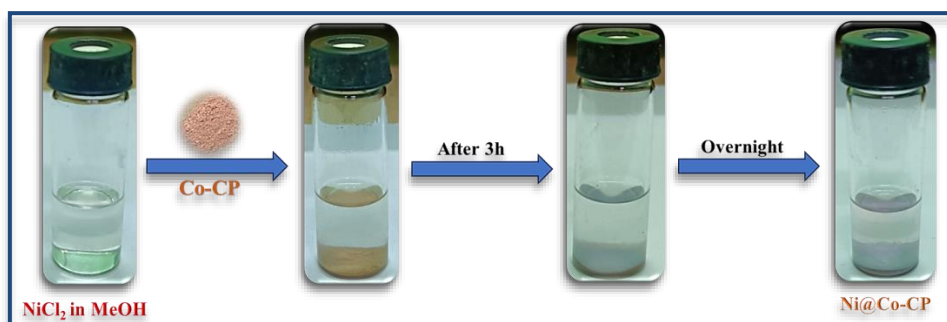


Figure 5.4. Synthesis of nickel-cobalt bimetallic composite at room temperature.

5.2.5 X-ray Crystallography Analysis

A suitably shaped block size Co-CP crystal was separated from mother liquor, coated with oil and then affixed to the goniometer head. A Bruker APEX II CCD diffractometer, paired with a graphite-monochromatic $\text{Cu K}\alpha$ radiation source ($\lambda = 1.54178 \text{ \AA}$) and maintained at 273 K, was employed for this analysis (Table 5.2). The matrices concerning crystal orientation, along with the parameters describing the unit cell, were assessed using least-square refinements applied to all reflections, with the hkl values falling within a specified range of $-8 \leq h \leq 8$, $-13 \leq k \leq 13$, $-17 \leq l \leq 17$. Data were systematically processed using the SAINT V8.38A program⁵⁴, adhering strictly to the integration criteria where $I > 2\sigma(I)$. Following this essential step, an absorption correction was meticulously performed

Chapter 5: Triazolyl-pyridyliminewater splitting reaction

using SADABS⁵⁵, reinforcing the reliability and precision expected in such critical analytical procedures. The molecular structure of the single crystal was determined through the application of SHELXT 2018/2 software and subsequent refinement of the structure was carried out using Olex2 version 1.5⁵⁶⁻⁵⁸, ensuring precision in the analysis process. The anisotropic thermal parameters are essential for accurately refining the non-hydrogen atoms within the compound. Meanwhile, the hydrogen atoms were precisely positioned, constrained to follow the parent atoms in their geometrically ideal locations, reflecting their critical role in ensuring structural integrity. All the data and molecular pictures are evaluated using the WinGX System and Mercury 3.10.3. Selected bond lengths and bond angle have been prescribed in **Table 5.3**. CCDC number for Co-CP: **2441349**.

Table 5.2 Crystal data and refinement parameters for Co-CP.

Formula	C ₂₈ H ₄₀ Co ₃ N ₁₀ O ₂₀ S ₂
CCDC	2441349
Formula weight	1077.61
Crystal system	Triclinic
space group	<i>P</i> -1
<i>a</i> (Å)	7.2003 (6)
<i>b</i> (Å)	12.0589 (9)
<i>c</i> (Å)	15.4657 (12)
α (deg)	72.683 (4)
β (deg)	79.504 (5)
γ (deg)	83.807 (4)
<i>V</i> (Å ³)	1258.47 (17)
<i>Z</i>	1
<i>D</i> _{calcd} (g/cm ³)	1.422
μ (mm ⁻¹)	9.098
λ (Å)	1.54178
data[<i>I</i> > 2 σ (<i>I</i>)]/params	2707/296
GOF on <i>F</i> ²	1.040
Final <i>R</i> indices[<i>I</i> > 2 σ (<i>I</i>)] ^{a,b}	<i>R</i> 1 = 0.0577 <i>w</i> R2 = 0.1660

$$^a R1 = \sum ||F_o| - |F_c|| / \sum |F_o|, \quad ^b wR2 = [\sum w(F_o^2 - F_c^2)^2 / \sum w(F_o^2)^2]^{1/2}$$

Table 5.3 Selected bond lengths and bond angles in Co-CP framework.

Bond length	(Å)	Bond Angles	(°)
Co(1) - O(1)	2.115(4)	O(1) - Co(1) - O(5)	92.40(17)
Co(1) - O(5)	2.032(5)	O(1) - Co(1) - O(6)	92.42(19)
Co(1) - O(6)	2.038(5)	O(1) - Co(1) - O(7)	88.79(16)
Co(1) - O(7)	2.174(5)	O(1) - Co(1) - N(1)	175.45(18)
Co(1) - N(1)	2.153(5)	O(1) - Co(1) - N(2)a	82.33(18)
Co(1) - N(2)a	2.187(5)	O(5) - Co(1) - O(6)	175.14(18)
Co(2) - O(8)	2.102(5)	O(5) - Co(1) - N(1)	88.15(18)
Co(2) - O(9)	2.070(4)	O(6) - Co(1) - O(7)	89.58(19)
Co(2) - N(5)	2.151(5)	O(8) - Co(2) - O(9)	87.87(19)
Co(2) - O(8)b	2.102(5)	O(9) - Co(2) - O(8)b	92.13(19)
Co(2) - O(9)b	2.070(4)	N(1) - Co(1) - N(2)a	102.19(18)
Co(2) - N(5)b	2.151(5)	O(8) - Co(2) - N(5)	88.64(18)
		O(9) - Co(2) - N(5)	91.67(19)
		N(5) - Co(2) - N(5)b	180.00
Symmetry Code: a = 1-x, 1-y, 2-z; b = 1-x, 3-y, 1-z.			

5.2.6 Electrochemical Measurements

The electrochemical properties were assessed with a Metrohm AUTOLAB-M240 device, utilizing methods like cyclic voltammetry (CV), linear sweep voltammetry (LSV), and chronoamperometry (CA). These experiments took place within a standard three-electrode system, consisting of a Hg/HgO as reference electrode, a graphite rod as the counter electrode, and nickel foam (NF) serving as the working electrode. To construct the working electrodes, 1 mg of polyvinylidene fluoride (PVDF) was used as a binder and N-Methyl-2-pyrrolidone (NMP) for preparing the slurry. Moreover, it is also stated that the powder form of the crystalline materials is used for the electrochemical measurement. To measure the electrochemical properties; typically, the $\approx 4:1$ (with respect to overall catalyst loading over the electrode surface) ratio of powder catalyst and PVDF had taken into a mortar, followed by the addition of NMP solvent with continuous mixing by a pestle. Then a certain amount of catalyst ink was fabricated over the 1 cm^2 area of the nickel foam (NF). The amount of loaded catalyst was calculated by measuring the difference in weight of coated and uncoated nickel foam (NF). Then, EIS analysis of all the catalysts were performed at an applied

potential of 0.7 V (vs Hg/HgO) for OER. Likewise, chronoamperometric analysis also carried out at a potential of 0.68 V (vs Hg/HgO) for OER.

5.3 Results and Discussion

5.3.1 General Characteristics of the Co-CP and Ni@Co-CP Composites

The FTIR spectrum of Co-CP was compared with the spectra of **pmta** and **H₂tda** (Figure 5.5). The broad absorption bands observed at 3460-2840 cm⁻¹ are characteristics of stretching vibrations from coordinated OH and/or H₂O molecules and aromatic C-H bonds found in the Co-CP. There are noticeable peaks at 1558 and 1362 cm⁻¹ those are corresponding to asymmetric and symmetric stretching vibrations of the -COO in 2,5-dicarboxylate ion (**tda**²⁻). The C=N bonds in the **pmta** ligand produce a prominent peak at 1526 cm⁻¹. In the Ni@Co-CP no significant alterations in the stretching frequencies of the functional groups have been noted.

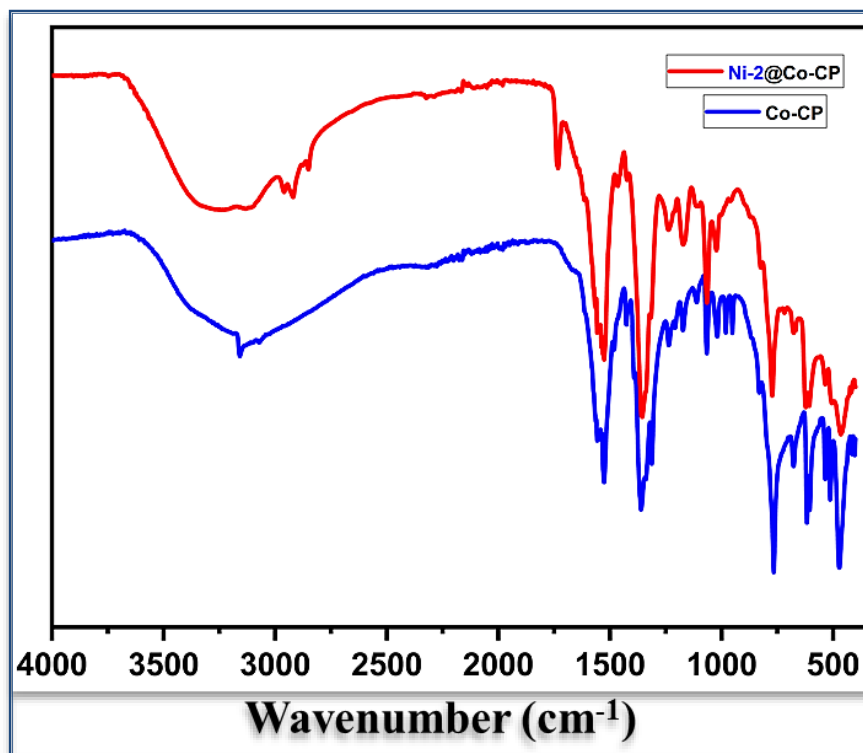


Figure 5.5 Comparison of IR-spectra between Co-CP and Ni-2@Co-CP.

The Powder X-ray Diffraction (PXRD) study conducted at room temperature and has been compared with the simulated spectra obtained from the single crystal diffraction coordinates. The spectra are matched well which suggests notable consistency and uniformity throughout the entire bulk material, indicating a high degree of phase purity (Figure 5.6). Likewise, PXRD analysis was carried out on the Ni-doped Co-CP (Ni-1@Co-CP, Ni-2@Co-

CP and Ni-3@Co-CP), and the results showed no notable alterations, except for the broadening of the main peaks as seen in the as-synthesized compound with higher nickel content (**Figure 5.6**). This validates their isostructural identity and exceptional phase purity.

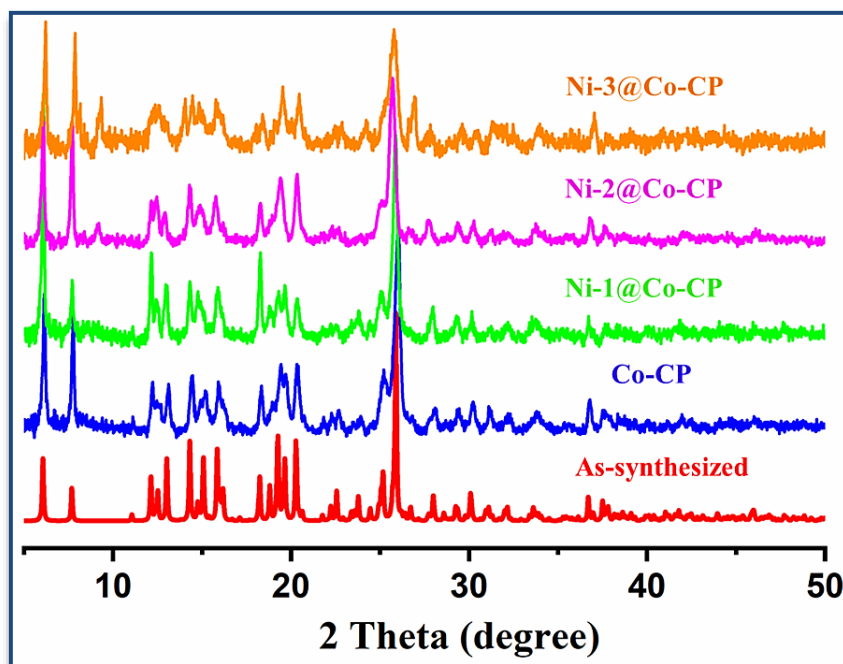


Figure 5.6 PXRD patterns of Co-CP.

In order to determine the thermal stability of the compounds, thermogravimetric analysis was conducted (TGA). It is revealed that Co-CP is stable till 265 °C (**Figure 5.7**). Despite the initial weight loss (18%) due to the release of coordinated water molecules of Co-CP.

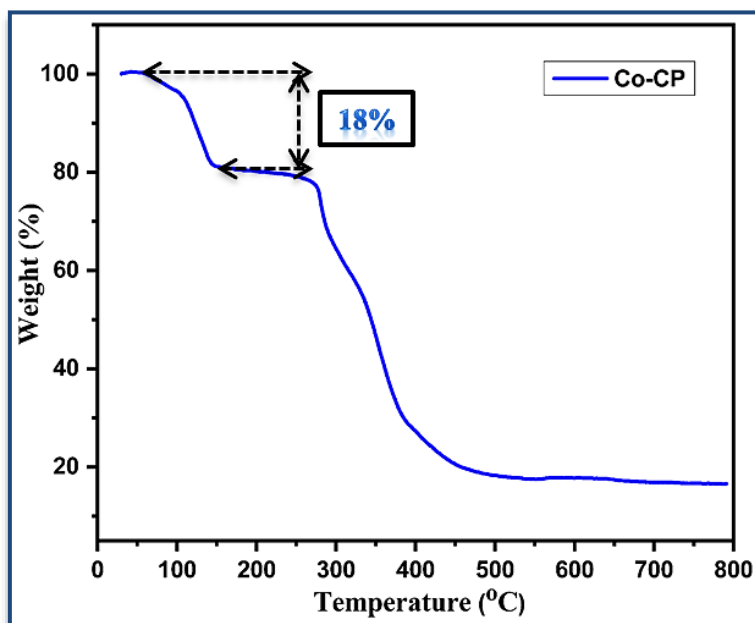


Figure 5.7 TGA plot of Co-CP.

5.3.2 Crystal Structure of $\{[\text{Co}_3(\text{pmta})_2(\text{tda})_2(\text{H}_2\text{O})_8(\text{OH})_2] \cdot x\text{H}_2\text{O}\}_n$ (Co-CP)

The Co-CP belongs to triclinic crystal system and space group *P-1* (Table 5.2). Each asymmetric unit consists of three Co(II) centres where two Co(II) centres are bridged by two triazolyl-Ns from two **pmta** and forms a six membered hexagonal unit (Co_2N_4) ((Co1-N1 = 2.153(5), Co1-N2_a = 2.187(5) Å; N(1)-Co(1)-N(2)a = 102.19(18)°, Co(1)-N(1)-N(2) = 129.1(3)°, N(1)-N(2)-Co(1)a = 128.7(4)°). The Co(II) centres of ‘ Co_2N_4 bridging motif’ are coordinated with one of the carboxylate-O of **tda**²⁻ while other -COO unit is hanging freely. A hydroxyl group, and two water molecules coordinate to Co(II) of ‘ Co_2N_4 ’ motif to satisfy charge and coordination number. The pyridyl-N of bridged **pmta** has been coordinated to third Co(II) centre (Co(2)-N(5) = 2.151(5) Å) (Figure 5.8a) which serves as linker unit to adjacent ‘ Co_2N_4 ’ motif and four H₂O ligands (Co2-N5 = 2.150(5), Co2-O8 = 2.098(5), Co2-O9 = 2.075(4), Co2-O8_b = 2.098(5), Co2-O9_b = 2.075(4), Co2-N5_b = 2.150(5) Å; N(5)-Co(2)-N(5)b = 180.00°) (Figure 5.8a) to satisfy the octahedral structure. The total charge of three Co(II) centres has been balanced by four carboxylates from two **tda**²⁻ and two hydroxyl groups. The propagation of ‘ Co_2N_4 ’ unit bridging with third Co(II) enables the formation of a 1D chain bridged by pyridyl-N to $[\text{Co}(\text{H}_2\text{O})_4]$ (Figure 5.8b). It is also fascinating to observe the H-bonding interaction between the coordinated hydroxyl group and the non-coordinated oxygen atom of the carboxylate group of **tda**²⁻ (H7...O2 = 2.519 Å) (Figure 5.9).

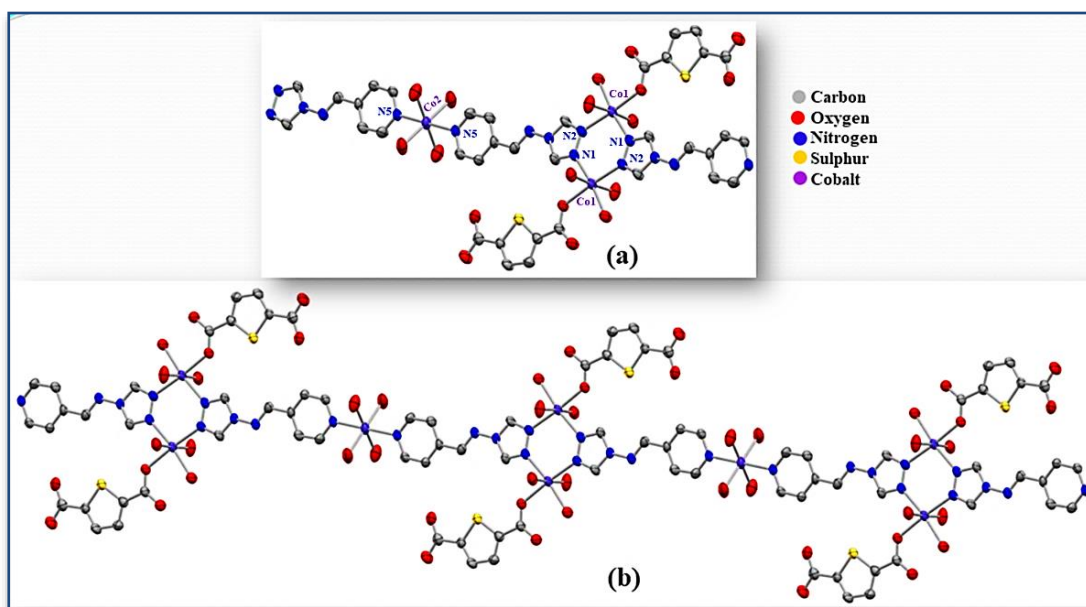


Figure 5.8 (a) Overview of the various coordination structures surrounding the metal centres of Co-CP. (b) Structure of the one-dimensional network with **tda**²⁻ and **pmta**.

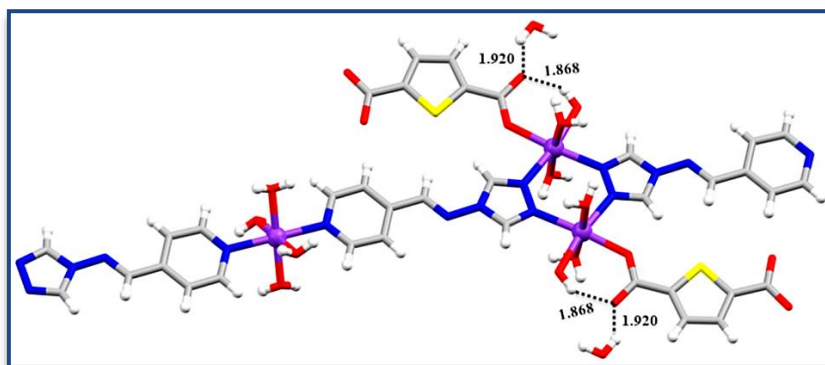


Figure 5.9 H-Bonding interaction in Co-CP.

Intermolecular hydrogen bonds have been strategically established with precise distances ($\text{O5-H5A}\cdots\text{O3}$, 2.097 Å; $\text{O6-H6A}\cdots\text{O4}$, 2.183 Å) (Figure 5.10a), to enhance the robustness and supramolecular attributes in the 1D chain (Figure 5.10b). Hence, this structural assembly is likely to impact charge mobilization and potentially alter the electrical properties when electrochemical performances have been drawn in accordance with the polymeric compound.

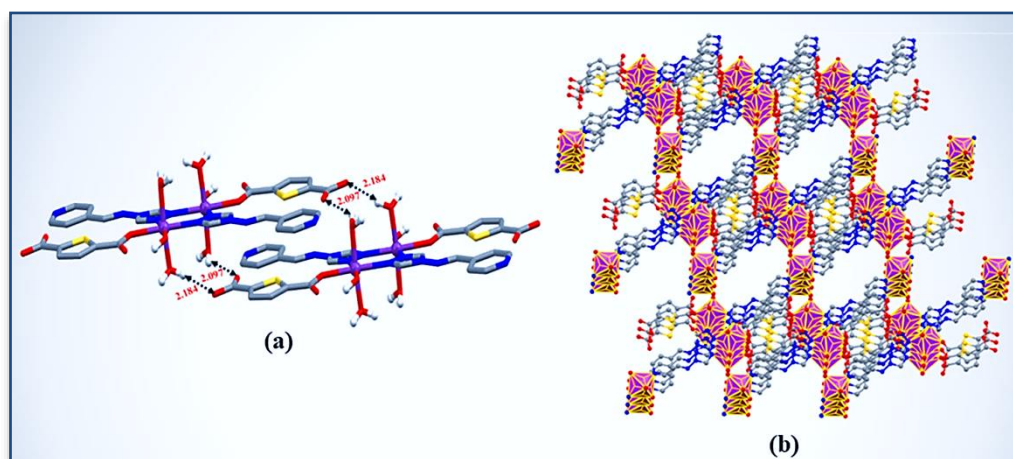


Figure 5.10 (a) A view of H-bonding interaction present in the network. (b) Polyhedral view of the supramolecular assembly of Co-CP.

5.3.3 Electron Microscopic Studies

A catalyst of a uniform and smooth texture, along with interconnected particles and a large specific surface area and pattern is instrumental in effectively supporting the active sites required for the OER. The morphology and microstructure of the Co-CP and Ni-2@Co-CP are examined by FE-SEM and HR-TEM studies. The FE-SEM images of the Co-CP shows the agglomeration of particle sizes are not uniform (Figure 5.11) and the occurrence of larger particles is likely due to the aggregation or overlapping of smaller particles. The Energy Dispersive X-ray (EDX) Spectroscopy was used to further ascertain the constituents of the Co-CP catalyst (Figure 5.12). The EDX findings are validated the presence of expected

Chapter 5: Triazoly-pyridyliminewater splitting reaction

elements such as Co, C, O, S, and N, which were found in weight percentages of 10.57, 43.25, 24.62, 6.12 and 15.44%, respectively. The HR-TEM images (Figure 5.13) further substantiate the agglomerated morphology of Co-CP.

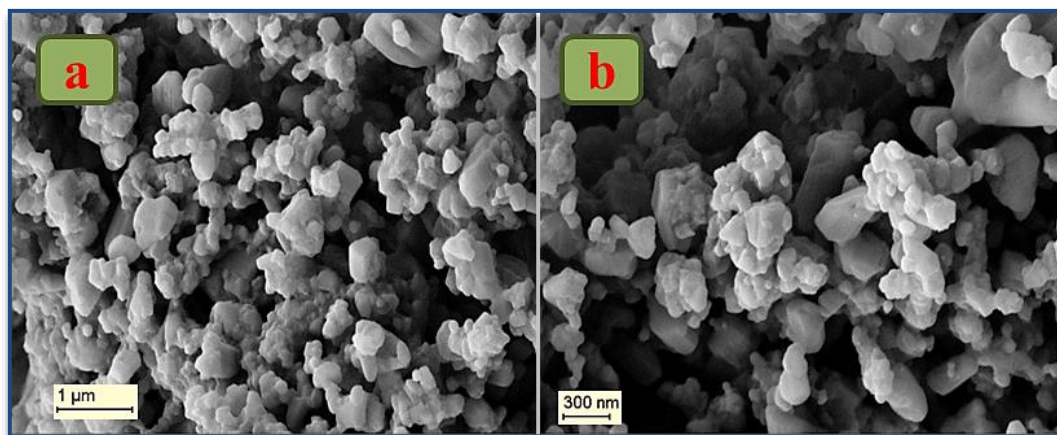


Figure 5.11 Low to high magnification (a, b) FESEM of Co-CP.

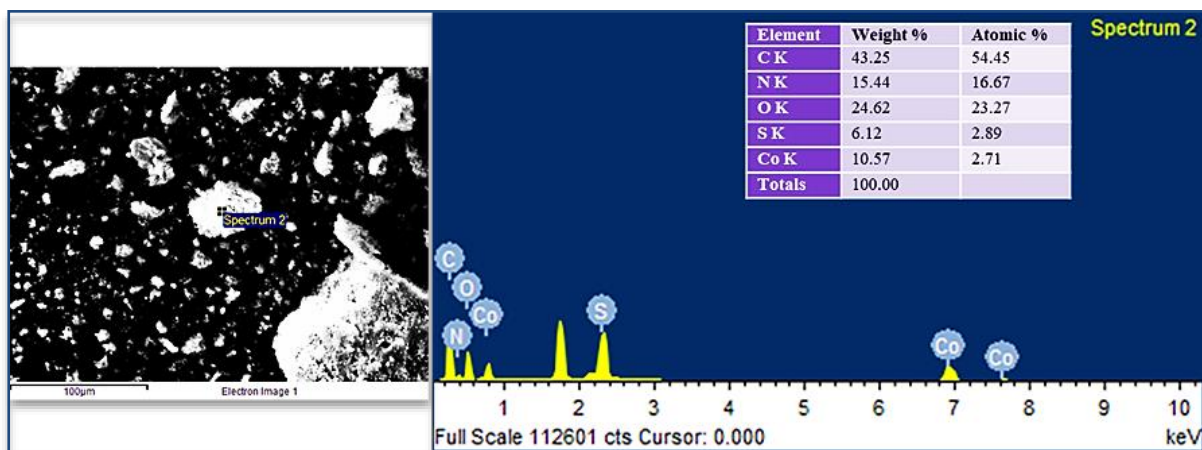


Figure 5.12 EDS spectrum of Co-CP at FE-SEM mode.

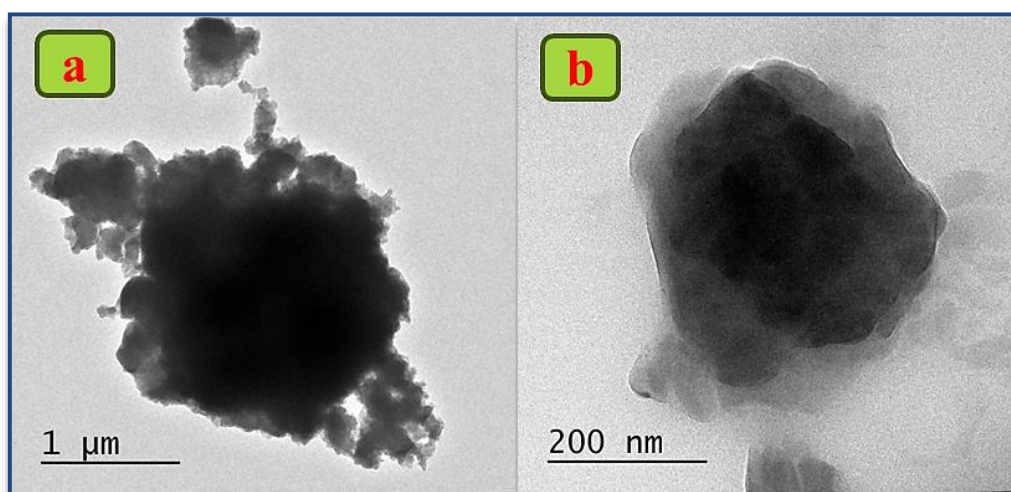


Figure 5.13 Low to high magnification (a, b) HRTEM images of Co-CP.

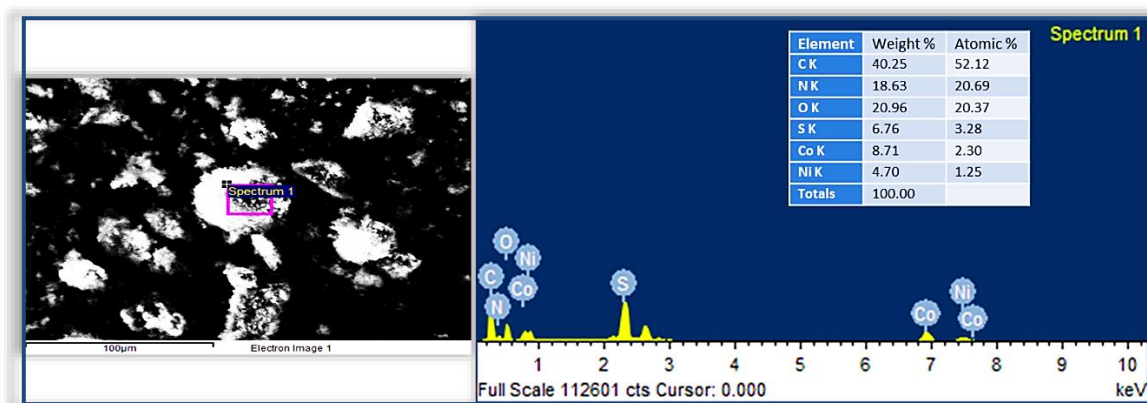


Figure 5.14 EDS spectrum of Ni-2@Co-CP at FE-SEM mode.

The EDX analysis shows that the elements- cobalt (Co), nickel (Ni), sulphur (S), nitrogen (N), oxygen (O), and carbon (C) were present in Ni-2@Co-CP (**Figure 5.14**). The elemental distribution of Ni-2@Co-CP is characterized by the following order: C > O > N > Co > S > Ni, indicating that carbon and oxygen are the most abundant components (**Figure 5.14**).

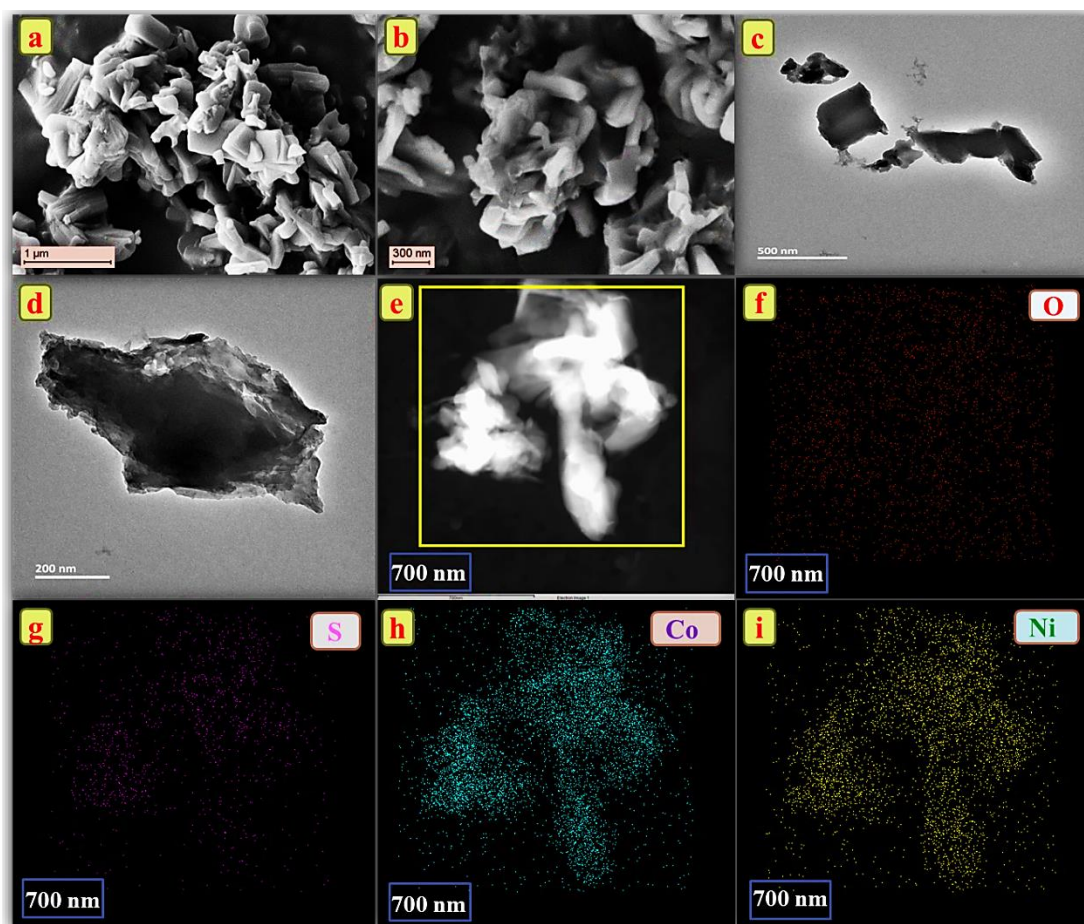


Figure 5.15 Low to high magnification (a, b) FE-SEM and (c, d) HR-TEM images; (e) area chosen for HAADF colour mapping; and (f-i) colour mapping O, S, Co and Ni, respectively of Ni-2@Co-CP.

The integration of Ni atoms into the Co-CP structure induces a transformation in the morphology of the optimal Ni-2@Co-CP electrocatalyst, changing from an agglomerated state to a sleek rectangular surface (**Figure 5.15a,b**). The elements detected in the EDX spectrum provide clear evidence of the successful synthesis of nickel-cobalt bimetallic composite, with these components expected to function as active sites on the surface, thereby supporting applications related to the OER. The HR-TEM images of Ni-2@Co-CP (**Figure 5.15c,d**) at varying magnifications validate the smooth rectangular nature of the surface of the catalyst. The high-angle annular dark-field scanning transmission electron microscopy (HAADF-TEM, **Figure 5.15e**) analysis, along with the corresponding elemental mapping results (**Figure 5.15f-i**), has convincingly established that the amorphous Ni-2@Co-CP catalyst exhibits a spatially uniform distribution of oxygen (O), sulphur (S), cobalt (Co), and nickel (Ni), without any indication of impurities.

5.3.4 X-ray photoelectron spectroscopy (XPS) measurements

In a broad sense, the heterometallic surface can be optimized through the adjustment of the electronic structures of metal sites in bimetallic systems, which can lead to a marked improvement in the OER activity of the catalyst. To this end, we compared the X-ray photoelectron spectroscopy (XPS) spectra obtained before and after the integration of nickel, aiming to elucidate the binding site of Ni(II) and how shifts in the electron binding energy of each element affect the catalytic performance of the material. The presence of oxygen (O), carbon (C), nitrogen (N), sulphur (S) and cobalt (Co) in the Co-CP has proved its composition (**Figure 5.16**).

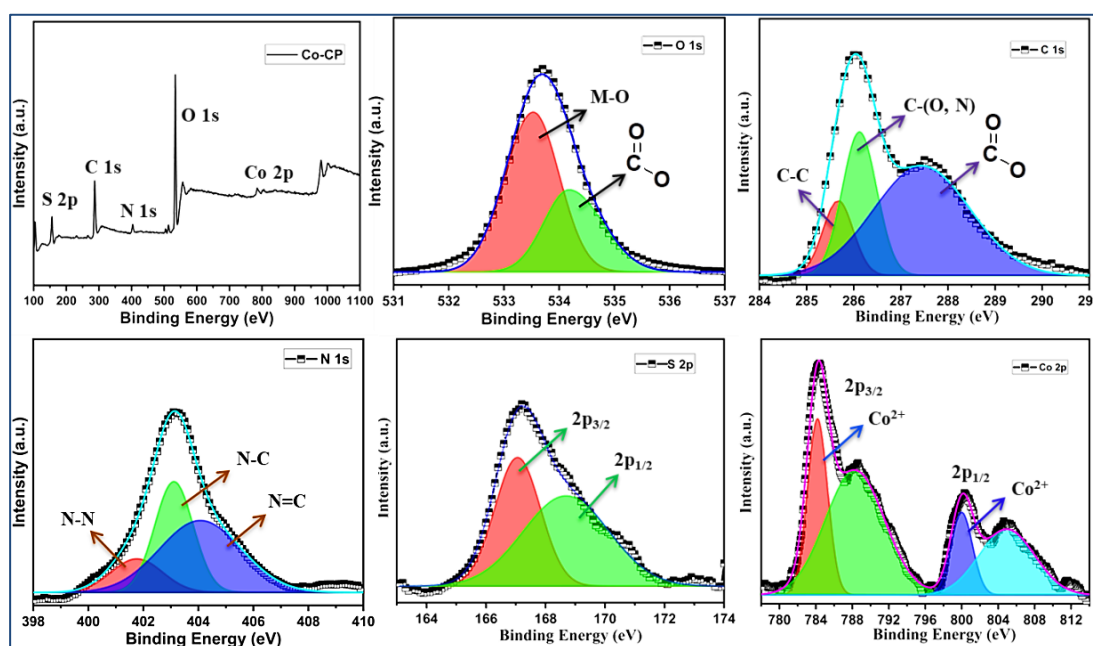


Figure 5.16 Deconvoluted XPS spectra of (a) O 1s, (b) C 1s, (c) Co 2p, (d) Ni 2p in Co-CP.

This finding aligns well with the results obtained from EDX spectrum analysis (Figure 5.12). High-resolution spectra for S 2s and N 1s indicate that there is a lack of significant change associated with Ni incorporation, thereby suggesting that the coordination environment of sulphur and nitrogen in the Co-CP matrix remains largely unaffected by the presence of Ni.

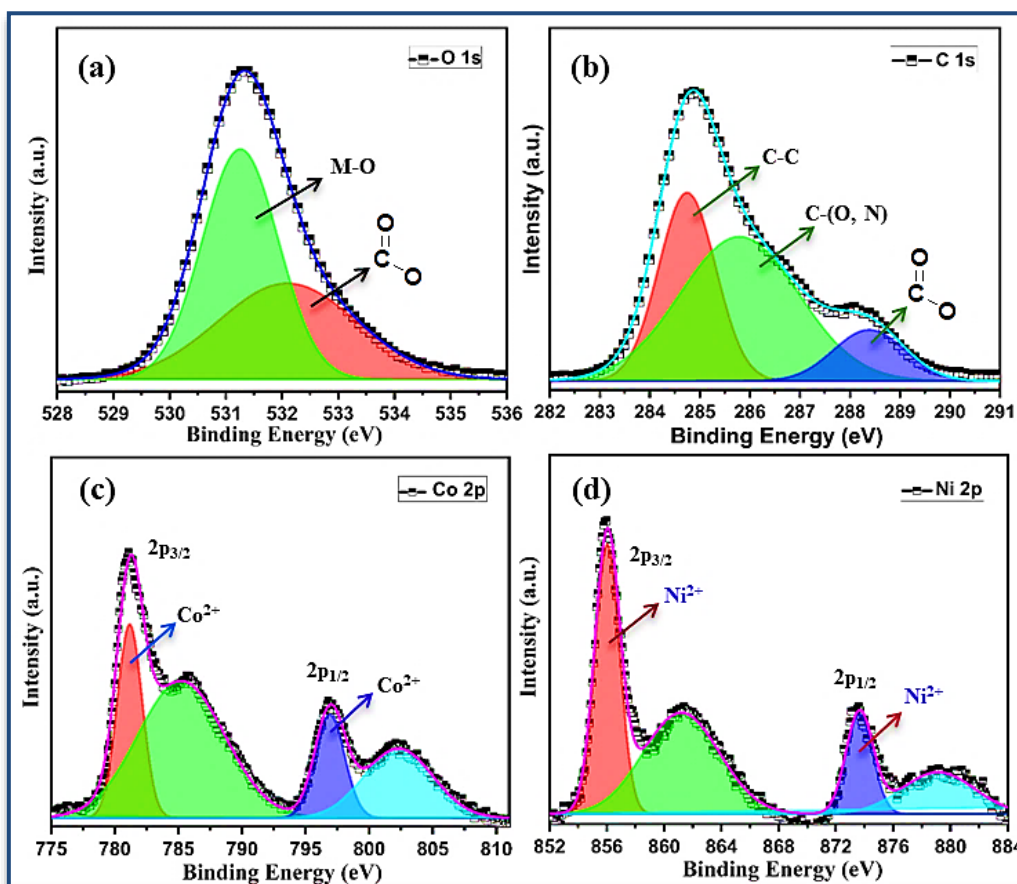


Figure 5.17 Deconvoluted XPS spectra of (a) O 1s, (b) C 1s, (c) Co 2p, (d) Ni 2p in the heterostructure catalyst Ni-2@Co-CP.

The O 1s spectra for Co-CP display prominent peaks at 533.53 eV and 534.20 eV, which correspond to Co-O (carboxylate) and free-CO, respectively (Figure 5.16); a noticeable alteration is the energy decrement in the Co-O (2.26 eV) to C-O (-COO-) (2.02 eV) peaks. The Co 2p spectrum (Figure 5.16) reveals that the binding energy is 784.19 and 800.04 eV, corresponding to Co 2p_{3/2} and Co 2p_{1/2}, respectively which proves the Co²⁺ redox state. Additionally, the satellite peaks observed at 788.25 eV and 805.10 eV are likely attributed to shakeup excitations associated with high-spin Co²⁺ states. Notably, the binding energy of Co 2p_{3/2} experiences a decrease for 3.0 eV upon the introduction of Ni. In contrast, the Co 2p_{1/2} peak exhibits even a lower binding energy 3.16 eV but also reduced peak intensity (Figure 5.17).⁵⁹ This phenomenon may be attributed to the partial electron transfer

occurring between Ni and Co ions via the bridging oxygen of the ligands, which alters the electron density at the Co centre. This observation strongly reinforces the crucial role of chemically bonded Ni(II) to regulate the local electronic structure of Co within Co-CP network.^{60,61} The high-resolution XPS survey (Figure 5.17 and 5.18) shows that the peaks at 856.13 eV and 873.71 eV are attributed to Ni 2p_{1/2} and Ni 2p_{3/2}, respectively and demonstrates the +2-oxidation state, along with corresponding satellite peaks detected at binding energy values of 861.34 eV and 879.76 eV. Compared to NiCl₂·6H₂O, the strikingly diminished binding energy level of Ni-2@Co-CP underscores a profound alteration in the electronic structure of nickel within the material as it undergoes post-treatment. This shift points to significant transformation in its characteristics, highlighting the serious implications for understanding the behaviour and potential applications of the material. The significant shift in binding energy within metallic elements serves as a clear indication of electron transfer, and the ensuing synergistic coupling between nickel and cobalt, which is anticipated to contribute positively towards the enhancement of the performance of the composites in the oxygen evolution reaction (OER).^{62,63}

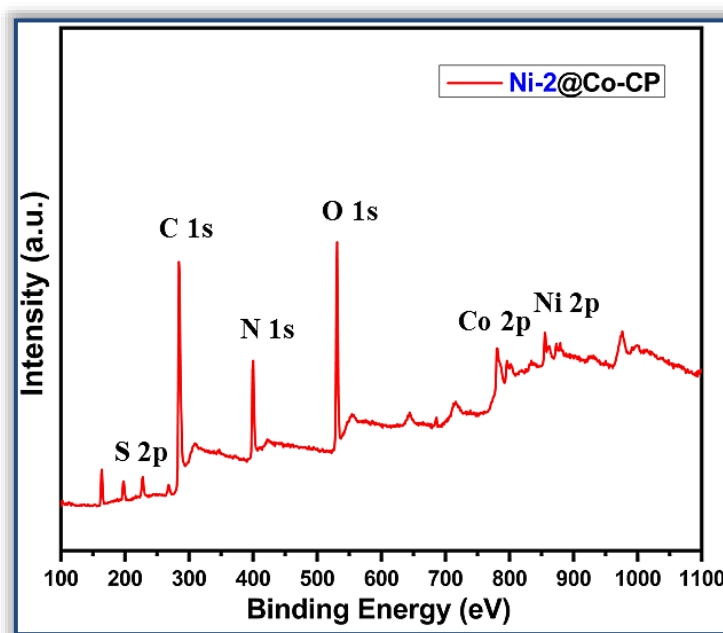


Figure 5.18 XPS survey spectrum of Ni-2@Co-CP.

5.3.5 Electrocatalytic OER studies

The electrochemical OER activity has been executed in a 1 M KOH solution in three-electrode system, incorporating an Hg/HgO reference electrode, a platinum counter electrode, and Ni foam as working electrodes. In order to assess the oxygen evolution reaction (OER) capabilities of Co-CP and Ni@Co-CP, a linear sweep voltammetry (LSV) experiment was

performed at a scan rate of 5 mV/s. Initially, it was observed that Co-CP demonstrated subpar oxygen evolution reaction (OER) activity, as evidenced by its low current density (10 mA cm^{-2}) even when subjected to high overpotentials of 430 mV (Figure 5.19a). In contrast, all Ni@Co-CP catalysts exhibited a remarkable improvement in OER performance, characterized by significantly decreased overpotentials. This enhancement strongly suggests that the integration of nickel (Ni) into the Co-CP framework substantially boosts its electrocatalytic efficiency for facilitating oxygen evolution reactions.

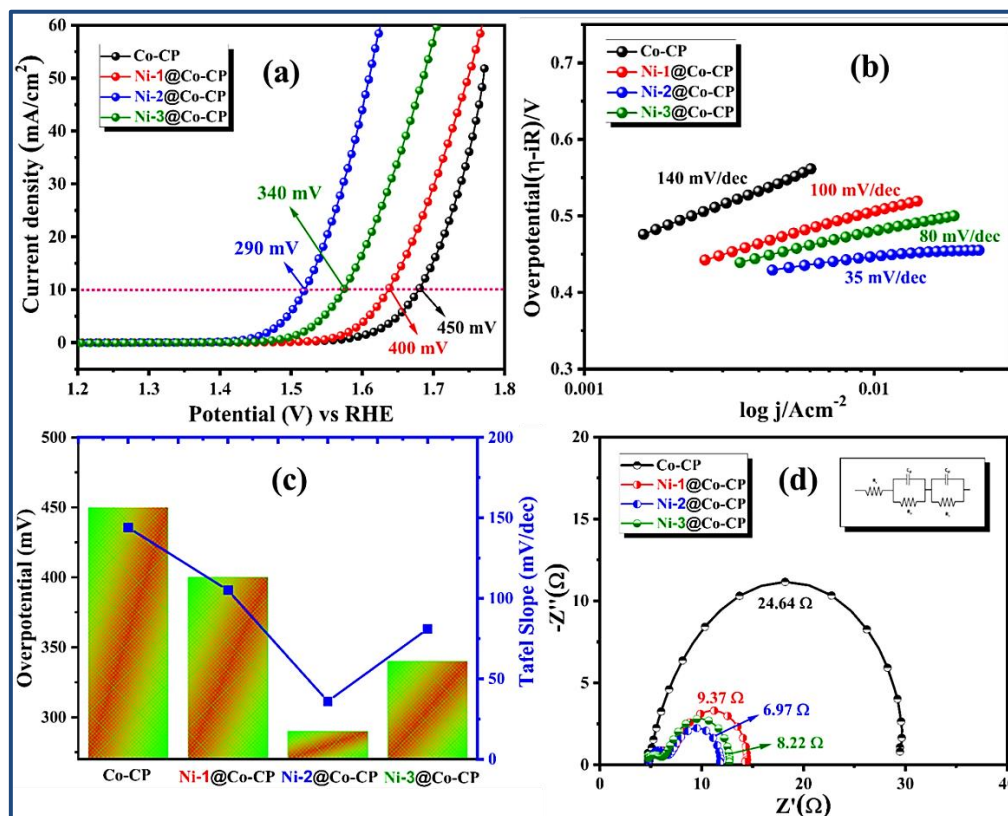


Figure 5.19 (a) The polarization curve for LSV recorded at a scan rate of 5 mV/s. (b) Tafel plot. (c) Comparative diagram of the overpotential and Tafel slope values. (d) EIS outcomes of Co-CP and Ni@Co-CP catalysts (Inset represents the equivalent circuit diagram).

The Ni-2@Co-CP is capable of reaching the benchmark current density of 10 mA cm^{-2} with overpotential of only 290 mV (Figure 5.19a). In comparison, other OER catalysts, necessitate much higher overpotentials of 400 (Ni-1@Co-CP) and 340 mV (Ni-3@Co-CP). In the context of catalyst evaluation, Tafel slope serves as a crucial metric for assessing the kinetic characteristics of internal charge transfer within a catalyst; with a smaller slope reflecting a more favourable condition for the electrocatalytic reaction. The Tafel slope analysis revealed that Ni-2@Co-CP has the most favourable value 35 mV/dec, while the results for Co-CP (140 mV/dec), Ni-1@Co-CP (100 mV/dec), Ni-3@Co-CP (80 mV/dec) are much higher than that of Ni-2@Co-CP (Figure 5.19b). This observation indicates that

Ni-2@Co-CP exhibits the highest efficiency in electron transfer, accompanied by enhanced kinetics, thereby serving as a highly effective catalyst for the OER. To facilitate better understanding, a comparative diagram has been drawn illustrating the recorded overpotential values at 10 mA/cm² alongside the Tafel slopes (Figure 5.19c). The EIS was studied to consider the charge transfer resistance (R_{ct}) at the interface between the electrode and electrolyte and the R_{ct} values are 24.64 Ω (Co-CP), 9.37 Ω (Ni-1@Co-CP), 8.22 Ω (Ni-3@Co-CP) and the lowest value is 6.97 Ω for Ni-2@Co-CP (Figure 5.19d).

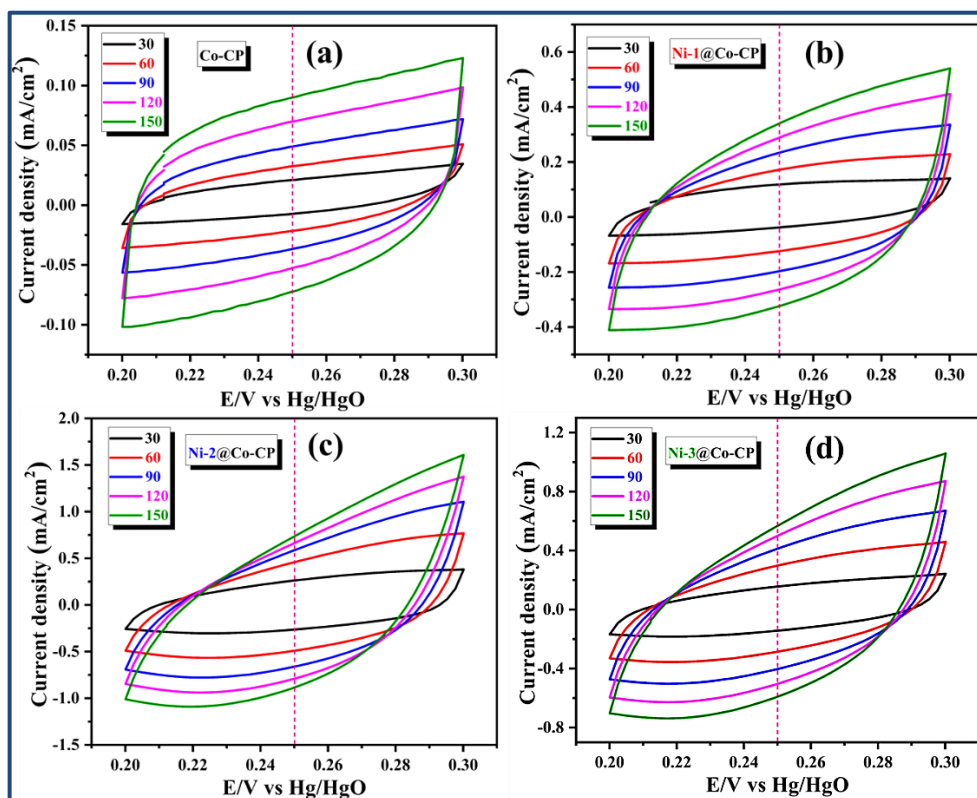


Figure 5.20 (a-d) CVs recorded for Co-CP and Ni@Co-CP composites in a non-Faradaic region (Potential: 0.2-0.3 V) in 1M KOH solution.

This indicates that Ni-2@Co-CP exhibits fastest charge transfer kinetics between the electrode and the electrolyte solution, thereby facilitating enhanced catalytic activity for the OER. It is noteworthy to mention that the impedance spectra of the electrocatalysts are pure semi-circle and the Ni-2@Co-CP shows the lowest radius. This finding further illustrates that the tuning of the electronic structure has the potential to significantly enhance the rate of electron transfer in the material and fastest for Ni-2@Co-CP. Ni is an active electrode material and its incorporation plays a crucial role in lowering the charge transfer resistance at the interface of the catalyst. However, an overabundance of Ni doping can cause considerable lattice distortion, which undermines this advantageous outcome.⁶⁴ Increase in Ni doping in the Co-CP lattice can improve reactivity by changing the reaction energy landscape more

regular and/or decreasing the barriers of rate-determining steps⁶⁵ compared to the pristine CPs. However, the catalytic performance is decreased after reaching an optimum level of Ni doping which may be due to the synergistic effect of Ni with Co in the pristine CP and the optimal electronic structure is achieved at this doping levels.

Electrochemically active surface area (ECSA) values for all the catalysts were derived by taking the ratio of the double-layer capacitance (C_{dl}) to the capacitance value (C_s) in a 1 M KOH solution that pertains to a flat electrode surface. The values of the ECSA for all the derived OER electrocatalysts are determined through cyclic voltammetry (CV) study in the potential range 0.2-0.3 V with varies scan rate (Figure 5.20a-d). The slope (Figure 5.21a) is critical for evaluating the double layer capacitance (C_{dl}); a high C_{dl} value implies that there are many surfaces intrinsic active sites available, which aids in accelerating the kinetics of OER. The observed C_{dl} values are 1.09 (Co-CP), 4.24 (Ni-1@Co-CP), 7.12 (Ni-3@Co-CP), and 9.01 $\mu\text{F}/\text{cm}^2$ (Ni-2@Co-CP).

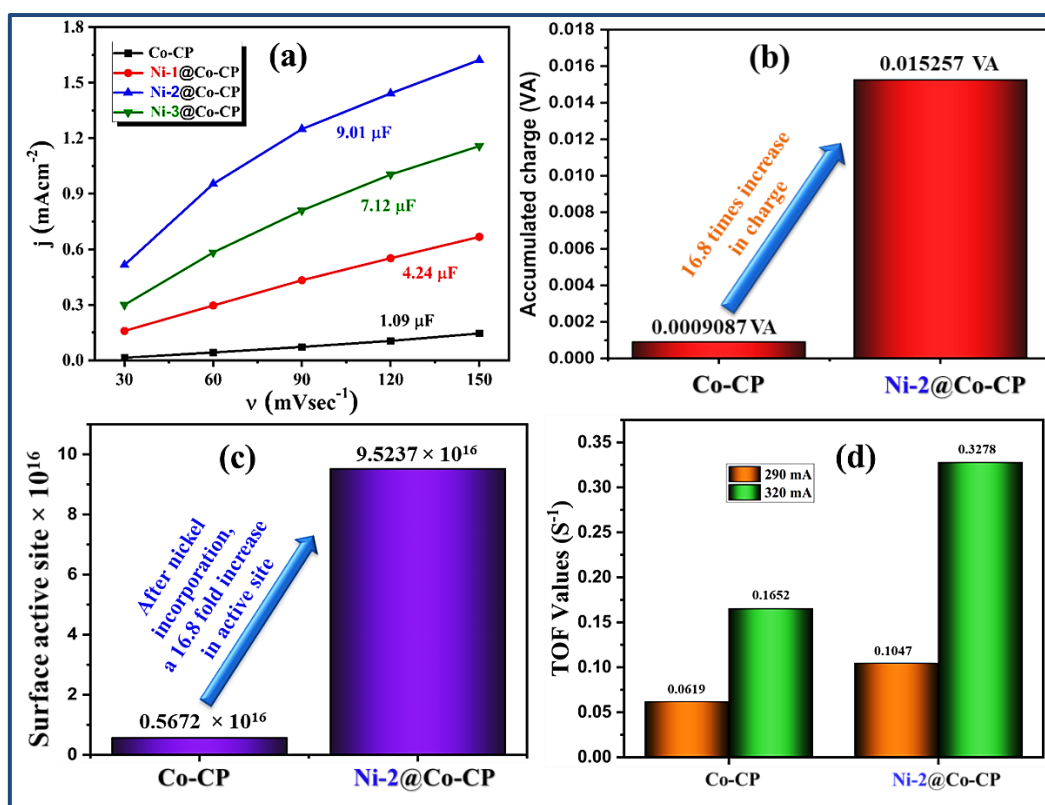


Figure 5.21 (a) Double layered capacitance (C_{dl}) of all four catalysts. (b,c) charge accumulated over the surface and surface-active sites of Co-CP and Ni-2@Co-CP, respectively. (d) TOF values of Co-CP and Ni-2@Co-CP determined at 290 and 320 mV overpotential for OER.

The active area of the Co-CP deposited electrode is being 4.5435×10^{-6} VA and has been increased to 7.6287×10^{-5} VA for Ni-2@Co-CP. The observation proposes that the

incorporation of Ni^{2+} in Co-CP framework enhances the surface area, which might be a contributing factor to the improved OER performance of the Ni-2@Co-CP. The calculated active sites due to Ni^{2+} (Ni-2@Co-CP) impregnation is 16.8 times higher than that of Co-CP only and hence the accumulated surface charge is substantially increased by the same amount (Figure 5.21b and 21c). Moreover, to obtain a deeper understanding of intrinsic activity, the turnover frequency (TOF) was analysed at two different overpotentials (290 and 320 mV) (Figure 5.21d) which identifies that Ni-2@Co-CP presents higher TOF values of 0.1652 and 0.3278 s^{-1} , suggesting that the rate of O_2 molecule conversion per active site per unit time is greater than that of Co-CP, which has TOF values of 0.0619 and 0.1047 s^{-1} , respectively. Alongside remarkable catalytic efficiency for OER, the durability of catalysts is a fundamental aspect. An assessment of the long-term durability of Ni-2@Co-CP was conducted utilizing the chronoamperometric (CA) technique at a fixed potential of 1.6 V against the reversible hydrogen electrode (RHE). The CA curve (Figure 5.22a) has revealed outstanding stability, showing no significant deviations in current density throughout a 9 h of continuous electrolysis in a 1 M KOH solution. Furthermore, the LSV curves (Figure 5.22b) exhibited a decline in performance after 1000 cycles of CV testing.

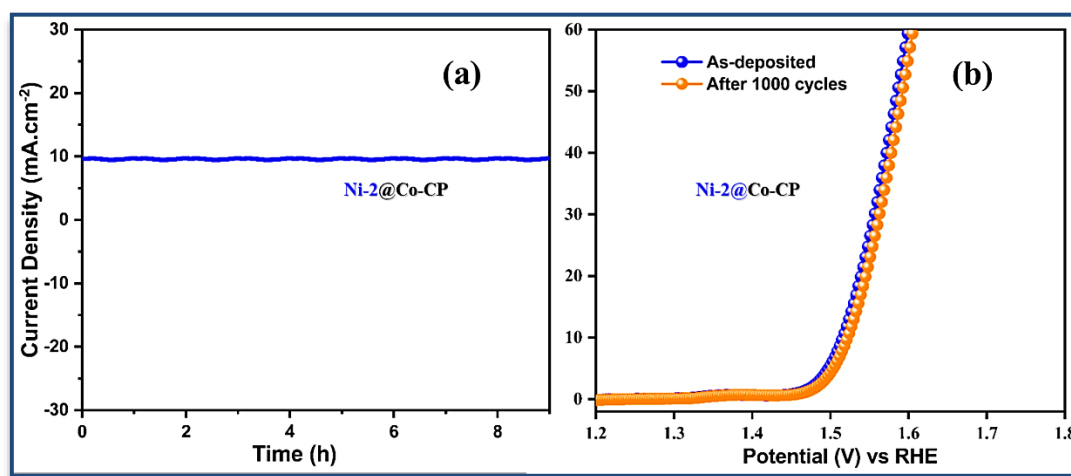


Figure 5.22 (a) Durability testing at 10 mA cm^{-2} for 9 h of Ni-2@Co-CP. (b) LSV plots of Ni-2@Co-CP before and after continuous OER study at 10 mA cm^{-2} .

A comparison⁶⁶⁻⁷⁹ of the overpotential values for the Ni-2@Co-CP catalyst in relation to previously reported MOF/CP-based electrocatalysts (Figure 5.23, Table 5.4) revealed that the OER activity of the Ni-2@Co-CP catalyst is comparable to, and in certain cases surpasses, that of other catalysts reported in the literature. This exceptional electrochemical performance can be primarily attributed to the structural characteristics and intrinsic properties of the bimetallic material.

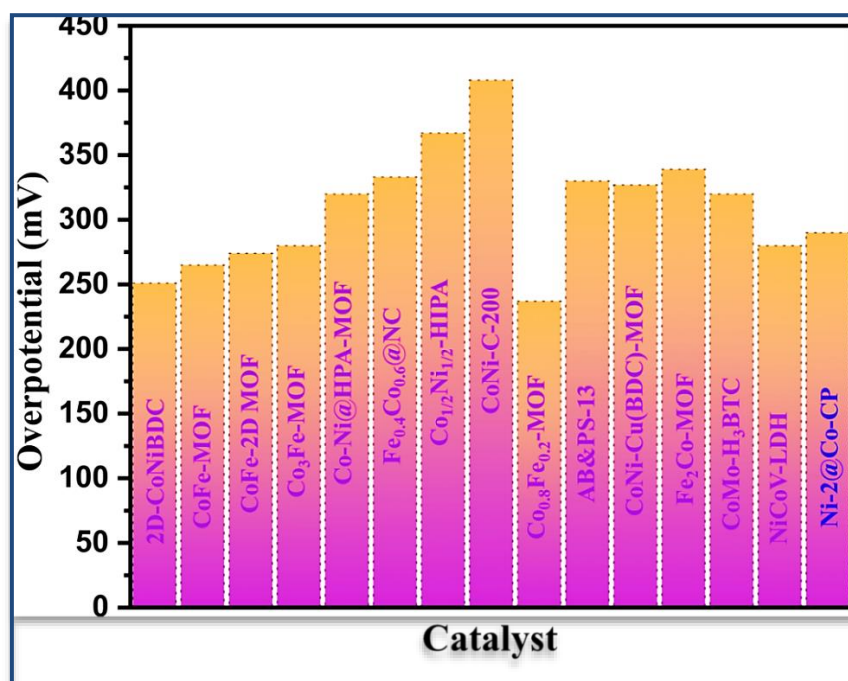


Figure 5.23 Histogram comparison of similar types of reported OER catalysts with Ni-2@Co-CP. ⁶⁶⁻⁷⁹

Table 5.4 Comparison of MOF/CP based electrocatalyst with our catalyst for OER study.

Sl. No	Electrocatalyst	Substrate	Electrolyte	Overpotential (mV)	Current density (mA. cm ⁻²)	Reference
1	2D-CoNiBDC	CC	1.0 M KOH	251	10	1
2	CoFe-MOF	GCE	1.0 M KOH	265	10	2
3	CoFe-2D MOF	NF	1.0 M KOH	274	10	3
4	Co ₃ Fe-MOF	GCE	1.0 M KOH	280	10	4
5	Co-Ni@HPA-MOF	GCE	1.0 M KOH	320	10	5
6	Fe _{0.4} Co _{0.6} @NC	GCE	1.0 M KOH	333	10	6
7	Co _{1/2} Ni _{1/2} -HIPA	GCE	1.0 M KOH	367	10	7
8	CoNi-C-200	GCE	1.0 M KOH	408	10	8
9	Co _{0.8} Fe _{0.2} -MOF	CC	1.0 M KOH	237	10	9
10	AB&PS-13	GSE	1.0 M KOH	330	10	10
11	CoNi-Cu(BDC)-MOF	GCE	1.0 M KOH	327	10	11
12	Fe ₂ Co-MOF	GCE	1.0 M KOH	339	10	12
13	CoMo-H ₃ BTC	GCE	0.1 M NaOH	320	10	13
14	NiCoV-LDH	CC	1.0 M KOH	280	10	14
15	Ni-2@Co-CP	NF	0.1 M KOH	290	10	This work

CC: Carbon Cloth; GCE: Glassy Carbon Electrode; NF: Nickel Foam; GSE: Graphite Strip Electrode.

5.3.6 Post OER Characterisation of Ni@Co-CP Composites

A notable feature of the electrode material in the colour change from bluish pink to greenish was observed during the OER test. The characterization of the Ni-2@Co-CP structure took place after the stability test. The integrity of the structure suggests that the catalyst possesses remarkable stability. To visualise any morphological change after prolonged electrocatalysis, FE-SEM and HR-TEM analyses were performed for Ni-2@Co-CP catalyst. It is evident that particle agglomeration has taken place during electrolysis, leading to a roughening of the catalysts surface when compared to its original pristine state (Figure 5.24). But no considerable change in their shape and morphology was detected, thereby demonstrating reasonable morphological stability throughout the process of electrocatalysis.

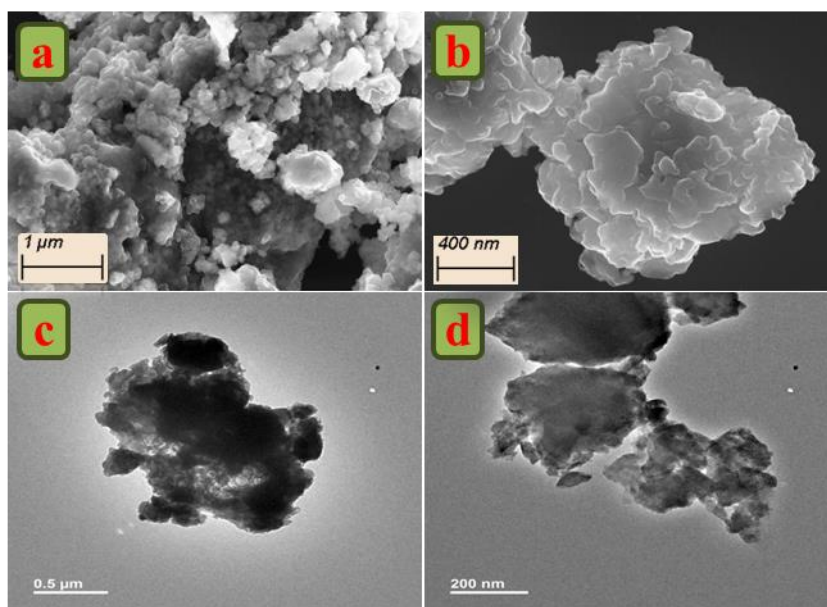


Figure 5.24 Low to high magnification (a, b) FE-SEM and (c, d) HR-TEM images of Ni-2@Co-CP after OER study.

An investigation into the chemical composition and elemental state of Ni-2@Co-CP by the XPS survey analysis (Figure 5.25) confirms the persistence of Co 2p, Ni 2p, O 1s, and C 1s, even after the OER assessment. The analysis of the deconvoluted XPS spectrum for Ni 2p (Figure 5.26) reveals two doublets associated with the Ni 2p_{3/2} and Ni 2p_{1/2} orbitals. The discernible energy splitting at 855.73 eV and 857.11 eV points to the existence of nickel in +2 and +3 oxidation states. It appears that Ni²⁺ is converted to Ni³⁺ during the electrochemical oxidation (OER), providing active catalyst sites for OER, as evidenced by the detection of Ni in the +3-oxidation state.⁸⁰ Similarly, the deconvoluted Co 2p_{3/2} spectrum (Figure 5.26) illustrates two distinct peaks. These peaks are associated with varying oxidation states of cobalt, specifically Co³⁺ at 780.61 eV and Co²⁺ at 782.23 eV.⁸¹ The

deconvolution of the O 1s spectrum provides clear evidence for the existence of distinct oxygen environments, supporting earlier findings. However, a new peak has been detected (**Figure 5.26**), which is associated with the adsorption of molecular water on the surface during the extended chronoamperometric analysis. The post-OER characterizations indicated a high degree of preservation in the material's nature, structure, and stability.

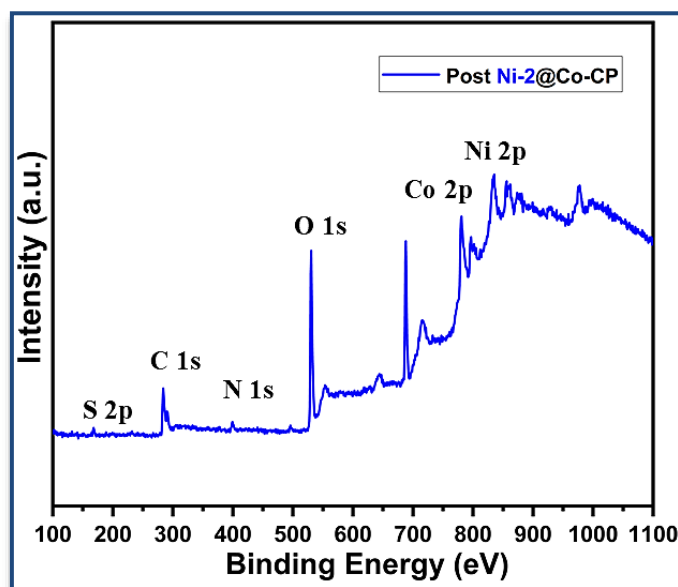


Figure 5.25 XPS survey spectrum of post Ni-2@Co-CP.

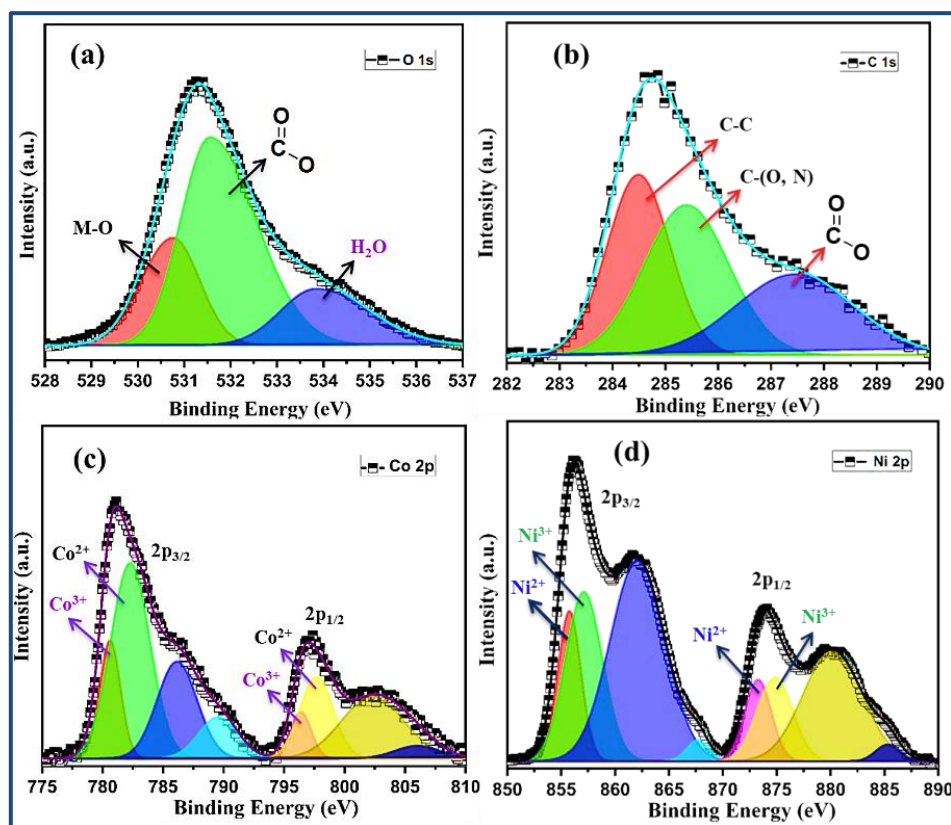


Figure 5.26 Deconvoluted XPS spectra of (a) O 1s, (b) C 1s, (c) Co 2p, (d) Ni 2p in the heterostructure catalyst Ni-2@Co-CP after continuous LSV study.

5.4 Conclusions

This study implemented a straightforward electrochemical based methodology at ambient temperature of cobalt-based coordination polymers (Co-CP), derived from 2,5-thiophenedicarboxylate and pyridinyltriazoleimine. Following the effective incorporation of nickel(II), the cobalt-nickel bimetallic composite (Ni-2@Co-CP in the molar ratio 0.75 : 1) demonstrated significant activity characterized by a minimal overpotential of 290 mV and a low Tafel slope of 35 mV dec⁻¹ in alkaline environment. Additionally, the introduction of nickel into cobalt-based framework (Co-CP) results in an enhancement of the electrochemically active surface area, thereby boosting the catalyst's performance. The presence of Ni (with a vacant d orbital) fosters a strong d π -p π interaction with O²⁻, thereby facilitating electron transfer in the Ni-2@Co-CP system. Additionally, this modification led to improved electron transfer kinetics, facilitating the OER process. This improved charge transfer capability allows for faster and more efficient reactions, making the material ideal for applications in energy conversion and storage. It is seen that the OER of Ni-2@Co-CP appears to be highest out of three Ni-doped materials. The combination of pyridinyltriazoleimine and thiophene opens up new opportunities for developing advanced materials that can revolutionize industries such as nanotechnology, renewable energy, and biotechnology. This research carries important ramifications for the electrochemical energy science for the effective application of Ni@Co-CP composites in cutting-edge energy conversion technologies.

5.5 References

- (1) Xu, Y.; Liu, M.; Wang, M.; Ren, T.; Ren, K.; Wang, Z.; Li, X.; Wang, L.; Wang, H. Methanol Electro reforming Coupled to Green Hydrogen Production over Bifunctional NiIr Based Metal Organic Framework Nanosheet Arrays. *Appl. Catal., B* **2022**, *300*, 120753.
- (2) He, Z. L.; Huang, X.; Chen, Q.; Zhai, C.; Hu, Y.; Zhu, M. Pt nanoclusters embedded Fe-based metal-organic framework as a dual-functional electrocatalyst for hydrogen evolution and alcohols oxidation. *J. Colloid Interface Sci.* **2022**, *616*, 279-286.
- (3) Hong, Q.; Wang, Y.; Wang, R.; Chen, Z.; Yang, H.; Yu, K.; Liu, Y.; Huang, H.; Kang, Z.; Menezes, P. W. In Situ Coupling of Carbon Dots with Co-ZIF Nanoarrays Enabling Highly Efficient Oxygen Evolution Electrocatalysis. *Small* **2023**, *19*, 2206723.

- (4) Zhao, H.; Yu, L.; Zhang, L.; Dai, L.; Yao, F.; Huang, Y.; Sun, J.; Zhu, J. Facet Engineering in Ultrathin Two-Dimensional NiFe Metal-Organic Frameworks by Coordination Modulation for Enhanced Electrocatalytic Water Oxidation. *ACS Sustainable Chem. Eng.* **2021**, 9, 10892-10901.
- (5) Du, Y.; Tang, H.; Zhang, D.; Liu, H.; Chen, Y.; Zhu, Z.; Yang, W.; Li, Z.; Tang, Y.; Liu, C. Boosting Electrocatalytic Oxygen Evolution: Superhydrophilic/Superaerophobic Hierarchical Nanoneedle/Microflower Arrays of $\text{Ce}_x\text{Co}_{3-x}\text{O}_4$ with Oxygen Vacancies. *ACS Appl. Mater. Interfaces* **2021**, 13, 42843-42851.
- (6) Yu, R.; Liu, D.; Yuan, M.; Wang, Y.; Ye, C.; Li, J.; Du, Y. J. Universal MOF-Mediated synthesis of 2D CoNi-based layered triple hydroxides electrocatalyst for efficient oxygen evolution reaction. *Colloid Interface Sci.* **2021**, 602, 612-618.
- (7) Jasimuddin, S.; Yamada, T.; Fukuju, K.; Otsuki, J.; Sakai, K. Photocatalytic hydrogen production from water in self-assembled supramolecular iridium-cobalt systems. *Chem. Commun.* **2010**, 46, 8466-8468.
- (8) Zhang, X.; Lin, R.; Meng, X.; Li, W.; Chen, F.; Hou, J. Iron Phthalocyanine/Two-Dimensional Metal-Organic Framework Composite Nanosheets for Enhanced Alkaline Hydrogen Evolution. *Inorg. Chem.* **2021**, 60, 9987-9995.
- (9) Jiao, Y.; Zheng, Y.; Jaroniec, M.; Qiao, S. Z. Design of electrocatalysts for oxygen- and hydrogen-involving energy conversion reactions. *Chem. Soc. Rev.* **2015**, 44, 2060-2086.
- (10) Tahir, M.; Pan, L.; Idrees, F.; Zhang, X.; Wang, L.; Zou, J.-J.; Wang, Z. L. Electrocatalytic oxygen evolution reaction for energy conversion and storage: A comprehensive review. *Nano Energy* **2017**, 37, 136-157.
- (11) Mahanta, A.; Barman, K.; Akond, U. S.; Jasimuddin, S. Cobalt (II) and nickel (II) coordination polymers derived from a naphthalene-based tetracarboxylic acid and N-donor linkers: structures, magnetic properties and electrocatalytic water oxidation. *New J. Chem.* **2021**, 45, 8676-8682.
- (12) Yan, Y.; Xia, B. Y.; Zhao, B.; Wang, X. A review on noble-metal-free bifunctional heterogeneous catalysts for overall electrochemical water splitting. *J. Mater. Chem. A* **2016**, 4, 17587-17603.
- (13) Han, L.; Dong, S.; Wang, E. Transition-metal (Co, Ni, and Fe)-based electrocatalysts for the water oxidation reaction. *Adv. Mater.* **2016**, 28, 9266-9291.

- (14) Dincer, I.; Acar, C. Review and evaluation of hydrogen production methods for better sustainability. *Int. J. Hydrogen Energy* **2014**, *40*, 11094-11111.
- (15) Zou, X.; Zhang, Y. Noble metal-free hydrogen evolution catalysts for water splitting. *Chem. Soc. Rev.* **2015**, *44*, 5148-5180.
- (16) Suen, N.-T.; Hung, S.-F.; Quan, Q.; Zhang, N.; Xu, Y.-J.; Chen, H. M. Electrocatalysis for the oxygen evolution reaction: recent development and future perspectives. *Chem. Soc. Rev.* **2017**, *46*, 337-365.
- (17) Wei, C.; Rao, R. R.; Peng, J.; Huang, B.; Stephens, I. E. L.; Risch, M.; Xu, Z. J.; Shao-Horn, Y. Recommended practices and benchmark activity for hydrogen and oxygen electrocatalysis in water splitting and fuel cells. *Adv. Mater.* **2019**, *31*, 1806296.
- (18) Farid, S.; Ren, S.; Hao, C. MOF-derived metal/carbon materials as oxygen evolution reaction catalysts. *Inorg. Chem. Commun.* **2018**, *94*, 57-74.
- (19) Audichon, T.; Napporn, T. W.; Canaff, C.; Morais, C.; Comminges, C.; Kokoh, K. B. IrO₂ Coated on RuO₂ as Efficient and Stable Electroactive Nanocatalysts for Electrochemical Water Splitting. *J. Phys. Chem. C* **2016**, *120*, 2562-2573.
- (20) Lee, Y.; Suntivich, J.; May, K. J.; Perry, E. E.; Shao-Horn, Y. Synthesis and activities of rutile IrO₂ and RuO₂ nanoparticles for oxygen evolution in acid and alkaline solutions. *J. Phys. Chem. Lett.* **2012**, *3*, 399-404.
- (21) Liang, Y. Y.; Li, Y. G.; Wang, H. L.; Zhou, J. G.; Wang, J.; Regier, T.; Dai, H. J. Co₃O₄ nanocrystals on graphene as a synergistic catalyst for oxygen reduction reaction. *Nat. Mater.* **2011**, *10*, 780-786.
- (22) Liu, Q.; Jin, J. T.; Zhang, J. Y. NiCo₂S₄@graphene as a Bifunctional Electrocatalyst for Oxygen Reduction and Evolution Reactions. *ACS Appl. Mater. Interfaces* **2013**, *5*, 5002-5008.
- (23) Song, F.; Hu, X. Ultrathin Cobalt-Manganese Layered Double Hydroxide Is an Efficient Oxygen Evolution Catalyst. *J. Am. Chem. Soc.* **2014**, *136*, 16481-16484.
- (24) Campos-Roldán, C. A.; Alonso-Vante, N. The Oxygen Reduction and Hydrogen Evolution Reactions on Carbon Supported Cobalt Diselenide Nanostructures. *J. Electrochem. Soc.* **2020**, *167*, 026507.
- (25) Xiong, D. H.; Wang, X. G.; Li, W.; Liu, L. F. Facile synthesis of iron phosphide nanorods for efficient and durable electrochemical oxygen evolution. *Chem. Commun.* **2016**, *52*, 8711-8714.

- (26) Xue, J.-Y.; Li, C.; Li, F.-L.; Gu, H.-W.; Braunstein, P.; Lang, J.-P. Recent advances in pristine tri-metallic metal-organic frameworks toward the oxygen evolution reaction. *Nanoscale* **2020**, *12*, 4816-4825.
- (27) Dou, S.; Li, X.; Wang, X. Rational Design of Metal-Organic Frameworks towards Efficient Electrocatalysis. *ACS Mater. Lett.* **2020**, *2*, 1251-1267.
- (28) McCarthy, B. D.; Beiler, A. M.; Johnson, B. A.; Liseev, T.; Castner, A. T.; Ott, S. Analysis of electrocatalytic metal-organic frameworks. *Coord. Chem. Rev.* **2020**, *406*, 213137.
- (29) Jin, S. How to Effectively Utilize MOFs for Electrocatalysis. *ACS Energy Lett.* **2019**, *4*, 1443-1445.
- (30) Huang, C.-J.; Xu, H.-M.; Shuai, T.-Y.; Zhan, Q.-N.; Zhang, Z.-J.; Li, G.-R. A review of modulation strategies for improving catalytic performance of transition metal phosphides for oxygen evolution reaction. *Appl. Catal. B: Environ.* **2023**, *325*, 122313.
- (31) Furukawa, H.; Cordova, K. E.; O’Keeffe, M.; Yaghi, O. M. The chemistry and applications of metal-organic frameworks. *Science* **2013**, *341*, 1230444.
- (32) Guo, J.; Qin, Y.; Zhu, Y.; Zhang, X.; Long, C.; Zhao, M.; Tang, Z. Metal-organic frameworks as catalytic selectivity regulators for organic transformations. *Chem. Soc. Rev.* **2021**, *50*, 5366-5396.
- (33) Li, Z.; Song, M.; Zhu, W.; Zhuang, W.; Du, X.; Tian, L. MOF-derived hollow heterostructures for advanced electrocatalysis. *Coord. Chem. Rev.* **2021**, *439*, 213946.
- (34) Zhao, H.; Zhang, L.; Dai, L.; Yao, F.; Huang, Y.; Deng, J.; Fu, Y.; Zhu, J.; Sun, J. Regulating the transformation behaviour of nickel iron metal-organic frameworks through a dual-ligand strategy for enhanced oxygen evolution reaction performance. *Appl. Surf. Sci.* **2022**, *592*, 153252.
- (35) Hao, Y.; Liu, Q.; Zhou, Y.; Yuan, Z.; Fan, Y.; Ke, Z.; Su, C. Y.; Li, G. A 2D NiFe Bimetallic Metal-Organic Frameworks for Efficient Oxygen Evolution Electrocatalysis. *Energy Environ. Mater.* **2019**, *2*, 18-21.
- (36) Jia, Y.; Xue, Z.; Yang, J.; Liu, Q.; Xian, J.; Zhong, Y.; Sun, Y.; Zhang, X.; Liu, Q.; Yao, D.; Li, G. Tailoring the Electronic Structure of an Atomically Dispersed Zinc Electrocatalyst: Coordination Environment Regulation for High Selectivity Oxygen Reduction. *Angew. Chem., Int. Ed.* **2022**, *61*, e202110838.

- (37) Xiao, Z.; Wang, Y.; Huang, Y.-C.; Wei, Z.; Dong, C.-L.; Ma, J.; Shen, S.; Li, Y.; Wang, S. Filling the oxygen vacancies in Co_3O_4 with phosphorus: an ultra-efficient electrocatalyst for overall water splitting. *Energy Environ. Sci.* **2017**, *10*, 2563-2569.
- (38) Duan, J.; Chen, S.; Zhao, C. Ultrathin metal-organic framework array for efficient electrocatalytic water splitting. *Nat. Commun.* **2017**, *8*, 15341.
- (39) Han, B.; Ou, X.; Deng, Z.; Song, Y.; Tian, C.; Deng, H.; Xu, Y.-J.; Lin, Z. Nickel Metal-Organic Framework Monolayers for Photoreduction of Diluted CO_2 : Metal-Node-Dependent Activity and Selectivity. *Angew. Chem., Int. Ed.* **2018**, *57*, 16811-16815.
- (40) Liao, P.-Q.; Shen, J.-Q.; Zhang, J.-P. Metal-organic frameworks for electrocatalysis. *Coord. Chem. Rev.* **2018**, *373*, 22-48.
- (41) Xue, Z.; Liu, K.; Liu, Q.; Li, Y.; Li, M.; Su, C. Y.; Ogiwara, N.; Kobayashi, H.; Kitagawa, H.; Liu, M.; Li, G. Missing-linker metal-organic frameworks for oxygen evolution reaction. *Nat. Commun.* **2019**, *10*, 5048.
- (42) Chai, L.; Hu, Z.; Wang, X.; Xu, Y.; Zhang, L.; Li, T. T.; Hu, Y.; Qian, J.; Huang, S. Stringing Bimetallic Metal-Organic Framework-Derived Cobalt Phosphide Composite for High-Efficiency Overall Water Splitting. *Adv. Sci.* **2020**, *7*, 1903195.
- (43) Han, W.; Li, M.; Ma, Y.; Yang, J. Cobalt-Based Metal-Organic Frameworks and Their Derivatives for Hydrogen Evolution Reaction. *Front. Chem.* **2020**, *8*, 592915.
- (44) Zhang, W.; Cui, L.; Liu, J. Recent advances in cobalt-based electrocatalysts for hydrogen and oxygen evolution reactions. *J. Alloys Compd.* **2020**, *821*, 153542.
- (45) Hua, Y.; Li, X.; Chen, C.; Pang, H. Cobalt based metal-organic frameworks and their derivatives for electrochemical energy conversion and storage. *Chem. Eng. J.* **2019**, *370*, 37-59.
- (46) Zhou, W.; Huang, D.-D.; Wu, Y.-P.; Zhao, J.; Wu, T.; Zhang, J.; Li, D.-S.; Sun, C.; Feng, P.; Bu, X. Stable hierarchical bimetal-organic nanostructures as high performance electrocatalysts for the oxygen evolution reaction. *Angew. Chem., Int. Ed.* **2019**, *58*, 4227-4231.
- (47) Senthil Raja, D.; Chuah, X.-F.; Lu, S.-Y. In Situ Grown Bimetallic MOF-Based Composite as Highly Efficient Bifunctional Electrocatalyst for Overall Water Splitting with Ultrastability at High Current Densities. *Adv. Energy Mater.* **2018**, *8*, 1801065.
- (48) Sun, F.; Wang, G.; Ding, Y.; Wang, C.; Yuan, B.; Lin, Y. NiFe-Based Metal-Organic Framework Nanosheets Directly Supported on Nickel Foam Acting as Robust Electrodes for Electrochemical Oxygen Evolution Reaction. *Adv. Energy Mater.* **2018**, *8*, 1800584.

- (49) Fang, X.; Jiao, L.; Yu, S. H.; Jiang, H. L. Metal-Organic Framework-Derived FeCo-N-Doped Hollow Porous Carbon Nanocubes for Electrocatalysis in Acidic and Alkaline Media. *ChemSusChem* **2017**, *10*, 3019-3024.
- (50) Cheng, W.; Wu, Z. P.; Luan, D.; Zang, S. Q.; Lou, X. W. D. Synergetic cobalt-copper- based bimetal-organic framework nanoboxes toward efficient electrochemical oxygen evolution. *Angew. Chem., Int. Ed.* **2021**, *60*, 26397-26402.
- (51) Cheng, W.; Zhao, X.; Su, H.; Tang, F.; Che, W.; Zhang, H.; Liu, Q. Lattice-strained Metal-Organic Framework Arrays for Bifunctional Oxygen Electrocatalysis. *Nat. Energy* **2019**, *4*, 115-122.
- (52) Sun, Y.; Xue, Z.; Liu, Q.; Jia, Y.; Li, Y.; Liu, K.; Lin, Y.; Liu, M.; Li, G.; Su, C. Y. Modulating electronic structure of metal-organic frameworks by introducing atomically dispersed Ru for efficient hydrogen evolution. *Nat. Commun.* **2021**, *12*, 1369.
- (53) Guo, Y.-M.; Du, M. 4-Amino-3,5-bis(4-pyridyl)-1,2,4-triazole. *Acta Crystallogr. E* **2002**, *58*, o966-o968.
- (54) Bruker AXS Inc. *SMART and SAINT*, Bruker AXS Inc., Madison, WI, 1998.
- (55) Bruker AXS Inc. *SADABS*, Bruker AXS area detector scaling and absorption correction, Bruker AXS Inc., Madison, WI, 2014.
- (56) Sheldrick, G. M. *SHELXT-Integrated space-group and crystal-structure determination*. *Acta Crystallogr., Sect. A* **2015**, *71*, 3-8.
- (57) Dolomanov, O. V.; Bourhis, L. J.; Gildea, R. J.; Howard, J. A. K.; Puschmann, H. OLEX2: a complete structure solution, refinement and analysis program. *J. Appl. Crystallogr.* **2009**, *42*, 339-341.
- (58) Bourhis, L. J.; Dolomanov, O. V.; Gildea, R. J.; Howard, J. A. K.; Puschmann, H. The anatomy of OLEX2: a complete structure solution package. *Acta Crystallogr., Sect. A* **2015**, *71*, 59-75.
- (59) Li, W.; Fang, W.; Wu, C.; Dinh, K. N.; Ren, H.; Zhao, L.; Liu, C.; Yan, Q. Bimetal-MOF nanosheets as efficient bifunctional electrocatalysts for oxygen evolution and nitrogen reduction reaction. *J. Mater. Chem. A* **2020**, *8*, 3658-3666.
- (60) Liu, M.; Kong, L.; Wang, X.; He, J.; Bu, X.-H. Engineering Bimetal Synergistic Electrocatalysts Based on Metal-Organic Frameworks for Efficient Oxygen Evolution. *Small* **2019**, *15*, 1903410.
- (61) Hutchings, G. S.; Zhang, Y.; Li, J.; Yonemoto, B. T.; Zhou, X.; Zhu, K.; Jiao, F. In Situ Formation of Cobalt Oxide Nanocubanes as Efficient Oxygen Evolution Catalysts. *J. Am. Chem. Soc.* **2015**, *137*, 4223-4229.

- (62) Xue, Z.; Li, Y.; Zhang, Y.; Geng, W.; Jia, B.; Tang, J.; Bao, S.; Wang, H.-P.; Fan, Y.; Wei, Z.; Zhang, Z.; Ke, Z.; Li, G.; Su, C. Y. Modulating Electronic Structure of Metal-Organic Framework for Efficient Electrocatalytic Oxygen Evolution. *Adv. Energy Mater.* **2018**, 8, 1801564.
- (63) Zhou, X.; Gao, J.; Hu, Y.; Jin, Z.; Hu, K.; Reddy, K. M.; Yuan, Q.; Lin, X.; Qiu, H. J. Theoretically Revealed and Experimentally Demonstrated Synergistic Electronic Interaction of CoFe Dual-Metal Sites on N-doped Carbon for Boosting Both Oxygen Reduction and Evolution Reactions. *Nano Lett.* **2022**, 22, 3392-3399.
- (64) Zhang, N.; Hu, Y.; An, L.; Li, Q.; Yin, J.; Li, J.; Yang, R.; Lu, M.; Zhang, S.; Xi, P.; Yan, C. H. Surface Activation and Ni-S Stabilization in NiO/NiS₂ for Efficient Oxygen Evolution Reaction. *Angew. Chem., Int. Ed.* **2022**, 61, e202207217.
- (65) Verma, C.; Rasheed, T.; Anwar, M. T.; Quraishi, M. A. From metal-organic frameworks (MOFs) to metal-doped MOFs (MDMOFs): Current and future scenarios in environmental catalysis and remediation applications. *Microchem. J.* **2023**, 192, 108954.
- (66) Bai, X. J.; Chen, H.; Li, Y. N.; Shao, L.; Ma, J. C.; Li, L. L.; Chen, J. Y.; Wang, T. Q.; Zhang, X. M.; Zhang, L. Y.; Fu, Y.; Qi, W. CoNi-based metal-organic framework nanoarrays supported on carbon cloth as bifunctional electrocatalysts for efficient water-splitting. *New J. Chem.* **2020**, 44, 1694-1698.
- (67) Zou, Z.; Wang, T.; Zhao, X.; Jiang, W. J.; Pan, H.; Gao, D.; Xu, C. Expediting in-Situ Electrochemical Activation of Two-Dimensional Metal-Organic Frameworks for Enhanced OER Intrinsic Activity by Iron Incorporation. *ACS Catal.* **2019**, 9, 7356-7364.
- (68) Cai, M.; Liu, Q.; Xue, Z.; Li, Y.; Fan, Y.; Huang, A.; Li, M. R.; Croft, M.; Tyson, T. A.; Ke, Z.; Li, G. Constructing 2D MOFs from 2D LDHs: a highly efficient and durable electrocatalyst for water oxidation. *J. Mater. Chem. A* **2020**, 8, 190-195.
- (69) Li, W.; Fang, W.; Wu, C.; Dinh, K. N.; Ren, H.; Zhao, L.; Liu, C.; Yan, Q. Bimetal-MOF nanosheets as efficient bifunctional electrocatalysts for oxygen evolution and nitrogen reduction reaction. *J. Mater. Chem. A* **2020**, 8, 3658-3666.
- (70) Lu, M.; Li, Y.; He, P.; Cong, J.; Chen, D.; Wang, J.; Wu, Y.; Xu, H.; Gao, J.; Yao, J. Bimetallic metal-organic framework nanosheets as efficient electrocatalysts for oxygen evolution reaction. *J. Solid State Chem.* **2019**, 272, 32-37.
- (71) Dong, B.; Li, M. X.; Zhou, Y. N.; Fan, R. Y.; Chai, Y. M Spin-state regulating of cobalt assisted by iron doping and coordination for enhanced oxygen evolution reaction. *Int. J. Hydrogen Energy* **2022**, 47, 27508-27515.

- (72) Lu, L.; Li, Q.; Du, J.; Shi, W.; Cheng, P. Bimetallic cobalt-nickel coordination polymer electrocatalysts for enhancing oxygen evolution reaction. *Chin. Chem. Lett.* **2022**, *33*, 2928-2932.
- (73) Xie, Z.; Wang, Y. Metal-organic framework-derived CoNi-embedded carbon nanocages as efficient electrocatalysts for oxygen evolution reaction. *Ionics* **2018**, *24*, 1773-1780.
- (74) Hou, X.; Zhou, J.; Xu, X.; Wang, X.; Zhang, S.; Wang, H.; Huang, M. Morphological modulation of CoFe-based metal organic frameworks for oxygen evolution reaction. *Catal. Commun.* **2022**, *165*, 106445.
- (75) Joshi, A.; Sood, P.; Gaur, A.; Rani, D.; Madaan, V.; Singh, M. Improved OER performance of an Anderson-supported cobalt coordination polymer by assembling with acetylene black. *J. Mater. Chem. A* **2022**, *10*, 12805-12810.
- (76) Ma, J.; Lu, B.; Wang, S.; He, W.; Bai, X.; Wang, T.; Zhang, X.; Li, Y.; Zhang, L.; Chen, J.; Meng, F. MOF-derived CuCoNi trimetallic hybrids as efficient oxygen evolution reaction electrocatalysts. *New J. Chem.* **2020**, *44*, 2459-2464.
- (77) Guo, J.; Gao, Y.; Cao, X.; Rong, X.; Chi, S.; Fan, G.; Zhang, L.; Tian, G.; Zhao, X. Fe-Co bimetallic MOF-derived carbon directly application as an efficient electrocatalyst for oxygen evolution reaction. *Inorg. Chem. Commun.* **2024**, *170*, 113394.
- (78) Subramanian, B. T.; Thomas, S.; Biju, V. M. N. Trifunctional cobalt-molybdenum metal-organic framework for electrochemical oxygen evolution reaction and aromatic nitrosensing applications. *J. Appl. Electrochem.* **2024**, *54*, 559-572.
- (79) Bera, K.; Karmakar, A.; Kumaravel, S.; Sankar, S. S.; Madhu, R. N.; Dhandapani, H.; Nagappan, S.; Kundu, S. Vanadium-Doped Nickel Cobalt Layered Double Hydroxide: A High-Performance Oxygen Evolution Reaction Electrocatalyst in Alkaline Medium. *Inorg. Chem.* **2022**, *61*, 4502-4512.
- (80) Konkena, B.; Masa, J.; Botz, A. J.; Sinev, I.; Xia, W.; Koßmann, J.; Drautz, R.; Muhler, M.; Schuhmann, W. Metallic NiPS₃@NiOOH Core-Shell Heterostructures as Highly Efficient and Stable Electrocatalyst for the Oxygen Evolution Reaction. *ACS Catal.* **2017**, *7*, 229-237.
- (81) Tang, T.; Jiang, Z.; Deng, J.; Niu, S.; Yao, Z. C.; Jiang, W. J.; Zhang, L. J.; Hu, J. S. Constructing hierarchical nanosheet-on-microwire FeCoLDH@Co₃O₄ arrays for high-rate water oxidation. *Nano Res.* **2022**, *15*, 10021-10028.

Chapter 6

Summary of the Research Work

6.1 Dissertation Summary

This dissertation presents a comprehensive investigation into the design, synthesis, structural engineering, and multifunctional applications of coordination polymers (CPs) and metal-organic frameworks (MOFs)-materials renowned for their dynamic architectures and adaptive functionalities. Through the deliberate selection of π -conjugated organic linkers and metal centers, the work explores how molecular interactions and crystal engineering can be harnessed to produce advanced materials with tunable optical, electronic, and catalytic properties.

Chapter 1 lays the groundwork by contextualizing CPs/MOFs within the broader landscape of functional materials. Emphasis is placed on the interplay between organic ligands and inorganic nodes in dictating the geometry, dimensionality, and robustness of the resulting frameworks. Key non-covalent interactions $\pi \cdots \pi$ stacking, C-H $\cdots\pi$ contacts, and hydrogen bonding-are shown to critically influence the self-assembly and stability of these structures. The chapter also highlights the methodologies employed in synthesis and characterization, providing a multidimensional view of how these materials are engineered for specific applications in sensing, catalysis, gas sorption, and electronic devices.

Chapter 2 introduces a cadmium-based one-dimensional coordination polymer, $[\text{Cd}(\text{glu})_2(\text{pbiq})_2(\text{H}_2\text{O})]_n$, whose supramolecular architecture is stabilized via extensive hydrogen bonding and π -interactions. This material exhibits notable photoluminescence in acetonitrile and demonstrates high sensitivity toward nitroaromatic explosives, particularly trinitrophenol (TNP), with a detection threshold in the sub-micromolar range. Its semiconducting behavior (band gap: 3.31 eV) and nonlinear current-voltage characteristics underscore its potential in optoelectronic sensing platforms.

Chapter 3 advances the discussion with the synthesis of a two-dimensional cadmium-based MOF, $\{[\text{Cd}_2(5\text{-nip})_2(\text{pdiq})_2(\text{H}_2\text{O})_2(\text{CH}_3\text{OH})]\cdot\text{H}_2\text{O}\}_n$. This system illustrates how subtle variations in ligand design and framework dimensionality can modulate luminescence and charge transport. Notably, the material responds selectively to TNP with high quenching efficiency, even in competitive environments, and displays enhanced electrical conductivity under illumination-a promising trait for photoresponsive sensor technologies.

Chapter 4 transitions to a three-dimensional zinc-based MOF, $[\text{Zn}_2(\text{tdc})_4(\text{pdiq})_3]$, integrating sulfur-containing ligands to explore the impact of heteroatoms on framework performance. The material exhibits dual functionality: precise and selective fluorescence quenching in the presence of Al^{3+} ions (LOD: 1.39×10^{-7} M) and exceptional sensitivity

Chapter 6: Summary of the Research Work

toward TNP. The pronounced photo-conductivity under ambient light conditions further accentuates its utility in next-generation semiconducting and sensing applications.

Chapter 5 shifts the focus to catalytic applications, showcasing a redox-active cobalt coordination polymer synthesized with a triazole-derived ligand and thiophenedicarboxylate. The incorporation of nickel ions into the Co-CP matrix results in a series of Ni@Co-CP composites, with the optimized variant (Ni-2@Co-CP) exhibiting remarkable electrocatalytic activity for the oxygen evolution reaction (OER). With a reduced overpotential, low Tafel slope, and minimal charge transfer resistance, this system demonstrates the promise of CPs as tunable electrocatalysts for energy conversion technologies.

In its entirety, this dissertation embodies a multifaceted exploration of coordination frameworks-bridging structural design with real-world application. The research not only deepens our understanding of the underlying chemistry that governs CP/MOF behavior but also opens new pathways for their integration into environmental sensing, energy systems, and electronic materials. The innovations presented here reflect a deliberate convergence of synthetic strategy, functional insight, and technological relevance, contributing meaningfully to the evolving landscape of advanced material science.

List of Publications

1. Patra, A.; Das, P.; [Bairry, G.](#); Sepay, N.; Maity, S.; Bhunia, S.; Ray, P.P.; Sinha, C. Noncovalent intermolecular interactions between pyrazine and thiophene: Harnessing a luminescent ‘binuclear cadmium (II)’ coordination complex for the trace quantity detection of Fe^{3+} ion and modelling a smart device. *Polyhedron*, **2025**, 117602. doi.org/10.1016/j.poly.2025.117602
2. Patra, A.; Bhunia, S.; Das, P.; [Bairry, G.](#); Ray, P. P.; Sinha, C. Structural Elucidation of the 1D Cd(II) Coordination Polymer and Its Application in the Selective Detection of TNP and the Schottky Diode Device Fabrication. *Cryst. Growth Des.*, **2024**, 24, 10171-10181. doi.org/10.1021/acs.cgd.4c01001
3. [Bairry, G.](#); Sinha, C. An Extensive Analysis of Current Synthetic Methodologies and Applications of Imidazo/Benzimidazo[1,2- c]Quinazolines. *ChemistrySelect*, **2024**, 9, e202400421. doi.org/10.1002/slct.202400421
4. [Bairry, G.](#); Das, P.; Dutta, B.; Bhowmik, S.; Ray, P. P.; Sinha, C. In Situ Oxidation of Pyridyl-Dihydrobenzoimidazoquinazoline and the Synthesis of a Highly Luminescent Cd(II) Coordination Polymer: A Promising Candidate for Mutagenic Nitroaromatic Detection and Device Fabrication. *Inorganic Chemistry*, **2023**, 62, 12773-12782. doi.org/10.1021/acs.inorgchem.3c01308
5. Maity, M. B.; Talukdar, D.; Dutta, B.; [Bairry, G.](#); Murmu, N.; Das, G.; Sinha, C. Application of a Rhodamine-chromone Schiff base probe for the sensing of Fe^{3+} , Al^{3+} , Cr^{3+} at low concentration and exploration of the anticancer activity and bio-imaging. *Inorg. Chim. Acta*, **2023**, 545, 121276. doi.org/10.1016/j.ica.2022.121276
6. [Bairry, G.](#); Dey, A.; Dutta, B.; Ray, P. P.; Sinha, C. 2D Cd (II)-MOF of pyridyl-imidazoquinazoline: structure, luminescence, and selective detection of TNP and fabrication of semiconducting devices. *Cryst. Growth Des.*, **2022**, 22, 3138-3147. doi.org/10.1021/acs.cgd.2c00017
7. Dutta, B.; Bera, S.; [Bairry, G.](#); Shit, M.; Sinha, C.; Khanra. S.; Mir, M. H. Exploitation of a Series of Zinc (II)-Coordination Polymers for Palladium (II)-Detection in Aqueous Medium. *ES energy environ.*, **2022**, 16, 74-81. [DOI:10.30919/esee8c651](https://doi.org/10.30919/esee8c651)
8. [Bairry, G.](#); Dey, A.; Dutta, B.; Maity, S.; Sinha, C. Rational synthesis of a pyridyl-imidazoquinazoline based multifunctional 3D Zn (II)-MOF: structure, luminescence,

- selective and sensitive detection of Al^{3+} and TNP, and its semiconducting device application. *Dalton Trans.*, **2022**, 51, 13749-13761. [DOI:10.1039/D2DT01790C](https://doi.org/10.1039/D2DT01790C)
9. [Bairry, G.](#); Nandi, A.; Manna, K.; Jana, R. Ruthenium (II)-Catalyzed Migratory C-H Allylation/Hydroamination Cascade for the Synthesis of Rutaecarpine Analogues. *Synthesis*, **2019**, 51, 2523-2531. [DOI:10.1055/s-0037-1611525](https://doi.org/10.1055/s-0037-1611525)
 10. [Bairry, G.](#); Das, S.; Begam, H. M.; Jana, R. Exceedingly Fast, Direct Access to Dihydroisoquinolino[1,2-*b*]quinazolinones through a Ruthenium(II)-Catalyzed Redox-Neutral C-H Allylation/Hydroamination Cascade. *Org. Lett.*, **2018**, 20, 7107-7112. doi.org/10.1021/acs.orglett.8b03048
 11. Polley, A.; **Bairry, G.**; Das, P.; Jana, R. Triple Mode of Alkylation with Ethyl Bromodifluoroacetate: *N*, or *O*-Difluoromethylation, *N*-Ethylation and *S*-(ethoxycarbonyl)difluoromethylation. *Adv. Synth. Catal.*, **2018**, 360, 4161-4167. doi.org/10.1002/adsc.201800824
 12. Manna, M. K.; **Bairry, G.**; Jana, R. Sterically Controlled Ru (II)-Catalyzed Divergent Synthesis of 2-Methylindoles and Indolines through a C-H Allylation/Cyclization Cascade. *J. Org. Chem.*, **2018**, 83, 8390-8400. doi.org/10.1021/acs.joc.8b01034
 13. Das, S.; [Bairry, G.](#); Jana, R. Ligand-Promoted $\gamma\text{-C}(\text{sp}^3)\text{-H}$ Arylation and Unsymmetrical Diarylation to Access Unnatural Amino Acid Derivatives. *Org. Lett.*, **2018**, 20, 2667-2671. doi.org/10.1021/acs.orglett.8b00874
 14. Singh, B. K.; **Bairry, G.**; Jana, R. A General Copper/Manganese Cocatalyzed C-H Selenation of Arenes, Heteroarenes, and Alkenes under Air. *ChemistrySelect*, **2017**, 2, 9227-9232. doi.org/10.1002/slct.201701758
 15. Manna, M. K.; **Bairry, G.**; Jana, R. Dual visible-light photoredox and palladium (II) catalysis for dehydrogenative C2-acylation of indoles at room temperature. *Org. Biomol. Chem.*, **2017**, 15, 5899-5903. [DOI:10.1039/C7OB01418J](https://doi.org/10.1039/C7OB01418J)

Right and Permission:**Chapter 1:**

Figure reprinted with permission from *Nat. Rev. Mater.* **2018**, 3, 431-440. Copyright 2018 Nature Portfolio. (**Figure 1.1; Ref. No-8**)

Figure reprinted with permission from *Korean J Chem Eng.*, **2013**, 30, 1667-1680. Copyright 2013 Springer. (**Figure 1.4; Ref. No-24**)

Figure reprinted with permission from *Coord. Chem. Rev.*, **2007**, 251, 2490-2509. Copyright 2013 Elsevier. (**Figure 1.5; Ref. No-25**)

Figure reprinted with permission from *EnergyChem* **2021**, 3, 100067. Copyright 2021 Elsevier. (**Figure 1.9; Ref. No-67**)

Chapter 2:

Reprinted (adapted) with permission from *Inorg. Chem.* **2023**, 62, 12773-12782. Copyright 2023: American Chemical Society.

Chapter 3:

Reprinted (adapted) with permission from *Cryst. Growth Des.* **2022**, 22, 3138-3147. Copyright 2022: American Chemical Society.

Chapter 4:

Reprinted (adapted) with permission from *Dalton Trans.* **2022**, 51, 13749-13761. Copyright 2022: Royal Society of Chemistry.

List of Conferences Attended:

1. **Oral Presentation:** 2-Days International Symposium On “Sustainable Technologies-The Way Forward” and 61st Annual Convention 2024 of Indian Photobiology Society (IPS), University of Engineering and Management, Kolkata, 31st Jan-1st Feb, 2025.
2. **Oral Presentation:** International Conference on “Recent Advances on Green and Sustainable Developments (ICRAGSD-2023)”, Akal University, Punjab, India, 6th-8th September, 2023.
3. **Poster Presentation:** Conference on "Sustainability and Interdisciplinarity in Chemical Sciences, ‘SICS 2023’, IISER Kolkata, India, 13th-15th July, 2023.
4. **Oral Presentation:** International Seminar on-Recent Advances in Chemistry and Material Science (RACMS-2022) organized by the Indian Chemical Society in association with the Bangladesh Chemical Society, Bangladesh.

Awards and Recognition:

1. RSC Best Poster Presentation Prize at the Sustainability and Interdisciplinarity in Chemical Sciences (SICS 2023) conference organized by IISER Kolkata, India, during July 13-15, 2023.
2. Graduate Aptitude Test in Engineering 2016, Chemistry, All India Rank-**128**.
3. Joint CSIR-UGC NET JRF in Chemical Sciences, June 2016, All India Rank-**046**.
4. Joint CSIR-UGC NET JRF in Chemical Sciences, December 2015, All India Rank-**023**.

In Situ Oxidation of Pyridyl-Dihydrobenzoimidazoquinazoline and the Synthesis of a Highly Luminescent Cd(II) Coordination Polymer: A Promising Candidate for Mutagenic Nitroaromatic Detection and Device Fabrication

Gurupada Bairy, Pubali Das, Basudeb Dutta, Saumitra Bhowmik, Partha Pratim Ray, and Chittaranjan Sinha*



Cite This: *Inorg. Chem.* 2023, 62, 12773–12782



Read Online

ACCESS |



Metrics & More

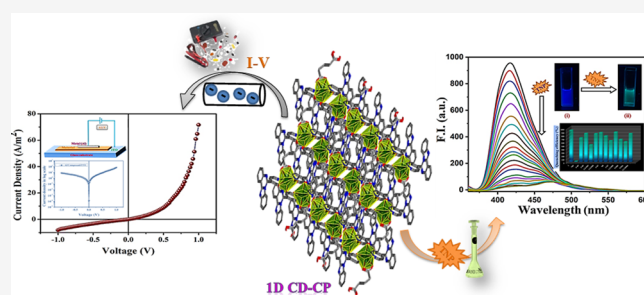


Article Recommendations



Supporting Information

ABSTRACT: Pyridyl-substituted imidazoquinoline, a potent fluorescent framework, is advantageous to architect multifunctional coordination networks for sensing and fabricating emergent electrical conductors. In this work, a Cd(II)-based one-dimensional (1D) coordination polymer (1D CP), $[\text{Cd}(\text{glu})_2(\text{pbiq})_2(\text{H}_2\text{O})]_n$ (**1**), $[\text{H}_2\text{glu} = \text{glutaric acid and pbiq} = 4\text{-(6-(pyridin-4-yl)benzo[4,5]imidazo[1,2-c]quinazoline)]$, has been structurally confirmed by single-crystal X-ray crystallography. The H-bonding and $\pi\cdots\pi$ interactions built a three-dimensional (3D) supramolecular structure that strongly emits at 416 nm in acetonitrile suspension. Potentially intrusive nitroaromatics (NAs) and trinitrophenol (TNP) selectively quench the strong emission of **1**, and the highest quenching is noted in the case of TNP. A detection limit (limit of detection (LOD)) of 1.51×10^{-7} M for TNP is determined. The band gap (3.31 eV) of **1** recognizes semiconducting behavior, and an electronic device is fabricated. The correlation of current vs voltage (I – V plot) reveals a substantial non-ohmic electrical conductivity of **1** (Λ : 1.10×10^{-5} S m^{-1}) along with a low energy barrier (Φ_{B} : 0.69), and the series resistance (R_{s}) becomes 6.21 k Ω .



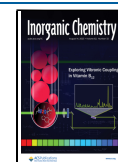
INTRODUCTION

Over the past few years, the design strategy is focused on integrating different functional properties in one system of coordination polymer (CP)/metal–organic framework (MOF) toward the design of multifunctional materials for achieving sustainable development goals (SDGs).^{1–4} Multifunctional materials, a sort of smart material, can be activated by stimulating agents (light, heat, magnetic field, mechanical) to induce new challenging property(ies) that have been associated with the change in geometry of the molecular component of the material.^{5,6} The CPs/MOFs have been drawn into fascinating network topologies in a variety of potent applications due to their tunable pores, large surface area, and variable functionality.^{7,8} They can be used in sensing, electrical conductivity manipulation, gas sorption and separation, variable-temperature magnetism, catalysis, drug delivery, etc.^{9–20} Out of many properties, the sensing of explosives and manipulation of energy-saving materials have attracted intensive attention in science and engineering fields.^{13,21,22} A great deal of interest is being paid to luminescent frameworks for the detection of ions and molecules.^{23–26} A country's defense and security is of primary importance when it comes to selective and sensitive molecular sensing. In comparison,

luminescent CPs are more useful because of higher structural stability even in strenuous and toxic environment, larger surface area and porosities, and faster response rates than those of molecular sensors.^{27–31} Based on the straightforward design approach and structural flexibility, one-dimensional (1D) luminescent CPs are extremely appealing, and such molecules can quickly recognize exogenous analytes because of the better availability of interacting sites with respect to higher-dimensional CPs.^{32,33} Such smooth interactions are extremely significant in terms of selectivity and time to recognition. Moreover, 1D luminescent CPs have the ability to self-assemble into supramolecular aggregates through secondary interactions, which led to better, faster, and smoother performance than their corresponding native form and improvement in thermal and mechanical stability. These supramolecular interactions and aggregation are crucial in the

Received: April 22, 2023

Published: August 2, 2023



2D Cd(II)-MOF of Pyridyl-Imidazoquinazoline: Structure, Luminescence, and Selective Detection of TNP and Fabrication of Semiconducting Devices

Gurupada Bairy,[†] Arka Dey,[†] Basudeb Dutta, Partha Pratim Ray,^{*} and Chittaranjan Sinha^{*}



Cite This: *Cryst. Growth Des.* 2022, 22, 3138–3147



Read Online

ACCESS |



Metrics & More

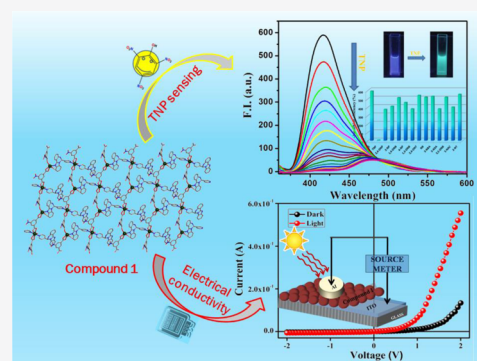


Article Recommendations



Supporting Information

ABSTRACT: Pyridyl-substituted imidazoquinolines are highly fluorescent probes and are useful for the design of smart materials. A hitherto unknown pyridyl-imidazoquinazoline-coordinated two-dimensional (2D)-Cd(II)-MOF $\{[\text{Cd}_2(\text{S-nip})_2(\text{pdq})_2(\text{H}_2\text{O})_2(\text{CH}_3\text{OH})]\cdot\text{H}_2\text{O}\}_n$ (CP 1), $[\text{H}_2\text{nip} = 5\text{-nitroisophthalic acid}$ and $\text{pdq} = 6\text{-(pyridin-4-yl)-5,6-dihydrobenzo}[4,5]\text{imidazo}[1,2-c]\text{quinazoline}]$ has been designed and structurally confirmed by single-crystal X-ray crystallography. The presence of $\text{C-H}\cdots\pi$ and $\pi\cdots\pi$ interactions in CP 1 makes it a three-dimensional (3D) supramolecular structure. The excellent luminescent behavior of CP 1 is selectively quenched by trinitrophenol (TNP) even in the presence of potentially intrusive nitroaromatic explosives (NAEs). A limit of detection (LOD) of 2.75×10^{-7} M for TNP is achieved ($3\sigma/m$). In addition, the CP 1 displays electrical conductivity on an electronic device with the metal–semiconductor (MS) junction. Current vs voltage (I – V plot) correlation reveals the substantial enhancement of electrical conductivity upon illumination (Λ : 1.12×10^{-3} S m^{-1} (dark), 6.33×10^{-3} S m^{-1} (light)) along with a decrease in energy barrier (Φ_B : 0.53 (dark), 0.42 (light)). The plots of $\log V$ vs $\log I$ show a non-Ohmic feature at a higher voltage ($\log V \geq 0$) both in the dark and the light phase, which is the characteristic of a Schottky diode barrier (SDB).



INTRODUCTION

The field of porous coordination polymers (PCPs) or metal–organic frameworks (MOFs) has been of immense interest for the last two decades owing to their high porosity and extraordinary crystallinity.¹ Due to the tunable pore size, large surface area, and variable functionality, intriguing network topologies of PCPs have attracted attention in the field of potent applications such as catalysis, gas sorption and separation, magnetism in variable temperatures, drug delivery, sensing, electrical conductivity, etc.^{2–12} The choice of the metal center, bridging organics, and/or capping groups/ligands define the structural motif of MOFs, whereas temperature, pressure, solvent, pH of the medium and counteranion of the metal salt, etc. represent the different dimensionalities within the MOFs. Both the π -electron-rich organic ligand and aromatic polycarboxylate as building blocks have been widely used to impart luminescent properties to the products. Among MOFs, luminescent frameworks are of great choice of interest to detect ions/molecules.^{13–19} In the field of selective and sensitive molecular sensing, the detection of explosives is of paramount importance, considering the defense and security purposes of a country. The structural stability, size, porosity, surface area, etc., of luminescent MOFs make them more attractive and effective over luminescent molecules because they increase sensitivity, decrease the limit of detection (LOD), increase the rate of response, and reduce the response

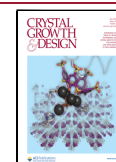
time.^{20–25} Two-dimensional (2D)-MOFs (metal–organic frameworks) have potential advantages over one-dimensional (1D) and three-dimensional (3D)-MOFs due to their more exposed dynamic sites, higher sensitivity, faster response time, better stability, and ultralow limit of detection for sensing applications.²⁶

Nitroaromatic explosives (NAEs), major constituents of explosive materials, are used in land mines, high-explosive shells and armed devices, etc.²⁷ Among various NAEs, 2,4,6-trinitrophenol (TNP) prevails, being even stronger than its well-known counterpart 2,4,6-trinitrotoluene (TNT), and has been broadly used in aniline synthesis, oxidative metal etching, fireworks, matches, and rocket fuels as well as in leather, pharmaceutical, and dye industries.^{28,29} During mass production and indiscriminate commercial uses, it is released into the environment and causes serious health issues.^{30–32} Similarly, TNP is widely used as NAEs in devastating terror attacks, which ultimately turn out to be fatal to human civilization. Therefore, a selective, sensitive, safe, economic, environ-

Received: January 6, 2022

Revised: March 31, 2022

Published: April 12, 2022



PAPER

[View Article Online](#)
[View Journal](#) | [View Issue](#)Cite this: *Dalton Trans.*, 2022, **51**, 13749

Rational synthesis of a pyridyl-imidazoquinazoline based multifunctional 3D Zn(II)-MOF: structure, luminescence, selective and sensitive detection of Al^{3+} and TNP, and its semiconducting device application†

Gurupada Bairy,^{‡a} Arka Dey,^{§c} Basudeb Dutta,^{§b} Suvendu Maity^a and Chittaranjan Sinha^{§*a}

In the age of sustainable development, the exploration of multifunctional materials is of high priority due to their economic benefits and environmental suitability. A stable luminescent coordination polymer, $[\text{Zn}_2(\text{tdc})_4(\text{pdiq})_3]$ (**1**), (pdiq = pyridyl-imidazoquinazoline; H_2tdc = 2,5-thiophenedicarboxylic acid) has been prepared and structurally confirmed by single-crystal X-ray diffraction analysis. The 3D framework consists of a distorted octahedral geometry with a ZnO_4N_2 coordination sphere where four carboxylato-O donations come from two tdc^{2-} as bridging ligands and two pyridyl-Ns come from two pdiq. The $\pi\cdots\pi$ interactions between the imidazolium and phenyl groups bestow robustness on the architecture. The compound is chemically stable to water, shows tolerance to acid/base aqueous solutions (pH = 2–12), and is stable to the impact of organic solvents. The high dispersibility of Zn-MOF (**1**) in acetonitrile may enhance the fluorescence intensity compared to that in water, which prompted fluorescence measurements in the former solvent and it is used for the efficient and selective turn-off ratiometric sensing of Al^{3+} ions (LOD, 1.39×10^{-7} M). In addition, the fluorescence emission of **1** is instantly quenched by trinitrophenol (TNP) and the LOD is 1.54×10^{-7} M. The Tauc's plot is used to measure the semiconducting band gap (3.33 eV) and the electrical conductivity is significantly increased upon illumination (λ : 1.14×10^{-3} S m^{-1} (dark), 5.35×10^{-3} S m^{-1} (light)) and the energy barrier declines marginally (FB: 0.57 (dark), 0.49 (light)). Transit time (τ) and diffusion length (L_D) at the quasi-Fermi level were analyzed to offer information on the charge transport mechanism of the compound. The better performance on photo-irradiation signifies the enhanced charge transfer kinetics of a Zn-MOF coated thin-film device (TFD **1**), which encourages its application in semiconductor devices.

Received 7th June 2022,
Accepted 3rd August 2022

DOI: 10.1039/d2dt01790c

rsc.li/dalton

Introduction

Coordination polymers (CPs) or metal-organic frameworks (MOFs) have received widespread attention as novel materials due to their intriguing architectures, stability, flexibility and versatile applications.^{1,2} Metal-organic frameworks (MOFs), as

a kind of ordered porous hybrid material, have attracted extensive attention in gas storage and separation, molecular magnetism, ion exchange, electrical conductivity, sensing, catalysis and drug delivery.^{3–16} MOFs have been widely engineered to have robust structures and chemical stability by incorporating both appropriate π -electron-rich organic ligands and inorganic secondary building units (SBUs).^{17–20} In recent years, luminescent MOFs (LMOFs) have attracted a lot of attention due to their high selectivity, sensitivity, rapid response, and reversibility as chemical sensors.^{21–25} It is possible to adjust the luminescent properties by picking different metal clusters, and selecting N, O, or S recognition sites, and post-synthesizing modified organic motifs. Sensors based on CPs/MOFs generally detect by either increasing (turning on) or decreasing (turning off) their luminescence intensity at a single wavelength. Ratiometric luminescent sensors, on the other hand,

^aDepartment of Chemistry, Jadavpur University, Kolkata 700 032, India.E-mail: crsjuchem@gmail.com^bDepartment of Chemical Sciences, Indian Institute of Science Education and Research Kolkata, Mohanpur 741246, West Bengal, India^cDepartment of Physics, National Institute of Technology Durgapur, Durgapur 713209, India†Electronic supplementary information (ESI) available. CCDC 2162910. For ESI and crystallographic data in CIF or other electronic format see DOI: <https://doi.org/10.1039/d2dt01790c>

‡These authors contributed equally to this work.

License date	Jun 14, 2025
Licensed Content Publisher	Springer Nature
Licensed Content Publication	Nature Reviews Materials
Licensed Content Title	Liquid, glass and amorphous solid states of coordination polymers and metal–organic frameworks
Licensed Content Author	Thomas D. Bennett et al
Licensed Content Date	Sep 7, 2018
Type of Use	Thesis/Dissertation
Requestor type	academic/university or research institute
Format	print and electronic
Portion	figures/tables/illustrations
Number of figures/tables/illustrations	1
Would you like a high resolution image with your order?	no
Will you be translating?	no
Circulation/distribution	200 - 499
Author of this Springer Nature content	no
Title of new work	Synthesis and Structural Characterization of Coordination Frameworks and Their Potential

SPRINGER NATURE LICENSE TERMS AND CONDITIONS

Jun 14, 2025

This Agreement between Gurupada Bairy ("You") and Springer Nature ("Springer Nature") consists of your license details and the terms and conditions provided by Springer Nature and Copyright Clearance Center.

License Number	6047550654891
License date	Jun 14, 2025
Licensed Content Publisher	Springer Nature
Licensed Content Publication	Korean Journal of Chemical Engineering
Licensed Content Title	Synthesis of metal-organic frameworks: A mini review
Licensed Content Author	Yu-Ri Lee et al
Licensed Content Date	Aug 17, 2013
Type of Use	Thesis/Dissertation
Requestor type	academic/university or research institute
Format	print and electronic
Portion	figures/tables/illustrations
Number of figures/tables/illustrations	1

ELSEVIER LICENSE
TERMS AND CONDITIONS

Jun 14, 2025

This Agreement between Gurupada Bairy ("You") and Elsevier ("Elsevier") consists of your license details and the terms and conditions provided by Elsevier and Copyright Clearance Center.

License Number	6047550394547
License date	Jun 14, 2025
Licensed Content Publisher	Elsevier
Licensed Content Publication	EnergyChem
Licensed Content Title	The chemistry and applications of flexible porous coordination polymers
Licensed Content Author	Nibedita Behera,Jingui Duan,Wanqin Jin,Susumu Kitagawa
Licensed Content Date	Nov 1, 2021
Licensed Content Volume	3
Licensed Content Issue	6
Licensed Content Pages	1
Start Page	100067
End Page	0

protect its copyright in the materials.

9. **Warranties:** Publisher makes no representations or warranties with respect to the licensed material.

10. **Indemnity:** You hereby indemnify and agree to hold harmless publisher and CCC, and their respective officers, directors, employees and agents, from and against any and all claims arising out of your use of the licensed material other than as specifically authorized pursuant to this license.

11. **No Transfer of License:** This license is personal to you and may not be sublicensed, assigned, or transferred by you to any other person without publisher's written permission.

12. **No Amendment Except in Writing:** This license may not be amended except in a writing signed by both parties (or, in the case of publisher, by CCC on publisher's behalf).

13. **Objection to Contrary Terms:** Publisher hereby objects to any terms contained in any purchase order, acknowledgment, check endorsement or other writing prepared by you, which terms are inconsistent with these terms and conditions or CCC's Billing and Payment terms and conditions. These terms and conditions, together with CCC's Billing and Payment terms and conditions (which are incorporated herein), comprise the entire agreement between you and publisher (and CCC) concerning this licensing transaction. In the event of any conflict between your obligations established by these terms and conditions and those established by CCC's Billing and Payment terms and conditions, these terms and conditions shall control.

14. **Revocation:** Elsevier or Copyright Clearance Center may deny the permissions described in this License at their sole discretion, for any reason or no reason, with a full refund payable to you. Notice of such denial will be made using the contact information provided by you. Failure to receive such notice will not alter or invalidate the denial. In no event will Elsevier or Copyright Clearance Center be responsible or liable for any costs, expenses or damage incurred by you as a result of a denial of your permission request, other than a refund of the amount(s) paid by you to Elsevier and/or Copyright Clearance Center for denied permissions.

LIMITED LICENSE

The following terms and conditions apply only to specific license types:

15. **Translation:** This permission is granted for non-exclusive world **English** rights only unless your license was granted for translation rights. If you licensed translation rights you may only translate this content into the languages you requested. A professional translator must perform all translations and reproduce the content word for word preserving the integrity of the article.

16. **Posting licensed content on any Website:** The following terms and conditions apply as follows: Licensing material from an Elsevier journal: All content posted to the web site must maintain the copyright information line on the bottom of each image; A hyper-text must be included to the Homepage of the journal from which you are licensing at <http://www.sciencedirect.com/science/journal/xxxxx> or the Elsevier homepage for books at <http://www.elsevier.com>; Central Storage: This license does not include permission for a scanned version of the material to be stored in a central repository such as that provided by Heron/XanEdu.



RightsLink



In Situ Oxidation of Pyridyl-Dihydrobenzoimidazoquinazoline and the Synthesis of a Highly Luminescent Cd(II) Coordination Polymer: A Promising Candidate for Mutagenic Nitroaromatic Detection and Device Fabrication

Author: Gurupada Bairy, Pubali Das, Basudeb Dutta, et al

Publication: Inorganic Chemistry

Publisher: American Chemical Society

Date: Aug 1, 2023

Copyright © 2023, American Chemical Society

Quick Price Estimate

This service provides permission for reuse only. If you do not have a copy of the portion you are using, you may copy and paste the content and reuse according to the terms of your agreement. Please be advised that obtaining the content you license is a separate transaction not involving RightsLink.

This type of permission/license, instead of the standard Terms and Conditions, is sent to you because no fee is being charged for your order. Please note the following:

- Permission is granted for your request in both print and electronic formats, and translations.
- If figures and/or tables were requested, they may be adapted or used in part.
- Please print this page for your records and send a copy of it to your publisher/graduate school.
- Appropriate credit for the requested material should be given as follows: "Reprinted (adapted) with permission from {COMPLETE REFERENCE CITATION}. Copyright {YEAR} American Chemical Society." Insert appropriate information in place of the capitalized words.
- One-time permission is granted only for the use specified in your RightsLink request. No additional uses are granted (such as derivative works or other editions). For any uses, please submit a new request.

If credit is given to another source for the material you requested from RightsLink, permission must be obtained from that source.

I would like to... ?	reuse in a Thesis/Dissertation ▼	Format ?	Electronic ▼
Requestor Type ?	Author (original work) ▼	Select your currency	USD - \$ ▼
Portion ?	Full article ▼		

Price: 0.00 USD

CONTINUE

To request permission for a type of use not listed, please contact [the publisher](#) directly.



RightsLink

[Sign in/Register](#)


2D Cd(II)-MOF of Pyridyl-Imidazoquinazoline: Structure, Luminescence, and Selective Detection of TNP and Fabrication of Semiconducting Devices

Author: Gurupada Bairy, Arka Dey, Basudeb Dutta, et al

Publication: Crystal Growth and Design

Publisher: American Chemical Society

Date: May 1, 2022

Copyright © 2022, American Chemical Society

Quick Price Estimate

This service provides permission for reuse only. If you do not have a copy of the portion you are using, you may copy and paste the content and reuse according to the terms of your agreement. Please be advised that obtaining the content you license is a separate transaction not involving RightsLink.

This type of permission/license, instead of the standard Terms and Conditions, is sent to you because no fee is being charged for your order. Please note the following:

- Permission is granted for your request in both print and electronic formats, and translations.
- If figures and/or tables were requested, they may be adapted or used in part.
- Please print this page for your records and send a copy of it to your publisher/graduate school.
- Appropriate credit for the requested material should be given as follows: "Reprinted (adapted) with permission from {COMPLETE REFERENCE CITATION}. Copyright {YEAR} American Chemical Society." Insert appropriate information in place of the capitalized words.
- One-time permission is granted only for the use specified in your RightsLink request. No additional uses are granted (such as derivative works or other editions). For any uses, please submit a new request.

If credit is given to another source for the material you requested from RightsLink, permission must be obtained from that source.

I would like to... ?

reuse in a Thesis/Dissertation ▼

Format ?

Electronic ▼

Requestor Type ?

Author (original work) ▼

Select your currency

USD - \$ ▼

Portion ?

Full article ▼

Price: 0.00 USD

CONTINUE

To request permission for a type of use not listed, please contact [the publisher](#) directly.



Order Confirmation

Thank you, your order has been placed. An email confirmation has been sent to you. Your order license details and printable licenses will be available within 24 hours. Please access Manage Account for final order details.

This is not an invoice. Please go to manage account to access your order history and invoices.

CUSTOMER INFORMATION

Payment by invoice: You can cancel your order until the invoice is generated by contacting customer service.

Billing Address

Mr. Gurupada Bairy
Analytical Chemistry Building, Jadavpur University
Kolkata, Jadavpur 700032
India

+91 8820340369
gurupadabairy@gmail.com

PO Number (optional)

N/A

Customer Location

Mr. Gurupada Bairy
Analytical Chemistry Building, Jadavpur University
Kolkata, Jadavpur 700032
India

Payment options

Invoice

PENDING ORDER CONFIRMATION

Confirmation Number: Pending

Order Date: 27-Jun-2025

1. Dalton transactions

0.00 USD

Article: Rational synthesis of a pyridyl-imidazoquinazoline based multifunctional 3D Zn(II)-MOF: structure, luminescence, selective and sensitive detection of Al³⁺ and TNP, and its semiconducting device application

Order License ID	Pending	Publisher	ROYAL SOCIETY OF
ISSN	1477-9234		CHEMISTRY
Type of Use	Republish in a	Portion	Page
	thesis/dissertation		

LICENSED CONTENT

Publication Title	Dalton transactions	Rightsholder	Royal Society of Chemistry
Article Title	Rational synthesis of a pyridyl-imidazoquinazoline based multifunctional 3D Zn(II)-MOF: structure, luminescence, selective and sensitive detection of Al ³⁺ and TNP, and its semiconducting device application	Publication Type	e-Journal
		Start Page	13749
		End Page	13761
		Issue	36
		Volume	51
Author / Editor	Royal Society of Chemistry (Great Britain)		
Date	01/01/2003		
Language	English		
Country	United Kingdom of Great Britain and Northern Ireland		

REQUEST DETAILS

Portion Type	Page	Rights Requested	Main product and any product related to main product
Page Range(s)	1	Distribution	Worldwide
Total Number of Pages	1	Translation	Original language of publication
Format (select all that apply)	Electronic	Copies for the Disabled?	No
Who Will Republish the Content?	Author of requested content	Minor Editing Privileges?	Yes
Duration of Use	Life of current edition	Incidental Promotional Use?	No
Lifetime Unit Quantity	Up to 499	Currency	USD

NEW WORK DETAILS

Title	Synthesis and Structural Characterization of Coordination Frameworks and Their Potential Applications	Institution Name	Jadavpur University
Instructor Name	Gurupada Bairy	Expected Presentation Date	2025-11-20

ADDITIONAL DETAILS

Order Reference Number	N/A	The Requesting Person / Organization to Appear on the License	Gurupada Bairy
------------------------	-----	---	----------------

REQUESTED CONTENT DETAILS

Title, Description or Numeric Reference of the Portion(s)	Synthesis and Structural Characterization of Coordination Frameworks and Their Potential Applications	Title of the Article / Chapter the Portion Is From	Rational synthesis of a pyridyl-imidazoquinazoline based multifunctional 3D Zn(II)-MOF: structure, luminescence, selective and sensitive detection of Al3+ and TNP, and its semiconducting device application
Editor of Portion(s)	Sinha, Chittaranjan; Bairy, Gurupada; Dey, Arka; Dutta, Basudeb; Maity, Suvendu	Author of Portion(s)	Sinha, Chittaranjan; Bairy, Gurupada; Dey, Arka; Dutta, Basudeb; Maity, Suvendu
Volume / Edition	51	Issue, if Republishing an Article From a Serial	36
Page or Page Range of Portion	13749-13761	Publication Date of Portion	2022-09-20

Total Items: 1

Total Due: 0.00 USD

Accepted: Marketplace Permissions General Terms and Conditions and any applicable Publisher Terms and Conditions